

# Sheffield Hallam University

*[57]Fe Mossbauer spectroscopy and complementary analysis of tin coated steel.*

ELLIS, Richard A.

Available from the Sheffield Hallam University Research Archive (SHURA) at:

<http://shura.shu.ac.uk/19618/>

## A Sheffield Hallam University thesis

This thesis is protected by copyright which belongs to the author.

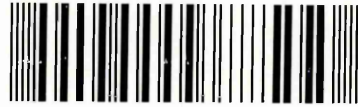
The content must not be changed in any way or sold commercially in any format or medium without the formal permission of the author.

When referring to this work, full bibliographic details including the author, title, awarding institution and date of the thesis must be given.

Please visit <http://shura.shu.ac.uk/19618/> and <http://shura.shu.ac.uk/information.html> for further details about copyright and re-use permissions.

CITY CAMPUS, HOWARD STREET  
SHEFFIELD S1 1WB

101 715 897 5



**REFERENCE**

ProQuest Number: 10694499

All rights reserved

INFORMATION TO ALL USERS

The quality of this reproduction is dependent upon the quality of the copy submitted.

In the unlikely event that the author did not send a complete manuscript and there are missing pages, these will be noted. Also, if material had to be removed, a note will indicate the deletion.



ProQuest 10694499

Published by ProQuest LLC (2017). Copyright of the Dissertation is held by the Author.

All rights reserved.

This work is protected against unauthorized copying under Title 17, United States Code  
Microform Edition © ProQuest LLC.

ProQuest LLC.  
789 East Eisenhower Parkway  
P.O. Box 1346  
Ann Arbor, MI 48106 – 1346



*Sheffield Hallam University*

**$^{57}\text{Fe}$  MÖSSBAUER SPECTROSCOPY AND  
COMPLEMENTARY ANALYSIS OF TIN COATED  
STEEL**

Mr. Richard A. Ellis BSc AMInstP

A thesis submitted in partial fulfilment of the requirements of Sheffield Hallam  
University for the degree of Doctor of Philosophy

June 2003

Collaborating Organisation : Corus plc.



## Declaration

The work described in this thesis was carried out by the author in the School of Science and Mathematics, Sheffield Hallam University, between October 1998 and June 2003. The author declares that this work was not submitted for any other degree. The work is original except where acknowledged by reference.

Author:

(Richard Andrew Ellis)

Supervisor:

(Dr. Sue Forder)

**Mr. Richard A. Ellis BSc AMInstP**

A thesis submitted in partial fulfilment of the requirements of Sheffield Hallam  
University for the degree of Doctor of Philosophy

**ABSTRACT**

<sup>57</sup>Fe Conversion Electron Mössbauer Spectroscopy (CEMS) has been used to identify intermetallic products in commercially and laboratory produced tinned steels. By removing the tin overlayers using a potassium iodate / sodium hydroxide solution any intermetallics from the uppermost surface layer of the samples can be identified. Commercially produced DWI tinplate shows some signs of FeSn<sub>2</sub> on the ironed walls where temperatures reach 200 °C, and no intermetallics on the base where compressive force has been used to compact the tinplate to a required thickness. By heat treating laboratory produced tin electroplated steel, intermetallics have been formed and identified as FeSn<sub>2</sub> using CEMS. The formation of these intermetallics at heat treatments of different temperatures and times has been investigated. The effect of steel surface roughness on the electrodeposition and subsequent identification of the intermetallics formed has also been investigated and increased substrate roughness was found to effectively increase the substrate signal. Carbon coating of the DWI can wall after etching was carried out. Such a technique is shown to be useful when analysing the samples using CEMS as there is an increased differentiation of signal between the substrate and the intermetallics dwelling on the surface.

## CONTENTS

1.	Acknowledgements.....	1
2.	Introduction.....	3
	Introduction References.....	5
3.	Mössbauer Spectroscopy.....	6
3.1	Introduction.....	6
3.2	Resonance Fluorescence.....	7
3.3	Mössbauer Effect Theory.....	10
3.3.1	Theoretical Linewidth of the Emitted 14.4keV $\gamma$ -Ray.....	10
3.3.2	Recoil Energy Loss and Doppler Broadening.....	13
3.3.3	Recoil Free Nuclear Resonance Absorption.....	18
3.4	Experimental Observation of the Mössbauer Effect.....	27
3.5	Hyperfine Interactions.....	28
3.5.1	The Isomer shift.....	30
3.5.2	The Quadrupole Interaction.....	34
3.5.3	The Magnetic Hyperfine Interaction.....	40
	Mössbauer Spectroscopy References.....	48
4.	Literature Review.....	50
4.1	Iron.....	50
4.2	Steel Production.....	54
4.2.1	Production and Refining.....	54
4.2.2	The Bessemer Process.....	55

4.2.3	The Siemens-Martin Open Hearth Process.....	55
4.2.4	The Basic Oxygen Process.....	56
4.2.5	The Electric Arc Furnace.....	58
4.2.6	Steel Refining.....	59
4.2.7	Ingot Production.....	60
4.2.8	Continuous Casting.....	60
4.2.9	Shaping and Finishing.....	61
4.2.10	Flat Roll Mills.....	62
4.2.11	Alloy Steels.....	65
4.3	Tin.....	67
4.4	Tinplate Production.....	68
4.5	Drawn and Wall Ironed Tinplated Steel.....	73
4.6	The Fe-Sn System.....	80
4.6.1	$\text{Fe}_3\text{Sn}$ Structure.....	83
4.6.2	$\text{Fe}_5\text{Sn}_3$ Structure.....	83
4.6.3	$\text{Fe}_3\text{Sn}_2$ Structure.....	84
4.6.4	$\text{FeSn}$ Structure.....	84
4.6.5	$\text{FeSn}_2$ Structure.....	85
4.7	Mössbauer Studies of Fe-Sn Phases.....	86
4.7.1	Mössbauer Studies of $\text{Fe}_3\text{Sn}$ .....	87
4.7.2	Mössbauer Studies of $\text{Fe}_5\text{Sn}_3$ .....	88
4.7.3	Mössbauer Studies of $\text{Fe}_3\text{Sn}_2$ .....	89
4.7.4	Mössbauer Studies of $\text{FeSn}$ .....	89
4.7.5	Mössbauer Studies of $\text{FeSn}_2$ .....	90

4.8	Studies of Tinplate.....	92
4.9	Mössbauer Studies of Tinplate.....	95
4.10	Mössbauer Studies of Intermetallics and Corrosion Products.....	96
4.11	Detection Techniques.....	99
4.12	Mössbauer Signal Depth.....	108
	4.12.1 Mössbauer Signal Depth Theory.....	108
	4.12.2 Studies of Signal Depth.....	109
	4.12.3 Adding Inert Layers for Signal Analysis.....	110
	Literature Review References.....	112
5.	Experimental.....	125
5.1	$\gamma$ -Ray Source for Mössbauer Studies.....	125
5.2	Backscatter Mössbauer Spectroscopy Instrumentation.....	128
	5.2.1 Introduction.....	128
	5.2.2 CEMS Introduction.....	129
	5.2.3 Operation of the CEMS Mössbauer Spectrometer .....	132
	5.2.4 Electron Detection.....	136
	5.2.5 Transmission Mössbauer Spectroscopy Instrumentation.....	138
	5.2.6 $\gamma$ -Ray Detection.....	140
	5.2.7 Spectrometer Calibration.....	141
5.3	Sample Preparation.....	142
	5.3.1 Introduction.....	142
	5.3.2 Electrodeposition of Tin onto Steel Substrates.....	145
	5.3.2.1 Sample Preparation.....	145
	5.3.2.2 Bath Preparation.....	146

5.3.3	Heat Treatment of Tinplate.....	150
5.3.4	Etching of Tinplate.....	152
5.3.5	Carbon Coating.....	152
5.3.5.1	Carbon Coating Experimentation.....	152
5.4	Mössbauer Software.....	155
	Experimental References.....	157
6.	Complementary Analytical Techniques.....	158
6.1	Introduction.....	158
6.2	Scanning Electron Microscopy (SEM).....	158
6.3	X-Ray Diffraction (XRD).....	161
6.3.1	X-Ray Diffraction Techniques.....	161
6.3.2	X-Ray Diffraction Experimental Detail.....	163
6.4	Glow Discharge Optical Emission Spectroscopy (GDOES).....	166
6.4.1	GDOES Theory.....	166
6.4.2	GDOES Experimental Detail.....	168
6.5	Inductively Coupled Plasma Mass Spectrometry (ICP-MS).....	170
6.6	Talysurf.....	171
	Complementary Analytical Techniques References.....	173
7.	Results and Discussion.....	174
7.1	Analysis of Steel Sheet.....	174
7.1.1	<sup>57</sup> Fe CEMS Analysis of Steel Sheet.....	174
7.1.2	SEM Analysis of Steel Sheet.....	176
7.2	Analysis of DWI Tinplated Steel Cans.....	178
7.2.1	<sup>57</sup> Fe CEMS Analysis of DWI Tinplated Steel Cans.....	179

7.2.2	<sup>119</sup> Sn Mössbauer Analysis of DWI Tinned Steel Cans.....	183
7.2.3	SEM Analysis of DWI Tinned Steel Cans.....	186
7.2.4	GDOES Analysis of DWI Tinned Steel Cans.....	197
7.2.5	Summary of Analysis of DWI Tinned Steel Cans.....	198
7.3	Analysis of Etched DWI Tinned Steel Cans.....	199
7.3.1	<sup>57</sup> Fe CEMS Analysis of Etched DWI Tinned Steel Cans..	199
7.3.2	<sup>119</sup> Sn Mössbauer Analysis of Etched DWI Tinned Steel Cans.....	203
7.3.3	SEM Analysis of Etched DWI Tinned Steel Cans.....	206
7.3.4	Summary of Analysis of Etched DWI Tinned Steel Cans.	208
7.4	Results of Analysis of Can Bases.....	208
7.4.1	<sup>57</sup> Fe CEMS Analysis of DWI Tinned Steel Can Bases..	209
7.4.2	SEM Analysis of DWI Tinned Steel Can Bases.....	211
7.4.3	Summary of Analysis of DWI Tinned Steel Can Bases....	214
7.5	Preliminary Analysis of Flowbrightened Tinplate.....	214
7.6	Preliminary Heat Treatment Studies.....	216
7.6.1	<sup>57</sup> Fe CEMS Analysis of Heat-Treated DWI Tinned Steel Cans.....	217
7.6.2	XRD Analysis of Heat-Treated DWI Tinned Steel Cans.....	223
7.7	Analysis of Lacquer Coated DWI Tinned Steel Cans.....	232
7.7.1	<sup>57</sup> Fe CEMS Analysis of Lacquer Coated DWI Tinned Steel Cans .....	232

7.7.2	SEM Analysis of Lacquer Coated DWI Tinplated Steel Cans.....	234
7.8	Analysis of Washed and Unwashed DWI Tinplated Steel Cans.....	235
7.8.1	<sup>57</sup> Fe CEMS Analysis of Washed and Unwashed DWI Tinplated Steel Cans.....	236
7.8.2	SEM Analysis of Washed and Unwashed DWI Tinplated Steel Cans.....	238
7.9	Results of Analysis of Tinplate Sheet Material.....	242
7.10	Results of Analysis of Tinplate With Defects.....	250
7.10.1	<sup>57</sup> Fe CEMS Analysis of Tinplate With Defects.....	250
7.10.2	SEM Analysis of Tinplate With Defects.....	255
7.10.3	Summary of Analysis of Tinplate With Defects.....	260
7.11	Results of Heat Treatment of Tinplate.....	261
7.11.1	SEM Analysis of Electrodeposited Tinplate.....	262
7.11.2	Discussion of Intermetallic Formation During Heat Treatment Process.....	263
7.11.3	<sup>57</sup> Fe CEMS Analysis of Varying Time of Heat Treatment...	266
7.11.4	<sup>57</sup> Fe CEMS Analysis of Varying Temperature of Heat Treatment.....	270
7.11.5	ICP-MS Analysis of Heat Treated Samples .....	275
7.11.6	GDOES Analysis of Heat Treated Samples.....	278
7.11.7	<sup>119</sup> Sn and <sup>57</sup> Fe Mössbauer Analysis of Heat Treated DWI Can.....	279
7.11.8	Summary of Analysis of Heat Treatment of Tinplate.....	284

7.12	Results of Carbon Coating.....	284
7.12.1	Profilometer Measurements of Carbon Thickness.....	285
7.12.2	<sup>57</sup> Fe CEMS Analysis of Carbon Coated Polished Steel Samples.....	289
7.12.3	<sup>57</sup> Fe CEMS Analysis of Carbon Coated DWI Tinplate Samples.....	293
7.13	Sample Roughness Effects in Mössbauer Spectroscopy.....	299
7.13.1	Roughness Measurements of Substrates.....	299
7.13.2	Sample Preparation and SEM Analysis of Electrodeposited Coatings .....	303
7.13.3	<sup>57</sup> Fe CEMS Analysis of Roughness Samples.....	312
7.13.4	XRD Studies of Substrate Roughness.....	324
7.13.5	Introduction to XRD Analysis of Heat-Treated Tinplate Samples.....	331
7.13.6	XRD Results for Polished 1 μm Sample Using Bragg-Brentano Configuration.....	331
7.13.7	XRD Results for Polished 1 μm Sample Using Glancing Angle Configuration.....	334
7.13.8	XRD Results for Ground P600 Sample Using Bragg-Brentano Configuration.....	336
7.13.9	XRD Results for Ground P600 Sample Using Glancing Angle Configuration.....	338
7.13.10	XRD Results for Ground P120 Sample Using Bragg-Brentano Configuration.....	341

7.13.11 XRD Results for Ground P120 Sample Using Glancing Angle Configuration.....	344
7.13.12 Summary of Roughness Analysis Findings.....	346
Results and Discussion References.....	348
8. Conclusions and Future Work.....	350
Appendix 1 : Carbon Evaporation Calculations.....	361
Appendix 2 : Courses and Events Attended.....	370
Appendix 3 : Publications.....	372

## 1. ACKNOWLEDGEMENTS

I would like to acknowledge the help and support of the following groups:

Materials Research Institute, Sheffield Hallam University.

Swinden Technology Centre, Corus.

The School of Science and Mathematics, Sheffield Hallam University.

In particular I would like to thank my director of studies Dr. Sue Forder, who throughout the period of my studies has been a source of sound advice and guidance. Also I would like to thank a host of other people who have been involved in this project. Firstly the Mössbauer group comprising Mr. Mark Bamford who gave particular help on the Mössbauer software side of things and played a mean game of pool and Mr. Martin Charlesworth for help with the Mössbauer equipment and the many games of football.

I would also like to acknowledge the assistance of the following people who have also been involved in this project. Dr. Tim English for the provision of samples and being my supervisor and Prof. Chris Breen for being my second supervisor; Mr. Bob Burton for technical assistance and sample preparation; Dr. Kevin Tinkham for assistance with the tinfoil etching; Mr. Paul Slingsby, Mrs. Cheryl Shaw and Mr. Stephen Porter for assistance with the SEM work; Dr. Brian Lewis for assistance with the XRD work; Dr Philip Gardiner and Mr. Paul Collins for assistance with the ICP-MS work; Dr. Mike Simmonds for assistance with the GDOES and profilometer work;

Mr. Mac Jackson for assistance with the Talysurf work; Dr. Petra Ernst and Mr. Tony Earnshaw for assistance with the tin electrodeposition and Dr. Fritz Wagner for  $^{119}\text{Sn}$  Mössbauer Spectroscopy work.

Finally I would like to thank my Mum and Dad for all the support they have given me throughout my life, and in particular throughout the long years of university study, and Charlotte for always being there for me and putting up with the never-ending thesis writing.

## 2. INTRODUCTION

The formation of intermetallic phases influences the physical properties of commercial alloys. It is therefore important to identify the phases that are formed under different conditions. Mössbauer spectroscopy has the resolution that enables the different intermetallic phases to be identified within such systems as the Fe-Sn, Fe-Zn and Fe-Al systems. Any corrosion products that are present can also be uniquely identified by using Mössbauer spectroscopy.

The use of other analytical techniques, such as X-Ray Diffraction (XRD) and Scanning Electron Microscopy (SEM), can be used to help characterise the intermetallic phases that are formed when steel substrates are given various industrial surface coatings including Tin, Zinc and Aluminium. These phases play an important role in determining the properties of the final product such as corrosion resistance, ductility, weldability, paintability and strength.

This study focuses on expanding knowledge of Fe-Sn intermetallic formation and the detection of these intermetallics using Conversion Electron Mössbauer spectroscopy (CEMS). To these ends samples of tinplated steels have been manufactured under laboratory conditions and analysed alongside commercially produced tinplate supplied by Corus. Intermetallics and corrosion products present in these samples can be detected by the use of CEMS. Scanning Electron Microscopy has been used to analyse sample topography in sheet tinplate and Drawn and Wall Ironed (DWI) tinplate (see

section 4.5) and CEMS of tinplate and DWI cans has been done and intermetallic formation has been analysed.

The DWI process is used to form food and beverage cans by using a series of dies to extrude a circular blank of tinplate into the can shape. A previous study [1] indicated varying tinplate thickness on the can wall of DWI cans and these results have been confirmed using SEM. The process of tinplate production and drawing and ironing of the blank is analysed to identify any formation of Fe-Sn intermetallics.

These studies of the DWI can will provide knowledge pertaining to the properties and behaviour of the material and the DWI process itself. Thus the information can be of great importance to industry, especially those industries involved in canmaking where information regarding intermetallic phases can be used to improve the can manufacture process. This study has also been used to evaluate the sensitivity of the Mössbauer technique for such analysis and thus the information obtained can be used to inform us of what future work is required and perhaps how the experiments can be modified, including any modifications to detector design.

## **Introduction References**

- [1] W. van Koesveld and J.S. van Westrum, From Blank to Can : Origin and Growth of the Morphology of the Wall of a DWI Can, Third International Tinplate Conference, ITRI, London (1985) 310-318.

### 3. MÖSSBAUER SPECTROSCOPY

#### 3.1 Introduction

Mössbauer spectroscopy was developed from the theory of resonant absorption, which was first observed in optical systems by Wood [1] in the early 20<sup>th</sup> century. The nuclear analogue of resonant absorption was predicted by Kuhn in 1929 [2] and observed by Moon in 1951 [3]. In 1958 Rudolf Mössbauer [4-8] observed the phenomenon of recoil free resonance fluorescence in a nuclear system. In his experiments, as the temperature was reduced, he observed an increased absorption cross section of the 129 keV  $\gamma$ -ray emitted in the decay mechanism of  $^{191}\text{Ir}$ . Previous theory had predicted a decrease in the absorption cross section as it was thought that a reduction of temperature should produce a decrease in linewidth of the thermal absorption and emission lines.

At least 111 transitions of 90 isotopes in 46 different elements have been identified [9,10] which exhibit the Mössbauer effect, and over 10 are used experimentally, without great difficulty, to investigate materials. The vast majority of experimentation has focused on two particular isotopes  $^{57}\text{Fe}$  and  $^{119}\text{Sn}$ . This is because of the suitability of the isotopes to the technique in terms of half-life and natural linewidth  $\Gamma$ . The  $^{57}\text{Fe}$  isotope is the most commonly used because of the wide use of iron and steels in industrial applications and is the primary isotope used within this study.

The Mössbauer effect uses  $\gamma$ -rays with energies of approximately 5 to 100 keV and the lifetimes of the associated excited states are  $10^{-10}$  s to  $10^{-6}$  s. Therefore the natural linewidths are of the order of  $10^{-8}$  eV which is small enough to allow analysis of the hyperfine structure of nuclear energy levels. The Mössbauer effect allows high energy resolutions of up to  $1 : 10^{12}$  which is much higher than other comparable spectroscopic techniques.

### 3.2 Resonance Fluorescence

The well-known physical phenomenon of resonance fluorescence, from which the Mössbauer effect was developed, comprises a resonance absorption and subsequent re-emission from the absorber. Resonance fluorescence was first demonstrated in the optical system by Robert Wood using the scattering of sodium light by sodium vapour [1]. Without absorption the system is as in figure 3.1 where S is the source, A is the absorber and I, and II are detectors used to detect fluorescent radiation, where in this case if nothing is detected at detector II then no absorption and re-emission has taken place and similarly if no reduction in transmitted intensity is observed at detector I then no absorption has occurred.

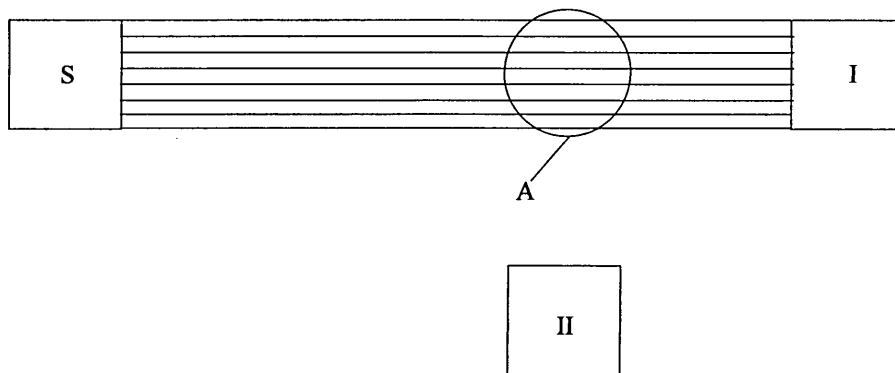


Figure 3.1. No resonant absorption.

Resonant absorption can occur at the nuclear level where  $\gamma$ -rays can be absorbed by a nucleus which raises its energy level. This is analogous to atomic systems where, for example, sodium light can be scattered by sodium vapour or a dipole can be excited by radio frequency radiation. When the absorbing nucleus relaxes back to the ground level it emits  $\gamma$ -rays, of the same energy as those absorbed, in a random direction. This is illustrated in figure 3.2. If a radioactive isotope, for example  $^{57}\text{Co}$ , decays producing an excited daughter nucleus, in this case  $^{57}\text{Fe}$ , and then this daughter nucleus de-excites by emitting  $\gamma$ -rays then it is possible to have a stable nucleus of that isotope absorbing and subsequently re-emitting those  $\gamma$ -rays. This is the effect known as resonance fluorescence.

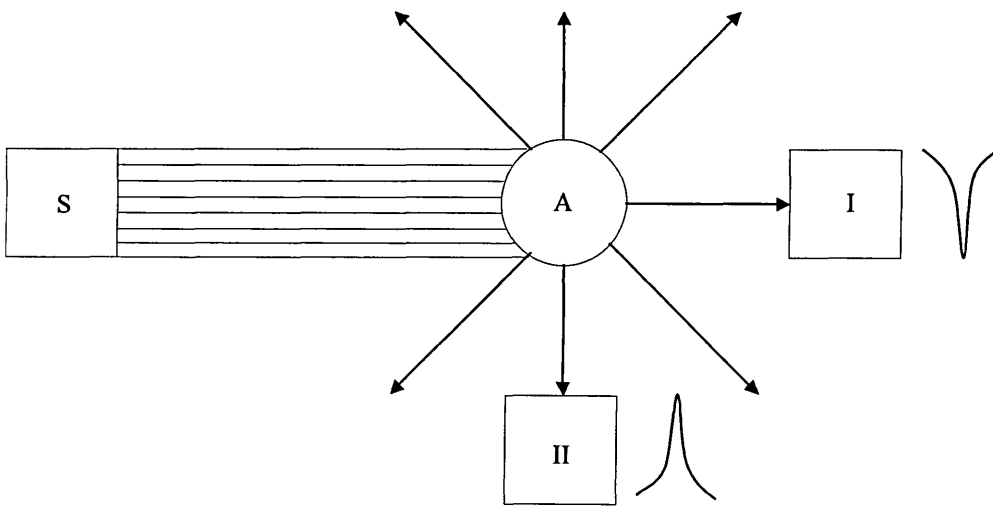


Figure 3.2. System with resonant absorption and re-emission.

Resonance fluorescence in a nuclear system involves much higher energies than in atomic systems and the effects of recoil and Doppler broadening are much greater. In the atomic system the energies involved are small and the atomic masses are comparatively large (see table 3.1) which means that recoil has little effect on the

momentum of the radiation and is negligible when compared to the Doppler broadening which arises from the random thermal velocity of the nuclei. The nuclear system however involves much higher energies and thus recoil in these systems is not negligible and is in fact comparable to the Doppler broadening.

Table 3.1 below illustrates the differences in energies for the excited state of the emitting nucleus,  $E_1$ , the recoil energy,  $E_R$  and the Doppler broadening,  $E_D$ , assuming an atomic mass of 100 at room temperature [11].

	Optical Emission	$\gamma$ -ray Emission
$E_1$	2 eV	$10^5$ eV
$E_R$	$2 \times 10^{-11}$ eV	$10^{-1}$ eV
$E_D$	$10^{-6}$ eV	$10^{-1}$ eV

Table 3.1. Differences between optical and nuclear systems.

Resonance absorption is possible when the excited level has a natural width,  $\Gamma$ , greater than the recoil energy. If the excited level has a natural width,  $\Gamma$ , that is less than the recoil energy then resonance absorption is not possible. Resonance absorption is always possible in atomic transitions because the recoil energy  $10^{-11}$  eV is very much less than the natural width,  $\Gamma = 10^{-8}$  eV. However for nuclear transitions the photons have energies of typically  $10^4 - 10^5$  eV compared to 1 eV for atomic transitions and so the recoil energy is greater than the natural width,  $\Gamma$ , of the nuclear levels. Thus resonance absorption is not always possible in nuclear transitions and therefore it is more difficult to observe nuclear resonance fluorescence.

### 3.3 Mössbauer Effect Theory

#### 3.3.1 Theoretical Linewidth of the Emitted 14.41 keV $\gamma$ -Ray

The radioactive isotope  $^{57}\text{Fe}$  is produced by the electron capture decay of  $^{57}\text{Co}$ , as shown in figure 3.3. The decay scheme of  $^{57}\text{Co}$  gives the emission of three  $\gamma$ -rays (14.41, 122.07, and 136.48 keV).

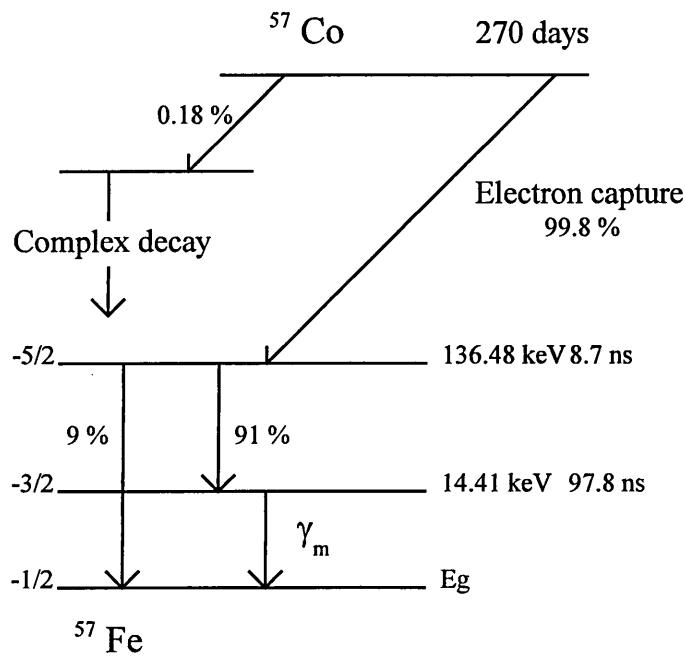
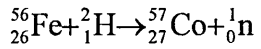


Figure 3.3. Decay scheme for  $^{57}\text{Co}$ .

These sources are produced by bombarding  $^{56}\text{Fe}$  (91.52% abundance in natural iron) with deuterons ( $^2_1\text{H}$ ), with energies of about 9.5 MeV, forming  $^{57}\text{Co}$  and neutrons as the following reaction shows,



The emitted Mössbauer  $\gamma$ -rays,  $\gamma_m$ , have a Lorentzian energy distribution centred about a mean energy,  $E_0$ , and have a natural linewidth,  $\Gamma$ , at half height as shown in figure 3.4.

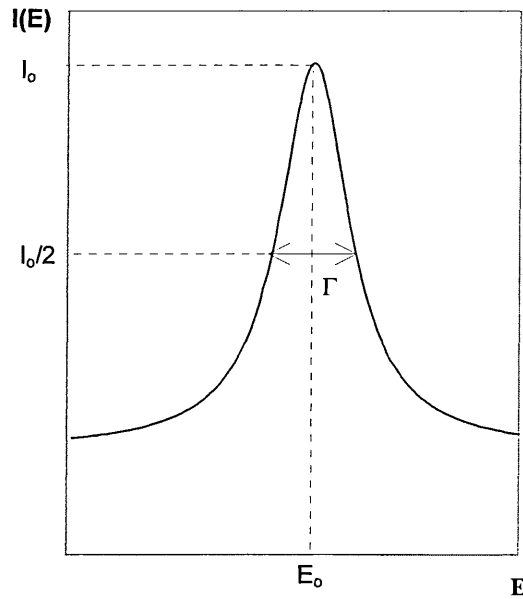


Figure 3.4. The Lorentzian distribution of the emitted  $\gamma$ -rays.

The Breit Wigner formula [12] describes an energy distribution about energy  $E_0$  and this leads to a Lorentzian  $\gamma$ -ray energy distribution described by the equation

$$I(E) = \text{const.} \left( \frac{\Gamma}{2\pi} \right) \frac{1}{(E - E_0)^2 + \left( \frac{\Gamma}{2} \right)^2} \quad (3.1)$$

The approximate linewidth,  $\Gamma$ , at half height may be determined from the Heisenberg uncertainty principle corresponding to an uncertainty in the energy  $\Delta E$ , where,

$$\Delta E \Delta t \approx \hbar \text{ and } \Delta E = \Gamma \quad (3.2)$$

i.e.  $\Gamma = \left( \frac{\hbar}{\Delta t} \right)$  where  $\hbar = \frac{h}{2\pi}$  and  $\Delta t$  is the lifetime of the excited state.

( $h = \text{Planck's constant} = 6.626 \times 10^{-34} \text{ J s}$ )

i.e.  $\Delta t \equiv \tau = 1/\lambda$  where  $\lambda$  is the Decay constant and  $\tau$  is the mean life, related to the half-life,  $t_{1/2}$ , by the relationship:

$$\tau = \frac{t_{1/2}}{\ln 2} \quad (3.3)$$

$$\text{Hence } \Gamma = \frac{\hbar \ln 2}{t_{1/2}} \quad (3.4)$$

The 14.4 keV excited state of the  $^{57}\text{Fe}$  nucleus has a half-life which has been given values of  $98 \pm 4 \text{ ns}$  [13],  $98 \pm 1 \text{ ns}$  [14],  $97.7 \pm 0.2 \text{ ns}$  [15],  $99.3 \pm 0.5 \text{ ns}$  [16] and  $97.81 \text{ ns}$  [17]. Substituting the last of these values, most commonly used today, into equation 3.4, the theoretical linewidth,  $\Gamma$ , is calculated to be  $4.7 \times 10^{-9} \text{ eV}$ .

This therefore gives a theoretical resolution of :

$$\frac{\Gamma}{E_0} = \frac{4.7 \times 10^{-9}}{14.4 \times 10^3} \approx \frac{1}{10^{12}} \quad (3.5)$$

Recoil free nuclear resonance fluorescence occurs by the superposition of the emission and absorption Mössbauer  $\gamma$ -ray energy distributions associated with both the source and the absorber.

### 3.3.2 Recoil Energy Loss and Doppler Broadening

In order to observe the energy transitions associated with the Mössbauer effect we must consider two factors. The first of these factors is that the effective linewidth is increased by Doppler broadening due to the vibration of atoms and the second factor is that there is a displacement of the emission line from the absorption line due to the recoil of the emitting nucleus. Thus resonance absorption is very difficult to observe. By having the emitting nucleus held at low temperature within a solid matrix Mössbauer discovered that rather than the recoil momentum of the emitted  $\gamma$ -ray acting on a single nucleus there is a high probability that the recoil will be absorbed by the whole crystal lattice.

The physical mechanisms of this discovery can be described by considering a nucleus of mass,  $M$ , moving with an initial velocity,  $v_T$ , due to thermal motion and with

excited state energy,  $E_e$ . The energy difference between the ground state of the nucleus,  $E_g$ , and the excited state,  $E_e$  is described as,

$$E = E_e - E_g \quad (3.6)$$

Then the total energy of the nucleus above the ground state before  $\gamma$ -ray emission is  $E + \frac{1}{2}M(v_T)^2$ . The  $\gamma$ -ray will have an energy  $E_\gamma$  after emission. The nucleus in the ground state with ground state energy  $E_g$  will have a velocity of  $v_T + v$  where  $v$  is the velocity due to recoil and is a vector such that it can be in the opposite direction to  $v_T$ . The total energy is then  $E_\gamma + \frac{1}{2}M(v_T + v)^2$ .

Therefore, by the law of conservation of energy:

$$E + \frac{1}{2}M(v_T)^2 = E_\gamma + \frac{1}{2}M(v_T + v)^2 \quad (3.7)$$

The difference between the nuclear transition energy and the emitted  $\gamma$ -ray energy is then,

$$E - E_\gamma = \frac{1}{2}M(v_T + v)^2 - \frac{1}{2}M(v_T)^2 \quad (3.8)$$

$$E - E_\gamma = \frac{1}{2}Mv^2 + Mv_Tv \quad (3.9)$$

which may be written as,

$$\delta E = E_R + E_D \quad (3.10)$$

It can be therefore be seen that the  $\gamma$ -ray energy differs from the nuclear energy level separation by an amount which depends on the recoil kinetic energy term,  $E_R = \frac{1}{2}Mv^2$ , and by the term  $E_D = Mv_T v$ , a Doppler-effect energy which depends on the magnitude and sign of the atom velocity,  $v_T$ , and therefore results in a broadening and not a shift.

At speeds below the speed of light it is permissible to determine the magnitude of the Doppler broadening for the one dimensional case using non-relativistic mechanics.

The mean kinetic energy of an atom in a gas with random thermal motion is given by

$$\overline{E_K} = \frac{1}{2}M\overline{v_T^2} = \frac{1}{2}kT \quad (3.11)$$

$$\left(\overline{v_T^2}\right)^{\frac{1}{2}} = \sqrt{\frac{kT}{M}} \quad (3.12)$$

where  $\overline{v_T^2}$  is the mean square velocity of the atoms,  $k$  is the Boltzmann constant and  $T$  is the absolute temperature.

So from equations 3.9 and 3.10,  $E_D = Mv_T v$ , and this can be rewritten substituting from equation 3.12 and thus we obtain,

$$E_D = Mv \left( \frac{v^2}{v_T^2} \right)^{\frac{1}{2}} = Mv \sqrt{\frac{kT}{M}} \quad (3.13)$$

$$E_D = \sqrt{MkTv^2} \quad (3.14)$$

However  $E_R = \frac{1}{2}Mv^2$  and so,

$$E_D = \sqrt{2kTE_R} \quad (3.15)$$

And thus by substituting 3.11 into 3.15 we obtain,

$$E_D = 2\sqrt{E_K E_R} \quad (3.16)$$

Therefore the probability that resonance will occur depends on the magnitude of  $E_R$ . The  $\gamma$ -ray distribution is shifted by  $E_R$  and broadened by twice the mean of the average thermal energy and the recoil energy. It can also be seen from equation 3.15 that if recoil is eliminated then the thermal broadening will be zero and theoretical resolution is achievable. Due to the quantised nature of the lattice vibrations this condition of zero recoil emission is achieved for some nuclear transitions. The values of  $E_R$  and  $E_D$  can be expressed in terms of  $\gamma$ -ray energy  $E_\gamma$ ,

$$E_R = \frac{1}{2}Mv^2 = \frac{(Mv)^2}{2M} = \frac{p^2}{2M} \quad (3.17)$$

where  $p$  is the atom's recoil momentum which is equal and opposite to the  $\gamma$ -ray photon momentum,  $p_\gamma$ ,

$$p = -p_\gamma = -\frac{E_\gamma}{c} \quad (3.18)$$

and hence,

$$E_R = \frac{E_\gamma^2}{2Mc^2} \quad (3.19)$$

Substituting equation 3.19 into equation 3.16 we obtain,

$$E_D = 2\sqrt{E_K E_R} = E_\gamma \sqrt{\frac{2E_K}{(Mc^2)}} \quad (3.20)$$

The same mechanism applies to a nucleus absorbing a  $\gamma$ -ray, the atom undergoing recoil in an equal and opposite reaction. Emission of the  $\gamma$ -ray from the source results in an energy shift of the emission profile,  $E_\gamma = E - E_R$  and similarly a  $\gamma$ -ray energy shift of  $E_\gamma = E + E_R$  occurs in the absorption profile. Figure 3.5 shows the effect of  $E_R$  and Doppler broadening on both the emission and absorption energy distributions.

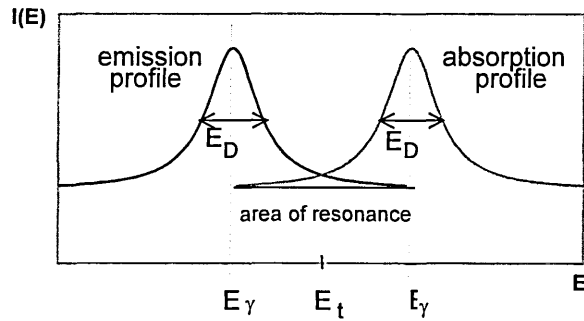


Figure 3.5. Energy distribution profiles showing the effect of recoil and thermal Doppler broadening.

It is necessary to eliminate the effects of recoil in order to observe resonance fluorescence as, for transition energies of the order of  $10^4$  eV,  $E_R$  is significant and there is little overlap of the energy profiles. The effect of Doppler broadening needs to be minimised as it increases the linewidth and therefore decreases resolution.

### 3.3.3 Recoil-Free Nuclear Resonance Absorption

Recoil free nuclear resonance fluorescence occurs by the superposition of the emission and absorption energy distributions associated with both the source and the absorber as discussed previously. Prior to the discovery of the Mössbauer effect efforts towards the experimental detection of nuclear resonance absorption focussed on compensating for the recoil energy whereas the Mössbauer effect eliminates the recoil energy removing the need to compensate for it. The energies of the source and the absorber could be made to overlap by using the Doppler effect in a number of ways including thermal motion [18] or, in the most direct method, by mechanical movement, first successfully achieved by Moon in 1950 [3] using an ultracentrifuge (high speed rotor) to accelerate a 411 keV  $\gamma$ -ray source, emitted in the decay of  $^{198}\text{Hg}$  to  $^{198}\text{Au}$ , to

$10^4 \text{ cm s}^{-1}$  (1600 mph /  $670 \text{ m s}^{-1}$ ) and shift the emission spectrum towards the absorption spectrum of a stationary absorber, figure 3.6 [3].

While investigating the 129 keV transition of  $^{191}\text{Ir}$  [6] Mössbauer found, contrary to prediction, that by cooling the  $^{191}\text{Ir}$  source and absorber a strong increase of nuclear resonance absorption was observed at low temperatures.

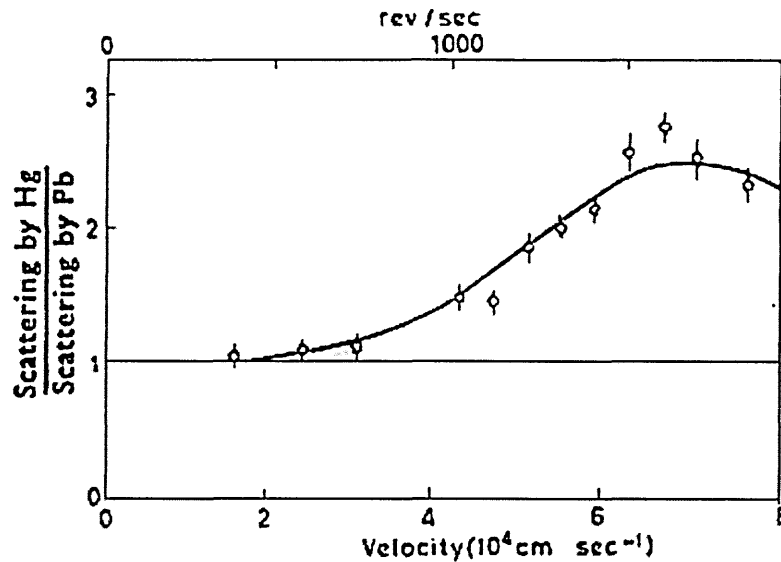


Figure 3.6. Increase in spectra overlap for increased source Doppler velocity [3].

By extrapolating from earlier theory on neutron capture  $\gamma$ -rays [19] Mössbauer assumed that the whole lattice took the effect of the recoil impulse and not the individual emitting atom. As can be seen from equation 3.19 the mass of the whole crystallite is then considered, and a powder, which contains at least  $10^{15}$  atoms will show a reduction in  $E_R$  by a factor of  $10^{15}$  making it negligible.  $E_D$ , from equation 3.20, is also negligible under these circumstances. Thus Mössbauer created the

conditions for recoil-free nuclear resonance absorption as opposed to all the preceding methods, which compensated for the recoil energy.

The free atom recoil energies are considerably smaller than the chemical binding and lattice energies in solids, which are of the order of 1-10 eV. If, due to such chemical binding, the emitting atom is unable to recoil without restriction then the mass affected by the recoil can be regarded to be the mass of the whole crystal. The nucleus in a solid is not however bound immovably in the crystal lattice, but is free to vibrate about its lattice position and so this assumption somewhat simplifies the system. However, during the period of the nuclear decay, the recoil energy is still transferred to the whole crystal because the mean displacement of the vibrating atom about its lattice position averages to zero over the decay time. The recoil energy of a single nucleus can be either absorbed by the whole crystal or transferred to the vibrational energy of the lattice.

The crystal lattice may be considered to be a quantum mechanical system with quantised phonon energy levels allowing the transfer of recoil energy to the lattice only if the energy closely corresponds to one of the discrete quantum jumps. This phonon quantisation will be extremely complex, and the simplest mathematical treatment considers the vibrational characteristics to be described by the Einstein model of solids [20].

Classically it had been accepted that a continuum of energy could be absorbed or emitted by an oscillator, however in 1906 Einstein proved that a solid was indeed a

quantum mechanical system with quantised energy levels. Then if the lattice energies were quantised only certain allowable transitions would be able to occur through phonon interactions.

The Einstein model of solids assumes that a single lattice vibration frequency,  $\omega_E$ , will have discrete allowed energy levels given by

$$E_n = n\hbar\omega_E, \quad (3.21)$$

where  $n$  is a positive integer. The minimum quantum of energy that is required to excite the lattice is thus

$$E_E = \hbar\omega_E, \quad (3.22)$$

where  $E_E$  is termed the Einstein energy which corresponds to a single phonon transition of the lowest allowed energy  $E_E$  and is thus the minimum energy required to excite the lattice. If the recoil energy is less than this quantised energy then no energy is transmitted and thus there is no recoil.

If  $E_R \gg E_E$ , many phonon interactions are involved due to the displacement of the nucleus from its mean position and the energy is transferred to the vibrational energy of the lattice. This is likely when the emitted  $\gamma$ -rays have energies between 0.1-1 MeV and causes the  $\gamma$ -rays to experience energy recoil and Doppler line broadening. Higher energy emitted  $\gamma$ -rays can have recoil energies large enough to be comparable to the

atomic binding energy and cause lattice defects by effectively ejecting the atom from its lattice site.

If  $E_R < E_E$  then a zero phonon interaction occurs and the energy is absorbed by the recoil of the whole crystal lattice and not into the phonon spectrum. The emitted  $\gamma$ -rays, which are those that have an energy range of 10-100 keV, then do not suffer any Doppler broadening effects. In this case, when numerous emission processes are considered, either zero or one unit of vibrational energy must be transferred to the lattice, this is because the average energy transferred during an event must be equal to  $E_R$  [21]. So a fraction,  $f$ , of the emission events will occur as zero phonon transitions resulting in no energy transfer to the lattice and a corresponding fraction  $(1-f)$  will transfer one phonon of energy. So

$$E_R = (1 - f)\hbar\omega_E \quad (3.23)$$

or

$$f = \frac{1 - E_R}{\hbar\omega_E} \quad (3.24)$$

In a zero phonon emission the whole crystal recoils and since  $E_R$  and  $E_D$  are dependent on the reciprocal of the mass,  $M$ , of the recoiling crystal, then both the recoil energy and Doppler broadening become much less than the natural linewidth,  $\Gamma$ , and are negligible.

The vibrational properties of a lattice are usually very complex and require a more suitable model. A more complex model, the Debye model [22,23,24], embodies a continuum of oscillator frequencies ranging from zero up to a maximum  $\omega_D$ , relinquishing the constraint of a single vibration frequency. The Debye model follows the distribution

$$N\omega = \text{const} \times \omega^2 \quad (3.25)$$

A characteristic temperature called the Debye temperature,  $\theta_D$ , is defined by

$$\hbar\omega_D = k\theta_D \quad (3.26)$$

with an average frequency

$$\bar{\hbar\omega} = \frac{3}{4}\hbar\omega_D \quad (3.27)$$

Due to the complexity of the vibrational properties of the lattice the Debye model is still inadequate especially for compounds and is not entirely accurate even for pure metals. The values of  $\theta_D$  used are merely an indication of the approximate lattice properties and therefore should only be used quantitatively.

It has been shown that the probability of zero phonon events occurring or the recoil-free fraction,  $f$ , depend on three conditions, the free atom recoil energy which is

proportional to the square of the  $\gamma$ -ray energy  $E_\gamma$ , the properties of the solid crystal lattice and the ambient temperature.

The greater the probability of exciting lattice vibrations the smaller the recoil free fraction,  $f$ , becomes. By using the dispersion theory [21,22], the probability  $W$  of a zero-phonon event arising from a nucleus embedded in a solid lattice which changes its vibration state is found quantitatively to be proportional to the square of the matrix element connecting the initial,  $|i\rangle$ , and final,  $\langle f|$ , states.

$$W = \text{const} \times \left| \langle f | H | i \rangle \right|^2 \quad (3.28)$$

where  $H$  is the interaction Hamiltonian operator. The forces within the lattice are long range compared to the extremely short range forces acting within the nucleus [19]. Therefore the matrix element can be split into two parts because the nuclear decay is independent of the vibrational state. The nuclear part is constant and so the matrix element can be reduced to just one term for the transition.

$$W = \text{const} \times \left| \langle L_f | e^{ik \cdot x} | L_i \rangle \right|^2 \quad (3.29)$$

where  $k$  is the wave vector for the emitted  $\gamma$ -photon, and  $x$  is the co-ordination vector of the decaying nucleus mass centre. The lattice modes are unchanged for a zero-phonon emission and then we can define the probability for recoilless emission as

$$f = \text{const} \times \left| \langle L_i | e^{ikx} | L_i \rangle \right|^2 \quad (3.30)$$

Since  $L_i$  is normalised the above equation can be written as

$$f = \left| e^{ikx} \right|^2 \quad (3.31)$$

$$f = e^{-k^2 x^2} \quad (3.32)$$

$x^2$  can be replaced by  $\langle x^2 \rangle$ , the component of the mean square vibrational amplitude of the emitting atom in the direction of the  $\gamma$ -ray, because  $x$  is a random vibration vector,

$$f = e^{-k^2 \langle x^2 \rangle} \quad (3.33)$$

since  $k^2 = \frac{4\pi^2}{\lambda^2} = \frac{E_\gamma^2}{(\hbar c)^2}$ , where  $\lambda$  is the  $\gamma$ -ray energy wavelength, we obtain,

$$f = \exp\left(\frac{-4\pi^2 \langle x^2 \rangle}{\lambda^2}\right) = \exp\left(\frac{-E_\gamma^2 \langle x^2 \rangle}{(\hbar c)^2}\right) \quad (3.34)$$

Using the Debye model for a monoatomic cubic lattice the temperature dependence of the recoil-free fraction,  $f$ , can be defined as [25,26]

$$f = \exp \left[ -\frac{6E_R}{k\theta_D} \left( \frac{1}{4} + \left( \frac{T}{\theta_D} \right)^2 \int_0^{\theta_D/T} \frac{x}{e^x - 1} dx \right) \right] \quad (3.35)$$

which is often written in shorter form as,

$$f = e^{-2W} \quad (3.36)$$

where  $W$  is called the Debye-Waller factor which was actually derived as a part of the Bragg X-ray scattering theory but is used frequently in this context. Equation 3.35 has the following high and low temperature approximations

$$f = \exp \left[ -\frac{E_R}{k\theta_D} \left( \frac{3}{2} + \frac{\pi^2 T^2}{\theta_D^2} \right) \right] \quad T \ll \theta_D \quad (3.37)$$

$$f = \exp \left[ -\frac{3E_R}{2k\theta_D} \right] \quad T = 0 \quad (3.38)$$

$$f = \exp \left[ -\frac{6E_R T}{k\theta_D^2} \right] \quad T \geq \frac{1}{2}\theta_D \quad (3.39)$$

Equation 3.39 shows that  $f$  is proportional to  $T$  at high temperatures, however it is often found experimentally that  $f$  at high temperatures has a non-linear relationship with temperature [27] indicating a deviation from the Debye model, which assumes harmonicity in the lattice vibrational modes [28].

### 3.4 Experimental Observation Of The Mössbauer Effect

The experimental arrangement for the emission of a 14.41 keV Mössbauer  $\gamma$ -ray emitted by a  $^{57}\text{Co}$  source and absorption in an absorber containing  $^{57}\text{Fe}$  in an identical lattice using transmission geometry are illustrated in figure 3.7. The intensity of the radiation that passes through the absorber is observed using the detector. Due to resonant absorption and subsequent re-emission over a  $4\pi$  solid angle this intensity will be less than the intensity prior to entering the absorber. See section 5.2 for detailed experimental details of the CEMS and transmission geometry systems.

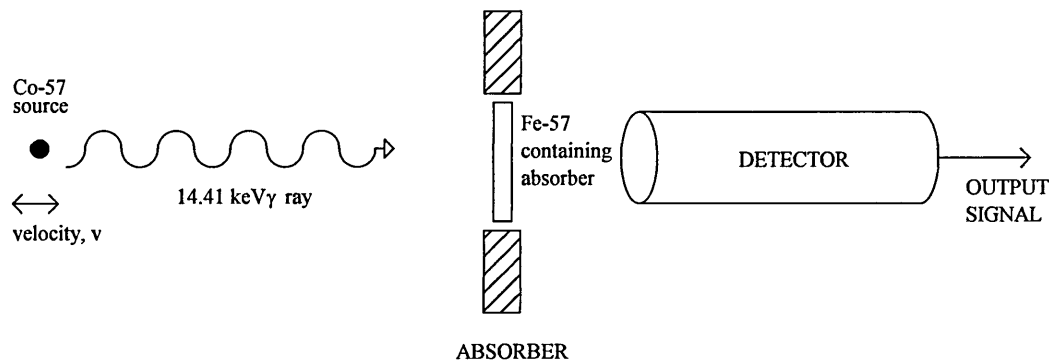


Figure 3.7. Schematic representation of a Mössbauer experiment.

In order to observe the resonance, a Doppler velocity,  $v$ , is applied to the source by mounting the source on a moving platform, with the absorber fixed in position, thereby producing an energy shift of the source spectral line. The emitted  $\gamma$ -ray will have its energy,  $E_\gamma$ , modified by the Doppler relationship

$$E_{\gamma} = E_0 \pm \frac{E_0 v}{c} \quad (3.40)$$

By using constant acceleration applied to the source, a range of velocities can be scanned. Resonance absorption will be observed when, at a particular velocity and hence energy, both the emission and absorption profiles are exactly coincident. The Mössbauer spectrum is then a plot of absorption against a series of Doppler velocities between the accelerated source and fixed absorber.

If the source and absorber have different transition energies, then by Doppler shifting, the emitted  $\gamma$ -ray energy resonance can be achieved. The differences in the nuclear energy levels between source and absorber are due to the electronic and magnetic environment of the absorbing nuclei. Thus the chemical and physical environment of the absorbing nucleus can be investigated using the Mössbauer spectroscopy technique.

### **3.5 Hyperfine Interactions**

Hyperfine interactions are the interactions between the nuclei and the surrounding atomic electrons that have interaction energies greater or equal to the natural linewidth of the Mössbauer radiation. Applications of the Mössbauer effect exploit its extremely high precision energy resolution, which for the  $^{57}\text{Fe}$  system has been shown to be approximately  $1 : 10^{12}$ , which makes possible the analysis of the hyperfine structure of the nuclear transitions.

Normally a single line source is used to analyse the hyperfine interactions of an absorber containing a stable Mössbauer isotope. The source matrix is chosen to have a large recoil free fraction and a linewidth as near to  $\Gamma$  as possible. The absorber is then mounted in place and the radioactive source is fixed to a velocity transducer. The hyperfine interactions cause splitting of the nuclear energy levels and Mössbauer absorption within the absorber then takes place at a number of distinct Doppler energies. The count rate registered then alters when absorption takes place when the emitted  $\gamma$ -ray coincides with the absorption energy as the Doppler velocity applied to the source.

The three hyperfine interactions studied in Mössbauer spectroscopy are :

- 1) The Isomer Shift
- 2) The Quadrupole Interaction
- 3) The Magnetic Hyperfine Interaction

These hyperfine interactions are explained in more detail in several reference books [23, 26, 29, 30, 31, 32]. The interactions can be described as a product of a nuclear and a solid state factor. The nuclear factors are constant for any given Mössbauer  $\gamma$ -ray transition and are determined when the isotope is chosen. It is the changes in the solid state factors in different absorbers or at different temperatures that are analysed experimentally. A schematic representation of the hyperfine interactions is given in table 3.2.

	Magnetic Hyperfine Interaction	Quadrupole Interaction	Isomer Shift
Solid State Factor	Magnetic Field H	Electronic Field Gradient $\nabla E$	Electron Density at Nuclear site $\rho(0)$
Interaction	$\Delta E = \mu H$	+ QVE	+ const $\langle R^2 \rangle \rho(0)$
Nuclear Factor	Nuclear Magnetic Moment $\mu$	Nuclear Quadrupole Moment Q	Mean Square Nuclear Charge Radius $\langle R^2 \rangle$

Table 3.2. Schematic representation of the hyperfine interactions.

### 3.5.1 The Isomer Shift

The term isomer shift pertains to the difference in electrostatic interaction as a consequence of the difference in the nuclear radii of the ground and excited states. Describing the nucleus as a point charge which interacts electrostatically with the electronic charge which surrounds and penetrates it is often adequate. However the nucleus has a finite volume and therefore for the purpose of understanding the attributes of the isomer shift,  $\delta$ , it is necessary to contemplate the nucleus-electron interaction in more depth. This finite volume must be taken into account when considering nucleus-electron interactions since the s-electron density wavefunction implies a non-zero electron charge density within the nuclear volume. A change in s-electron density such as might arise from a change in valency will result in a change in the coulomb interaction which produces a shift in the nuclear energy levels as shown in figure 3.8.

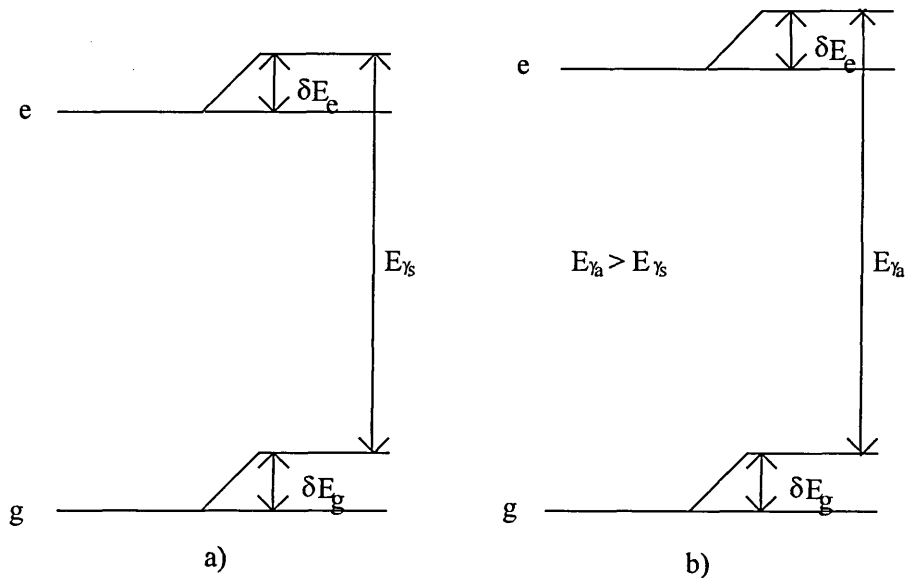


Figure 3.8. Isomer shift of the nuclear energy levels (a) single line source and (b) single line absorber.

(Not to scale)

This results in the following Mössbauer spectrum :

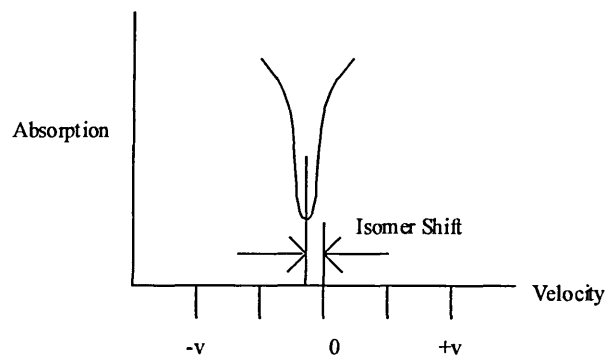


Figure 3.9. Mössbauer spectra showing isomer shift.

Since the change in the coulomb interaction is only a small fraction of the total coulomb interaction it is not possible to measure the energy change directly. However comparison of the values is possible by using a suitable reference such as the  $\gamma$ -ray emitted from the Mössbauer source.

The isomer shift of a nuclear level can be calculated using a simple model of the nucleus where the nucleus is considered as a uniformly charged sphere of radius,  $R$  with a constant s-electron density  $|\Psi(0)|^2$  at the nucleus.

By calculating the difference between the electrostatic interaction of a nucleus having a radius  $R$  and the interaction of a point nucleus, the interaction energies can be estimated. The energy difference,  $\delta E$ , is given by the following equation:

$$\delta E = \frac{2\pi}{5} Z e^2 |\Psi(0)|^2 R^2 \quad (3.41)$$

The nuclear radius,  $R$ , is usually different for the ground and excited states,  $\delta E_{gd}$  and  $\delta E_{ex}$  respectively and therefore equation 3.41 becomes:

$$\delta E_{ex} - \delta E_{gd} = \frac{2\pi}{5} Z e^2 |\Psi(0)|^2 (R_{ex}^2 - R_{gd}^2) \quad (3.42)$$

where the values of the nuclear radii,  $R$ , are nuclear constants and  $|\Psi(0)|^2$  varies dependent upon the material.

The energy difference becomes measurable in a Mössbauer experiment by comparing the nuclear transition energy in the source,  $E_s$  with the nuclear transition energy in the absorber,  $E_a$ .

$$E_s = E_0 + \frac{2\pi}{5} Ze^2 \left[ |\Psi_s(0)|^2 \right] (R_{ex}^2 - R_{gd}^2) \quad (3.43)$$

$$E_a = E_0 + \frac{2\pi}{5} Ze^2 \left[ |\Psi_a(0)|^2 \right] (R_{ex}^2 - R_{gd}^2) \quad (3.44)$$

The isomer shift is given by the difference in transition energies for the source and absorber :

$$E_a - E_s = \delta = \frac{2\pi}{5} Ze^2 \left[ |\Psi_a(0)|^2 - |\Psi_s(0)|^2 \right] (R_{ex}^2 - R_{gd}^2) \quad (3.45)$$

The change in the radius  $R_{ex} - R_{gd}$  is very small and thus the isomer shift can be represented by :

$$\delta = \frac{4\pi}{5} Ze^2 R^2 \left( \frac{\delta R}{R} \right) \left[ |\Psi_a(0)|^2 - |\Psi_s(0)|^2 \right] \quad (3.46)$$

where  $\delta R = R_{ex} - R_{gd}$  is the change in nuclear radius.

For a given nucleus both  $\delta R/R$  and  $|\Psi_s(0)|^2$  are constant, and the isomer shift can be related to  $|\Psi_a(0)|^2$  once the sign of  $\delta R/R$  is known.  $\delta R/R$  for the  $^{57}\text{Fe}$  system is less than zero and as  $|\Psi_a(0)|^2$  increases the isomer shift decreases. Hence an increase in the isomer shift indicates a decrease in s-electron density.

It is not only s-electron density variations that cause isomer shift changes though, addition or removal of p-electrons or d-electrons also cause isomer shift changes. However p-electrons and d-electrons do not directly interact with the nuclear charge density but instead provide a screening effect that effectively decreases the s-electron density at the nucleus. So the isomer shift provides information relating to the chemical bonding in the atom. Therefore the Mössbauer absorption line for non-identical source and absorber does not occur at zero Doppler velocity and the Doppler velocity necessary for resonance is measured as the isomer shift in  $\text{mm s}^{-1}$ .

### 3.5.2 The Quadrupole Interaction

When considering the isomer shift it is assumed that the nucleus is spherical with uniform charge density distribution, however this is only true for nuclei with spin angular momentum of 0 or  $\frac{1}{2}$ . Nuclei with a greater spin angular momentum have a non-spherical charge density distribution and therefore assume either an oblate or prolate shape. The nuclear quadrupole interaction arises from the interaction of the nuclear quadrupole moment,  $Q$ , with the gradient of the localised electric field. The nuclear quadrupole moment reflects the deviation of the nucleus from spherical symmetry as shown in figure 3.10. The sign of  $Q$  is positive when the nucleus is elongated along the spin axis (prolate) and negative when flattened along the spin axis (oblate).

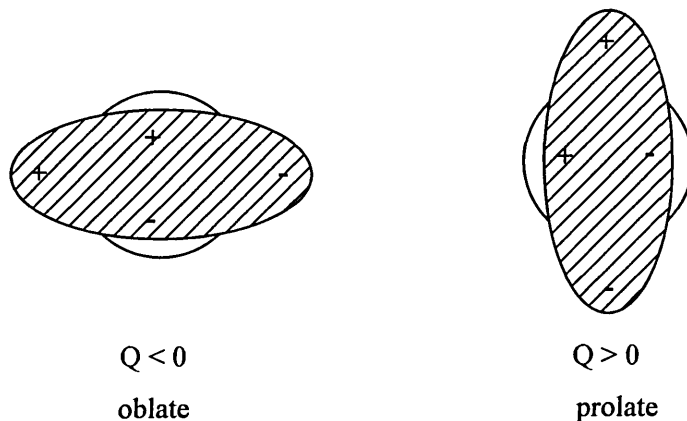


Figure 3.10. Deviation of nucleus from spherical symmetry.

$Q$  is expressed by equation 3.47 [26]

$$eQ = \int \rho r^2 (3 \cos^2 \theta - 1) d\tau \quad (3.47)$$

where  $e$  is the charge of the proton, and  $\rho$  is the charge density in the volume element  $d\tau$  which is at a distance  $r$  from the centre of the nucleus and at an angle  $\theta$  to the nuclear spin quantisation axis.

The quadrupole interaction comprises two factors. A nuclear factor,  $eQ$ , which is constant for a given isotope and a solid state factor,  $e q$ , which is a function of the chemical environment due to the nature of the electric field gradient (EFG).

The electric field gradient is found by applying the gradient operator to the three components of the electric field that is itself a vector. The result is a  $3 \times 3$  tensor which can be reduced to three finite 'principal' components which are usually written as  $V_{xx}$ ,

$V_{yy}$  and  $V_{zz}$ . These components do not exist independently and are related by the Laplace equation [33] in a region where the charge density vanishes such that,

$$V_{xx} + V_{yy} + V_{zz} = 0 \quad (3.48)$$

and the asymmetry parameter defined as:

$$\eta = \frac{|V_{xx} - V_{yy}|}{V_{zz}} \quad (3.49)$$

The components are usually chosen using the convention  $|V_{zz}| > |V_{xx}| > |V_{yy}|$  which ensures that  $0 \leq \eta \leq 1$ . Evaluation of  $\eta$  from a Mössbauer spectrum is relatively straightforward, however, relating  $\eta$  to the electronic structure of the material being studied is more difficult because the observed sign of  $e^2qQ$  is an important factor in deciding the origin of the EFG. To overcome this problem the simplest approach is to consider a point charge model of the EFG for computing the relative magnitude of the EFG [23, 34, 35].

The EFG has two sources. The first source of the EFG is termed the valence contribution,  $q_{val}$ . In an atom each electron contributes to a component of the EFG tensor. The total value of  $V_{zz} \neq 0$  if the electron orbital population is non-spherical. The second source of the EFG is termed the lattice contribution,  $q_{lat}$ , resulting from distant ion charge from associated ligands.  $q_{val}$  and  $q_{lat}$  are not independent components due to shielding effects. By assuming an inverse cubic dependence on

distance,  $q_{\text{val}}$  is also much larger than  $q_{\text{lat}}$ . The resulting quadrupole splitting of a Mössbauer spectrum is therefore particularly useful for supplying detail regarding the spin state and the distribution geometry of the material under study.

The quadrupole interaction produces an energy change,  $E_Q$ , which is given by the following equation [29, 36] :

$$E_Q = \frac{e^2 q Q}{4I(2I-1)} [3m_I^2 - I(I+1)] \left(1 + \frac{\eta^2}{3}\right)^{1/2} \quad (3.50)$$

where  $e$  is the electronic charge,  $eq$  is the maximum value of the field gradient,  $Q$  is the nuclear quadrupole moment,  $I$  is the spin state of the level,  $m_I$  is the magnetic quantum number and  $\eta$  is the associated asymmetry factor.

The quadrupole interaction results in a splitting of the excited nuclear energy levels and partial removal of degeneracy, which produces two equal probability energy transitions. For the  $^{57}\text{Fe}$  system  $I_e = 3/2$  and  $I_g = 1/2$ . The  $I_e = 3/2$  level splits into two levels,  $m_I = \pm 3/2$  and  $m_I = \pm 1/2$ . The  $I_g = 1/2$  level does not exhibit a quadrupole interaction and remains degenerate. This produces a characteristic Mössbauer 'doublet' spectrum which, in general, will be combined with an isomer shift. The separation of the two peaks is the quadrupole splitting,  $\Delta$  (or  $\Delta E_Q$ ), and by convention is quoted in units of  $\text{mm s}^{-1}$ . Figure 3.11 shows the quadrupole splitting of the nuclear energy levels and figure 3.12 shows the resulting Mössbauer spectrum.

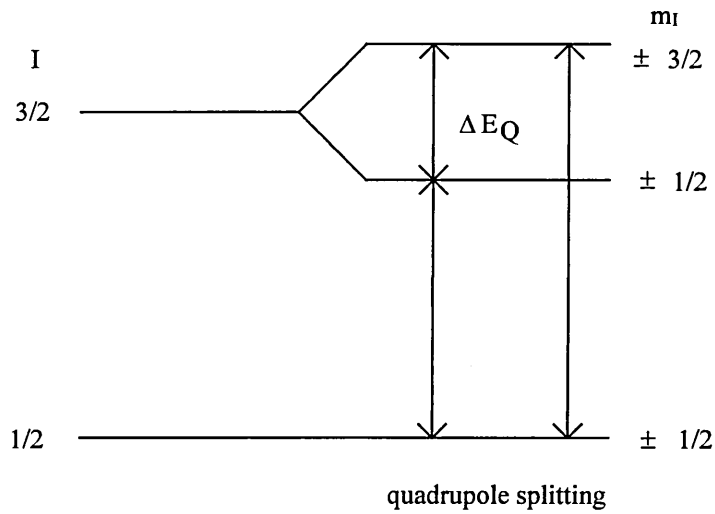


Figure 3.11. Energy level diagram of quadrupole splitting of nuclear energy levels for  $^{57}\text{Fe}$  system. (Not to scale)

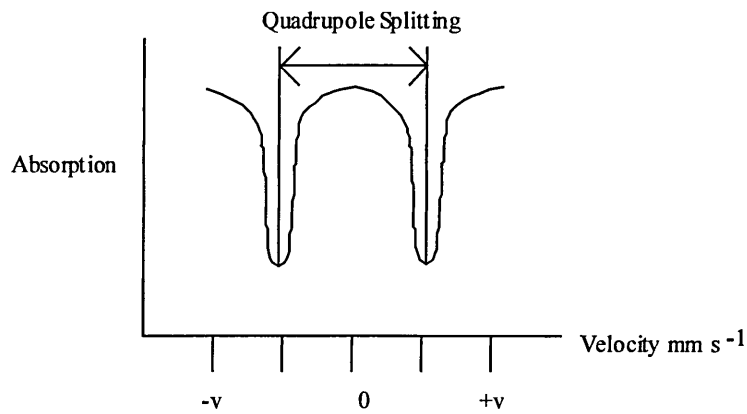


Figure 3.12. Mössbauer spectrum showing quadrupole splitting of nuclear energy levels for  $^{57}\text{Fe}$  system.

The characteristic Mössbauer 'doublet' spectrum from the quadrupole interaction will, in general, be combined with an isomer shift. The separation of the two peaks is the quadrupole splitting and the shift from having the peak at zero velocity is the isomer shift.

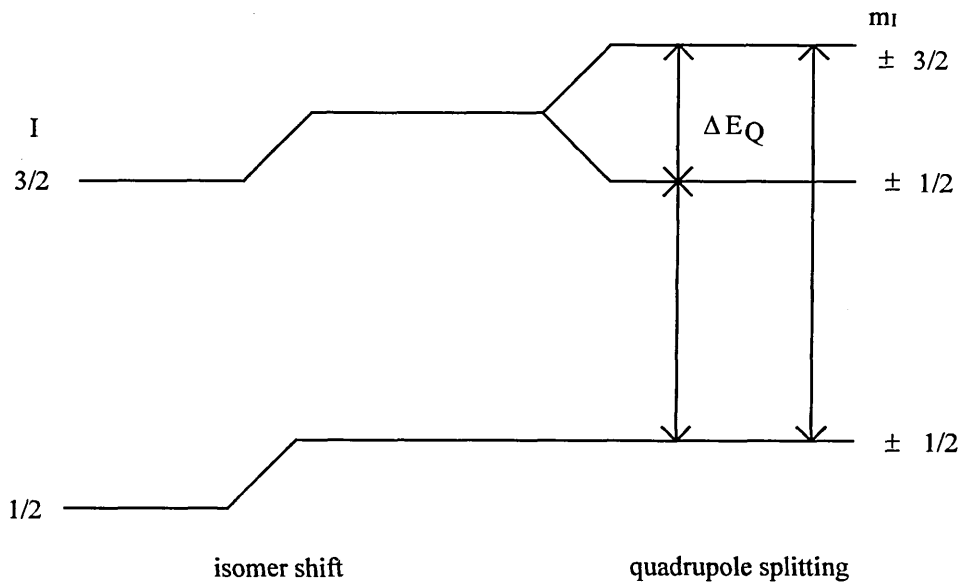


Figure 3.13. Energy level diagram of quadrupole splitting of nuclear energy levels and isomer shift for  $^{57}\text{Fe}$  system. (Not to scale)

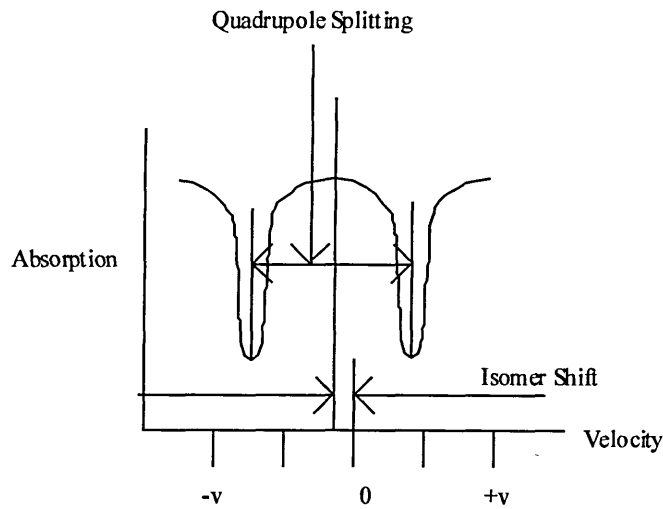


Figure 3.14. Mössbauer spectrum showing quadrupole splitting of nuclear energy levels and isomer shift for  $^{57}\text{Fe}$  system.

Figure 3.13 shows the quadrupole splitting of the nuclear energy levels combined with the isomer shift and figure 3.14 shows the resulting Mössbauer spectrum. In terms of

<sup>57</sup>Fe CEMS analysis in this study no quadrupole splitting was identified, however, the <sup>119</sup>Sn work does include some quadrupole splitting in combination with the other hyperfine interactions and therefore is important for such analysis.

### 3.5.3 The Magnetic Hyperfine Interaction

The magnetic hyperfine interaction, like the other two hyperfine interactions, is the product of the interaction of a nuclear factor, the nuclear magnetic dipole moment,  $\mu$ , with the magnetic hyperfine field,  $H$ , existing at the nucleus which is a solid state factor. The nuclear magnetic dipole moment is constant for a given isotope, and the magnetic hyperfine field is dependent on the electronic structure of the material under study.

This interaction results in energy levels given by

$$E_m = -\mu H \frac{m_I}{I} = -\mu_N g H m_I \quad (3.51)$$

where,

$I$  = nuclear spin

$\mu_N$  = nuclear magneton

$g$  = gyromagnetic ratio or nuclear g-factor

The magnetic interaction completely removes the spin degeneracy of the Zeeman splitting, splitting each level into  $(2I + 1)$  equally spaced sub-levels. The splitting

between adjacent levels being  $g\mu_N H$ . For the  $^{57}\text{Fe}$  system  $g$  differs in sign for the ground and excited states. A characteristic  $^{57}\text{Fe}$  Mössbauer spectrum arises from application of the selection rule ( $\Delta m_I = 0$  or  $\pm 1$ ) which describes the allowed Mössbauer transitions.

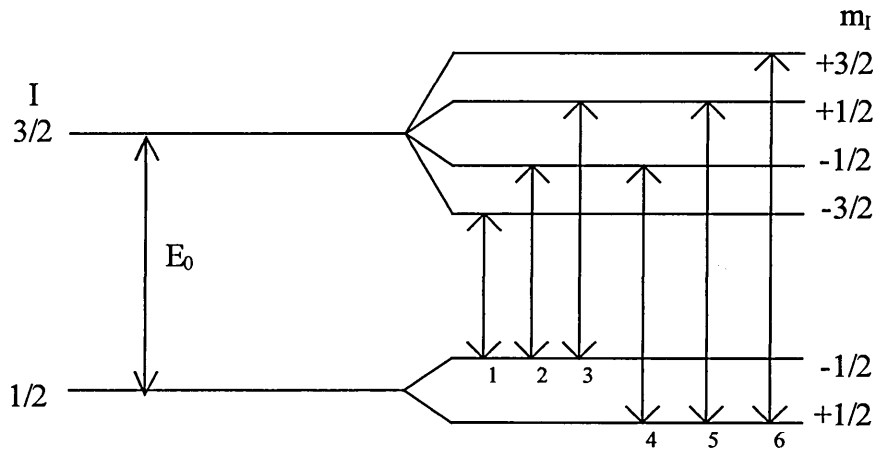


Figure 3.15. Nuclear energy level scheme of magnetic splitting. (Not to scale)

The excited state with  $I = 3/2$  splits into four levels, and the ground state,  $I = 1/2$ , splits into two levels. This gives the possibility of six allowed transitions, figure 3.15, producing a sextet spectrum as shown in figure 3.16. The separation of the peaks is directly proportional to the magnetic hyperfine field strength,  $H$ , at the nucleus, which in the case of  $\alpha\text{-Fe}$  is 33T.

The linewidths of the six transition peaks are generally equal however the relative intensities of the peaks depend on whether the incident  $\gamma$ -ray beam is perpendicular or parallel to the magnetic field. If the beam is parallel the relative intensities of the six

transition peaks will be 3:2:1:1:2:3, if the beam is perpendicular then they will be 3:4:1:1:4:3.

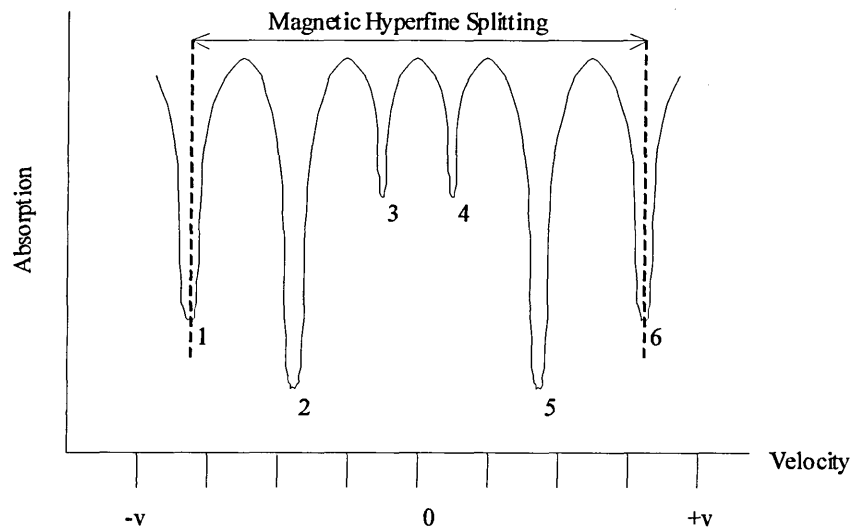


Figure 3.16. Mössbauer spectrum of the magnetic splitting of the  $^{57}\text{Fe}$  system.

The line intensities are calculated from the following equations :

$$I_1 = I_6 = 3(1 + \cos^2\theta) \quad (3.52)$$

$$I_2 = I_5 = 4\sin^2\theta \quad (3.53)$$

$$I_3 = I_4 = 1 + \cos^2\theta \quad (3.54)$$

where  $\theta$  is the angle relative to the principal axis of the magnetic field.

The effective magnetic hyperfine field,  $H_{\text{eff}}$ , may be from an external source or, as is the case with  $^{57}\text{Fe}$ , originate from the material itself.

$$H_{\text{eff}} = H + H_{\text{external}} \quad (3.55)$$

$H$  originates from a number of factors arising from the motion of the electrons within the material [37,38]. These factors can all produce field strengths at the nucleus in the order of 1 - 100 T [23].

The direct coupling between the nucleus and the s-electron density at the nucleus is called the Fermi contact term,  $H_s$ , which is given by the following expression,

$$H_s = -\frac{16\pi}{3} \mu_B \left( \sum (S \uparrow - S \downarrow) \right) \quad (3.56)$$

where  $S \uparrow$  and  $S \downarrow$  are the s-electron densities at the nucleus with spin up and spin down respectively. A slight imbalance of spin density is seen at the nucleus as the interaction of an unpaired d-electron with the s-electrons of parallel spin will be different to that with the s-electrons of opposite spin. The force of interaction between an unpaired d-electron and an s-electron of parallel spin is attractive while that of an unpaired d-electron with an s-electron of opposite spin is repulsive. This results in the radial parts of the two s wave functions being different.

If the parent atom has a non-zero orbital magnetic moment then there is a contribution,  $H_L$ , to the hyperfine magnetic field given by,

$$H_L = -2\mu_B \left( \frac{1}{r^3} \right) \langle \underline{L} \rangle \quad (3.57)$$

A further contribution to the magnetic hyperfine field,  $H_D$ , arises from the dipolar interaction with the spin angular momentum of the parent atom. The following expression is used to quantify the contribution,

$$H_D = -2\mu_B \left( \frac{3\vec{r}(\vec{s} \cdot \vec{r})}{r^5} - \frac{\vec{s}}{r^3} \right) \quad (3.58)$$

The terms  $H_S$ ,  $H_L$  and  $H_D$  can all be of the order of 1 - 10 T and their sum is the internal magnetic hyperfine field,  $H$ , given by,

$$H = H_S + H_L + H_D \quad (3.59)$$

The sign of  $H$  can be found by applying an external magnetic field  $H_0$  that alters the effective magnetic hyperfine field,  $H_{\text{eff}}$ , to the sum of  $H$  and  $H_0$ . As a result of applying this external field the hyperfine field at the nucleus will either increase or decrease depending upon whether the external field was applied parallel or antiparallel, respectively, with respect to  $H$ .

The internal magnetic field of a magnetically ordered material is usually proportional to the magnetisation and hence the temperature dependence of the magnetic splitting will follow a Brillouin function, approaching zero at the Curie temperature (for

ferromagnetic materials) or the Néel temperature (for antiferromagnetic materials) [23, 38].

Magnetic splitting is not observed in all materials with unpaired valence electrons however, it depends on the relaxation time of electronic spins compared with the Mössbauer event time. In equation 3.51,  $H$  is a vector product and the observation time scale is of the order of  $10^{-8}$  s. The electronic pairs which generate  $H$  undergo changes of direction known as spin relaxation. No magnetic splitting is observed in paramagnetic materials as the spin relaxation is rapid and results in  $H$  having a time average of zero. Ferromagnetic and antiferromagnetic materials exhibit splitting because the spin relaxation rate is slower.

Intermediate conditions exist where the electronic spins relax in a time scale comparable with that of the Larmor frequency (typically tens of MHz) resulting in complex Mössbauer spectra [23,38,39]. Mössbauer spectra from materials with two or more distinct magnetic lattices will reveal the internal field at each individual site, therefore observation of the magnetic splitting is particularly useful for confirming that magnetic ordering is present within the material. The three hyperfine interactions discussed here can be observed singularly or acting in combinations giving rise to more complicated Mössbauer spectra, figure 3.17.

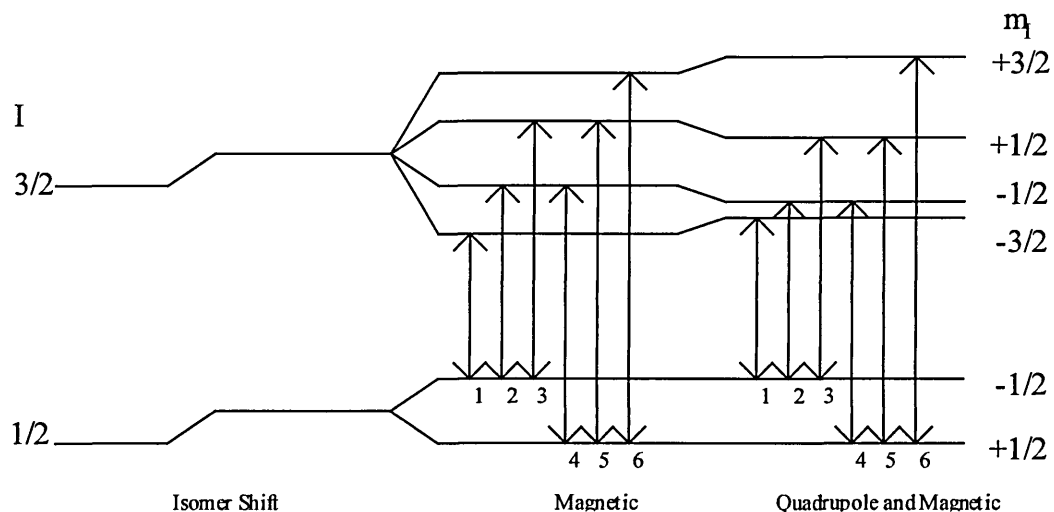


Figure 3.17. Nuclear energy level splitting, magnetic interaction and quadrupole interaction. (Not to scale)

The magnetic hyperfine interaction causes a sextet and the quadrupole interaction causes shifts in the peaks so that peaks 1 and 2 are closer together and 5 and 6 are further apart. Lines 3 and 4 are shifted but stay the same distance apart. In most cases the quadrupole interaction is classed as a perturbation as its effect is usually much smaller than the effect of the magnetic hyperfine interaction. The isomer shift acts on the whole sextet and shifts it slightly. The resultant spectra, shown in figure 3.18, shows how all three of the hyperfine interactions may combine in a non-cubic ferromagnetic sample to give a complex spectrum.

In terms of  $^{57}\text{Fe}$  CEMS analysis in this study no quadrupole splitting or perturbation was identified and so the combination of quadrupole splitting with other hyperfine interactions above is mainly of academic interest only for such work. The  $^{119}\text{Sn}$  work

does include some quadrupole splitting in combination with the other hyperfine interactions and therefore is important in this respect.

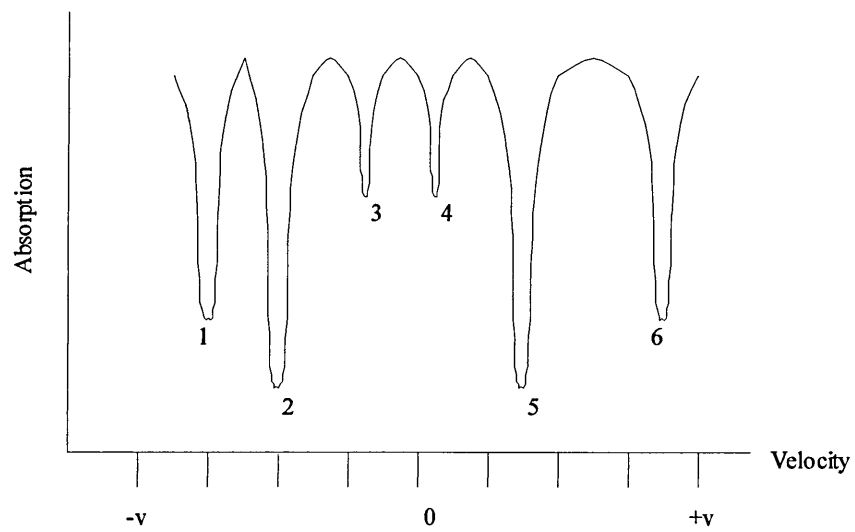


Figure 3.18. Mössbauer spectrum of the complex splitting of the  $^{57}\text{Fe}$  system.

## Mössbauer Spectroscopy References

- [1] R. W. Wood, Amer. Acad. 11 (1904) 396.
- [2] W. Kuhn, Philos. Mag. 8 (1929) 625.
- [3] P. B. Moon, Proc. Phys. Soc. 64 (1951) 76.
- [4] R. L. Mössbauer, Z Physik 151 (1958) 124.
- [5] R. L. Mössbauer, Z. Naturforsch, 14a (1959) 211.
- [6] R. L. Mössbauer, Naturwissenschaften, 45 (1958) 538.
- [7] R. L. Mössbauer, Nobel Lecture, December 11, 1961.
- [8] R. L. Mössbauer, Hyperfine Interactions 126 (2000) 1.
- [9] S. Nasu, High Temperature Materials and Processes, Vol. 17, Nos. 1-2, 1998.
- [10] R.V. Parish, Chemistry in Britain, June 1985.
- [11] T. E. Cranshaw, B. W. Dale, G. O. Longworth, C. E. Johnson. "Mössbauer spectroscopy and its applications." (Cambridge University Press, 1985).
- [12] G. Breit, E. Wigner, Phys. Rev. 49 (1936) 519.
- [13] S. L. Ruby, Y. Hazony and M. Pasternak, Phys. Rev., 129 (1963) 826.
- [14] O. C. Kistner and A. W. Sunyar, Phys. Rev., 139 (1965) B295.
- [15] M. Eckhause, R. J. Harris, Jr, W. B. Shuler and R. E. Welsh, Proc. Phys. Soc., 89 (1966) 187.
- [16] C. Hohenemser, R. Reno, H. C. Bensi and J. Lehr, Phys. Rev., 184 (1969) 298.
- [17] G. J. Long in "Mössbauer Spectroscopy Applied to Inorganic Chemistry", Ed. G. J. Long, (Plenum Press, New York, 1984).
- [18] K. G. Malmfors Ark. Fysik, 6, (1952) 49.
- [19] W. E. Lamb, Phys Rev 55 (1939) 190.
- [20] P. Wilkes, " Solid State Theory in Metallurgy", (Cambridge University Press, London, 1973).
- [21] H. J. Lipkin Ann. Phys., 9, (1960) 332.
- [22] H. Frauenfelder, "The Mossbauer Effect", (W. A. benjamin Inc., New York 1962).
- [23] N. N. Greenwood, T. C. Gibb, "Mössbauer Spectroscopy", (Chapman and Hall, London, 1971).

- [24] R. V. Parish in "Mössbauer Spectroscopy Applied to Inorganic Chemistry", Ed. G. J. Long, (Plenum Press, New York, 1984).
- [25] A. J. F. Boyle, H. E. Hall, Repts Progr in Phys 25 (1962) 441.
- [26] T. C. Gibb "Principles of Mössbauer Spectroscopy", (Chapman and Hall, London, 1976).
- [27] S. Bharati, R. Parthasarathy, K.J. Rao, C.N.R. Rao, Sol Stat Comm 46 (1983) 457.
- [28] A. J. F. Boyle, D. P. Burbury, C. Edwards, H. E. Hall, Pro Phys Soc 77 (1960) 129.
- [29] A. Vertes, L. Korecz, K. Burger, "Mössbauer Spectroscopy", (Elsevier, London, 1979).
- [30] "Mössbauer Spectroscopy Applied to Inorganic Chemistry", Ed. G. J. Long, (Plenum Press, New York, 1984).
- [31] D. P. E. Dickson and F. J. Berry, "Mössbauer Spectroscopy", (Cambridge University Press, Cambridge, 1986).
- [32] R. L. Cohen, "Applications of Mössbauer Spectroscopy Volume 1", (Academic Press, 1976).
- [33] K. A. Stroud, "Further Engineering Mathematics", (Macmillan, London, 1990).
- [34] R. L. Collins, J. C. Travis, "Mössbauer Effect Methodology", (Plenum Press, New York, 1967).
- [35] R. V. Parish, R. H. Platt, Inorg. Chim. Acta. 4 (1970) 65.
- [36] H. Spiering in "Mössbauer Spectroscopy Applied to Inorganic Chemistry", Ed. G. J. Long, (Plenum Press, New York, 1984).
- [37] V. I. Goldanskii and E. F. Makarov in "Chemical Applications of Mössbauer Spectroscopy", ed. V. I. Goldanskii, R. H. Herber, (Academic Press, 1968).
- [38] T. E. Cranshaw and G. Longworth in "Mössbauer Spectroscopy Applied to Inorganic Chemistry", Ed. G. J. Long, (Plenum Press, New York, 1984).
- [39] S. S. Hana, J. Heberle, G. J. Perlow, R. S. Preston, D. H. Vincent, Phys Rev Letts 4, (1960) 513.

## **4. LITERATURE REVIEW**

This literature review traces the production of the DWI can from ore, through the tinning procedure and on to the final product giving some historical background. Mössbauer studies of the relevant Fe-Sn phases are reviewed along with the various analyses of tinplate. This gives indications of what structure the final material will take and provides information for the discussion of the results. The various detection techniques are reviewed, showing the application of the various techniques to various analyses.

### **4.1 Iron**

Iron (Fe - from the Latin ferrum) is a transition element in Group VIII of the periodic table, atomic number 26 and atomic weight 55.847. The melting point of iron is 1536 °C and the boiling point is 3000 °C, density 7870 kg m<sup>-3</sup> at 20 °C [1,2] and valence +2, +3, +4, or +6. Iron in its pure form is a lustrous silvery-white metal and is ductile and malleable at room temperature. The Mössbauer effect has been observed for about one-third of the elements. However, iron compounds can easily be studied using this technique, as the corresponding  $\gamma$ -source is highly suited for the analysis. The study of  $\alpha$ -Fe by <sup>57</sup>Fe Mössbauer Spectroscopy is summarised by Gonser and Fischer [3]. The technique can be used as a probe of the chemical behaviour of iron containing systems as the analysis is strongly influenced by the electron configuration, oxidation state, and chemical environment of the iron atom.

Throughout the universe iron is an abundant element found in many stars and grains in interstellar clouds [4]. Along with C, N, O, Mg, and Si, Fe forms one of the six most commonly condensed solid elemental forms contributing 7.8 atoms relative to 100 oxygen atoms in interstellar dust grains [5], oxygen being the most abundant element in such grains. In its various compounds iron is the fourth most abundant element of the Earth's crust contributing about 5.1% by weight. Elemental iron is believed to be the primary constituent of the molten core of the Earth.

Since prehistoric times man has known of iron with early examples obtained from meteors as it is rarely found uncombined in nature. The iron age, which began around 1200 B.C., was characterised by iron being obtained from its ores which are abundant and widely distributed. Iron ores are those geological deposits that are 3.4 times the crustal abundance and are economically viable in iron production. In low concentrations iron is also found distributed in soil and is found dissolved in ocean and groundwaters. Even with the development of other materials, including other metals and plastics, iron and its alloys remains a substantially significant material in the economies of modern countries and is used in building construction, transportation and food and beverage packaging.

Iron has four natural isotopes, the most abundant has a mass number of 56 (91.66%), with the other isotopes having mass numbers of 54 (5.82%), 57 (2.19%), and 58 (0.33%). Iron is abundant in naturally occurring iron ores but occasionally occurs naturally in its pure form most often in meteorites. The predominate iron ores are hematite ( $\alpha\text{-Fe}_2\text{O}_3$ ) with some magnetite ( $\text{Fe}_3\text{O}_4$ ) [6], both of which have been

extensively analysed using Mössbauer spectroscopy [7,8]. Combined with other elements it forms other oxides, carbonates, silicates and sulphides such as goethite ( $\alpha$ -FeOOH), siderite ( $\text{FeCO}_3$ ), kirschsteinite (an iron silicate) and iron pyrite ( $\text{FeS}_2$ ).

Iron can exist in two structurally distinct crystalline or allotropic forms. At room temperature the iron atoms are arranged in the  $\alpha$ -form, a body-centred cubic (bcc) lattice, and is often called ferrite. In this form iron exhibits ferromagnetism, a strong magnetic behaviour that remains even in the absence of an applied external magnetic field. When iron is heated to between 768 °C and 911 °C iron transforms into  $\beta$ -form. It retains its bcc structure but loses its ferromagnetism and exhibits paramagnetism meaning it is capable of being only weakly magnetised and only as long as the external magnetising field is applied. At 911 °C the structure is transformed into a cubic close-packed face-centred cubic (fcc) structure designated the  $\gamma$ -form. At 1,392 °C iron returns to a body-centred cubic structure, called the  $\delta$ -form [1].

Iron ore deposits have been largely depleted, and iron is now generally produced from low-grade ores that are treated, using a process known as beneficiation [9], to improve their quality. Beneficiation uses such methods as washing and flotation and magnetic separation, for example in high magnetite content ores. Some ores need to be heated to temperatures of 500 °C in a reducing atmosphere to convert various iron products in the ore to magnetite prior to magnetic beneficiation. After beneficiation the fine ore particles are processed in one of four agglomeration processes, sintering, pelletising, nodulising or briquetting [6] ready for introduction into the blast furnace.

A blast furnace is used to refine iron ore the product of which is called pig iron containing about 3.5% to 5.0% carbon, 0.3% to 1.0% silicon, up to 2.5% manganese, up to 1.0% phosphorous and up to 0.08% sulphur [6]. Raw material preparation and blast conditions are instrumental in the final iron quality, Bouman [10] discusses these in detail including ore sizing where ore agglomerate size controls the transport of CO and H<sub>2</sub> into and CO<sub>2</sub> and H<sub>2</sub>O out of the particles in the furnace and oxygen enrichment, which can increase production. Beneficiated iron ore, coke and fluxes are fed into the top of the furnace and liquid iron and slag is collected through the tap holes at its base. By alloying iron with carbon the physical properties can be greatly altered. Three main types of carbon containing iron are produced, wrought iron, steel and cast iron.

Wrought iron, which is used to make such products as pipes, bolts, chains, and anchors, is commercially purified iron with carbon content below 0.035%. After processing it has a fibrous structure containing slag threads through it and is durable, malleable, corrosion resistant, and has a high melting point. Steel is formed when the carbon content is from 0.035% to 2%, the greater the carbon content, the greater the tensile strength of the steel. Further discussion of steel properties and production is given in section 4.2. Cast iron is produced when pig iron is re-melted and cooled producing iron of high carbon content (2 to 5%). The cooling process defines the final properties of the cast iron. If it is cooled quickly then hard and brittle white cast iron is formed. The carbon in the iron remains as cementite (Fe<sub>3</sub>C) [11] and is distributed throughout the iron. By annealing white iron malleable cast iron can be made where some of the carbon separates from the cementite and is finely divided in the iron in the

form of graphite. A slower cooling process results in soft but tough gray cast iron, which is easily machined. The carbon separates out as less finely divided graphite but still remains physically mixed in the iron. Cast iron is used to make many products such as stoves, baths, machine parts and steam radiators. By adding magnesium to the molten pig iron the carbon forms tiny spherical nodules around the magnesium when the iron is cast. A ductile iron is the result that is strong, shock resistant, and easily machined.

## **4.2 Steel Production**

### **4.2.1 Production and Refining**

About 95% of pig iron produced is further processed to make steel, by one of four principal processes. The Siemens-Martin open-hearth process and the Bessemer process, both used since the 19<sup>th</sup> century, and more recently by the basic oxygen process (BOP) or by an electric arc furnace (EAF). Pig iron usually contains about 4% carbon and small amounts of manganese, phosphorus, silicon and sulphur. Much of the carbon, silicon and manganese is oxidised in the steel making process. The phosphorous and sulphur content are also reduced during the steel-making process as these can be detrimental to the quality of the steel whereas manganese is often added to refined steel to increase its strength and ductility. Other elements such as copper, chromium and nickel, which can affect the physical and chemical properties of the steel, can be present due to the use of contaminated scrap. These elements are not removed during steel-making and thus careful selection of scrap materials used is

essential in producing steel with consistent properties. Inclusion of elements such as nickel, chromium, molybdenum, and vanadium can be added during the production process to alter the steel performance.

#### 4.2.2 The Bessemer Process

The early steel industry began with the change from smelting iron ores with charcoal to smelting with coke [12], coke furnaces being built from the 1750s onward. The process of crucible steel melting was pioneered by Benjamin Huntsman [13] and was instrumental in the development of the steel industry that made Sheffield a centre for steel production.

The modern steel industry began with the invention of the pneumatic Bessemer process in the late 1850s by Henry Bessemer. In the process a vessel lined with refractory material contains the molten iron through which air is forced in a process known as gas oxidation. On contact with the carbon in the iron the oxygen causes CO gas to form reducing the carbon content as required. The first Bessemer converters were capable of producing just a few tons of steel at any one time.

#### 4.2.3 The Siemens-Martin Open-Hearth Process

The Siemens-Martin open hearth steelmaking process [6] was introduced in 1863. The long, narrow refractory lined furnace has doors across the front providing access to the shallow hearth, where raw materials known as ‘charge’ are added. The charge consists

of liquid pig iron, scrap metal, iron ore and lime, with more modern furnaces utilising pure oxygen as an oxidant injected by the use of oxygen lances. The charge is melted by the flames projected by the burners at each end of the furnace.

The Siemens-Martin open hearth process is superior to the Bessemer process as up to 55% scrap can be used in the charge compared to just 10% for the Bessemer converter. It can also refine high phosphorous pig iron and the steels produced contain lower concentrations of nitrogen providing less brittle steels. However the refining cycle is 4 to 10 hours making the steel production a slow and expensive operation. Despite this, such furnaces are still used for production of steels used in DWI processing, though are generally being replaced by furnaces with quicker production cycles such as the basic oxygen furnace as used by Corus plc.

#### 4.2.4 Basic Oxygen Furnace Process

The basic oxygen process (BOP) [6] is carried out in a basic oxygen furnace (BOF) [6,14], which was developed in the late 1940s, with most modern furnaces having a capacity of around 300 tonnes. The Corus plc steel-making process uses 340 tonne capacity BOF. The time needed to produce a batch of steel in the BOF is less than one hour compared to the minimum 4 hours with a Siemens-Martin open hearth furnace. For this reason, more basic oxygen furnaces are used for the production of steels and in particular those steels used for DWI processing.

The refractory lined basic oxygen furnace, roughly resembling the Bessemer converter, is first tilted on its horizontal axis to receive the scrap and hot metal charge, then brought upright. A number of different basic oxygen furnaces are used to transfer oxygen to the metal and slag. In the top blowing BOF, figure 4.1, used by Corus plc, pure oxygen under pressure is blown down vertically on top of the charge. The oxygen is introduced at  $900 \text{ m}^3$  per minute for 18 minutes using a water cooled copper lance which is lowered into the vessel to a point about 2 m above the charge materials. The bottom blowing BOF introduces oxygen through concentric submerged tuyeres that produce stronger agitation and, due to more oxygen being transferred through the steel, increases decarburisation. The bottom blowing BOF has a number of advantages over a top blowing BOF [15] that include low nitrogen content, lower slag iron content and a better iron yield. However there is higher bottom wear and a lower capability for scrap melting and is thus not as commercially appealing as the top blowing BOF. Mixed blowing (both top blowing with lesser amounts of bottom blowing) has been found to be beneficial in controlling the various steel parameters and reducing costs [6,15].

Generally the BOF is charged with 85% liquid pig iron, 10% scrap and 5% lime. The oxygen jet oxidises the iron, which in turn oxidises the silicon, manganese and phosphorous forming a slag with the lime. The slag then absorbs sulphur in the form of CaS and MnS and the carbon is converted to CO gas.

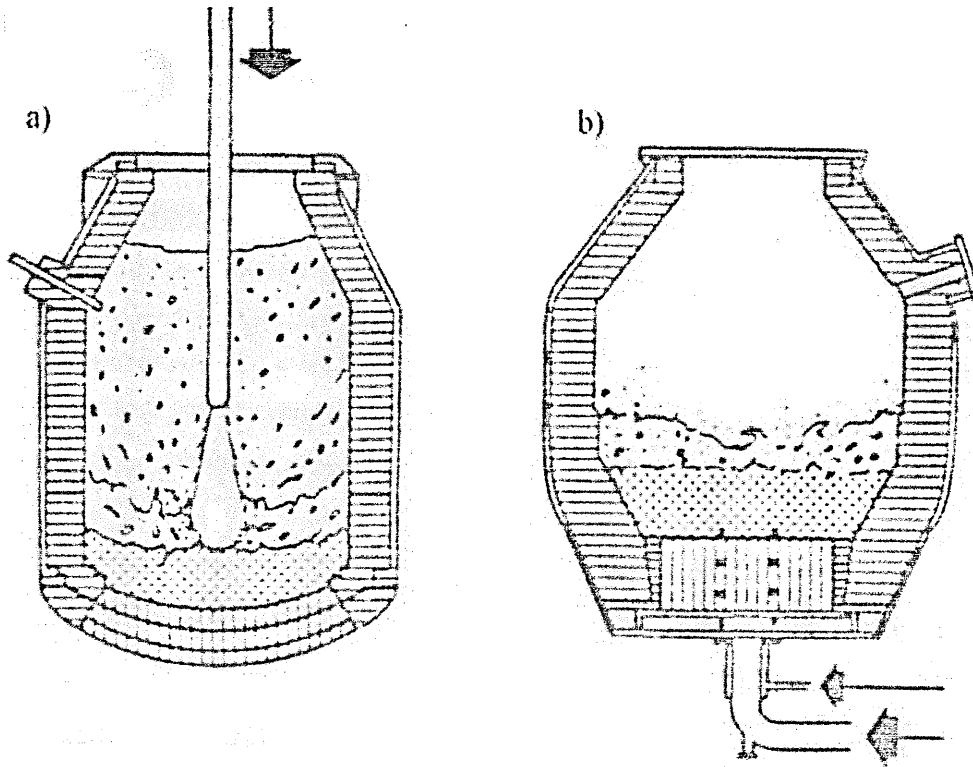


Figure 4.1. Comparison of top (a) and bottom (b) blowing BOF [15].

#### 4.2.5 The Electric-Arc Furnace

Steel production in an electric-arc furnace (EAF) first took place in 1900. However the EAF is not generally used to produce steel for tinplate as the EAF is essentially used for melting with minimal refining. EAF capacity in modern furnaces is about 200 tonnes. With the charge in place an electrode assembly comprising three carbon electrodes is brought into near contact with the charge. The EAF uses iron and steel scrap exclusively, although conditions may sometimes warrant the use of direct reduced iron (DRI) [16,17] where the iron ore has been mixed and heated above 1000 °C with a suitable reducing material, e.g. coal, the product of which is a material

with 92% minimum iron content. Arc temperatures approaching 3300 °C cause rapid melting of the charge. Oxygen can be injected to accelerate scrap meltdown and the steel production can be carried out in under two and a half hours.

#### 4.2.6 Steel Refining

Steel which is intended for drawn and wall ironed (DWI) tinplate has aluminium added during production as this reduces the steel, aluminium having great affinity with oxygen. This has the effect of increasing the R-value of the steel [18], which is defined as the ratio of the width true strain to the thickness true strain, greater R-values implying that the material will take greater strain in the width direction than the thickness direction. Once oxygen is removed, the remaining aluminium forms a stable compound of aluminium nitride, which affects crystallographic texture in the processed strip, which affects the R-value.

For DWI tinplate clean steel is required with low content of non-metallic inclusions (NMI) of oxides, sulphides and slag in the metal [19, 20]. Such inclusions give rise to reductions in the performance of the steel so ductility and corrosion resistance can be reduced and material failure can occur. After the basic oxygen furnace cycle is complete the liquid steel, at 1625 °C, is tapped and transferred via a ladle to a secondary steel-making processing station where it undergoes vacuum degassing [21,22,23] which reduces NMIs. Detrimental gases such as hydrogen are removed from the molten steel during the degassing process and the uniformity of composition is improved by circulating the metal through the introduction of an inert gas such as

argon. After the refining steps are complete, the steel goes into either ingot production or continuous casting.

#### 4.2.7 Ingot Production

The molten steel is released at a controlled rate and temperature into cleaned cast iron ingot moulds and allowed to solidify into specific shape ingots which can weigh up to 100 tonnes. After stripping the mould away the ingot is “soaked” which is where it is heated in a pit to a uniform temperature. The ingot is then hot rolled in a primary rolling mill which shapes the ingot into either a slab, which is a rectangular shape varying in width from 50 to 100 cm, with thickness of 5 to 25 cm and in length up to 9 m, or a bloom, which is a specific type of slab with a square end. Blooms are sometimes processed further by sectioning into billets. These steel sections are known as semi-finished steel.

#### 4.2.8 Continuous Casting

The steel from the secondary steel-making process can be processed into semi-finished steel without the intermediate steps of ingot production by using the continuous casting process that reduces the amount of NMIs and gives faster throughput of steel. This process is used by Corus plc in the production of semi-finished steel product that is used for DWI production. The liquid steel is released into a water-cooled copper mould with the temperature still around 1550 °C, figure 4.2, and then slowly extruded from the mould.

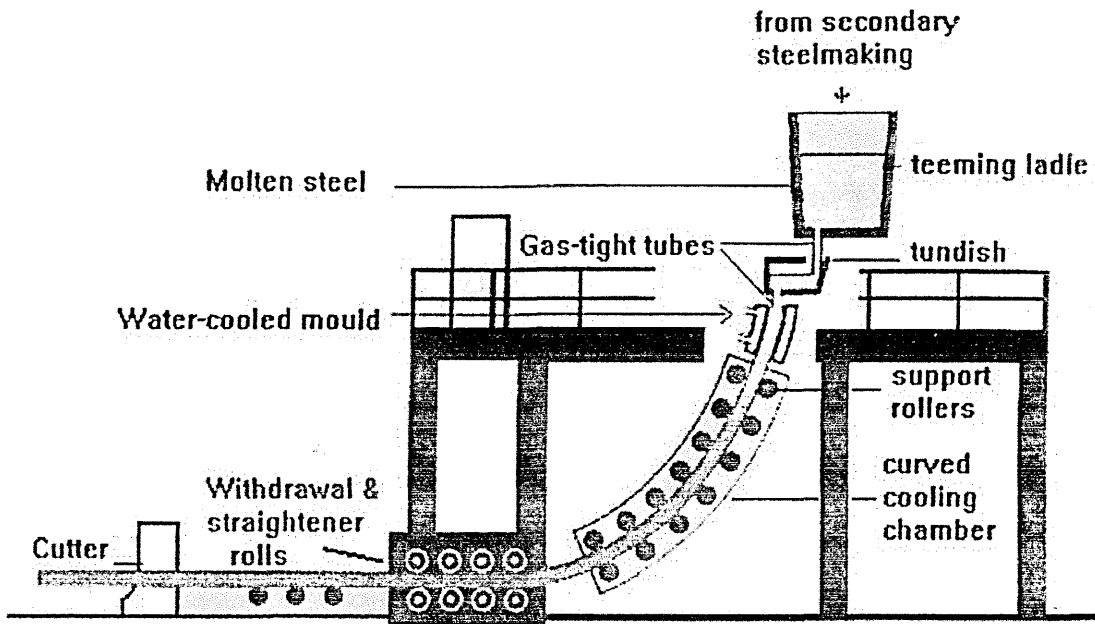


Figure 4.2. Continuous casting mould.

The steel is drawn from the mould in a semi-solidified state through a series of withdrawal rollers and bent through 90° into a horizontal orientation. The cast steel in the Corus plc continuous casting facility is 234 mm thick and up to 1875 mm wide and is cut into required length slabs (7 m to 10 m) by an oxy-propane flame.

#### 4.2.9 Shaping and Finishing

In most steel sheet production facilities, including those used by Corus plc, the slabs are then reheated and passed through a series of rolling mills to produce steel of the final sheet thickness. However some facilities use a thin-slab continuous casting technique, known as near net shape casting, producing slabs 50 mm thick which are

then reheated on the line and rolled into sheets of required final thickness reducing cost and time for sheet production.

Except for the sheet produced in near net shape casting facilities the semi-finished steel products must be reheated to 1250 °C and then processed to final thickness in two stages, hot rolling in a continuous hot mill, and final reduction using cold rolling.

To produce sheet steel flat roll mills are used with smooth faced rolls.

For some applications grooved and shaped mill rolls are used to produce specific steel products from blooms, billets and ingots. Applications include constructional steel components such as concrete reinforcing bars and I beams, wire rods, which are drawn through dies to produce wire and seamless pipe where tube rounds are hollowed and brought to required diameters for high pressure applications including steam boilers.

#### 4.2.10 Flat-Roll Mills

The heated, semifinished steel is hot rolled by a series of seven huge rollers that exert vertical pressure on the steel strip to compress the steel to a thickness of about 2 mm while being stretched to over 900 m in length at a rate of 1200 m per minute with minimal lateral spread. The precision of strip shape and modification to internal structure of the strip is vital as this stage deeply affects the quality of the final steel product. One of the main factors affecting the hot rolled strip is the rolling and cooling temperatures [6,24], which affect the metallographic structure and therefore mechanical properties of the final steel product. With low carbon steel the rolling

should be done above 870°C and cooling of the strip through the critical range of 870°C down to 720°C will determine the size and distribution of cementite ( $\text{Fe}_3\text{C}$ ). More even distribution occurs with quicker cooling times giving more uniform material properties. Since cementite is hard and brittle large formations will give rise to crack nucleation centres reducing the strip ductility. Strip cooling procedures [25] involve passing the rolled strip through computer controlled water curtains on the mill run out table giving uniform cooling of the desired rate.

The steel strip is then coiled for ease of handling between rolling stages and allowed to cool. Over half of the hot rolled steel is further processed to create tinplate the remainder being used to meet the needs of sheet steel customers.

Due to the high temperatures used during the hot rolling stage oxides are formed on the steel surface. Such surface oxides need to be removed prior to cold rolling to avoid imparting defects into the strip surface. Generally the oxide layer is comprised of a thick inner FeO (wüstite) layer with a thick  $\text{Fe}_3\text{O}_4$  (magnetite) and FeO mixed intermediate layer and a thin  $\alpha\text{-Fe}_2\text{O}_3$  (hematite) outer layer. The strip is uncoiled and oxide “mill scale” is removed by “pickling” [26,27], a process that involves immersing the strip in either a 10% sulphuric acid ( $\text{H}_2\text{SO}_4$ ) solution used either at room temperature [28] or warm [26,29] or a 5-10% HCl solution at either room temperature [28,29] or at slightly elevated temperatures [26] in a continuous pickler. The strip is then thoroughly rinsed and dried to prevent over-pickling as this would cause roughing of the strip surface which will then lead to uneven coating when

tinplating [26]. Under-pickling will also cause non-integral coatings to be formed as the remaining corrosion products prevent even coating.

Cold rolling [30] is then performed on the thin strip to reduce the thickness from about 2 mm down to gauges used for tinplating of 0.16 mm to 0.28 mm. The modern process is fully automated [31,32,33,34] providing high strip quality with precise gauge strip. The cold rolling also increases smoothness and imparts the strip with greater strength and hardness but reduces ductility.

In order to increase ductility the coils are heated in an annealing furnace which reduces the crystal dislocation density and transforms the elongated ferrite grains into finer strain free grains giving rise to an increase in ductility and decrease in strength. Some low alloyed steels have been found to increase in hardness over long (6 hours) annealing times [35] for example in Fe-Cr-Ni where Ni carbide is formed, however in steel production only short annealing times are used. Temperature control during annealing is critical as at higher temperatures the grains begin to increase in size and will create defects when the material is drawn. Annealing is done by one of two processes, batch or continuous annealing. Batch annealing involved heating the coils in a furnace over a four hour cycle. Continuous annealing takes place in complex sophisticated lines [36], as at the Trostre works of Corus plc, where the strip is taken through a long furnace at speeds of up to  $800 \text{ m min}^{-1}$  which can reduce the cycle time to less than 90 seconds. The effects of coiling temperature and continuous annealing variables on the final tensile and metallographic properties of DWI have been studied [37] showing that the variations in annealing temperature have little effect on the final

DWI tinplate properties. The hot mill conditions were found to be much more influential on the properties. The strip is then temper rolled, a light cold rolling that provides a smooth flat surface finish and gives the desired mechanical properties to the strip as required.

Demands on tinplate strength led to the development of double reduced plate. After the annealing process a second cold rolling process is used to increase strength instead of the light cold rolling in normal strip. In the double reduction process thickness of the strip is in the region of 30-40 % giving thickness below 0.18 mm making appreciable savings in material usage.

#### 4.2.11 Alloy Steels

The mechanical and magnetic properties of iron, as well as its resistance to corrosion, can be improved by mixing iron with other elements to form alloys [38]. By combining iron and carbon with specific amounts of other elements steels with desirable properties, such as corrosion resistance, heat resistance, high strength and high ductility can be produced [39]. An important component of many steels is cementite,  $\text{Fe}_3\text{C}$  [9,11]. Three carbon steel classifications are used and the greater the carbon content the greater the tensile strength of the steel. Because of high ductility, mild steel, which has 0.25% carbon content, is used to make wire and sheet steel, the sheet steel being subsequently used for DWI can-making. Harder medium steels have about 0.45% carbon and are used to make structural steel. High carbon steels, which are extremely hard and brittle, contain 0.60 - 2.00% carbon and are used for the

fabrication of tools and cutting instruments. By heating steel and quickly cooling it, known as quench hardening, the hardness of the steel can be increased.

The other elements added to steels include nickel, chromium, molybdenum and vanadium which can produce higher-strength steels. The inclusion of tungsten up to 50% increases hardness and allows steel to be used as high-speed drill bits and cutting blades even at high temperatures. Silicon inclusions of 1-5% result in a hard and highly magnetic alloy but can have a detrimental effect on corrosion resistance [39]. Sulphur reduces strength and improves machinability but, as with silicon, it has a detrimental effect on corrosion resistance [39]. Copper may be added for better resistance to corrosion. The inclusion of chromium and nickel in low carbon steel improves the corrosion resistance, ductility, steel strength and, in certain compositions, is termed stainless steel. Commonly stainless steel contains approximately 18% chromium, and 10% nickel. The inclusion of manganese causes it to react with other elements in the steel, such as sulphur, reducing their detrimental effects.

Alloy steels are generally formed by adding the specific elements during the steel-making process but may also be produced in electric arc furnaces by using carefully selected steel scrap or carbon steel that is remelted with selected amounts of the alloying elements. Sheet steel for the DWI process is mild steel with low carbon content and no added elements. This means that the sheet is ductile but also not particularly corrosion resistant.

### 4.3 Tin

Tin (Sn - from the Latin stannum) is an element in group IVA of the periodic table, atomic number 50 and atomic weight 118.69. Tin is fairly unreactive which accounts for its use as a corrosion inhibitor. The melting point of tin is 231.968 °C, the boiling point is 2270 °C and it has a density of 7300 kg m<sup>-3</sup> at 20 °C [40,41]. In its chemical compounds, tin exhibits two common oxidation states, +2 and +4. Tin has ten naturally occurring isotopes, the most abundant of which has a mass number of 120 (32.85%). Tin has been used in bronze since the bronze age (2500-2000 BC) and is relatively rare being only about 0.001% abundant in the Earth's crust. Its predominant ore is a naturally occurring tin oxide, cassiterite (SnO<sub>2</sub>) [42].

Tin can exist in two structurally distinct crystalline or allotropic forms. Above 13.0 °C tin is found as white tin, which is the more familiar allotropic form where the tin atoms are arranged in a tetragonal lattice. White tin is a metal of silvery white colour and is soft and ductile. Below 13.0 °C tin slowly converts to grey tin where the tin atoms are arranged in a diamond lattice, which is less dense and lacks the metallic properties of white tin. Grey tin is seldom used. Tin forms a corrosion resistant oxide coating when exposed to air and moisture. Due to its high corrosion resistance, a protective coating of tin is sometimes applied to steel and other metals that are easily corroded. The tin also aids the prevention of organic acids from foods from reacting with the steel in food and beverage packaging.

#### **4.4 Tinfoil Production**

The first recorded use of tinfoil was in fourteenth century Bavaria where hammered sheets of iron were dipped into molten tin. This technique continued until the eighteenth century where rolling replaced the hammering process and iron sheets were replaced with sheets of steel. Later during the eighteenth century the introduction of automatic tinning machines gave rise to a substantial increase in tinfoil output from tinfoil plants [42,43].

Improvements in steel-making, high precision rolling mills and tinfoiling methods, driven by the growing need for tinfoil products, increased production to an estimated 14 million tonnes by the mid 1980s. Most of the tinfoil produced in recent years has been used in the manufacture of food and beverage cans, however improvements in aluminium can production and plastics has meant that tinfoil is in fierce competition with these other materials in the modern packaging market.

Tinfoil produced in modern tinfoil plants consists of low carbon mild steel sheet or coiled strip varying in thickness from about 0.15 mm to 0.50 mm. A thin coating of commercially pure tin is applied with coating weights from  $2.8 \text{ g m}^{-2}$  to  $17 \text{ g m}^{-2}$  (0.4  $\mu\text{m}$  to 2.5  $\mu\text{m}$  thick). For modern tinfoil the use of certain grade steels provides good strength and drawability for the production of cans whereas the tin coating provides solderability, corrosion resistance, lustre and acts as a lubricant in the drawing process.

Canmaking techniques such as Drawing and Wall Ironing (DWI), Draw and Redraw (DRD) and Easy Open ends (EO) have led to developments in the production of a wide variety of tinplate material with different gauges, sheet size, tincoating weight, surface roughness and passivation procedures.

Most strip meant for tinplating is coated in a continuous electrolytic tinning line, the other possible method being hot dip tinning [42] which is rarely used today. Hot dip tinning leads to formation of the intermetallic  $\text{FeSn}_2$  between the tin and steel substrate. In electrolytic tinning the temperatures used are below the melting point of tin and so significant amounts of  $\text{FeSn}_2$  are not generally formed.

The strip is first cleaned before electroplating to remove grease, dirt and rolling lubricants. This is a procedure that varies throughout the tinplate-producing world and can include solvent cleaning [29], electrolytic and non-electrolytic alkaline cleaning [27] and emulsion cleaning [44] followed by pickling in acid baths.

Solvent cleaning is adept at removing organic compounds such as oils and grease and is carried out at either room temperature in “cold cleaning” baths or by vapour degreasing which uses a non-flammable solvent at boiling point condensed onto the steel surface. Emulsion cleaning uses organic solvents dispersed in an aqueous medium with emulsifying agents to promote solvent dispersion.

The pre-pickling cleaning used for steel strip is usually electrolytic alkaline cleaning, as used by Corus plc, which provides good removal of surface contamination thus

helping coating adhesion and preventing de-wetting of the tin in subsequent flowbrightening procedures. The cleaning electrolytes used are usually composed of a mixture of sodium hydroxide and alkaline phosphates and silicates along with surfactants. Sodium hydroxide is highly alkaline and provides high conductivity to the electrolyte, phosphates aid in the removal of surface contamination, silicates offer good emulsifying characteristics and the surfactants give the required wetting and dispersion properties to the cleaner. There are three electrolytic alkaline cleaning (electrocleaning) procedures, anodic electrocleaning, cathodic electrocleaning and periodic reverse electrocleaning. In anodic electrocleaning the steel strip passes between two negatively charged cathodes with the strip acting as the anode. Four hydroxyl ( $\text{OH}^-$ ) ions at the anode discharge four electrons which liberate a molecule of oxygen ( $\text{O}_2$ ). The gaseous oxygen acts to scrub the strip surface free of dirt. Cathodic electrocleaning uses the strip as the cathode passing between two positive anodes, positively charged hydrogen ions react with electrons at the steel surface and results in the liberation of hydrogen gas, which, as with oxygen in anodic electrocleaning, cleans the strip surface. A third type of electrocleaning is periodic reverse cleaning whereby the strip is subjected to alternating anodic and cathodic electrocleaning.

After the preliminary cleaning stages which remove soils that do not readily react with acid it is necessary to remove any surface oxide films and this is completed by using a pickling procedure. In the pickling procedure the strip is immersed in either a sulphuric acid ( $\text{H}_2\text{SO}_4$ ) or a hydrochloric acid ( $\text{HCl}$ ) solution [26,28], hydrochloric acid solution being preferred by Corus plc.

With sulphuric acid lines this pickling procedure produces satisfactory results for low carbon steel, however high carbon steels have a tendency to develop darkened surfaces and produce smut. Using hydrochloric acid eliminates this problem but introduces greater problems with fume control. For this reason mechanical scale removal followed by short pickling times are often used for high carbon steel in sulphuric acid pickling.

Once thoroughly cleaned the strip is ready for electroplating. Electrolytically plated tin has a light grey colour and is matt. A flowbrightening stage may subsequently be applied where the tin is reflowed on the surface by heating momentarily over the melting point of tin. The strip acts as the cathode with a sacrificial tin anode.

There are four general electrolytic systems in use, the acid stannous sulphate bath, the halide bath, the fluoborate bath and the alkaline stannate bath. The acid stannous sulphate bath, often known as the Ferrostan process [42,45] typically contains 40-60 g l<sup>-1</sup> stannous sulphate (SnSO<sub>4</sub>), 50 g l<sup>-1</sup> sulphuric acid (H<sub>2</sub>SO<sub>4</sub>), 30-60 g l<sup>-1</sup> cresolsulphonic acid or phenolsulphonic acid, 2-6 g l<sup>-1</sup> gelatin and 1 g l<sup>-1</sup> β-naphthol. The Ferrostan process is operated at room temperature at a current density of 0.011 A cm<sup>-2</sup> with tin anodes. The halide bath, often known as the Halogen process [46] contains a solution of chlorides and fluorides with 75 g l<sup>-1</sup> stannous chloride (SnCl<sub>2</sub> 2H<sub>2</sub>O) and 1-2 g l<sup>-1</sup> gelatin. The fluoborate bath [45] typically consists of 80 g l<sup>-1</sup> tin as stannous fluoborate, 50 g l<sup>-1</sup> fluoboric acid, 25 g l<sup>-1</sup> boric acid, 6 g l<sup>-1</sup> gelatin and 1 g l<sup>-1</sup> β-naphthol and is operated at room temperature at a current density of 0.08 to 0.14 A cm<sup>-2</sup> with tin anodes.

For a given current the alkaline stannate bath [45] deposits tin at half the speed of the three acid baths because the valence of tin in alkaline electrolytes is four rather than two as in the acid electrolytes and thus twice as much current is required to deposit the same amount of tin at the cathode. The alkaline stannate bath generally contains 40-100 g l<sup>-1</sup> sodium stannate and 8-15 g l<sup>-1</sup> sodium hydroxide. Instead of sodium hydroxide, potassium hydroxide can be used [27] which has been shown to give increased cathode efficiency [47]. The stannate bath should be operated between 60 °C and 80 °C with an anode cathode ratio of around 1:1 whilst maintaining a greenish-yellow film on the anode [48]. An anode area  $\frac{3}{4}$  that of the cathode has been shown to give more stable deposition [45]. A current density of 0.005 to 0.032 A cm<sup>-2</sup> gives the best deposition.

For certain applications, though not for DWI, the tinplate is then flowbrightened by heating at temperatures between 250 and 270 °C by immersion in hot fat or oil and rapidly quenching in water. During this procedure FeSn<sub>2</sub> can be formed the structure and weight of which depends on the steel surface quality and time and temperature of treatment. Chemical passivation treatment of the surface helps to stabilise it against oxidising in the atmosphere. The passivation treatment involves applying a film of chromium, chromium oxides and tin oxides with the film being less than 1µm thick. Lubrication is then applied to minimise abrasion during handling and help prevent oxide formation.

## **4.5 Drawn and Wall Ironed Tinned Steel**

Drawn and wall ironed (DWI) tinned steel cans have been commercially produced since 1975 and were developed because of the competition to the tinned packaging industry from the aluminium can which was developed as a drawn and wall ironed can in 1965 [49] whilst tinned was still used to form three piece welded cans [50]. The DWI process is now used to make tinned cans for both beverage and food packaging. The requirements and benefits of DWI food cans has been investigated elsewhere [51,52] and is beyond the scope of this work which will focus on beverage cans. There have been no previous Mössbauer studies on DWI tinned steel cans, however other techniques including scanning electron microscopy and physical testing have been used to analyse such cans [37,53,54,55] and also drawn and wall-ironed aluminium cans [54,55,56].

The DWI process is a can-making process ideal for large height : diameter ratio cans which are to be pressurised such as those used in the soft drinks industry. DWI cans are of two piece construction, that is a top end and a body, which offer better rigidity than soldered three piece cans since there is no side seam. Other advantages over soldered three piece cans include lower metal usage and therefore lower cost and less environmental impact.

A circular blank is used to form the cylindrical body. This blank comes from a coiled strip of tinned that is fed into an inspection unit which checks for defects. The tinned strip should have completely smooth surfaces and be completely covered in

tin. It has been shown [57] that cans produced with tinplate with tin coating weights of  $5.6 \text{ g m}^{-2}$  or lighter experience much greater porosity than when using tinplate with heavier coatings. The tin is used as a defence against corrosion and also acts as a lubricant during can forming. However metal usage is a major consideration in can production and so much work has been done on analysing light gauge tinplate [58] and differentially coated tinplate [59] from which metal usage can be reduced. Differentially coated tinplate can be used to form cans with the inside of the can having a lighter tin coating than the outside. Forces in the processing of the can are greater on the outside of the can wall and thus the tin on the inside is not as distorted by the process and lighter coatings are suitable for DWI processing. Ultra-lightweight cans made from 0.24 mm thick tinplate are possible to use if canmakers use delicate can handling systems [60], these tinplates are used to form cans with final wall thickness of 0.070 mm with a reduction in material use of 25 % over the more commonly produced cans which are generally made from 0.28 mm tinplate with wall thickness of 0.085 mm. It has also been speculated that cans made from 0.18mm tinplate can be produced [61] if the steel is of sufficient quality and strength as the limits adhered to in present can making are not ultimate limits for high quality steel. By using the microseam closure system [62] for attaching the ends to the can further reduction in metal usage is attained. So a combination of new materials and new processes can be used to reduce costs and improve the product.

During the DWI drawing process lubricant is applied to the chosen tinplate strip and the cupping process can proceed where disc shaped pieces of metal are stamped out from the sheet. From these disc blanks a first stage cup is drawn in a heavy-duty high

precision double action press, figure 4.3. Aspects of this process in terms of tooling accuracy and tool life have been summarised by Kohn [63].

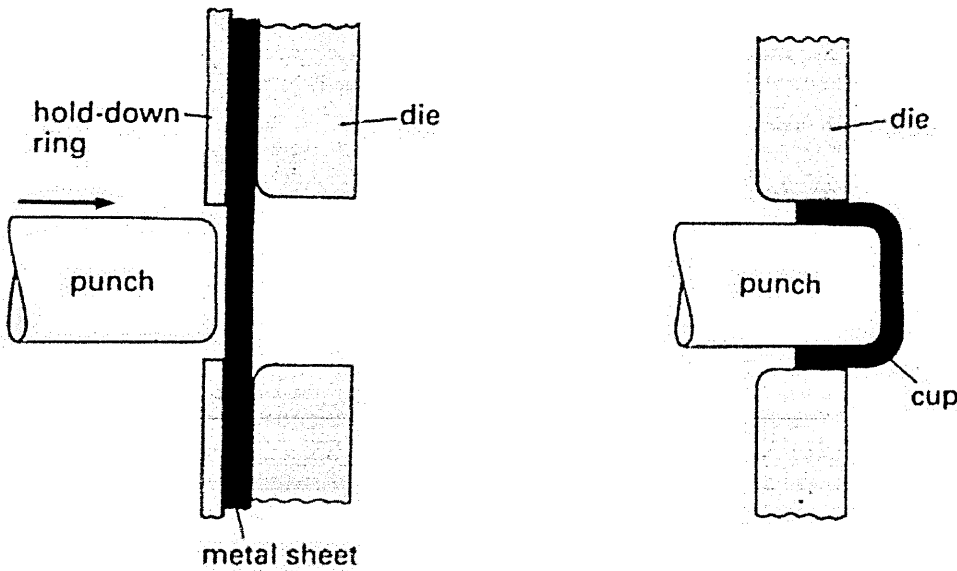


Figure 4.3. Sheet drawing through die [24].

The cups are fully drawn through the die without residual flange whilst retaining uniform wall thickness. The cup is then redrawn to the final can diameter in another press, without any change in wall thickness, or as part of the wall ironing process.

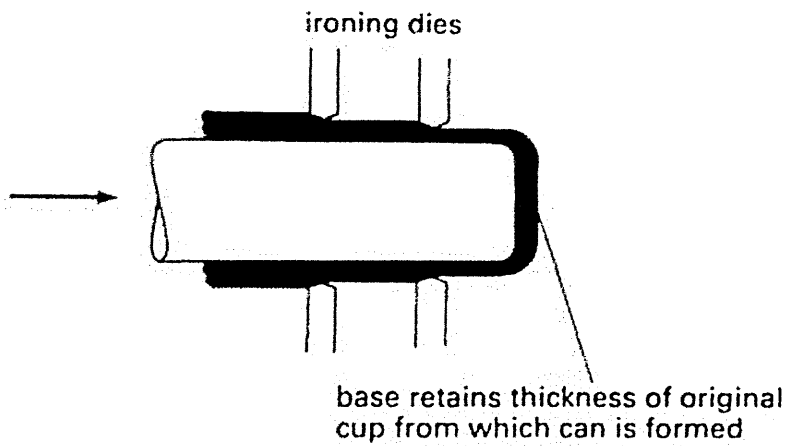


Figure 4.4. Wall ironing [24].

Wall ironing, figure 4.4, is used to reduce the wall thickness which produces a corresponding increase in the height of the can wall. Normally three tungsten-carbide ironing rings are used to reduce the wall thickness by up to two thirds from 0.30 mm to 0.10 mm however the thickness will increase from the base to the top by up to 0.03 mm. The base of the can retains the original material thickness. Each ironing stage requires lubrication to avoid damage to the tool surface and provide a good can surface. The can wall reduction from each ironing die is critical if tearing of the material is to be avoided.

The cans are overdrawn to provide extra can height as the ironing process will often draw the can to different heights around the diameter of the can, which is known as earing of the can. Excess can wall height is then trimmed off using rotary trimmers and the base of the can is domed inwards to provide enough strength to withstand high internal pressures.

The can must then be cleaned before lacquering and decorating. The top of the can is necked and flanged to enable the top end to be subsequently seamed on. The internal surface is then spray lacquered and stoved (dried and cured in an oven). The type of lacquer used depends on the final use of the can. For beverage cans it is often epoxy-urea formaldehyde or vinyl lacquers that are used. The lacquer layers should be greater than 20  $\mu\text{m}$  as any pores or defects in the lacquer layer can lead to serious detinning. The DWI cans provided by Corus plc for this study, have not been lacquer coated so that the preferred Conversion Electron Mössbauer Spectroscopy (CEMS) technique, as described in section 5.2.2, can be used. This technique analyses upper surface

layers only and therefore the addition of inert lacquer layers makes material analysis more difficult. Further details of the process of drawing and wall ironing, with respect to subsequent can processing, are given by Morgan [64] and Panknin [65].

Theoretical predictions of the stresses and strains involved in cup drawing, prior to the introduction of the DWI process, have been suggested [66,67] and presented as possible prediction tools for drawing press conditions. An appraisal of the suggested theories [68] concluded that the application of the theory to physical systems is extremely complicated, but does provide a powerful tool to help solve sheet deformation problems. It was suggested in that appraisal that the theory could be extended to other systems other than cup drawing and that even simplified theoretical systems could be used to predict the onset of material fracture. Generally theoretical predictions of system parameters have concentrated on the axially symmetrical (axi-symmetric) systems [67], which is of course the system that DWI falls into. More recent work has been summarised by Pearce [18]. That review of recent work showed that materials are considered much more than in the older pre-DWI theories by using strain ratio values arising from material anisotropy. Panknin [65] discusses the theoretical principles of the wall ironing process, showing that wall thickness reduction and the ironing die angle are critical in reducing applied forces, the optimum angle being dependent on frictional forces and moving towards smaller values as the coefficient of friction reduces in the ironing die.

Scanning electron microscopy (SEM) has shown that the tin distribution on both the inner and outer sides of the can wall is a product of the successive can production

processes [53]. That study showed that tin was forced into grooves on the steel substrate and there was more tin on the top of the can wall, after processing, than on the bottom of the can wall. Another similar study [69] showed that the degree of iron exposure increased with increased deformation of the tinplate, SEM micrographs showed that the draw procedure caused roughening of the tinplate surface due to tilting of grains in the material. Subsequent ironing was shown to smooth the surface whilst destroying the integrity of the tin coating. These SEM results were reflected in X-ray maps taken of the surface at each processing stage. Wall ironing load is reduced with greater tinplate coating [70] even without lubricant [71] showing that tin acts as a lubricant in the wall ironing process. Greater tin thickness leads to improved drawability of the material and with added lubricant in the process over 25% thickness reduction can be achieved over steel without tin and lubricant. The tin coatings have been found to have a greater benefit, in terms of reducing ironing forces, when matt as opposed to when flowbrightened [72] but a separate study [69] has discovered that matt tinplate leads to increased steel exposure. The effect of higher ironing forces for flowbrightened material has been speculated to be due to the presence of an intermetallic layer causing higher frictional forces through the process. With tin coating weight held constant it has been shown that the carbon content of the tinplated steel also has an effect on the level of wrinkling during the can forming processes of DWI canmaking [73], lower carbon levels leading to less wrinkling.

The grooving of the steel and displacement of the tin coating has been previously studied in depth using a number of analytical techniques [74] as summarised below. The origin of the surface roughness which leads to the grooving of the sample during

ironing was found to be due to the drawing procedure, which agrees with a previous study [69], though the roughness of the cup is also dependent on the initial blank roughness, in some cases rough blanks were shown to have decreased roughness after the drawing. During the ironing stages the plateaus were found to elongate and smooth and new plateaus were found to form from the rising bottom of the valleys and free deformation effects within the grooves. Tin is wiped from the plateaus and increasingly fills the grooves. During drawing the tin in areas of non-contact with the die were found to rupture as the substrate is elongated. Surface analysis by Scanning Auger Microscopy (SAM) [74] showed the very uppermost layer of the plateaus after wall ironing contained Fe and Sn and complementary XRD analysis indicated the possible presence of  $\text{FeSn}_2$  in a layer 1 to 5 nm thick, though XRD data from this analysis were not included in the published work. Temperature at the can wall / die tip interface is critical in terms of  $\text{FeSn}_2$  formation and it was shown that the temperature can rise to 200 °C at this point. This agrees with previous work [18], which discusses lubricant use to reduce the temperature in order to prevent damage to both can and die.

Changes in tensile and metallographic properties due to the variation of the annealing parameters of the steel strip have been studied [37] and the importance of plate thickness, tensile strength and the co-efficient of work hardening have been examined in relation to the manufacture of DWI cans [54]. These properties were found to be influential in the manufacture of the cans but current production processes are able to minimise the effects of variation. Another study [55] analysed the shear stresses in the can walls during the DWI process. Defect forming non magnetic inclusions (NMIs) were identified using micro-probe analysis and were found to originate from the slag

and powders used in the continuous casters, specifically the inclusions were identified as aluminium oxides with some calcium and sodium. The flex draw test described within that work helps to identify NMIs in the strip prior to plating and thus can be used to help avoid tinplate failure in the DWI process. NMIs not only cause failure to the cans leading to low yield from production lines but can lead to damaged tooling mainly from the presence of macro inclusions which are NMIs greater than 200 $\mu\text{m}$  in length [75]. Aluminium killed steels, generally used for DWI canmaking, have NMIs which are generally less than 25  $\mu\text{m}$  compared to inclusions in rimmed-capped steels, which has also been used in canmaking which are generally less than 80  $\mu\text{m}$ .

#### **4.6 The Fe-Sn System**

The first attempt at the construction of an equilibrium diagram for the Fe-Sn system was made by Isaac and Tammann [76] in 1907 and expanded by Wever and Reinecken in 1926 [77] and Edwards and Preece in 1931 [78], though this last work incorrectly identified one particular intermediate phase, which entered much of the literature including later phase diagrams [79]. The Fe-Sn binary phase diagram, figure 4.5, is that suggested by Kubaschewski [80] based on the diagram from Hansen [81], and includes temperatures from 400 °C to 1800 °C.

The temperatures of more interest to this current study are included in the earlier Hansen diagram but not in the Kubaschewski diagram. A later redraw of the Hansen diagram by Moffatt [82], figure 4.6, shows temperatures from 0 °C to 1600 °C with

only a few minor revisions to the earlier diagram, and is in reasonable agreement with the Kubaschewski revision for temperatures above 400 °C.

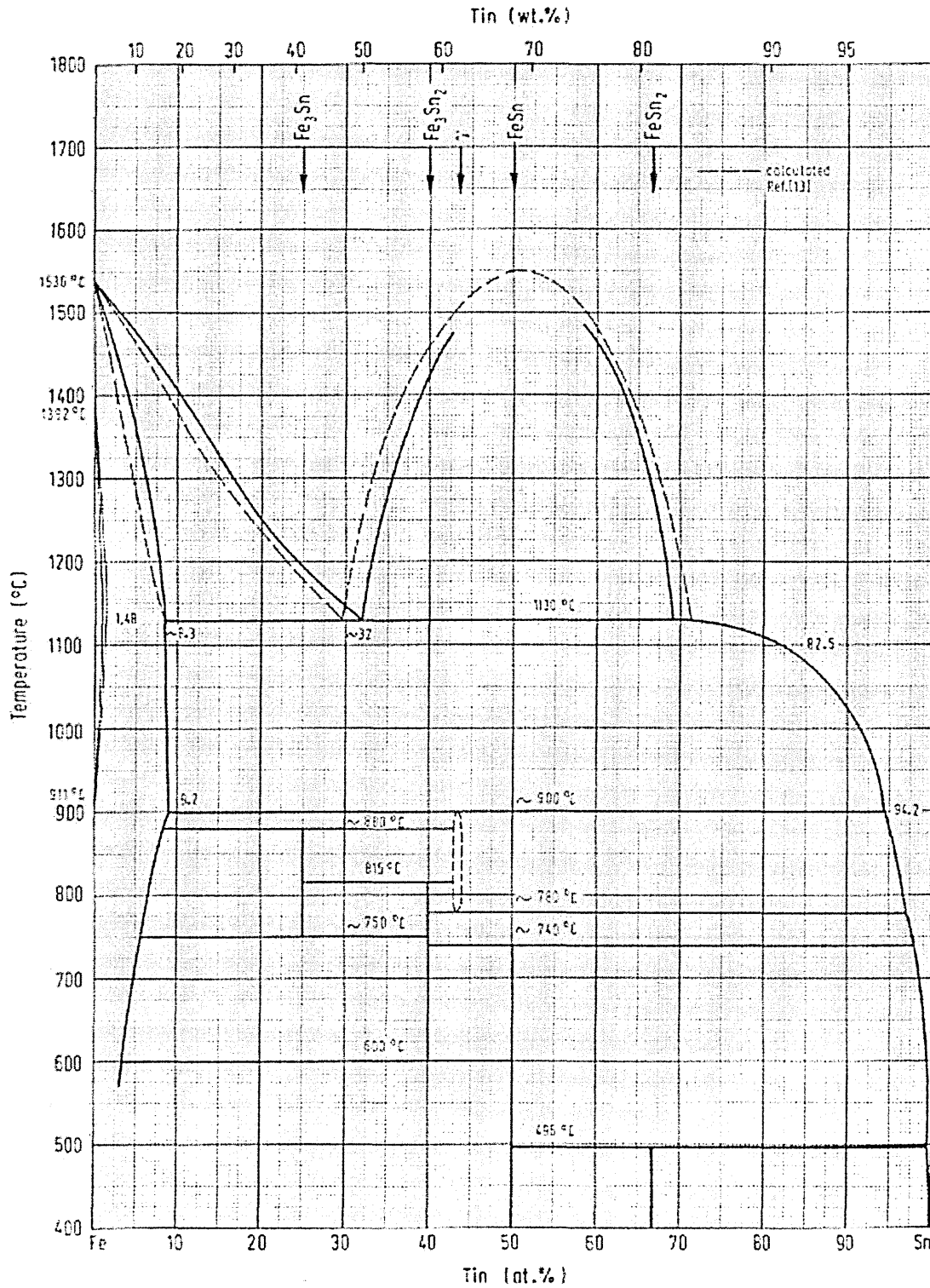


Figure 4.5. Fe-Sn phase diagram for temperatures from 400 °C to 1800 °C [80].

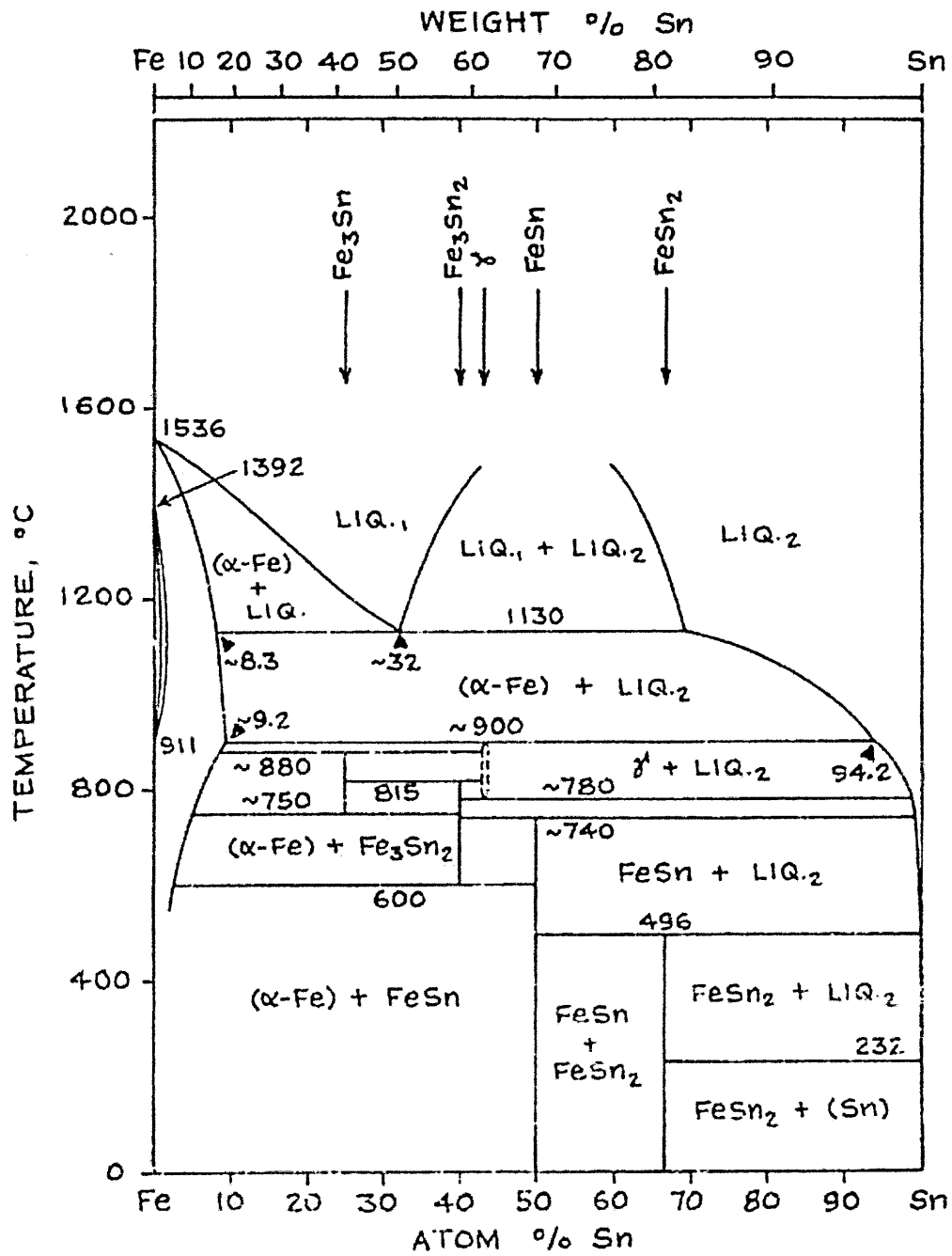


Figure 4.6. Fe-Sn phase diagram for temperatures from 0 °C to 1600 °C [82].

The Fe-Sn system contains five intermediate phases, Fe<sub>3</sub>Sn, Fe<sub>5</sub>Sn<sub>3</sub> (γ - NiAs structure), Fe<sub>3</sub>Sn<sub>2</sub>, FeSn and FeSn<sub>2</sub>.

#### 4.6.1 Fe<sub>3</sub>Sn Structure

Fe<sub>3</sub>Sn is the intermediate phase richest in iron and was identified in the earliest literature for the Fe-Sn system. A number of groups later identified the phase as Fe<sub>2</sub>Sn [78,83,84,85] but subsequent work [86,87] showed that the Fe<sub>2</sub>Sn hexagonal structure was in fact Fe<sub>3</sub>Sn being analogous to Ni<sub>3</sub>Sn and Mg<sub>3</sub>Cd hexagonal (P6<sub>3</sub>/mmc) structure and that is now the accepted phase. The lattice parameters are,  $a = 0.5458$  nm,  $c = 0.4361$  nm [87]. Fe<sub>3</sub>Sn forms peritectoidally [88], is stable between 750 °C and 850 °C and is ferromagnetic with a Curie temperature,  $T_c = 470$  °C [89].

#### 4.6.2 Fe<sub>5</sub>Sn<sub>3</sub> Structure

The  $\gamma$ -FeSn phase (also called the “NiAs” phase), which forms peritectically [88] and is stable between the temperatures of 780 °C and 900 °C, was originally thought to be Fe<sub>1.3</sub>Sn with a hexagonal (P6<sub>3</sub>/mmc) type of structure [88,90] and lattice parameters  $a = 0.4216$  nm and  $c = 0.5244$  nm. Later X-ray-powder patterns identified the phase as ferromagnetic Fe<sub>5</sub>Sn<sub>3</sub> [89] but with a high temperature and low temperature formation structure. The lattice parameters at low temperature (840 °C) are  $a = 0.4217$  nm,  $c = 0.5245$  nm, and at high temperature (900 °C) are  $a = 0.4230$  nm,  $c = 0.5208$  nm, with Curie temperatures of  $315 \pm 3$  °C and  $359 \pm 3$  °C respectively for the two structures [89]. The  $\gamma$ -FeSn phase has a narrow region of homogeneity estimated to be 0.3 - 1.0 at. % wide [86] and studies of the two sides of the range have shown the

lattice parameters to vary from  $a = 0.4230$  nm,  $c = 0.5208$  nm at the Fe rich side to  $a = 0.4233$  nm,  $c = 0.5213$  nm at the Sn rich side [86].

#### 4.6.3 Fe<sub>3</sub>Sn<sub>2</sub> Structure

The Fe<sub>3</sub>Sn<sub>2</sub> phase has been described as hexagonal [85] and monoclinic (R3m) [86]. Powder photographs by Nial did not agree with hexagonal cells by Ehret and Gurinsky and was shown to be monoclinic with 40 atoms per unit cell (= 8 Fe<sub>3</sub>Sn<sub>2</sub>) and  $a = 1.358$  nm,  $b = 0.534$  nm,  $c = 0.920$  nm and  $\beta = 103^\circ$ . More recent work by Malaman et al. [91,92] give the structure as belonging to the rhombohedral system, having a hexagonal unit cell with  $a = b = 0.5344$  nm and  $c = 1.9845$  nm. Fe<sub>3</sub>Sn<sub>2</sub> is ferromagnetic, is formed peritectoidally [88] and stable between 600 °C and 815 °C with a Curie temperature,  $T_c = 339$  °C [89].

#### 4.6.4 FeSn Structure

FeSn has a hexagonal (P6/mmm) type of structure. The lattice parameters have been described as  $a = 0.5287$  nm,  $c = 0.4437$  nm [88] and  $a = 0.5297$  nm,  $c = 0.4481$  nm [93]. FeSn forms peritectically [88] and is stable up to 740 °C. It is also antiferromagnetic with a Néel point of 95 °C [89]. It should be noted that the JCPDS data for FeSn shows a hexagonal structure with  $a = 0.5302$  nm,  $c = 0.4449$  nm and is based on data obtained in 1933, preceding the work above by some 31 years and 53 years respectively.

#### 4.6.5 FeSn<sub>2</sub> Structure

FeSn<sub>2</sub> has a tetragonal (I4/mcm) (CuAl<sub>2</sub>) type of structure [94]. The lattice parameters have been described as  $a = 0.6520$  nm and  $c = 0.5312$  nm [6.10] and as late as 1986 as  $a = 0.6542$  nm and  $c = 0.5326$  nm [93] with the latest JCPDS file using  $a = 0.6539$  nm and  $c = 0.5325$  nm but being based on data obtained in 1973. FeSn<sub>2</sub> was earlier described as having a hexagonal structure [85] but has been subsequently shown to be tetragonal. The density of this phase is  $7743 \text{ kg m}^{-3}$ .

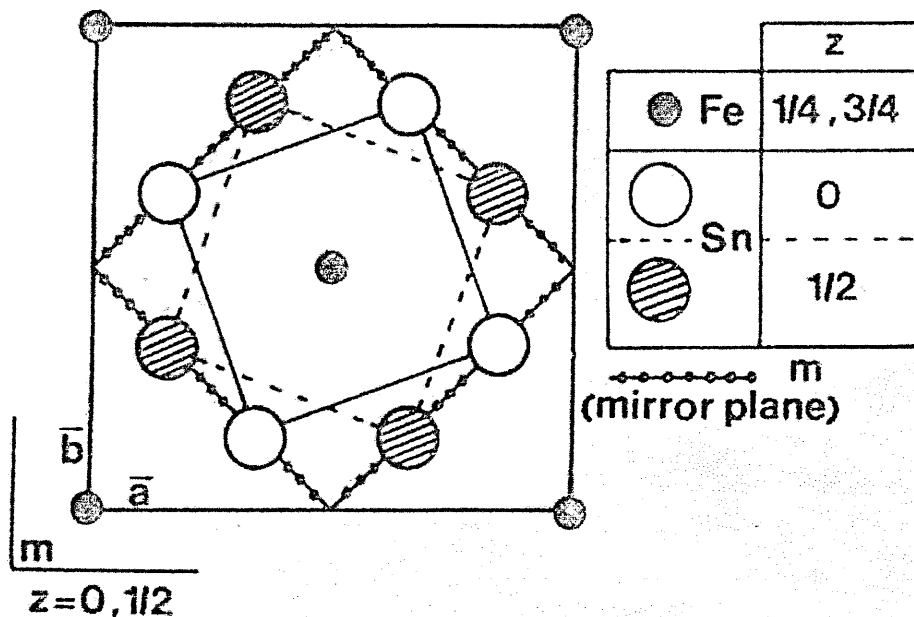


Figure 4.7. FeSn<sub>2</sub> structure diagram [94].

FeSn<sub>2</sub> forms peritectically [88] and is antiferromagnetic with a Néel point ranging from 104 °C to 111 °C (104 °C [11], 107 °C [89,95], 111 °C [96]) above which no magnetic splitting is observed. There is also a second transition at -180 °C (which only affects the tin sites [97]), between this temperature and the Néel temperature the magnetic structure is collinear with ferromagnetic planes (100), antiferromagnetically

coupled along the [100] direction, the spin direction lies in the (001) plane near the a axis. At the second transition point a spin rotation to the [110] direction is observed. Below the temperature of the second transition FeSn<sub>2</sub> becomes non-collinear antiferromagnetic and the iron moments form a canted structure along the c axis. The angle between the two spin directions is 18° [94,98].

FeSn<sub>2</sub> is the hardest phase of the Fe-Sn system and is also the most noble in acids such as citric acid and NaCl meaning that its corrosion resistance is higher than the other Fe-Sn phases. Such intermetallic can therefore be desirable in materials for improved corrosion resistance and hardness.

#### **4.7 Mössbauer Studies of Fe-Sn Phases**

The five intermediate phases, Fe<sub>3</sub>Sn, Fe<sub>5</sub>Sn<sub>3</sub>, Fe<sub>3</sub>Sn<sub>2</sub>, FeSn and FeSn<sub>2</sub> have been studied using <sup>57</sup>Fe and <sup>119</sup>Sn Mössbauer spectroscopy. From the literature reviewed for this present project it would appear that most of this work has been on the FeSn<sub>2</sub> phase which is directly relevant to this study. The other phases have been analysed previously and sections 4.7.1 to 4.7.4 summarise the parameters for the Fe<sub>3</sub>Sn, Fe<sub>5</sub>Sn<sub>3</sub>, Fe<sub>3</sub>Sn<sub>2</sub> and FeSn phases with section 4.7.5 discussing the FeSn<sub>2</sub> phase. Isomer shifts for the <sup>57</sup>Fe Mössbauer spectroscopy are given here relative to α-Fe, isomer shifts for the <sup>119</sup>Sn Mössbauer spectroscopy are given relative to CaSnO<sub>3</sub> (same as BaSnO<sub>3</sub> or SnO<sub>2</sub>) and all fields are given in tesla.

#### 4.7.1 Mössbauer Studies of Fe<sub>3</sub>Sn

Fe<sub>3</sub>Sn gives six narrow single lines with both Fe and Sn sources showing that each type of nucleus has only one distinct magnetic hyperfine field. Trumphy et al. [89] concluded that the field was directed along the c axis as any other magnetisation direction would result in combinations of magnetic hyperfine fields. Using <sup>57</sup>Fe Mössbauer spectroscopy with the Fe<sub>3</sub>Sn absorber at 800 °C, where it is stable but paramagnetic since it is above the Curie temperature for this phase, a quadrupole splitting of  $\Delta = 0.08 \text{ mm s}^{-1}$  ( $+0.01 \text{ mm s}^{-1} / - 0.02 \text{ mm s}^{-1}$ ) was obtained which was found to be in reasonable agreement with the displacement of the Zeeman lines in the ferromagnetic state. Measurements between 200 °C and 750 °C were unsuccessful due to the decomposition of the absorber. At 77 K Fe<sub>3</sub>Sn shows one field,  $H = 26.8 \pm 0.2 \text{ T}$  with isomer shift  $\delta = 0.71 \pm 0.02 \text{ mm s}^{-1}$  and quadrupole splitting  $\Delta = 0.06 \pm 0.02 \text{ mm s}^{-1}$ . Ujihira et al. [99] identify Fe<sub>3</sub>Sn as a single component at room temperature with  $H = 25.4 \text{ T}$ , isomer shift  $\delta = 0.26 \text{ mm s}^{-1}$  and quadrupole splitting  $\Delta = 0.29 \text{ mm s}^{-1}$ .

Using <sup>119</sup>Sn Mössbauer spectroscopy with the Fe<sub>3</sub>Sn absorber [89] at 77 K there is one field  $H = 10.3 \pm 0.2 \text{ T}$  with isomer shift  $\delta = 0.99 \pm 0.04 \text{ mm s}^{-1}$  and quadrupole splitting  $\Delta = 0.02 \pm 0.04 \text{ mm s}^{-1}$ . At room temperature Ujihira et al. [99] fitted two sextets with no quadrupole splitting the first has a field  $H = 8.28 \text{ T}$  with an isomer shift  $\delta = 1.92 \text{ mm s}^{-1}$  and the second has the same field  $H = 8.28 \text{ T}$  with an isomer shift  $\delta = 1.45 \text{ mm s}^{-1}$ .

#### 4.7.2 Mössbauer Studies of $\text{Fe}_5\text{Sn}_3$

Using  $^{57}\text{Fe}$  Mössbauer spectroscopy  $\text{Fe}_5\text{Sn}_3$  gives spectra at 77 K with broad lines suggesting disorder in the absorbers. Both the high and low temperature formation spectra show a combination of three components having different fields, one at  $H = 19.5 \pm 0.5$  T with isomer shift  $\delta = 0.71 \pm 0.06$  mm s<sup>-1</sup> and quadrupole splitting  $\Delta = -0.02 \pm 0.06$  mm s<sup>-1</sup>, one at  $H = 20.4 \pm 0.4$  T with isomer shift  $\delta = 0.82 \pm 0.06$  mm s<sup>-1</sup> and quadrupole splitting  $\Delta = 0.09 \pm 0.06$  mm s<sup>-1</sup> and one at  $H = 25.5 \pm 1.5$  T with isomer shift  $\delta = 0.71 \pm 0.06$  mm s<sup>-1</sup> and quadrupole splitting  $\Delta = -0.02 \pm 0.06$  mm s<sup>-1</sup> [89]. With a formation temperature of 840 °C the intensity of the fields are  $54 \pm 7$  % for  $H = 20.4$  T,  $36 \pm 7$  % for  $H = 19.5$  T and  $10 \pm 5$  % for  $H = 25.5$  T. With a formation temperature of 900 °C the intensity of the fields are  $37 \pm 5$  % for  $H = 20.4$  T,  $38 \pm 5$  % for  $H = 19.5$  T and  $25 \pm 5$  % for  $H = 25.5$  T. The overall effect of these differences in intensity is for the spectra from the sample formed at 900 °C to be less resolved with only the 19.5 T field being easily observed. The smaller contribution from the high field component to the spectra arising from the analysis of the sample formed at 840 °C was determined to be due to greater ordering of the structure [89].

Using  $^{119}\text{Sn}$  Mössbauer spectroscopy with the  $\text{Fe}_5\text{Sn}_3$  absorber [89], again at 77 K there are multiple fields and since the spectrum is highly smeared only an average field can be quoted, that being  $H = 7.4 \pm 0.6$  T with an isomer shift  $\delta = 0.85 \pm 0.10$  mm s<sup>-1</sup>.

#### 4.7.3 Mössbauer Studies of Fe<sub>3</sub>Sn<sub>2</sub>

Using <sup>57</sup>Fe Mössbauer spectroscopy Fe<sub>3</sub>Sn<sub>2</sub> at room temperature exhibits one field  $H = 19.9 \pm 0.2$  T. At 77 K Fe<sub>3</sub>Sn<sub>2</sub> has two fields, one at  $H = 21.9 \pm 0.2$  T with isomer shift  $\delta = 0.77 \pm 0.02$  mm s<sup>-1</sup> and quadrupole splitting  $\Delta = 0.06 \pm 0.02$  mm s<sup>-1</sup> and one at  $H = 21.1 \pm 0.2$  T with isomer shift  $\delta = 0.72 \pm 0.02$  mm s<sup>-1</sup> and quadrupole splitting  $\Delta = -0.02 \pm 0.03$  mm s<sup>-1</sup>. These two fields have an intensity ratio of 2:1 [89]. The transition from one field to two occurs at a temperature of  $114 \pm 3$  K. Using <sup>119</sup>Sn Mössbauer spectroscopy with the Fe<sub>3</sub>Sn<sub>2</sub> absorber [89] again gives multiple fields but in this case these were not resolved.

#### 4.7.4 Mössbauer Studies of FeSn

FeSn for a <sup>57</sup>Fe spectrum comprises two six line spectra in the ratio 2:1 [89,93]. At 77 K FeSn has two fields, one at  $H = 16.7 \pm 0.2$  T with isomer shift  $\delta = 0.83 \pm 0.02$  mm s<sup>-1</sup> and quadrupole splitting  $\Delta = 0.00 \pm 0.02$  mm s<sup>-1</sup> and one at  $H = 13.9 \pm 0.2$  T with isomer shift  $\delta = 0.77 \pm 0.02$  mm s<sup>-1</sup> and quadrupole splitting  $\Delta = -0.17 \pm 0.03$  mm s<sup>-1</sup> [89]. At room temperature the two components are observed one at  $H = 11.4$  T with isomer shift  $\delta = 0.43$  mm s<sup>-1</sup> and one at  $H = 10.3$  T with isomer shift  $\delta = 0.39$  mm s<sup>-1</sup> [93]. Ujihira et al. [99] earlier had identified FeSn as a single component at room temperature with  $H = 11.2$  T with isomer shift  $\delta = 0.38$  mm s<sup>-1</sup> and quadrupole splitting  $\Delta = 0.23$  mm s<sup>-1</sup>, though the two component system is quoted most often.

Using  $^{119}\text{Sn}$  Mössbauer spectroscopy with the  $\text{FeSn}$  absorber [89] at 77 K there are two observed fields, one quoted as  $H = 0 (+ 0.5 / - 0)$  T with isomer shift  $\delta = 1.28 \pm 0.04 \text{ mm s}^{-1}$  and quadrupole splitting  $\Delta = 0.74 \pm 0.04 \text{ mm s}^{-1}$ , the second as  $H = 4.9 \pm 0.1$  T with isomer shift  $\delta = 1.46 \pm 0.08 \text{ mm s}^{-1}$  and quadrupole splitting  $\Delta = 0.26 \pm 0.08 \text{ mm s}^{-1}$ . Ujihira et al. [99] identified two components at room temperature using  $^{119}\text{Sn}$  Mössbauer spectroscopy both with  $H = 1.4$  T. The first component had an isomer shift  $\delta = 1.87 \text{ mm s}^{-1}$  and quadrupole splitting  $\Delta = 1.60 \text{ mm s}^{-1}$ , the second had an isomer shift  $\delta = 2.06 \text{ mm s}^{-1}$  and quadrupole splitting  $\Delta = 2.90 \text{ mm s}^{-1}$ .

#### 4.7.5 Mössbauer Studies of $\text{FeSn}_2$

$\text{FeSn}_2$  has been the most widely studied of all the Fe-Sn intermetallic phases. Early determinations of the internal magnetic field at the iron nuclei by Nikolaev et al., using  $^{57}\text{Fe}$  Mössbauer spectroscopy, resulted in a value of  $12.1 \pm 0.4$  T with an isomer shift of  $0.51 \pm 0.1 \text{ mm s}^{-1}$  [100] at room temperature. Subsequent work, also by Nikolaev et al. [101] determined that there was no quadrupole interaction and gave a value for the magnetic field  $H = 11.5 \pm 0.4$  T, with an isomer shift  $\delta = 0.56 \text{ mm s}^{-1}$ . This latter work studied the temperature dependence of the Mössbauer spectra from  $\text{FeSn}_2$ . Fabri et al. [102] also analysed the  $\text{FeSn}_2$  alloy at various temperatures finding a field  $H = 15.0$  T at  $-190$  °C (83 K). Though no value was given for the spectra at room temperature (22 °C), extrapolating from the spectra given it is estimated that a field of  $11.7 \pm 0.5$  T was obtained, which is in reasonable agreement with the study by Nikolaev et al. [101]. The  $\text{FeSn}_2$  parameters at 77 K have also been determined [89]

and were found to be  $H = 15.2 \pm 0.2$  T and  $\delta = 0.91$  mm s<sup>-1</sup> with a small quadrupole interaction  $\Delta = 0.02 \pm 0.03$  mm s<sup>-1</sup>. The FeSn<sub>2</sub> parameters at room temperature were again studied by Ujihira et al. (1983) [99] who identified a single component with  $H = 11.5$  T and an isomer shift  $\delta = 0.61$  mm s<sup>-1</sup>. Le Caër et al. (1985) [103] quote the values as  $H = 11.3 \pm 0.1$  T and  $\delta = 0.51 \pm 0.01$  mm s<sup>-1</sup> at 295 K and studied in some depth the temperature dependence of the <sup>57</sup>Fe parameters in FeSn<sub>2</sub>. Van Der Kraan and Buschow (1986) [93] found the parameters to be  $H = 11.2$  T and  $\delta = 0.52$  mm s<sup>-1</sup> with no quadrupole interaction. Since the present study is primarily concerned with room temperature studies these values are of primary importance.

Using <sup>119</sup>Sn Mössbauer spectroscopy with the FeSn<sub>2</sub> absorber [89] at 77 K there is a single observed field quoted as  $H = 3.3 \pm 0.2$  T with isomer shift  $\delta = 1.53 \pm 0.05$  mm s<sup>-1</sup> and quadrupole splitting  $\Delta = 0.15 \pm 0.05$  mm s<sup>-1</sup>. Ujihira et al. [99] identified a single component also at room temperature using <sup>119</sup>Sn Mössbauer spectroscopy and quoted the parameters as  $H = 2.45$  T with an isomer shift  $\delta = 2.1$  mm s<sup>-1</sup> and no quadrupole splitting. Nikolaev [101] obtained  $H = 2.5$  T at room temperature but gives no indication as to isomer shift values. Nikolaev does state that some quadrupole splitting is observed in the spectra obtained but does not quantify this. At 4.2 K three FeSn<sub>2</sub> components are identified [94] with the parameters for these three components being,  $H = 6.65 \pm 0.1$  T with  $\delta = 2.30 \pm 0.02$  mm s<sup>-1</sup> and  $\Delta = 0.86$  mm s<sup>-1</sup>,  $H = 0.4 \pm 0.1$  T with  $\delta = 2.30 \pm 0.02$  mm s<sup>-1</sup> and  $\Delta = 0.86$  mm s<sup>-1</sup> and  $H = 3.25 \pm 0.1$  T with  $\delta = 2.30 \pm 0.02$  mm s<sup>-1</sup> and  $\Delta = 0.86$  mm s<sup>-1</sup>.

## **4.8 Studies of Tinplate**

Numerous studies have analysed the formation of  $\text{FeSn}_2$  when flowbrightening electrodeposited tinplate [104,105,106]. In all of these studies only  $\text{FeSn}_2$  was formed, though by depositing iron tin alloy onto steel substrates and subsequently heating  $\text{FeSn}$  has been formed [107] and  $\text{Fe}_3\text{Sn}_2$  has been suggested as being part of the alloy layer [108]. From analysis of commercially produced material  $\text{FeSn}$  and  $\text{Fe}_3\text{Sn}_2$  have not been identified and this would be expected since in the short heating times used during flowbrightening the weight percentage of tin to iron at the interface is regarded as 100%.

$\text{FeSn}_2$  is a harder phase than both Fe and Sn and is correspondingly more brittle [109], which proves to be a problem when forming material with  $\text{FeSn}_2$  layers. Such layers could prove to be a problem if they were present in tinplate used in the DWI process. The presence of  $\text{FeSn}_2$  also has an effect on the corrosion resistance. The corrosion of  $\text{FeSn}_2$  itself has been described as insignificant [110] and is not easily measurable but the protection value of the alloy layer on tinplate depends on the coverage of the layer.

From a number of studies using electron microscopy the grey coloured  $\text{FeSn}_2$  alloy layer has been identified and was seen to be in the form of a network of interwoven alloy crystallites lying on the steel substrate [104,111]. The formation occurs during the initial heating of the tinplate by solid state reactions and then by reaction between the steel substrate and molten tin above the melting point of tin [104].

Two main factors identified as being crucial in the formation of the alloy layer are the alloy formation process itself, e.g. electrodeposition or hot dip tinning and the grain structure of the steel. The grain structure is affected by temperatures during steel production and so the annealing process becomes increasingly important when considering the subsequent alloy production as the deposited alloy layer shows epitaxy with the underlying substrate grains, though this effect is less observable with thick alloy layers and with electrodeposits from alkaline baths. Alkaline baths, as are used in the present study, produce less oriented deposits [111].

Analysis of the growth of  $\text{FeSn}_2$  on specifically oriented iron single crystals has been previously done [112] by heating tinplate samples (in a cycle from 25 °C to 325 °C), finding that three specific types of structure form depending on which iron face it is grown on. The three basic structures grow on the  $\{100\}$ ,  $\{110\}$  and  $\{111\}$  faces, with the structures grown on other iron faces being similar to the three basic structures. On the  $\{100\}$  face the crystallites initially form as small scattered crystallites below the melting point of the tin and progress to form an orthogonal array with increased heating. Growth arrests when the iron surface is covered and then continues with the crystals coalescing to form large alloy particles many retaining flat edges. On the  $\{110\}$  face numerous small crystallites form below the tin melting point and progress to form columnar crystallites, parallel to each other on the surface, until the substrate becomes completely covered, when the growth briefly arrests. On continued heating the crystallites coalesce and form large globular particles. The third type of growth was observed on  $\{111\}$  iron faces. The nucleation rate in this case was greater than the other two cases with the substrate being completely covered before the tin melt stage.

Globular crystallites begin to form around the melting point of tin. After melting the globular crystallites expanded to form columnar crystallites protruding from the substrate surface and on continued heating coalesced into large globules similar to those found with the  $\{110\}$  face. Tinplate produced commercially would be expected to have a combination of  $\text{FeSn}_2$  crystallite formation of those types discussed.

In another study [104] heating tinplate, with polycrystalline steel substrates, below the melting point of tin was shown to generally produce a more nodular  $\text{FeSn}_2$  structure than the structure formed above the melting point where rectangular crystallites were the more common form. Thus comparing this work and the work on single crystals [112], it can be inferred that less of the  $\{100\}$  orthogonal type structure was formed on the polycrystalline substrates and more of the  $\{111\}$  globular type structure was formed. Another study [113] analysing  $\text{FeSn}_2$  formed on polycrystalline substrates showed the difference in  $\text{FeSn}_2$  morphology on different grains leads to areas of exposed substrate where the  $\{100\}$  orthogonal type structure was formed and covered substrate where the other forms grow. The  $\{100\}$  face oxidises more readily than the other faces and so the formation of  $\text{FeSn}_2$  on these faces can be slower due to the presence of oxide layers inhibiting growth. As may be expected the nodular form of crystallites leads to a more compact  $\text{FeSn}_2$  layer [104]. This more compact layer may improve corrosion resistance by decreasing alloy layer porosity.

Defects in the steel substrate are also translated to defects in the alloy layer. NMIs and carbide particle inclusions do not alloy with the tin and so the alloy layer is incomplete [111]. Early experiments on the formation of  $\text{FeSn}_2$  during electrodeposition [105]

noted that FeSn<sub>2</sub> could be observed by X-ray diffraction on material newly electrodeposited in the alkaline bath, but not in acid baths. This was postulated to be due to the hydrogen codeposited in the bath and experiments were carried out to test this hypothesis and tended to agree.

#### **4.9 Mössbauer Studies of Tinfoil**

The initial aim of this present study was to analyse the interface region of tinfoiled steel DWI cans. Tinfoiled steel sheet has been analysed previously [114] using <sup>119</sup>Sn Mössbauer spectroscopy and determinations of interface layer thicknesses have been made within that study. The tinfoil was commercial grade, though the process of manufacture was not stated within the published results. Tinfoil that was flowbrightened showed the formation of FeSn<sub>2</sub> after heating to 290 °C to 300 °C, the parameters obtained using <sup>119</sup>Sn Mössbauer spectroscopy were  $H = 2.5 \pm 0.1$  T and  $\delta = -0.07 \pm 0.02$  mm s<sup>-1</sup> and  $\Delta = 0.01 \pm 0.02$  mm s<sup>-1</sup> which is in agreement with previous results on bulk FeSn<sub>2</sub> by Nikolaev et al. [101]. Tinfoil prior to flowbrightening showed no FeSn<sub>2</sub> but was found to have a 1 nm thick oxide layer.

Intermetallic phase formation at the interface of an iron substrate electrodeposited with tin has been analysed using <sup>119</sup>Sn Mössbauer spectroscopy [108]. An interfacial phase was identified before heat treatment the primary constituent of which was Fe<sub>3</sub>Sn<sub>2</sub> with some FeSn<sub>2</sub>. Heat treating the system caused greater amounts of FeSn<sub>2</sub> to be formed.

Experimentation in this present study has concentrated on the analysis of a Drawn and Wall Ironed (DWI) tinned steel can which was provided by Corus plc. A number of different areas of the can were identified as being useful in analysing the structure of the can and therefore the effect of the DWI process on the tinned steel. Prior to this analysis DWI tinned steel has only been studied using scanning electron microscopy (SEM) [53] and by physical testing methods [37,54,55].

#### **4.10 Mössbauer Studies of Intermetallics and Corrosion Products**

This aim of this project is to study tinned steel drinks cans and other tinplate products supplied by Corus plc. In particular the intermetallics formed are of interest in this study and these are discussed more for the Fe-Sn system in section 4.6. Intermetallics and corrosion products on the cans can be uniquely identified in Mössbauer spectra. Mössbauer Spectroscopy has been used in previous studies of iron-zinc intermetallics [115,116,117,118,119] and iron-aluminium intermetallics [120,121,122,123,124] amongst other intermetallics in which Fe is combined with transition metals and metalloids [93,125,126] in order to identify and characterise these intermetallics.

Much work has been done on galvanized steel where four iron-zinc phases, Zeta, Delta, Gamma-1 and Gamma have been identified and characterised [115,116,118]. Studies of galvanized steel are particularly important as it is widely used in the automotive industry. The corrosion resistance of such Fe-Zn alloy coatings on steel have also been studied [119]. Addition of aluminium into the molten zinc bath has

been found to help in the control of Fe-Zn phase formation [117]. As well as analysis of Al-Fe phases in situ [120,124], Al-Fe phase extraction has been carried out in order to analyse the phases with improved signal to noise ratios [123].

Protection against corrosion is often one of the reasons for coating steels with tin, zinc or aluminium. Corrosion inhibitors, including inorganic compounds (chromates and nitrates) and organic compounds (benzoates and phosphonates) have been analysed [127,128,129] to test their effectiveness at preventing corrosion reactions on steel. Paint and varnish, used as protective films on steel have also been analysed using Mössbauer spectroscopy [130,131].

Mössbauer Spectroscopy has also been used in numerous previous studies of corrosion products [7,132-141] and is often regarded as the technique of choice when analysing thin corrosion layers, at the early stages of the corrosion reaction [130]. Surface enrichment with  $^{57}\text{Fe}$ , as used in previous studies using Conversion X-ray Mössbauer Spectroscopy (CXMS) [130], can be used to try to identify early stage corrosion however there is no significant corrosion on the cans analysed within this study and so only a brief overview of possible corrosion products is given here.

Iron is easily oxidized and reacts directly with most common nonmetallic elements, producing compounds in which iron is in the +2 or +3 oxidation state forming the bivalent iron (II), or ferrous, compounds and the trivalent iron (III), or ferric, compounds. Iron can absorb hydrogen and nitrogen at high temperatures and also forms phosphides, carbides, and silicides.

Without the presence of water iron can react with oxygen above 150 °C to form mixed oxides and at temperatures above 575 °C with low concentrations of oxygen, FeO is formed. With the presence of water iron reacts with oxygen to form hydrated iron oxide (rust). At room temperature, three components in addition to iron must be present in order for rust to form, oxygen, water, and an electrolyte (an ionic substance dissolved in the water). Iron rusts most readily in the atmosphere when the relative humidity exceeds 50 %, forming a complex mixture of compounds that is mostly a ferrous-ferric oxide with the composition Fe<sub>3</sub>O<sub>4</sub>. This is a process that occurs in two steps. Firstly iron dissolves in the air, which is acidic due to the presence of carbon dioxide, and this forms ferrous iron (iron(II)), and liberates hydrogen. Then oxygen from the air oxidizes the ferrous iron to form hydrated iron(III) oxide. The presence of other air pollutants, such as the sulphur oxides, increases the rate of formation of the rust. With air and water present, sulphur dioxide forms sulphuric acid which oxidizes the iron. The formation of rust can be inhibited by coating the iron surface with certain chemicals or by galvanizing (zinc plating) or tin plating.

The main iron corrosion products are FeO (wüstite) [142], Fe<sub>3</sub>O<sub>4</sub> (magnetite) [143,144,145], α-Fe<sub>2</sub>O<sub>3</sub> (hematite) [146,147], γ-Fe<sub>2</sub>O<sub>3</sub> (maghemite) [148,149], α-FeOOH (goethite) [150,151,152], β-FeOOH (akaganeite) [152,153,154,155], γ-FeOOH (lepidocrocite) [152,156,157], δ-FeOOH (feroxyhite) [152,154,158,159], Fe(OH)<sub>2</sub> (iron hydroxide) [160,161], Fe(OH)<sub>3</sub> (iron trihydroxide) [162,163].

These corrosion products have been heavily studied using many techniques, including Raman spectroscopy [7], X-ray photoelectron spectroscopy (XPS) [133], X-ray

diffraction [133,135], electron microscopy [163] and infra-red spectroscopy [137]. Mössbauer studies in particular have been carried out on all of these oxides and hydroxides. A useful summary of the hyperfine parameters, deduced from spectra recorded at 300 K, 77 K and 4 K, for most of these oxides and hydroxides is given by Oh et al. [7]. Raman peak positions are also given in that study and compared to previously published results. Another summary and explanation of the oxides and hydroxides is given by Simmons and Leidheiser [164]. The crystal structures of these oxides and hydroxides are given by Bernal et al. [165] along with the structural transformations between the various oxides and hydroxides.

#### **4.11 Detection Techniques**

For  $^{57}\text{Fe}$  Mössbauer spectroscopy there are a range of detectors, which are used in both transmission and backscatter geometries. Transmission measurements of Mössbauer  $\gamma$ -rays are usually taken using cylindrical gas filled proportional counters, but others can be used. In particular Li drifted Ge/Si detectors and scintillation counters. In the backscatter geometry  $\gamma$ -rays can be detected [166], but generally either X-rays or electrons are detected for either CXMS or CEMS and again there are a number of types of detector that are used.

For surface studies CEMS is generally the method employed. There are two basic types of CEMS experiment, either integral CEMS, where the total backscattered electron flux is detected, or depth selective CEMS (DCEMS), which is often also referred to as the energy differential mode of CEMS, where selected bands of electron

energies are detected allowing, to some degree, the study of surface regions as a function of depth.

The theories concerning Mössbauer signal depth that provide the underlying principles of understanding depth selectivity extend from basic exponential electron attenuation and are discussed more in section 4.10. The DCEMS technique for the study of sample surfaces, originated by Bonchev et al. [167], has been analysed theoretically and experimentally in previous studies [168-176]. The technique provides a method of obtaining Mössbauer spectroscopic information for various depths within a sample. DCEMS studies have generally employed the K-conversion electrons with energies from 6.5 keV to 7.3 keV [177,178] though some studies analyse a wider electron energy range because of energy resolution problems [179,180], which leads to the requirement of the use of large bands of energy in the analysis of the electrons. Depth selectivity is based on the fact that electrons from deeper within the sample lose more energy due to attenuation. The mean free path for penetration without energy loss depends on the electron energy. Unfortunately the electrons coming through the sample do not travel in straight paths (see figure 4.8).

Therefore electrons originating from the same depth in a sample may provide a widespread range of emergent electron energies. This effect is known as straggling and is a serious drawback for the DCEMS technique. Despite this drawback some studies have determined where the signal may come from in samples [181, 182].

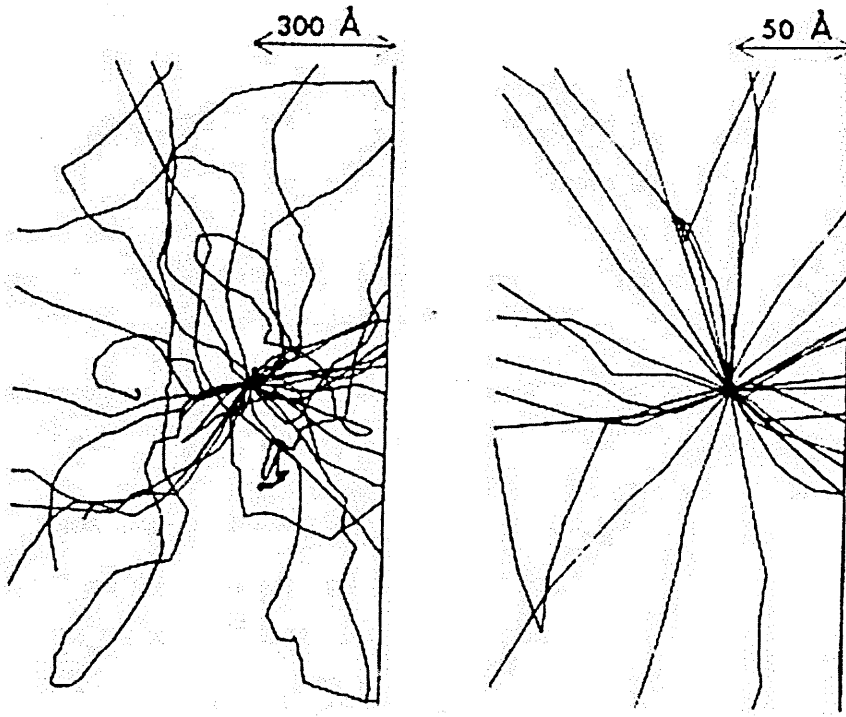


Figure 4.8. Diagrammatical representation of straggling (from [20]).

The DCEMS method of probing certain depths of a sample generally employs an electron analyser, most often with a channeltron detector, to detect electrons with well defined energies corresponding to K-conversion electron values. This requires good electron energy analysis, which can be achieved with electrostatic (deflection based) analysers [183-189].

Cylindrical analysers used by Parellada et al (1981) [183] provide good energy resolution but have poor luminosity (which is the ratio of electron output detected at detector to the electron input) because the sample radiates electrons with a  $2\pi$  angle and the acceptance angle of the analyser is much smaller. Spherical analysers also offer good resolution and are found to have reasonable luminosity (ratio of electron output at detector to electron input) [184,185,186,190].

However the DCEMS method of using electron analysers has a poor counting efficiency and for the analysis of small amounts of intermetallics the use of this method would prove to be less helpful than CEMS with a gas flow proportional counter. In such experiments the counting time would be weeks rather than days even with a strong source making experimentation very time consuming. In this case the use of an electron analyser might not be an efficient use of time and resources, instead the integral mode of CEMS should be used where the total flux of electrons from the sample is detected, however this provides no depth resolution.

DCEMS is a powerful technique but is costly in terms of equipment and time as the experimental arrangement generally requires an ultra high vacuum (UHV), a vibration free environment, long counting times and is also best performed with high activity sources (100 mCi and above sources are common for the technique).

One other problem with DCEMS, which is especially relevant in the analysis of DWI tinplated steel is that the sample is required to be very flat [177] as DCEMS loses much of its potential if the sample has an uneven surface. The effects of surface roughness in CEMS and DCEMS experiments has been analysed by Liljequist and Ismail (1985) [191] using a Monte Carlo simulation of varying roughness iron surfaces and results showed that the degree of roughness is not too much of an issue in CEMS provided that the ratio of amplitude to wavelength of surface undulation is no greater than 1:10 with amplitude being no greater than 100 nm. It was found to be more of an issue with DCEMS and especially experiments using DCEMS at glancing angles (GA-DCEMS) [178,181,192,193] even with smaller amplitude undulations.

Studies by Kuprin et al. [194,195] were aimed at experimentally refining the Monte Carlo simulations whilst also considering roughnesses of 1  $\mu\text{m}$  to 1mm in size on iron coated stainless steel substrates. The electron energy interval most affected by the roughness was found to be that containing the low energy electrons (1.1 - 5.1 keV), which tended to arise from lower in the specimen as roughness increased. Thus 50 % of the low energy electrons were found below 40 nm for the smoothest sample, 60 nm for the intermediate sample and below 75 nm for the roughest sample. However, both the integral CEMS signal and that from the higher energy electrons (11.5 - 14.5 keV) were almost unaffected by the increase in roughness.

With a very flat sample the use of GA-DCEMS enhances the signal from the very near surface region when at high glancing electron emission angles [178,192]. However this method is not entirely suitable for the analysis of the intermetallics on DWI tinplated steel as the sample surface roughness is relatively high.

DCEMS has also been applied to the study of very thin (<50  $\text{\AA}$ ) surface layers e.g. Belozerskii et al (1982) [196]. In that study the technique proves to be useful in the identification of very thin oxide layers on the surface of air exposed iron. However the particular oxide was not identified. The usefulness of DCEMS in corrosion studies is dependent on the surface roughness of the sample [177,191] and since corrosion leads to roughening of the surface this technique is not suitable for studies of corrosion beyond initial surface corrosion formation.

A number of DCEMS studies have been carried out using proportional counters [179, 180,194,195,197,198]. Poor energy resolution means that a large energy range needs to be analysed with the outgoing electron energies being detected with varying discrimination levels set on the single channel analysers. Usually levels are set at around 2-5 keV, 6-9 keV and 11-14 keV [180,194,195]. Though some analysis has been done with three energy bands set only below 7 keV [179] not taking into account pulses created by the simultaneous detection of a multiple conversion or Auger electrons, or the L (13.6 keV) conversion electrons (except those that have lost sufficient energy in collisions to enter into the selected energy bands).

Other experimental designs for DCEMS include scintillation electron detectors described by Kajcsos et al (1988) [199] and semiconductor detectors described by Petersen (1984) [200] and Pancholi, de Waard and Petersen (1984) [201]. Scintillation detectors have been found to give slight performance improvements in counting times over channeltrons [199], which are used in most DCEMS experiments. Channeltrons are also prone to long term instability and suffer from non-linear energy responses. Scintillation detectors require very low noise, high quantum efficiency and high gain of the photomultiplier. With such a photomultiplier cooled and with the photocathode grounded a higher overall counting efficiency is achieved. The semiconductor detectors provide higher efficiency but with a loss of resolution over other types of detector.

Since CEMS is used to detect low energy internally converted electrons the sample needs to be inside the detector as the electrons are unable to pass through detector

window materials. In CEMS there are a number of different detectors which can be used, these include scintillation counters, channeltrons and proportional counters, both gas filled and gas flow [202]. Descriptions of the various detectors can be found in references [203,204,205] and references therein.

For the detection of low energy conversion and Auger electrons gas flow proportional counters are widely used because of their ease of construction and operation at room temperature, however designs vary greatly. In the experiments within this study the type of detector used is a single wire anode gas flow proportional counter with a cylindrical sample chamber. A number of different sample chambers have been used for CEMS experiments, which can be made of aluminium, lucite or brass [204,206,207] with one, two [208] or three [205, 209] stainless steel, tungsten or gold coated tungsten anode wires. The position of the anode wires relative to the sample is important, as the electrons with low energy are not able to reach the counter wires when the distance is large [209]. The gasses used for CEMS are usually a mixture of He with 5% to 10% CH<sub>4</sub> which is used as a quenching agent though a number of different gasses are used for varying temperature experiments. The gas flows through the counter at approximately 1-3 cm<sup>3</sup> / min. CXMS uses 95% Ar with 5% CH<sub>4</sub> which allows for detection of the 6.3 keV X-rays rather than the conversion and Auger electrons [208].

The CEMS detector must have a high detection efficiency of both the resonantly produced 7.3 keV conversion and 5.6 keV Auger electrons generated by the 14.4 keV  $\gamma$ -rays. By setting a mylar window between the collimator and the main body of the

detector the Fe K X-rays from the incoming beam are absorbed without significant absorption of the 14.4 keV  $\gamma$ -rays which helps to reduce the production of other non-resonantly produced electrons.

The sample constitutes the cathode and the application of a positive HT voltage to the wire anode enables the detection of the 7.3 keV conversion and 5.6 keV Auger electrons. The stainless steel, or more commonly, tungsten anode wire, with a diameter of 25  $\mu\text{m}$ , is maintained at a potential of 1.0 kV to 1.5 kV, which ensures the formation of ion pairs in the gas mixture.

Increased spectral resolution can be attained by reducing the temperature of the sample and previous work has been done on techniques to lower sample temperature in particular using channeltron detectors [210], gas flow proportional counters [204] and gas filled proportional counters with or without an evacuated cryostat [211].

Gas filled proportional counters have been operated with pure helium gas at temperatures below 15 K successfully but have been found to be unstable above that temperature [212,213]. A number of different gas mixtures can be used at temperatures from 15 K up to liquid nitrogen temperature (77 K) [214] including purified neon and helium / neon mixtures. For CEMS experiments around liquid nitrogen temperature it is necessary to use either He / 2 %  $\text{CH}_4$  gas or He / 10 % CO, greater concentrations of  $\text{CH}_4$  have been found to freeze at these temperatures [211]. He / 5%  $\text{CH}_4$  is commonly used above liquid nitrogen temperature. Another gas that

has been used is hydrogen in the range of 15 K to room temperature [214] and has been found to be stable within this temperature range.

Without using an evacuated cryostat temperatures of 100 K have been shown to be achievable by using gas flow proportional counters with He / 5% CO gas [204]. At these lower temperatures the gas multiplication rate is lower and it is therefore necessary to adjust anode potential and gas flow rate to compensate.

A simple method of reducing temperature of the sample in a gas flow proportional counter is to use peltier devices stacked on the backplate of the detector [215]. However these experiments were carried out using He / 5% CH<sub>4</sub> and the CH<sub>4</sub> slowly freezes. A gas mixture with lower CH<sub>4</sub> levels would lead to less CH<sub>4</sub> freezing and therefore improved results from longer experiments.

Another technique to help improve the surface sensitivity of CEMS is to vary the angle of the incident  $\gamma$ -ray beam relative to the specimen surface [179, 209]. This technique shows that the percentage contribution of the top layer to the overall CEMS signal is increased as the angle of the incident  $\gamma$ -ray beam relative to the specimen normal is increased. This technique has been carried out on samples enriched with <sup>57</sup>Fe and it was suggested that this is the limiting factor of angle sensitive CEMS making it unsuitable for the analysis of unenriched samples.

## 4.12 Mössbauer Signal Depth

The depth from which the Mössbauer signal arises is important in a number of analysis situations, in particular the analysis of multilayer materials or to improve surface sensitivity by selecting electron energies as in the DCEMS technique described previously. This section of the literature study also details some work done on adding inert layers to systems under analysis, which has been used to distinguish between overlayer and substrate signals in dual layer systems.

### 4.12.1 Mössbauer Signal Depth Theory

The theories concerning Mössbauer signal depths that provide the underlying principles of understanding depth selectivity extend from the basic exponential electron attenuation law described by Coslett and Thomas [216]. The present mathematical analysis of Mössbauer signal depth is extended from that early theory. Krakowski and Miller [168] presented electron slowing down models based on the exponential attenuation law and diffusion theory. The attenuation of monoenergetic electrons by a material is complex being composed of a series of processes the theories of which themselves do not describe exponential attenuation, but combined and observed experimentally follow such a trend. The energy weighting of the emergent electrons is such that electrons arising from deeper within the material under analysis have an energy distribution weighted towards the low energy end of the range and electrons emerging from the upper region produce an energy distribution weighted towards the maximum electron energy. Using CEMS these electrons are detected with

the same signal, independent of electron energy. The very low energy electrons, which statistically originate from deeper within an analysed material, are often not detected, as the system will include a signal cut-off in order to reduce the influence of noise in the signal.

#### 4.12.2 Studies of Signal Depth

Experimentally, in one particular study of steel by Williamson et al (1986) [182], it was found that 75% of the signal in CEMS came from the first 100 nm, 90% from the first 200 nm and 92% in the top 300 nm.

One study by Shigematsu, Pfannes and Keune (1980) [181] was able to determine that with an iron coated stainless steel sample (25 nm thick coating) 91% of the 7.3 keV electrons originated from the first 25 nm and 89% of the 6.6 keV electrons came from deeper within the sample beyond 25 nm. These results agreed with theoretical calculations by Krakowski and Miller (1972) [168] and Liljequist, Ekdahl and Baverstam (1978) [173]. Krakowski and Miller [168] note that the relation of electron energy to specific depth is poor for energies below half of the maximum electron energy. Since electrons with high energy, close to the maximum value for the system (7.3 keV for  $^{57}\text{Fe}$  Mössbauer spectroscopy), have high probability of originating from the very near surface of the resonator then by analysing electrons of such energies some depth related spectra can be obtained. The limit for such spatial energy resolution is defined by half the maximum energy giving spectra originating from regions near the resonator surface (depths from 0 to 80 nm).

### 4.12.3 Adding Inert Layers for Signal Analysis

Knowledge of the distribution of the signal, in terms of electron energy to depth of origin, in the samples of DWI tinplated steel is desirable. One method that has been tried by a number of researchers is the evaporation of a series of layers of known thickness of a Mössbauer inert substance, such as Al, Au, Cr or Cu, onto an Fe surface. This method was expected to produce a depth profile from which the distribution of the signal from the sample could be seen. However it has been found [217,218] that secondary electrons are produced as a result of approximately 30% of the excited  $^{57}\text{Fe}$  nuclei emitting K X-rays and subsequently producing non-resonant photo-electrons in the applied surface layer. The  $\gamma$ -rays falling on the specimen cause the production of X-rays throughout the specimen which are only weakly absorbed by the specimen and therefore produce the photo-electrons in surface layers which contribute to the signal. These secondary electrons are detected by the detector and cause the overall signal from the sample to increase with thin overlayers to a maximum when the coating is of the order of 40 nm for aluminium.

Addition of more evaporated layers causes the signal to then decrease due to the dominance of the absorption of conversion electrons in the Mössbauer inert coating over photoelectron production. One study by Tricker, Ash and Cranshaw (1977) [217] showed that for natural iron coated stainless steel substrates the evaporation of Al and Au overlayers caused the ratio of the stainless steel signal to the natural iron signal to increase with increasing overlayer thickness. This coating technique has also been used as a method for distinguishing overlayer and substrate signals [219].

Bonchev et al. [172] used Cu as the evaporated overlayer on a SnO<sub>2</sub> substrate. The maximum signal was observed when an overlayer of 110 nm was present and the detected electron energy was 15 keV (using <sup>119</sup>Sn Mössbauer spectroscopy). With increasing electron energy the maximum signal was obtained when using thinner overlayers.

Coatings with smaller atomic numbers are not such efficient converters of X-rays to photoelectrons. Au has been found [217] to be a very efficient converter of X-rays into electrons. The non-resonant electrons have a masking effect that increases with the abundance of heavy elements as the probability of photoelectric interactions increases linearly with  $Z^5$  [220].

In this current project carbon coatings have been investigated as a method of analysing the depth profile of tinplate samples and to distinguish overlayer and substrate signals. The initial DWI tinplated steel samples that were analysed had possible intermetallic signals that were weak and difficult to fit using the standard spectrum fitting software and so if the intermetallics at the very near surface could be enhanced relative to the substrate they may become easier to distinguish. This would require the absorption of the lower energy electrons arising from deeper within the samples to be greater than the effect of photoelectron production in the sample and overlayer.

## Literature Review References

- [1] O. Kubaschewski, Iron - Binary Phase Diagrams, Springer-Verlag (1982) p. 180.
- [2] L. Crovini, R. E. Bedford and A. Moser, Extended List of Secondary Reference Points. Metrologica 13 (1977) 197.
- [3] U. Gonser and H. Fischer, Hyperfiner Interactions 72, 1992, pp 31-44.
- [4] D. C. B. Whittet, Dust in the Galactic Environment, Institute of Physics Publishing, 1992.
- [5] C. R. Kitchin, Stars, Nebulae and the Interstellar Medium : Observational Physics and Astrophysics, Institute of Physics Publishing, 1987.
- [6] E. Morgan, Tinplate and Modern Canmaking Technology, Pergamon Press, 1985.
- [7] S. J. Oh, D. C. Cook and H. E. Townsend, Hyperfine Interactions 112 (1998) 59-65.
- [8] R. E. Vandenberghe, C. A. Barrero, G. M. da Costa, E. Van San and E. De Grave, Hyperfine Interactions 126 (2000) 247-259.
- [9] G. P. Huffman and F. E. Huggins, Applications of Mössbauer Spectroscopy in the Steel Industry in "Mössbauer Spectroscopy and its Chemical Applications" Eds. J.G. Stevens and G.K. Shenoy, American Chemical Society, 1981.
- [10] R. W. Bouman, Iron & Steelmaker, February 1981, p 20.
- [11] N. N. Greenwood, T. C. Gibb, "Mössbauer Spectroscopy", (Chapman and Hall, London, 1971).
- [12] D. Cardwell, The Fontana History of Technology, Fontana Press 1994.
- [13] R. A. Mott, Journal of The Iron and Steel Institute, March 1965, p227.
- [14] J. A. Botta, Jr. and Fernando Mendez de Andes, Iron and Steel Engineer, May 1973.
- [15] P. E. Nilles, Iron & Steelmaker, June 1982.
- [16] C. G. Davis, J. F. McFarlin and H. R. Pratt in : Ironmaking and Steelmaking, Vol 9, No 3, ed. T.L. Hughes (The Metals Society, 1982) p. 93.
- [17] R. L. Stephenson, Iron & Steelmaker, February 1982.
- [18] R. Pearce, Sheet Metal Forming, Adam Hilger / IOP Publishing, 1991.

- [19] P. H. Salmon Cox and J. A. Charles, *Journal of the Iron and Steel Institute*, 1963, p. 863.
- [20] P. H. Salmon Cox and J. A. Charles, *Journal of the Iron and Steel Institute*, 1965, p. 493.
- [21] D. H. Houseman, *Bull. Fuel and Metals*, 1978, 101.
- [22] Z. Yamamoto, H. Nakagawa, and T. Shima, "Recent Development of RH Vacuum Treatment at Nippon Steel Corporation", Third IISC, ASM and AIMI Conference, Chicago, 1978.
- [23] T. Kohno and T. Yukawa, "Composition Adjustment by New Methods", *ISS-AIME*, 62 (1979) p. 125.
- [24] I. Boustead et al. *The Metal Can*, The Open University Press, 1980.
- [25] E. C. Hewitt, *Iron & Steelmaker*, September 1982.
- [26] R. M. Hudson, R. J. Joniec and S. R. Shatynski in : *Metals Handbook 9<sup>th</sup> Edition Volume 5 Surface Cleaning, Finishing and Coating*, ed. W.G. Wood (American Society for Metals, 1982) p. 68.
- [27] M. Sittig, *Electroplating and Related Metal Finishing*, Noyes Data Corporation, 1978.
- [28] MOD Defence Standard 03 - 2/1, 28<sup>th</sup> December 1970.
- [29] P. N. Burkard in : *Modern Electroplating*, ed. F.A. Lowenheim (John Wiley and Sons, Inc. New York, 1974) p. 571.
- [30] M. P. Henry, Presentation of a New 5-Stand Tandem Cold-Rolling Mill, First International Tinsplate Conference, ITRI, London (1976) 72-77.
- [31] H. Johan ter Maat, *Automatica* vol. 18, no. 2, 1982, pp 63-69.
- [32] W. D. King and R. M. Sills, *Iron and Steel Engineer*, May 1973 pp 40-51.
- [33] H. Johan ter Maat, *Journal A*, vol. 20, no. 4, 1979, pp 203-208.
- [34] R. E. Kalman, *AIEE Trans.*, 73 (1955) pp 383-390.
- [35] F. Z. Bentayeb, B. Bouzabata and S. Alleg, *Hyperfine Interactions* 128 (2000) 375-380.
- [36] W. O. W. Price and E. H. Vaughan, *Iron and Steel Institute. Special Report no. 79*.
- [37] S. C. Ball, D. T. Llewellyn and N. D. Jenks, *Ironmaking and Steelmaking Vol. 25, No. 1*, 1998, pp 55-62.

- [38] R. A. Higgins, Properties of Engineering Materials, Hodder and Stoughton, 1977.
- [39] W. E. Hoare, E. S. Hedges and B. T. K. Barry, The Technology of Tinplate, Edward Arnold Publishers, London, 1965.
- [40] O. Kubaschewski, Iron - Binary Phase Diagrams, Springer-Verlag 1982, p. 181.
- [41] R. Hultgren, R. L. Orr, P. D. Anderson and K. K. Kelley, Selected Values of Thermodynamic Properties of Metals and Alloys, New York, Wiley 1963.
- [42] W. E. Hoare, E. S. Hedges and B. T. K. Barry, The Technology of Tinplate, Edward Arnold Publishers, London, 1965.
- [43] A Guide to Tinplate, International Tin Research Institute, London, 1983.
- [44] W. J. Roberts and B. Srinivasan in : Metals Handbook 9<sup>th</sup> Edition Volume 5 Surface Cleaning, Finishing and Coating, ed. W.G. Wood (American Society for Metals, 1982) p. 33.
- [45] N. V. Parthasaradhy, Practical Electroplating Handbook, 1989, Prentice Hall.
- [46] R. M. Macintosh in : Modern Electroplating, 3<sup>rd</sup> Edition, ed. F.A. Lownheim, John Wiley and Sons, 1974, p. 401.
- [47] F. A. Lownheim in : Modern Electroplating, 3<sup>rd</sup> Edition, ed. F. A. Lownheim, John Wiley and Sons, 1974, p. 377.
- [48] P. E. Davis in : Metals Handbook 9<sup>th</sup> Edition Volume 5 Surface Cleaning, Finishing and Coating, ed. W. G. Wood (American Society for Metals, 1982) p. 270.
- [49] I. E. N. Soepenbergh, Development of Tinplate and Tinplate Substitutes for Beverage and Food Can Application, Sheet Metal Industries, May 1988.
- [50] M. E. Warwick, The Effects of Changes in Can-Making Technology on the Consumption of Tin, Tin and its Uses, No. 133, 1982.
- [51] J. Siewert and M. Sodeik, Seamless Food Cans Made of Tinplate, First International Tinplate Conference, ITRI, London, (1976).
- [52] B. N. Moss, Two Piece Food Containers - The Next Development, First International Tinplate Conference, ITRI, London, (1976).

- [53] W. van Koesveld and J. S. van Westrum, From Blank to Can : Origin and Growth of the Morphology of the Wall of a DWI Can, Third International Tinplate Conference, ITRI, London (1985) 310-318.
- [54] P. D. C. Rogers and G. Rothwell, D. W. I. Canmaking : The Effect of Tinplate and Aluminium Properties, Metals Soc., Book 301, Developments in the Drawing of Metals, Proceedings of the International Conference, London, (1983) 95-101.
- [55] J. M. Anne, J. F. Bailleul, C. Brun and F. Sauvage, Flex Draw Test for D&I, Metals Soc., Book 301, Developments in the Drawing of Metals, Proceedings of the International Conference, London, (1983) 107-112.
- [56] H. D. Merchant, D. S. Hodgson, I. O'Reilly and J. D. Embury, Structure and Property Evolution During Drawing and Wall Ironing of Aluminium Alloy 3004, Materials Characterization 25 (1990) 251-261.
- [57] P. R. Carter, L. L. Lewis and M. V. Murray, Surface Properties of Drawn and Ironed Tinplate Containers, First International Tinplate Conference, ITRI, London, (1976).
- [58] C. G. Carson, T. E. Johnson, E. W. Gilbreath, Material and Design Factors Affecting the Manufacture of Lightweight Drawn and Ironed Tinplate Cans, Second International Tinplate Conference, ITRI, London, (1980).
- [59] D. C. Shah, Differentially Coated Tinplate for Drawn and Ironed Cans, Second International Tinplate Conference, ITRI, London, (1980).
- [60] L. Hartman, Essential Activities Leading to a Reduction in Material Costs for a 12-oz. DWI Container of Tinplate, Third International Tinplate Conference, ITRI, London, (1984).
- [61] J. F. Renard, Tinplate Potential for DWI Canmaking, Fifth International Tinplate Conference, ITRI, London, (1992).
- [62] R. M. Soler, A. A. Vitali, M. S. Sadahira and V. A. Junqueira, Microseam : A New Closure System for Metal Containers, Fifth International Tinplate Conference, ITRI, London, (1992).
- [63] E. O. Kohn, Tooling Aspects of High-Speed Can Production, Sheet Metal Industries, June 1976, p331.

- [64] E. Morgan, *Tinplate and Modern Canmaking Technology* (Pergamon Press, Oxford, 1985) 166-175.
- [65] W. Panknin, *Principles of Drawing and Wall-ironing for the Manufacture of Two-piece Tinplate Cans*, First International Tinplate Conference, ITRI, London, (1976).
- [66] S. Y. Chung and H. W. Swift, *Cup Drawing from a Flat Blank*, Proceedings of the Institute of Mechanical Engineers, Volume 165, (1951), 199-228.
- [67] J. L. Duncan and W. Johnson, 9<sup>th</sup> International MTDK Conference, Pergamon Press, 1969.
- [68] J. M. Alexander, *Metallurgical Reviews*, 1960, Vol. 5, No.19.
- [69] T. P. Murphy and H. Smith, *Changes in Tinplate Surfaces During DWI Can Manufacture*, Third International Tinplate Conference, ITRI, London, (1984).
- [70] F. Fidler, *Two-Piece Container Developments - Some Influences of Tin*, First International Tinplate Conference, ITRI, London, (1976).
- [71] R. Duckett, B.T.K. Barry and D.A. Robins, *Effect of Tin Coatings on the Drawability of Steel Sheet*, Sheet Metal Industries, September 1968.
- [72] R. Duckett and C. J. Thwaites, *A Note on the Wall-Ironing of Cups Drawn From Tinplate*, Sheet Metal Industries, April 1971.
- [73] A. Tosaka and K. Okuda, *Effect of Mechanical Properties of Tinplate on DWI Canmaking*, Sixth International Tinplate Conference, ITRI, London, (1996).
- [74] J. A. van der Hoeven, E. Janssen, F. Jonker and W. van Koesveld, *Material Flow and Surface Aspects in D & I Can-Making*, Fourth International Tinplate Conference, ITRI, London, (1988).
- [75] G. A. Jenkins, G. Jefford and D. W. Evans, *Seamless Food Cans Made of Tinplate*, First International Tinplate Conference, ITRI, London, (1976).
- [76] E. Isaac and G. Tammann, *Zeitschrift für anorganische Chemie*, vol. 53 (1907) pp 281-290.
- [77] F. Wever and W. Reinecken, *Zeitschrift für anorganische und allgemeine Chemie*, Vol. 151 (1926) p. 349.
- [78] C. A. Edwards and A. Preece, *J. Iron and Steel Inst.*, 124 (1931) p. 41.
- [79] "Equilibrium Data for Tin Alloys", Tin Research Institute, 1949.

- [80] O. Kubaschewski, *Iron - Binary Phase Diagrams*, Springer-Verlag 1982, p. 139.
- [81] M. Hansen and K. Anderko, *Constitution of Binary Alloys*, McGraw Hill, New York, 1958.
- [82] W. G. Moffatt, *The Handbook of Binary Phase Diagrams*, General Electric, 1994.
- [83] W. F. Ehret and A. F. Westgren, *Journal of the American Chemical Society*, Vol. 55 (1933) p.1339.
- [84] W. D. Jones and W. E. Hoare, *J. Iron and Steel Inst.*, 129 (1934) p. 273.
- [85] W. F. Ehret and D. H. Gurinsky, *Journal of the American Chemical Society*, Vol. 65 (1943) p.1226.
- [86] O. Nial, "X-ray studies on Binary Alloys of Tin with Transition Metals", University of Stockholm, 1945.
- [87] M. Hansen, "Constitution of Binary Alloys", 2<sup>nd</sup> ed., McGraw Hill, 1958.
- [88] W. B. Pearson, "A Handbook of Lattice Spacings and Structures of Metals and Alloys Vol. 1, Pergamon Press, (1964), p. 658.
- [89] G. Trumphy, E. Both, C. Djéga-Mariadassou and P.Lecocq, *Physical Review B*, Volume 2, Number 9, 1 November 1970, p. 3477.
- [90] M. Asanuma, *J. Phys. Soc. Japan*, 15, 1960, 1343.
- [91] B. Malaman and B. Roques, *Acta Crystallogr. B*32 (1976) p. 1348.
- [92] B. Malaman, D. Fruchart and G. Le Caer, *J. Phys F: Met. Phys.*, 8 (1978) p. 2389.
- [93] A. M. van der Kraan and K. H. J. Buschow, *Physica B*138 (1986) 55-62.
- [94] G.Venturini, B. Malaman, G. Le Caër and D. Fruchart, *Physical Review B*, Vol. 35, No. 13 (1987), p. 7038.
- [95] R. P. Elliott, "Constitution of Binary Alloys", 2<sup>nd</sup> ed. 1<sup>st</sup> Supplement, McGraw Hill, 1965.
- [96] W. B. Pearson, "A Handbook of Lattice Spacings and Structures of Metals and Alloys Vol. 2, Pergamon Press, (1967).
- [97] F. H. Sanchez, L. Socolovsky, A. F. Cabera and L. Mendoza-Zélis, *Materials Science Forum Vols. 225 - 227 (1996) pp. 713 - 718.*

- [98] G. Venturini, D. Fruchart, G. Le Caër, J. Hübsch, B. Malaman and B Roques, *J. Phys. F : Met. Phys.* 15 (1985) pp. 427 - 438.
- [99] Y. Ujihira, M. Fujinami, K. Yoshida and M. Terasaka, in “Applications of the Mössbauer Effect”, Vol. 3, Y. M. Kagan and I. S. Lyubutin (Eds.) (1983) pp. 1213 – 1220.
- [100] V. I. Nikolaev, Yu. I. Shcherbina and A. I. Karchevskii, *Zh. Eksperim, i Teor. Fiz.* 44, 1963, p. 775. (*J. Exptl. Theoret. Phys. (U.S.S.R.)* 17, 1963, p. 524)
- [101] V. I. Nikolaev, Yu. I. Shcherbina and S. S. Yakimov, *Zh. Eksperim, i Teor. Fiz.* 45, 1963, p. 1277. (*J. Exptl. Theoret. Phys. (U.S.S.R.)* 18, 1964, p. 878).
- [102] G. Fabri, E. Germagnoli, M. Musci and G. C. Locati, *Il Nuovo Cimento*, Vol. 40B, No. 1 (1965) p. 178.
- [103] G. Le Caër, B. Malaman, G. Venturini, D. Fruchart and B Roques, *J. Phys. F : Met. Phys.* 15 (1985) pp. 1813 - 1827.
- [104] B. T. K. Barry and C. J. Thwaites, *Transactions of the Institute of Metal Finishing*, Vol 44 (1966) p. 143.
- [105] W. R. Buck and H. Leidheiser, *Journal of the Electrochemical Society*, February 1965, p. 243.
- [106] H. E. Biber, *Journal of the Electrochemical Society*, Vol. 113, No. 4, April 1966, p. 362.
- [107] H. Leidheiser and J. Sachdev, *Journal of the Electrochemical Society*, Vol. 117, No. 12, December 1970, p. 1532.
- [108] A. Vértes, S. Nagy and M. Z. Awad, *Nuclear Instruments and Methods* 199 (1982) pp. 367 - 369.
- [109] R. A. Covert and H. H. Uhlig, *Journal of the Electrochemical Society*, Vol. 104, No. 9, September 1957, p. 537.
- [110] S. C. Britton and K. Bright, *Corrosion*, Vol. 17. (1961) p. 120.
- [111] D. R. Gabe and R. J. Mort, *Journal of The Iron and Steel Institute*, January 1965, p. 64.
- [112] H. E. Biber and W. T. Harter, *Journal of the Electrochemical Society*, Vol. 113, No. 8, August 1966, p. 828.
- [113] C. Luner and M. V. Murray, *Journal of the Electrochemical Society*, Vol. 111, No. 4, April 1964, p. 407.

- [114] G. P Huffman and G. R. Dunmyre, Electron Reemission Mössbauer Study of Tinplate, *Journal of the Electrochemical society*, 125 (1978) pp 1652 – 1656.
- [115] D. C. Cook, *Hyperfine Interactions* 111 (1998) 71-82.
- [116] O. Kubaschewski, *Iron - Binary Phase Diagrams*, Springer-Verlag 1982, pp. 172-175.
- [117] T. Q. Coddington and D. C. Cook, Modification of Galvannealed Steel Through Aluminium Addition, *Hyperfine Interactions* 111, 1998, 205-209.
- [118] R. F. G. Grant, Identification and Characterisation of the Iron-Zinc Intermetallics formed in Galvanneal Steel, PhD Thesis, Old Dominion University, May 1995.
- [119] J. C. Chang and H. H. Wei Electrochemical and Mössbauer studies of the corrosion behaviour of electrodeposited Fe-Zn Alloys on Steel, *Corrosion Science*, Vol.30, No. 8/9, 1990, pp 831-837.
- [120] S. D. Forder, J. S. Brooks and P. V. Evans, *Scripta Materialia*, Vol. 35, No. 10, 1996, pp 1167-1173.
- [121] S. Nasu, U. Gonser and R. S. Preston, *Journal De Physique*, C1, 41, 385-386, 1980.
- [122] A. J. Reeder, An investigation of Aluminium Intermetallic Phases using  $^{57}\text{Fe}$  Mössbauer Spectroscopy and Complementary Techniques, PhD Thesis, Sheffield Hallam University, 1999.
- [123] S. D. Forder, J. S. Brooks, A. Reeder and P. V. Evans, *Scripta Materialia*, Vol. 40, No. 1, 1999, pp 45-48.
- [124] S. D. Forder, A. Reeder, J. S. Brooks, M. Rignall and P. V. Evans, *Hyperfine Interactions* 126 (2000) pp.193-197.
- [125] H. Reuther, *Surface and Interface Analysis*, Vol. 22 (1994) pp. 547-550.
- [126] H. Reuther and M. Dobler, *Surface and Interface Analysis*, Vol. 24 (1996) pp. 411-415.
- [127] I. L. Rosenfeld, *Corrosion-NACE*, Vol. 37, No.7 (1981) pp. 371- 377.
- [128] F. H. Kármán, C. Vértes and E. Kálmán, *Materials Science Forum*, Vols. 185-188 (1995) pp. 357-364.
- [129] T. M. Peev, B. R. Plachkova, *Radiochem. Radioanal. Letters*, Vol. 51, No. 5 (1982) pp. 331-338.

- [130] J. S. Brooks and S. Thorpe, *Hyperfine Interactions* 47 (1989) 159-178.
- [131] R. K. Nigam, B. P. Hajela, S. Sengupta, B. C. Srivastava and K. N. Gupta, *Hyperfine Interactions* 28 (286) pp. 935-939.
- [132] J. F. Marco, J. Dávalos, M. Gracia, and J. R. Gancedo, *Hyperfine Interactions* 83 (1994) 111-123.
- [133] J. R. Gancedo, J. F. Marco, M. Gracia, G. Joseph and R. A. Núñez, *Hyperfine Interactions* 83 (1994) 363-366.
- [134] A. S. Camara and W. Keune, *Corrosion Science*, Vol. 15 (1975) pp. 441-453.
- [135] M. J. Graham and M. Cohen, *Corrosion-NACE*, Vol. 32, No.11 (1976) pp.432-438.
- [136] V. Ramshesh and K. Ravichandran, *Radiochem. Radioanal. Letters*, Vol. 29, No. 3 (1977) pp. 87-92.
- [137] D. C. Cook, A. C. Van Orden, J. J. Carpio and S. J. Oh, *Hyperfine Interactions* 113 (1998) pp. 319-329.
- [138] H Leidheiser and S. Music, *Corrosion Science*, Vol. 22, No. 12 (1982) pp. 1089-1096.
- [139] H Leidheiser and I. C. Nagy, *Corrosion Science*, Vol. 24, No. 7 (1984) pp. 569-577.
- [140] Y. Fujio, *Japanese Journal of Applied Physics*, Vol. 12, No. 12 (1973) pp. 1850-1853.
- [141] B. K Jain, A. K. Singh, K. Chandra and I. P. Saraswat, *Japanese Journal of Applied Physics*, Vol. 16, No. 12 (1977) pp. 2121-2123.
- [142] D. P. Johnson, *Solid State Commun.* 7 (1969) 1785.
- [143] R. S. Hargrove and W. Kundig, *Solid State Commun.* 8 (1970) 303.
- [144] S. Mørup and H. Topsøe, *Journal of Magnetism and Magnetic Materials* 31-34 (1983) pp. 953-954.
- [145] B. J. Evans and S. S. Hafner, *Journal of Applied Physics*, Vol. 40, No. 3 (1969) pp. 1411-1413.
- [146] F. van der Woude, *Phys. Stat. Sol.*17 (1966) 417.
- [147] Q. A. Pankhurst, C. E. Johnson and M. F. Thomas, *J. Phys. C: Solid State Physics.* 19 (1986) pp. 7081-7098.

- [148] R. J. Armstrong, A. H. Morrish and G. A. Sawatzky, *Phys. Letters* 23(1966) 414.
- [149] J. M. D Coey and D. Khalafalla, *Phys. Stat. Sol.* Vol. 11 (1975) pp. 229-241.
- [150] J. B. Forsythe, I. G. Hedley and C. E. Johnson, *J. Phys. C Ser. 2*, 1 (1968) 179.
- [151] A. Meagher, Q. A. Pankhurst and D. P. E. Dickson, *Hyperfine Interactions* 28 (1986) 533.
- [152] M. J. Rossiter and A. E. M. Hodgson, *J. Inorg. Nucl. Chem.*, Vol. 27 (1965) pp. 63-71.
- [153] D. Rezel and J. M. R. Genin, *Hyperfine Interactions* 57 (1990) 2067.
- [154] I. Dezsi, L. Keszthelyi, D. Kulgawczuk, B. Moinar and N. A. Eissa, *Phys. Stat. Sol.* 22 (1967) 617.
- [155] D. G. Chambaere, E. De Grave, R. L. Vanleerberghe and R. E. Vandenberghe, *Hyperfine Interactions* 20 (1984) pp. 249-262.
- [156] C. E. Johnson, *J. Phys. C Ser. 2*, 2, (1969) 1996.
- [157] E. De Grave, R. M. Persoons, D. G. Chambaere, R. E. Vandenberghe and L. H. Bowen, *Phys. Chem. Minerals*, Vol. 13 (1986) pp. 61-67.
- [158] M. Pernet, X. Obradors, J. Fontcuberta, J. C. Joubert and J. Tejada, *IEEE Transactions on Magnetics*, Vol. 20, No. 5 (1984) pp. 1524-1526.
- [159] S. Okamoto, *Journal of the American Ceramic Society*, Vol. 51, No. 10 (1968) pp. 594-599.
- [160] J. M. Genin, P. H. Bauer, A. A. Olowe and D. Rezel, *Hyperfine Interactions* 29 (1986) 1355.
- [161] H. Miyamoto, T. Shinjo, Y. Bando and T. Takada, *J. Phys. Soc. Japan* 23 (1967) 1421.
- [162] S. C. F Au-Yeung, G. Denes, J. E. Greedan, D. R. Eaton and T. Birchall, *Inorg. Chem.*, 23, (1984) 1513.
- [163] S. C. F. Au-Yeung, D. R. Eaton, T. Birchall, G. Dénès, J. E. Greedan, C. Hallett and K. Ruebenbauer, *Can. J. Chem.*, Vol. 63 (1985) pp. 3378-3385.
- [164] G. W. Simmons and H. Leidheiser Jr. In : *Applications of Mössbauer Spectroscopy*, Vol. 1, ed. R. L. Cohen, (Academic Press, New York, 1976) p.85.

- [165] J. D. Bernal, D. R. Dasgupta and A. L. Mackay, *Clay Minerals Bull.* 4 (1959) pp. 15-30.
- [166] B. Keisch, *Nuclear Instruments and Methods* 104 (1972) pp. 237-240.
- [167] ZW. Bonchev, A. Jordanov and A. Minkova, *Nuclear Instruments and Methods* 70 (1969) pp. 36-40.
- [168] R. A. Krakowski and R. B. Miller, *Nucl. Instr. Meth.* 100 (1972) 93.
- [169] U. Baverstam, T. Ekdahl, C. Bohm, B. Ringstrom, V. Stefansson and D. Liljequist, *Nucl. Instr. Meth.* 115 (1974) 373.
- [170] J. Bainbridge, *Nucl. Instr. Meth.* 128 (1975) 531.
- [171] G. P. Huffman, *Nucl. Instr. Meth.* 137 (1976) 267.
- [172] T. S. V. Bonchev, A. Minkova, G. Kushev and M. Grozdanov, *Nucl. Instr. Meth.* 147 (1977) 481.
- [173] D. Liljequist, T. Ekdahl and U. Baverstam, *Nucl. Instr. Meth.* 155 (1978) 529.
- [174] A. Proykova, *Nucl. Instr. Meth.* 160 (1979) 321.
- [175] F. A. Deeney and P. J. McCarthy, *Nucl. Instr. Meth.* 159 (1979) 381.
- [176] D. Liljequist, C. Bohm and T. Ekdahl, *Nucl. Instr. Meth.* 177 (1981) 495.
- [177] J. R. Gancedo, M. Gracia, J. F. Marco and J. A. Tabares, *Hyp. Interact.* 111 (1998) 83-92.
- [178] D. Liljequist and M. Ismail, *Phys. Rev. B* 31 (1985) 4131.
- [179] J. J. Bara and B. F. Bogacz, *Hyperfine Interactions* 58 (1990) pp. 2497-2502.
- [180] Y. Yonekura, T. Toriyama, J. Itoh and K. Hisatake, *Hyperfine Interactions* 15/16 (1983) pp 1005-1008.
- [181] T. Shigematsu, H. -D. Pfannes and W. Keune, *Phys. Rev. Lett.* 45 (1980) 1206.
- [182] D.L. Williamson et al. *J. Appl. Phys.* 60 (1986) 1493.
- [183] J. Parellada, M. R. Polcari, K. Burin and G. M. Rothberg, *Nucl. Instr. Meth.* 179 (1981) 113.
- [184] T. S. Yang, B. Kolk, T. Kachnowski, J. Trooster and N. Benczer-Koller, *Nucl. Instr. Meth.* 197 (1982) 545.
- [185] Z. M. Stadnik, H. R. Borsje, A. E. M. Swolfs, W. H. A. Leenders and J. C. Fuggle, *Rev. Sci. Instrum.* 60 (1989) 708.

- [186] P. Auric, A. Baudry, M. Bogé, J. Rocco and L. Trabut, *Hyp. Interact.* 58 (1990) 2491.
- [187] T. Toriyama, K. Asano, K. Saneyoshi and K. Hisatake, *Nucl. Instr. Meth. Phys. Res. B* 4 (1984) 170.
- [188] H. M. van Noort, F. J. Ferguson, C. J. G. Verwer, A. A. van Gorkum, J. M. E. van Laarhoven and C.J.M. Denissen, *Nucl. Instr. Meth. Phys. Res. B* 34 (1988) 391.
- [189] H. M. Van Noort and A. A. Van Gorkum, *J. Phys. E. Sci. Instrum.* 21 (1988) 587.
- [190] J. Korecki and U. Gradmann, *Hyp Interact* 28 (1986) 931.
- [191] D. Liljequist and M. Ismail, *Nucl. Instr. Meth. Phys. Res. A* 239 (1985) 273-280.
- [192] D. Liljequist, K. Saneyoshi, K. Debusmann, W. Keune, R. A. Brand, W. Kiauka and M. Ismail, *Phys. Rev. B* 31 (1985) 4137.
- [193] D. Liljequist, *Nucl. Instr. Meth.* 185 (1981) 599.
- [194] A. P. Kuprin, A. A. Novakova, Yu. A. Durasova and S. I. Kharat'yan, *Pribory i Technika Éksperimenta*, No. 2, pp 216-222, March-April 1992.
- [195] A. P. Kuprin and A. A. Novakova, *Nucl. Instr. Meth. B* 62 (1992) 493-504.
- [196] G. N. Belozerskii, C. Bohm, T. Ekdahl and D. Liljequist, *Nucl. Instr. Meth* 192 (1982) 539-543.
- [197] H. Nakagawa, Y. Ujihira and M. Inaba, *Nucl. Instr. Meth.* 196 (1982) 573-574.
- [198] A. A. Kislev, R. N. Kuzmin and A. A. Novakova, *Sov. Tech. Phys. Lett* 12(1) 1986.
- [199] Z. Kajcsos, C. Sauer, A. Holzwarth, R. Kurz, W. Zinn, M. A. C. Ligtenberg and G. van Aller, *Nucl. Instr. Meth. Phys. Res. B* 34 (1988) 383-390.
- [200] J. L. W. Petersen, *Nucl. Instr. Meth.* 221 (1984) 582.
- [201] S. C. Pancholi, H. de Waard, J. L. W. Petersen, A. van der Wijk and J. van Klinken, *Nucl. Instr. Meth.* 221 (1984) 577-581.
- [202] W. J. Price, *Nuclear Radiation Detection*, 2<sup>nd</sup> Ed., McGraw Hill, 1964.
- [203] J. R. Ganecedo, M. Gracia and J. F. Marco, *Hyperfine Interactions* 83 (1994) 71-78.

- [204] D. C. Cook and E. Agyekum, Nuclear Instruments and Methods in Physics Research B12 (1985) 515-520.
- [205] F. J. Berry, Transition Met. Chem. 4 (1979), 209-218.
- [206] M. J. Tricker in : Mössbauer spectroscopy and its Chemical Applications, ed. J. G. Stevens and G. K. Shenoy (American Chemical Society, 1981) p. 63.
- [207] J. A. Sawicki and B. D. Sawicka, Hyperfine Interactions 13 (1983) pp. 199-219.
- [208] K. R. Swanson and J. J. Spijkerman, Journal of Applied Physics, Vol. 41, No. 7, June 1970, p. 3155.
- [209] M. J. Tricker, A. G. Freeman, A. P. Winterbottom and J. M. Thomas, Nuclear Instruments and Methods in Physics Research 135 (1976) pp. 117-124.
- [210] R. Atkinson and T. E. Cranshaw, Nuclear Instruments and Methods 204 (1983) 577-579.
- [211] K. Fukumura, T. Makita, T. Kobayashi and Y. Isozumi, Nuclear Instruments and Methods in Physics Research A301 (1991) 485-488.
- [212] K. Fukumura, R. Katano, T. Kobayashi, A. Nakanishi and Y. Isozumi, Nuclear Instruments and Methods in Physics Research A301 (1991) 482-484.
- [213] S. Kishimoto, Y. Isozumi, R. Katano and H. Takekoshi, Nuclear Instruments and Methods in Physics Research A262 (1987) 413-418.
- [214] K. Fukumura, A. Nakanishi and T. Kobayashi, Nuclear Instruments and Methods in Physics Research B86 (1994) 387-389.
- [215] M. Bamford, Internal Report, Sheffield Hallam University, 1999.
- [216] V. E. Coslett and R. N. Thomas, Brit. J. Appl. Phys. 15 (1964).
- [217] M. J. Tricker, L. A. Ash and T. E. Cranshaw, Nucl. Instr. Meth. 143 (1977) 307.
- [218] J. L. Davidson PhD Thesis: “<sup>57</sup>Fe Mössbauer Studies of Surface Interactions in a PVD Process”, Sheffield Hallam University, (1997).
- [219] M. J. Tricker, L. Ash and W. Jones, Surface Science 79 (1979) L333-L336.
- [220] J. R. Gancedo, J. Z. Dávalos, M. Gracia and J. F. Marco, Hyp. Interact. 110 (1997) 41-50.

## 5. EXPERIMENTAL

### 5.1 $\gamma$ -ray Source for Mössbauer Studies

In order to observe Mössbauer resonance the  $\gamma$ -ray source must fulfil several criteria :

1. The  $\gamma$ -ray energy must be within a certain range, the limits of which are 6.25 keV for  $^{181}\text{Ta}$  up to 155.0 keV for  $^{188}\text{Os}$ . However more useful isotopes have their  $\gamma$ -ray energies in the range of 10 - 50 keV. Low  $\gamma$ -ray energies mean that the  $\gamma$ -ray will be absorbed in solid matter and high  $\gamma$ -ray energy leads to a decrease in the recoil free fraction,  $f$ , and resonant absorption cross-section,  $\sigma_0$ . Since the energy level separations for lighter elements are usually large, giving highly energetic  $\gamma$ -rays, no Mössbauer resonance has been observed for isotopes below  $^{40}\text{K}$ .
2. The half-life of the excited state  $t_{1/2}$  which is the factor influencing the linewidth of the  $\gamma$ -ray should be ideally within the range 1 - 100 ns. For the isotopes presently identified as exhibiting Mössbauer resonance the range is from 0.0101 ns for  $^{187}\text{Re}$  to  $44.3 \times 10^9$  ns for  $^{107}\text{Ag}$  [1,2] though a more recent review [3] of the isotopes available does not include  $^{107}\text{Ag}$ , giving  $^{67}\text{Zn}$  with the largest excited state half life of 9400 ns.
3. The probability of the  $\gamma$ -transition of the source producing a  $\gamma$ -ray photon is affected by the value of the internal conversion coefficient,  $\alpha$ . A high coefficient means greater production of conversion electrons and a lower value means a greater

production of  $\gamma$ -ray photons. Therefore the value is required to be as low as possible ideally less than 10.

4. The absorption cross-section,  $\sigma_0$  should be as large as possible,  $> 0.06 \times 10^{-18} \text{ cm}^2$ , and the recoil energy  $E_R$  should be as small as possible  $< 5 \times 10^{-2} \text{ eV}$ .

5. The half-life of the parent decay process should be as long as possible to give consistency to long series of experiments. Source lifetimes of months or years are preferential.

6. The non-resonant scattering of the  $\gamma$ -rays inside the source should be reduced as much as possible and so the source matrix encapsulating the source isotope should have as high a recoil free fraction as possible and therefore a high Debye temperature [2]. The source isotope is contained within the host matrix in a single, cubic, non-magnetic environment in order to prevent quadrupole and magnetic interactions and to ensure that the source nuclei all have the same isomer shift. Most common matrix materials are high melting point metals and refractory oxides, for example metals such as palladium, platinum and rhodium are used to host the  $^{57}\text{Co}$  source for  $^{57}\text{Fe}$  studies and the oxides  $\text{BaSnO}_3$  and  $\text{CaSnO}_3$  are used to host  $^{119\text{m}}\text{Sn}$  for  $^{119}\text{Sn}$  studies. By reducing the depth to which the source isotope is diffused into the host matrix the non-resonant scattering of the  $\gamma$ -rays can be further reduced.

7. Stability of the ground state isotope along with high natural abundance means that the enrichment of absorbers will not be necessary.

The  $\gamma$ -ray source used needs to produce large numbers of recoil free  $\gamma$ -rays. Thus the  $^{57}\text{Co}$  source isotope is embedded in a thin foil rhodium (Rh) metal matrix. The  $^{57}\text{Co}$  source has a parent half-life of 270 days, which allows for consistency over a fairly long experimental run. Three sources have been used over the three-year period of this project. The initial source activities were 31 mCi (milli-Curie) produced in March 1997, 26.1 mCi produced in February 1999 and 26 mCi produced in November 2000. Over time the source activity is reduced and experiments begin to take longer.

The  $^{57}\text{Co}$  decay scheme is shown in figure 3.3. The  $^{57}\text{Co}$  nucleus decays by 99.8% electron capture to the 136.48 keV level of  $^{57}\text{Fe}$ . Approximately 91% of the decays from the 136.48 keV level then proceed to the 14.41 keV level resulting in a 122.07 keV  $\gamma$ -ray and 9% result in a 136.48 keV  $\gamma$ -ray. The lifetime of the 14.41 keV level is 97.8 ns giving a Heisenberg linewidth of  $0.194 \text{ mm s}^{-1}$  with the decays resulting in the 14.41 keV  $\gamma$ -rays, which satisfies the criteria above. The internal coefficient is high at 8.21 and the ground state isotope natural abundance is low at 2.19% but both parameters still satisfy the relevant criteria. The absorption cross section at  $2.57 \times 10^{-18} \text{ cm}^2$  is high and allows for acceptable resonance at room temperature despite the low ground state natural abundance and high internal coefficient.

## 5.2 Mössbauer Spectroscopy Instrumentation

### 5.2.1 Introduction

A Mössbauer spectrum is considered to be a representation of the rate of interactions occurring within a sample as a function of energy, the occurrence of which can be detected by the absorption of either  $\gamma$ -rays from the beam as in transmission Mössbauer spectroscopy, or by the detection of X-rays by Conversion X-Ray Mössbauer Spectroscopy (CXMS) or, more commonly, conversion electrons by Conversion Electron Mössbauer Spectroscopy (CEMS) in backscatter Mössbauer spectroscopy. It is this last technique that has been extensively used for the experimental work in this study, although some transmission work is included. By changing the energy of the  $\gamma$ -rays from the source according to the Doppler effect given by,

$$\delta E_{\gamma} = \frac{E_{\gamma} v}{c} \quad (5.1)$$

a relative motion between the source and the sample is introduced giving a variation of  $\gamma$ -ray energy. The constant acceleration method has been used in this project. In this method the source is swept through a range of velocities by giving it constant acceleration. Figure 5.1 shows the acceleration and velocity waveforms.

The Mössbauer spectrometers used in this study were used in the constant acceleration mode using WissEl function generator/driver systems. The main system was set up for

backscatter experiments as the backscatter geometry is the preferred method of analysing the near surface of materials. This experimental arrangement is ideal for analysing the intermetallics formed on the surface of DWI tinplated steel samples.

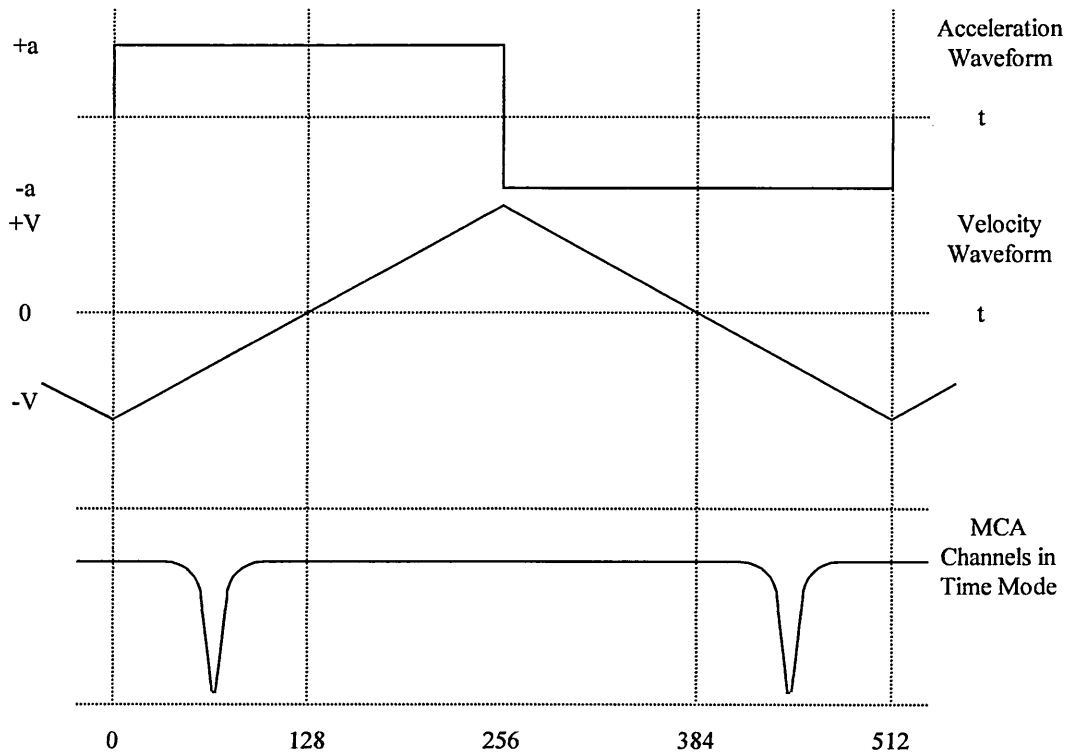


Figure 5.1. Acceleration and velocity waveforms.

### 5.2.2 CEMS Introduction

For the analysis of sample surfaces Conversion Electron Mössbauer Spectroscopy (CEMS) is the method that is employed. CEMS utilises the secondary effects of emission of the 14.41 keV  $\gamma$ -ray from an excited absorber.

When emission occurs some of the  $\gamma$ -rays will interact with the atomic electrons, in a process known as internal conversion, producing a 7.3 keV electron, a 5.6 keV Auger electron and a 6.3 keV X-ray. This is illustrated in figure 5.2, which shows the number of electrons and X-rays emitted per 100 incident  $\gamma$ -ray photons.

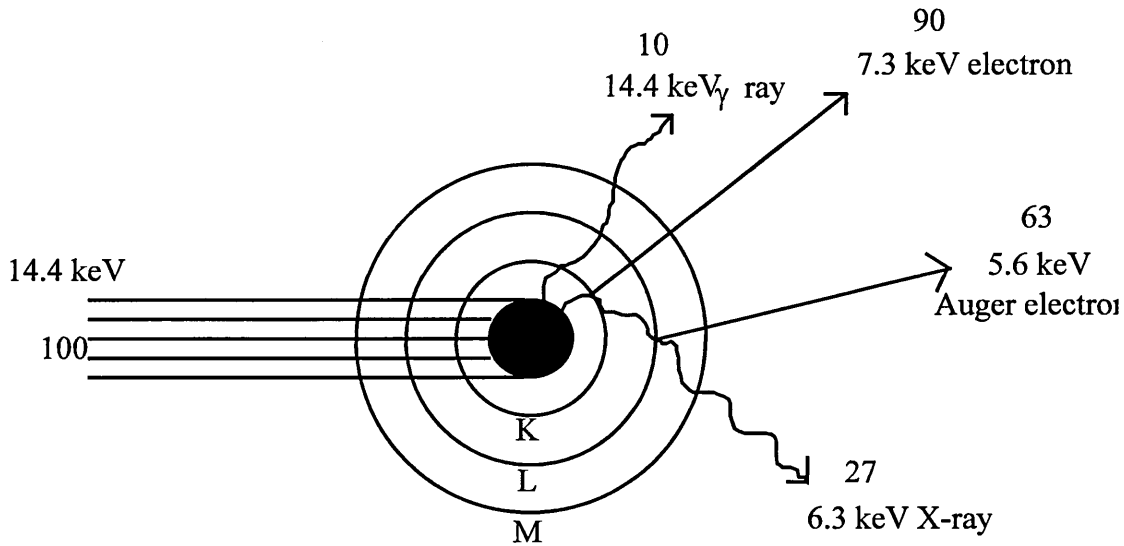


Figure 5.2. Production of conversion electrons and X-rays from an  $^{57}\text{Fe}$  nucleus.

The backscatter Mössbauer spectroscopy experimental arrangement is shown in figure 5.3.

In order to allow the backscattered electrons to be analysed the absorber is placed inside a gas flow proportional counter behind the E.H.T. wire rather than between the source and counter.

The gas flow proportional counter is filled with 95% He and 5% CH<sub>4</sub> when detecting electrons. It is possible to detect X-rays by filling the counter with 95% Ar and 5% CH<sub>4</sub>. When this gas is used the technique is known as Conversion X-ray Mössbauer Spectroscopy (CXMS).

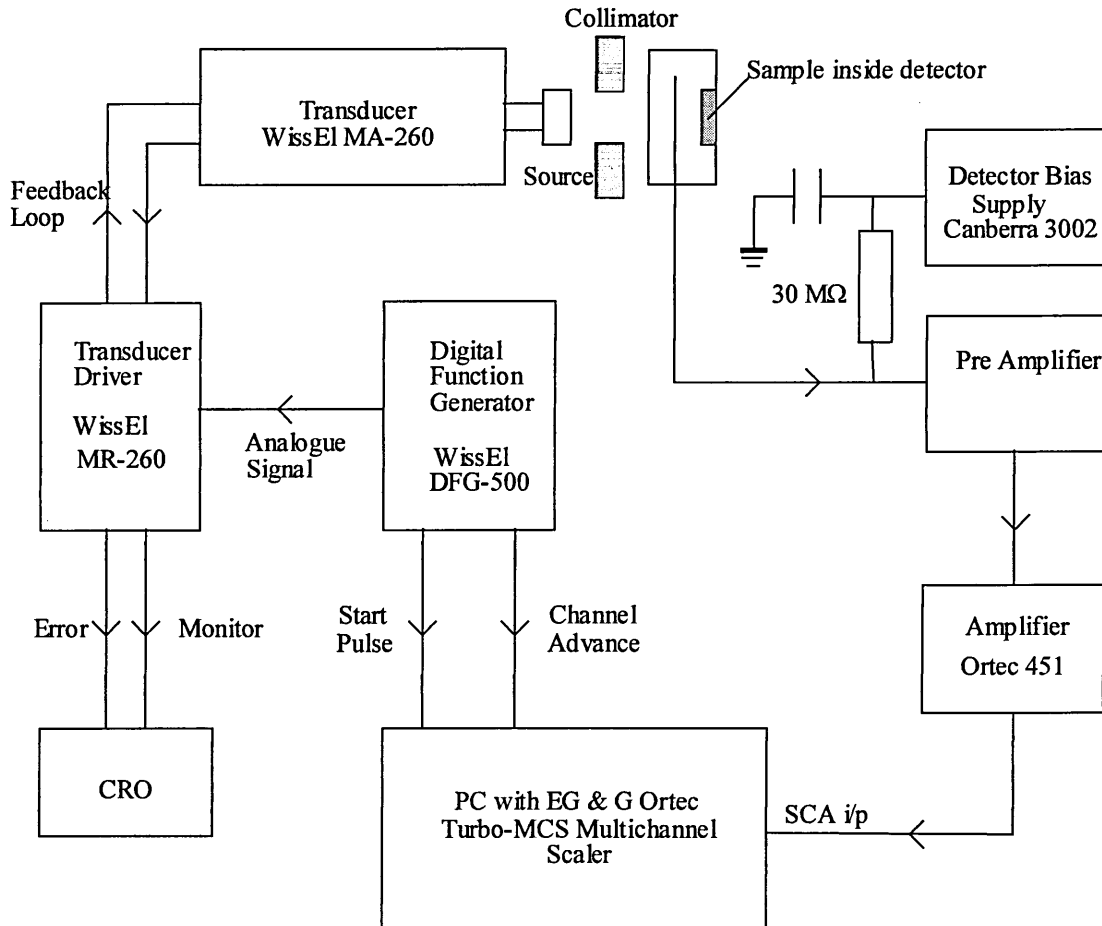


Figure 5.3. Experimental arrangement used for backscatter Mössbauer spectroscopy.

CEMS is more widely used since it has a higher percent effect than CXMS. In fact it is 153% for CEMS as compared with 27% for CXMS. However CXMS has a higher penetrating depth of around 2 - 3  $\mu\text{m}$  compared with 0.3 - 0.4  $\mu\text{m}$  for CEMS and so is more useful in bulk analysis.

### 5.2.3 Operation of the CEMS Mössbauer Spectrometer

The driving system for this spectrometer consists of a Mössbauer velocity transducer MA-260 and a Mössbauer driving unit MR-260. The digital function generator DFG-500 provides an ideal triangular reference signal for the Mössbauer driving system which is derived from the constant acceleration given to the source. All functions are generated digitally which ensures that the motion of the source during the Mössbauer experiment is completely synchronous with the channel sweep of the Multichannel Scaler. A start pulse and channel advance pulse are sent when the waveform is at its maximum.

The analog output, which has a frequency set to 20 Hz, is divided into 512 channels and is amplified by the driver unit MR260 giving precise motion of the Mössbauer source. The Mössbauer velocity transducer, figure 5.4, has two mechanically coupled coils, the first of which is a drive coil, which causes the motion of the transducing elements. The second coil is a pickup, which gives the driving unit information on the value of the velocity. The driving unit compares the pickup signal from the transducer to the reference signal from the digital function generator. The difference between the two signals is the deviation of actual velocity from the ideal value and can be observed by using a CRO. A feedback loop is maintained between the driver unit and transducer by amplifying the difference signal and feeding it to the driving coil in order to minimise the deviation of the source motion with the given waveform.

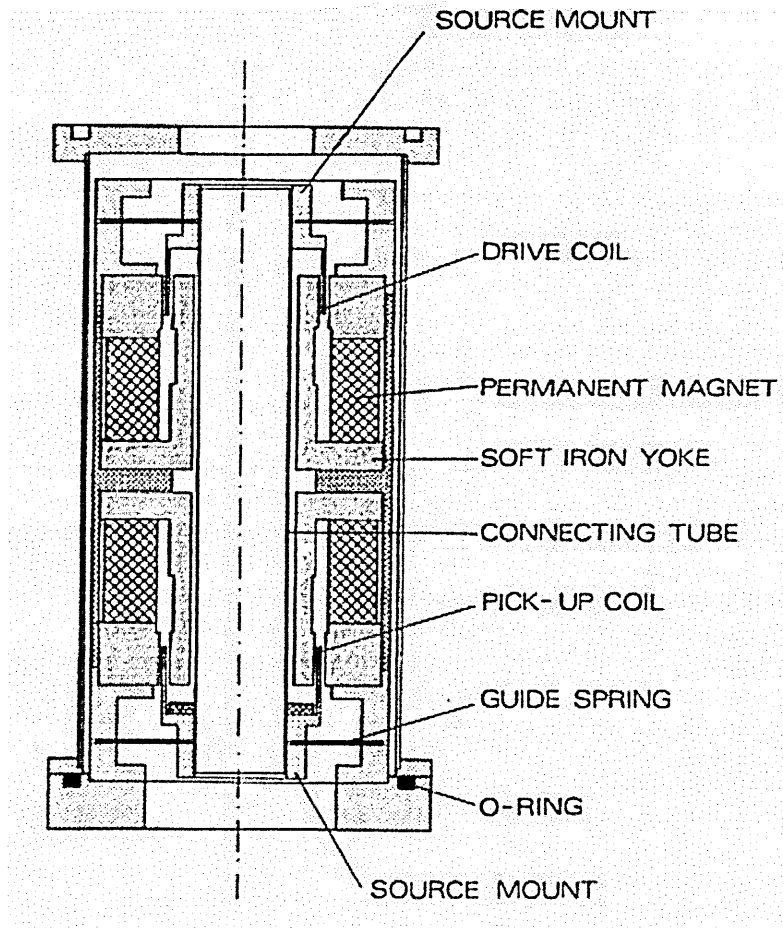


Figure 5.4 Mössbauer velocity transducer MA-260 [4].

The source of the  $\gamma$ -rays is moving in relation to the detector and the solid angle subtended by the source will therefore vary during the motion. The Doppler shift,  $E_\gamma v/c$  is only accurate along the axis of source motion. Those  $\gamma$ -photons, travelling to the detector off axis at an angle  $\theta$ , will have a modified Doppler shift of  $E_\gamma v \cos\theta/c$ . For small solid angles when the source is distant from the detector the distortion that this modified Doppler shift creates in the Mössbauer absorption line is negligible. A large solid angle will create a distortion to the Mössbauer absorption line, which is not negligible, and is known as the cosine effect. To eliminate the distortion an adequate source-detector separation should be maintained. Alternatively the  $\gamma$ -rays can be

collimated to provide a source of  $\gamma$ -photons, which travel along the axis of source motion.

A Canberra Model 3002 3-kV Detector Bias Supply provides the operating bias of 1.2 kV through a filter and a large 30 M $\Omega$  resistance, along a 93  $\Omega$  impedance coaxial signal input cable to the counter as shown in figure 5.3. The use of lower impedance cable increases noise pickup which reduces the performance of the EG&G ORTEC Model 142PC preamplifier which is powered from an EG&G ORTEC Model 451 amplifier.

A quantity of charge is generated within the counter with the formation of ion pairs. The charge is channelled as a narrow current pulse through to the preamplifier. The preamplifier is a charge sensitive unit designed for use with proportional counters that generates an output voltage proportional to the charge by integrating the charge through an operational amplifier with a capacitive feedback. The resultant output voltage is the input for the 451 amplifier which is powered by a NIM-standard bin unit. The 451 amplifier then provides Gaussian pulse shaping and amplification of the voltage to a suitable level for further signal processing.

By adjusting the amplifier gain, the output voltage pulses can be increased to maximum without saturation. The internal Single Channel Analyser (SCA) of the Turbo MCS Multichannel Scaler (MCS) takes the bipolar voltage pulses from the amplifier and generates an output pulse for input voltages between lower and upper level thresholds. The thresholds are selectable via the PC from 0 to 10V and for

CEMS it is only necessary to adjust at the lower voltage level to eliminate counts associated with the amplifier noise as the pulse height spectrum consists of a continual energy loss electron profile. Typical thresholds selected for the SCA are 0.2V for the lower threshold and 10V for the upper threshold, which allows all pulses except the amplifier noise pulses to be recorded by the MCS.

Synchronised by the digital function generator, the MCS records the number of counts over 512 channels. Repetitive scanning allows for the statistical scatter in the recorded spectrum to be reduced. A mirror image spectrum is obtained as the velocity transducer is driven by a symmetrical waveform and on folding the spectrum data any baseline curvature is reduced. A lack of mirror symmetry is an indication of loss of linearity of the system.

Once this equipment is in place the software is initialised and the transducer is switched on. The length of time experiments are set to run is dependant on the amount of  $^{57}\text{Fe}$  in the samples being analysed, the amount of coating on the samples and the source strength. For good results in the case of calibrations with enriched  $^{57}\text{Fe}$  foils the experiment needs to be left for just a few hours. In the case of samples such as the as-produced DWI tinplated steel a few days are required to obtain meaningful results. In order to better compare between samples the same counting time needs to be used on the same size sample areas.

#### 5.2.4 Electron Detection

The photons generated from a  $^{57}\text{Co}$  source decay consist of 14.4 keV  $\gamma$ -rays (8.4 %), 122 keV  $\gamma$ -rays (85 %), 136 keV  $\gamma$ -rays (11 %) and Fe K X-rays (52 %). In backscatter Mössbauer spectroscopy it is the resonantly produced conversion and Auger electrons generated by the 14.4 keV Mössbauer  $\gamma$ -rays that are detected by the electron detector. Therefore the detector must have a high detection efficiency of both the resonantly produced 7.3 keV conversion and 5.6 keV Auger electrons, whilst rejecting the non-resonantly produced electrons associated with all incident radiations. Rejection of the other non-resonantly produced electrons is required as these add to the background signal creating lower signal to noise ratios. These non-resonant electrons are generated by Compton scattering for interactions with low Z elements and the photoelectric effect for interactions with high Z elements.

These experiments use a gas flow proportional counter for CEMS measurements as shown in the cross section diagram in figure 5.5. The gas used for CEMS is a mixture of 95% He and 5%  $\text{CH}_4$  which is used as a quenching agent. The gas flow rate is in the order of 5 ml per minute. If CXMS was to be used to detect the 6.3 keV fluorescent X-rays then the gas would be 95% Ar and 5%  $\text{CH}_4$ .

The detector has a cylindrical chamber measuring 55 mm in diameter. Collimation of the incident  $\gamma$ -rays is provided by a 6 mm diameter hole in a 3 mm thick lead plate ensuring accurate beam alignment of the incident  $\gamma$ -rays. By reducing beam interactions with the counter walls, through collimation of the incident  $\gamma$ -rays, the

production of non-resonant photo and Compton electrons is reduced hence improving the signal to noise ratio.

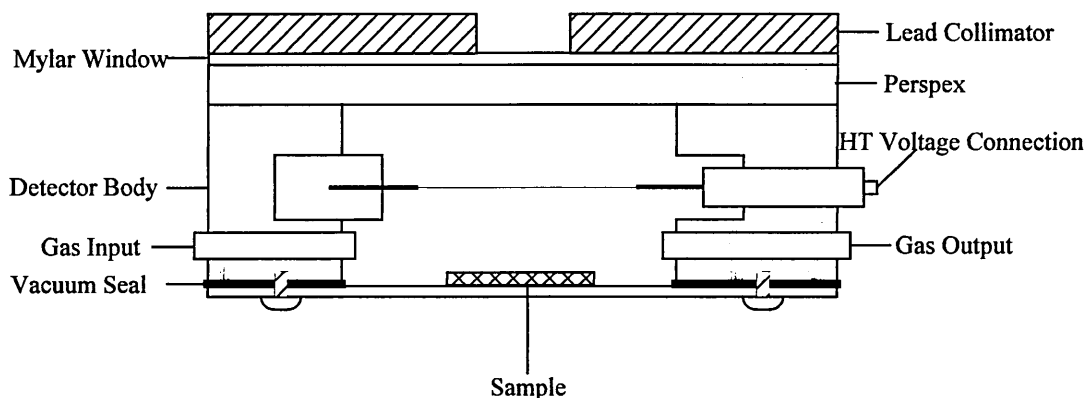


Figure 5.5. Gas flow proportional counter.

Rejection of the other non-resonantly produced electrons is performed by a thin aluminised mylar layer and a 4 mm thick perspex layer being set between the collimator of the detector and the main body of the detector which absorb the Fe K X-rays without significant absorption of the 14.4 keV  $\gamma$ -rays.

The sample constitutes the cathode and the application of a positive HT voltage to a single wire anode enables the detection of the 7.3 keV conversion and 5.6 keV Auger electrons. The stainless steel anode wire, which has a diameter of  $25\mu\text{m}$ , is maintained at 1.2 kV, which ensures the formation of ion pairs in the gas mixture and reduces the recombination of positive and negative ions. If CXMS is to be performed, as well as the changes to gas mixture the HT voltage should be operated at 1.3 kV.

### 5.2.5 Transmission Mössbauer Spectrometry Instrumentation

Although most of the  $^{57}\text{Fe}$  Mössbauer experiments carried out in the course of this study use the CEMS technique there have been some experiments carried out using the transmission geometry. The results from these experiments are generally not included here as their importance is limited due to the fact that signals are difficult to obtain due to the sample thickness. Thus this section provides only an overview of the experimental arrangement. The absorber in transmission experiments is required to contain enough of the resonant isotope to record a spectrum within a reasonable time, however the thickness of the sample is required to be thin enough to obtain a reasonable signal. The DWI can walls are thin enough to be used but can bases are not and require further processing to reduce sample thickness. Such processing inevitably deforms the material structure and thus may lead to misrepresentative results. The transmission experimental arrangement is shown in figure 5.6.  $^{119}\text{Sn}$  transmission experiments have also been run on a low temperature system external to the Sheffield Hallam University Mössbauer laboratory where a  $^{119}\text{Sn}$  source was available. Results from the  $^{119}\text{Sn}$  analysis are included and discussed in the relevant parts of section 7.0.

The digital function generator DFG-1200 provides a triangular reference signal for the Mössbauer driving system MR 260 which is derived from the constant acceleration given to the source. The digitally generated signal ensures that the motion of the source during the Mössbauer experiment is synchronous with the channel sweep of the Multichannel Scaler. A start pulse and channel advance pulse are sent when the waveform is at its maximum.

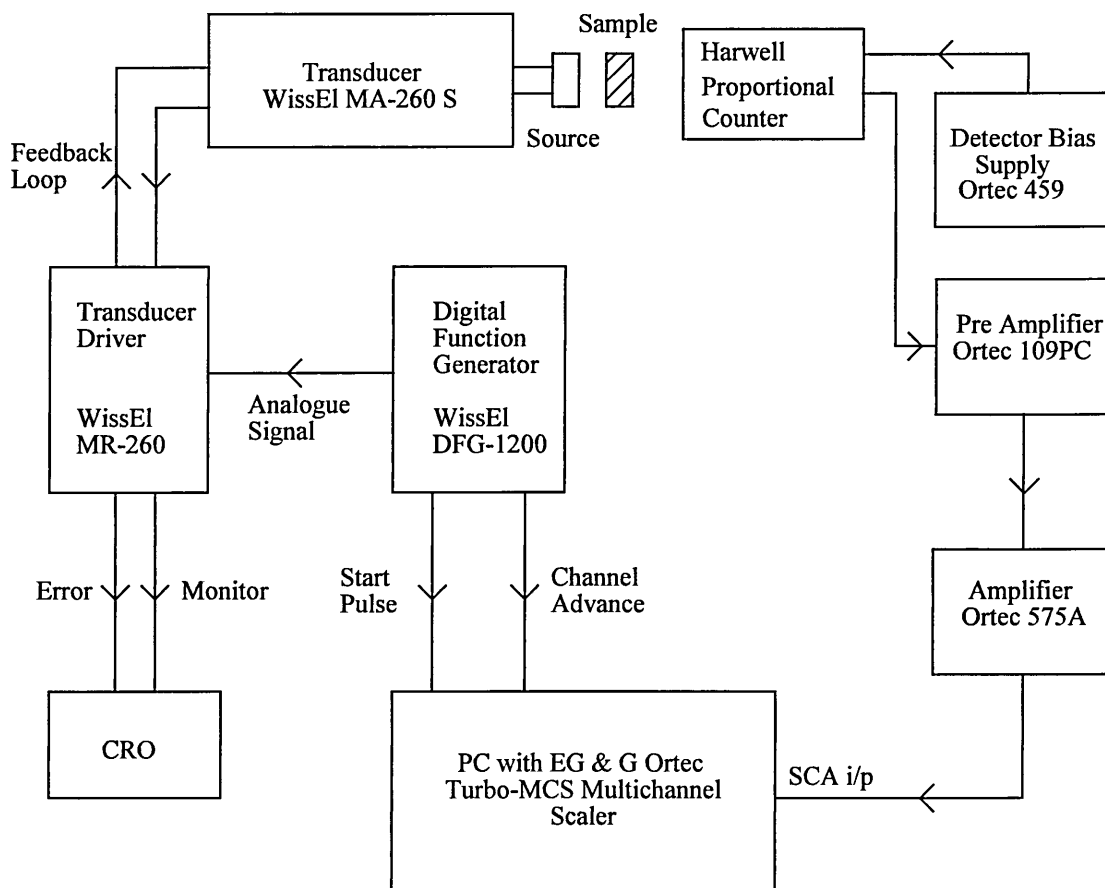


Figure 5.6. Experimental arrangement used for transmission experiments.

The analogue output is divided into 512 channels and is amplified by the driver unit MR260 giving precise motion of the Mössbauer source. A feedback loop is maintained to minimise the deviation of the source motion with the given waveform. Calibrations on the transmission equipment have been carried out using natural Fe foils because no enriched  $^{57}\text{Fe}$  foils were available.

Operating bias for the counter is provided by an Ortec 459 supply unit, and is set at -2.6 kV, fed directly into the Harwell gas filled proportional counter. The amplifier gain is adjusted to give a good pulse height spectrum and the output pulses of the amplifier are fed to the internal single channel analyser of the Turbo multichannel

scaler (MCS). The MCS generates an output pulse for input voltages between lower and upper threshold levels, which are set  $\pm 50$  channels around the 14.41 keV  $\gamma$ -ray peak eliminating any contribution to the Mössbauer signal from the 7.3 X-ray and the amplifier noise.

### 5.2.6 $\gamma$ - Ray Detection

The photons generated from a  $^{57}\text{Co}$  source decay consist of 14.4 keV  $\gamma$ -rays (8.4 %), 122 keV  $\gamma$ -rays (85 %), 136 keV  $\gamma$ -rays (11 %) and 6.5 keV Fe K X-rays (52 %). A Mössbauer transmission  $\gamma$ -ray detector must therefore ensure high detection efficiency of the resonantly produced 14.4 keV  $\gamma$ -rays generated by the sample, rejecting non-resonant radiations, which contribute only to the background signal.

A gas filled proportional counter is used, as the detection of low energy  $\gamma$ -rays, where  $E_{\gamma} < 40$  keV, is efficient using such a counter and is ideal as long as high energy resolution is not required. The gas filled proportional counter contains a mixture of 95% Ar, and 5%  $\text{CH}_4$ . Aluminised mylar windows absorb Fe K X-rays from the incident beam without significantly absorbing the higher energy 14.41 keV Mössbauer  $\gamma$ -rays.

The 50 $\mu\text{m}$  diameter anode wire was operated at -2.6 kV, with the inner aluminium case kept at 0V. When the incident  $\gamma$ -rays pass into the counter they cause the gas mixture to ionise, and thus the charge flows to the inner aluminium case giving voltage pulses which are recorded.

### 5.2.7 Spectrometer Calibration

To determine the velocity range associated with a specific helipot setting on the transducer drive unit, the spectrometer is periodically calibrated. Calibrations were completed with an enriched  $^{57}\text{Fe}$  foil as the calibration standard for CEMS and a Fe foil for transmission experiments. The data output was taken from the PC running the experiment and transferred to a secondary PC where the data was fitted using Lorentzian lines on dedicated software. The resultant fitted data set of the calibration experiment yields values of the line positions that are used to determine the velocity range of experimental data. A typical CEMS spectrum calibration is shown in figure 5.7. The line positions associated with the enriched  $^{57}\text{Fe}$  foil are at the following Doppler velocities that are used to calibrate the subsequent data.

lines 1,6 =  $\mp 5.312 \text{ mm s}^{-1}$  : lines 2,5 =  $\mp 3.076 \text{ mm s}^{-1}$  : lines 3,4 =  $\mp 0.840 \text{ mm s}^{-1}$

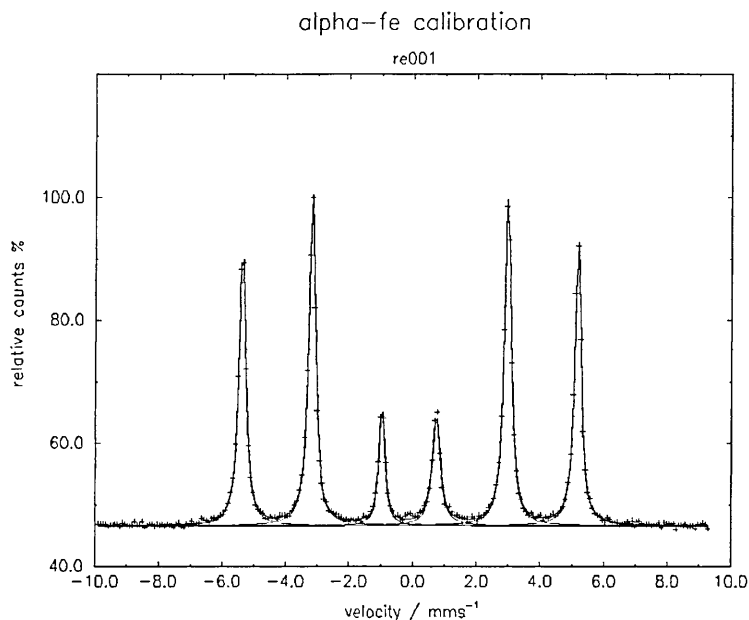


Figure 5.7. Typical CEMS calibration from an  $^{57}\text{Fe}$  enriched iron foil.

## **5.3 Sample Preparation**

### **5.3.1 Introduction**

Studies have been carried out on a tinplated steel drinks can supplied by Corus plc along with the base mild steel and the pre-pressed tinplated steel (both flowbrightened and unflowbrightened) and a number of laboratory-produced samples.

Initial CEMS experiments on samples of matte tinplated steel provided by Corus plc used to press the DWI cans show no intermetallics, even when etched of tin. Samples of flowbrightened tinplated steel provided by Corus plc show the intermetallics without any etching of tin, however etching of these samples provides a much less noisy signal that makes the intermetallic identification easier. The results from the analysis of these commercial tinplates are shown in section 7.9.

The commercially produced cans had to be cleaned ultrasonically and rinsed with acetone to remove any traces of contamination from the can surfaces. There was however some evidence of corrosion on a number of the cans which could not be removed. Corrosion products can be uniquely identified in Mössbauer spectra, however samples for analysis were chosen from cans, and specifically areas, without visible corrosion. CEMS has been used in previous studies of corrosion products [5,6,7,8,9] and is often regarded as the technique of choice when analysing thin corrosion layers, at the early stages of the corrosion reaction. Surface enrichment

techniques used in previous studies using Conversion X-ray Mössbauer Spectroscopy CXMS [5] can be used to try to simplify the identification of these corrosion products.

Specimens were then cut from positions of interest on the wall of the can as shown in figure 5.8. Odd numbered areas are from the top edge of the can walls and even numbered areas are from the bottom of the can walls. This was to allow easier identification of the top and bottom areas during analysis.

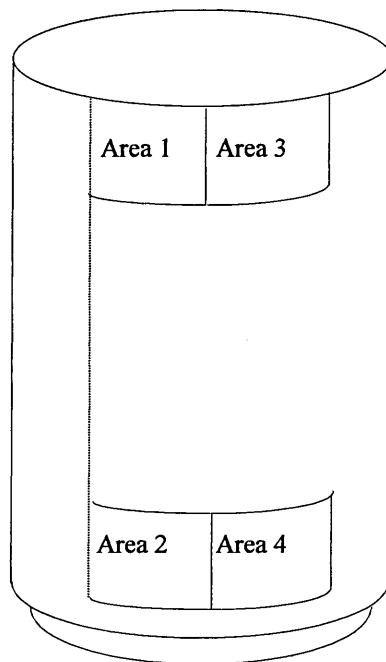


Figure 5.8. Diagram of tinplated steel can and sample areas.

Both the inside and outside of the can walls have been studied using Conversion Electron Mössbauer Spectroscopy (CEMS). SEM analysis (including X-ray Microanalysis) has also been completed for the inside and outside of the can walls and the results are detailed in section 7.2.

A number of different methods have been used to try to enhance the Mössbauer signal from the intermetallics in these commercially produced samples. Firstly etching of the tin coating was carried out, initially at the Corus plc Swinden Technology Centre, and later at Sheffield Hallam University. Results from the etched sample analysis are shown in section 7.3. Heat treating of the samples has also been used to promote intermetallic growth with results being shown in section 7.6. Use of both techniques, both separately and in conjunction with each other, has led to the identification of intermetallics in the DWI tinplated steel can wall material. Analysis of the can bases has also been carried out, with no intermetallics being identified even after etching. Results for the can base analysis is shown in section 7.4.

A number of laboratory-produced samples have been produced and analysed, including samples of polished mild steel electrodeposited with tin and heat treated with different heating temperatures and times. These various heat treatments produce various levels of intermetallics and have been used to analyse intermetallic formation and to determine how low a level of intermetallic formation could be detected by the CEMS detector. This analysis is discussed in section 7.11.

Samples of carbon coated tinplated steels have been analysed to identify the effects of such a coating. Previous studies using coating materials of higher atomic number have been found to provide a way to discriminate between substrate and resonant surface layers by increasing the substrate to surface signal ratio. However the carbon coating has been found to give the inverse effect of these other coating materials. This analysis is discussed in section 7.12.

The following sections 5.3.2 through 5.3.5 provide the experimental details of the techniques and procedures used to process the samples as detailed above.

### 5.3.2 Electrodeposition of Tin onto Steel Substrates

#### 5.3.2.1 Sample Preparation

The steel substrates were sectioned from a larger sheet of mild steel strip. The samples, which are approximately 3 cm × 2 cm, were individually mounted using double sided sticky pads onto a polished stainless steel mount. They were then ground smooth on a series of rotating grinding discs with gradually reducing roughness grades and subsequently polished to a mirror finish using two grades of diamond paste on rotating polishing pads. The final polishing stage was finished with 1µm diamond paste to provide the smoothest possible finish.

The samples have been inspected in an optical microscope and the SEM for surface roughness. Apart from a few light scratches and some light pitting in some areas the samples are free of marking and are ideally prepared for the electroplating process. Analysis of the effects of various roughness substrates on the formation and identification of intermetallics in tinned samples is discussed in section 7.13.

Prior to plating there is a thorough cleansing procedure that has to be followed. Firstly the samples are immersed in acetone for 2 minutes and this is followed by an anodic decrease in alkaline cleaner (40g/l NaOH + 2g/l O<sub>3</sub>Na<sub>2</sub>Si<sub>5</sub>H<sub>2</sub>O) then the samples are

dipped into a 50% solution of HCl. Between each stage the samples are rinsed in de-ionised water. Samples are then ready for plating.

### 5.3.2.2 Bath Preparation

The bath used for this particular electrodeposition is known as a stannate tin bath. The bath itself is suitable for elevated temperature and is made of plastic. Figure 5.9 shows a cross section of the bath arrangement.

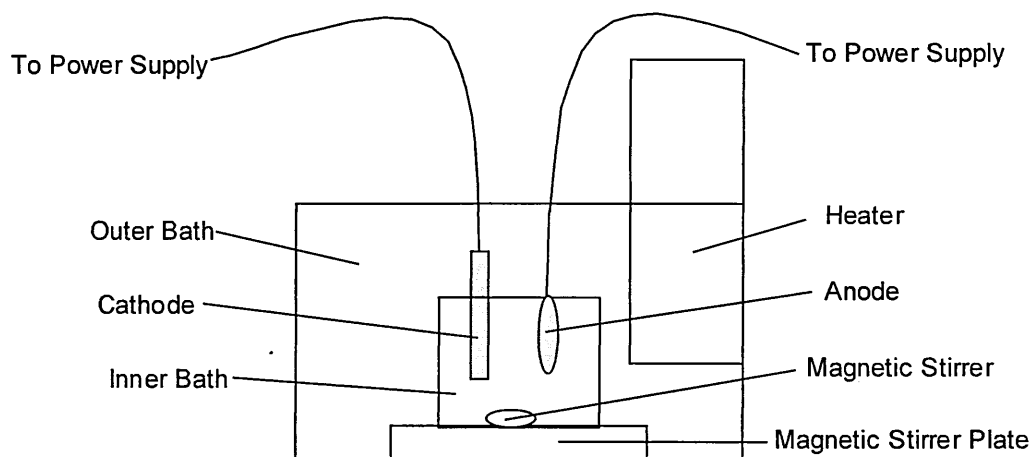


Figure 5.9. Cross section of bath arrangement.

The following are the details of the bath constituents and equipment details.

#### Bath Constituents

Sodium stannate	90 g l <sup>-1</sup>
Free sodium hydroxide	8 g l <sup>-1</sup>

### Bath Details

Temperature	60 °C
Current density	0.03 A cm <sup>-2</sup> (agitated)
Cathode efficiency	70 to 85%

An elliptical tin anode was used and the solution was agitated with a magnetic stirrer. The anode/cathode area ratios were approximately 1:1 with slightly less anode area as recommended by Parthasaradhy who found this to be beneficial in the process [10]. The outer bath was filled with water for the conduction of heat to the inner bath.

The solution was made up in the inner bath and, prior to tinplating the samples, scrap steel was introduced along with the anodes. This pre-plating procedure cleans the bath of any impurities. A current density twice that of the operating current density was applied and once a film was formed on the scrap steel the samples were introduced into the bath. A greenish/yellow film was maintained on the anode as this occurs when the tin is dissolving satisfactorily as stannate. The thickness of tin deposited in this bath depends on time within the bath and will range from 0 to 25 µm [10]. Initially the thickness deposited was approximately 10 µm. However this has led to problems later on with etching such a thick layer of tin. Subsequent electrodeposition experiments were set to deposit a thinner layer of tin so that problems with etching later on were minimised. The deposited layer on these samples was approximately 2 µm. The calculation of tin coating thickness is based on calculations made prior to the deposition which give a time of deposition to give the desired thickness. Accurate

mass measurements made before and after the deposition to check coating masses and are given in section 7.13.

The mass of tin deposited at the cathode is determined using Faraday's laws of electrolysis [10,11]. Since the alkaline stannate bath is used the valence of tin is four rather than two which is observed for acid baths. The mass of tin deposited on the substrate,  $W$ , in grams is given by,

$$W = \frac{It}{F} \times \frac{A}{z} \text{ grams} \quad (5.2)$$

where  $I$  is the current passed in amperes,  $t$  is the time of deposition,  $A$  is the atomic weight of the deposited metal,  $F$  is the Faraday constant which is equivalent to 96500 C (coulomb) and  $z$  is the valence of the ion from which the discharge is taking place. The Faraday is the quantity of electricity required to deposit  $A/z$  grams of the metal, in this case  $A$  is 118.7 and  $z$  is 4 and thus 96500 C deposits 29.675 g of tin. For this electrodeposition procedure the time of deposition to give the desired thickness of 2  $\mu\text{m}$  can be calculated using equation 5.2.

The area coated is approximately 8  $\text{cm}^2$  with a thickness of 2  $\mu\text{m}$  and therefore the volume of tin required is  $1.6 \times 10^{-3} \text{ cm}^3$ . With a tin density of  $7.31 \text{ g/cm}^3$  the mass of tin to deposit,  $W$ , is,

$$W = 1.6 \times 10^{-3} \text{ cm}^3 \times 7.31 \text{ g/cm}^3 \quad (5.3)$$

This gives the desired mass of tin as  $W = 0.0117$  g. Now by using equation 5.2 and substituting  $W$  along with values for the other parameters we can determine a suitable time for deposition  $t$ . The values for the other parameters are  $I = 0.24$  A,  $A/z = 29.675$  g and  $F = 96500$  C and thus,

$$0.0117 \text{ g} = \frac{0.24 \text{ A} \times t}{96500 \text{ As}} \times 29.675 \text{ g} \quad (5.4)$$

giving,

$$t = \frac{0.0117 \text{ g} \times 96500 \text{ As}}{29.675 \text{ g} \times 0.24 \text{ A}} = 158.5 \text{ s} \quad (5.5)$$

So the deposition for  $2 \mu\text{m}$  would be carried out for approximately 2 minutes and 40 seconds with 100% efficiency. This particular deposition however is defined as being between 70 and 85% efficient. Adjusting the time for the cathode inefficiency results in a range of deposition times between and 186 and 226 seconds. The electrodeposition procedure carried out during this study uses a deposition time of 220 seconds or 3 minutes 40 seconds erring on the side of caution to give enough tin coating for subsequent processing. It should be noted that these calculations are an indication only and physical measurements of the coating masses were carried out and are discussed in sections 7.11 and 7.13.

### 5.3.3 Heat Treatment of Tinplate

The heat treatment of the tinplate samples causes the growth of more intermetallics within the samples. Intermetallics are formed in these samples when diffusion between the tin and steel occurs. The melting point of tin is 232°C. The samples were heated in the arrangement shown in figure 5.10.

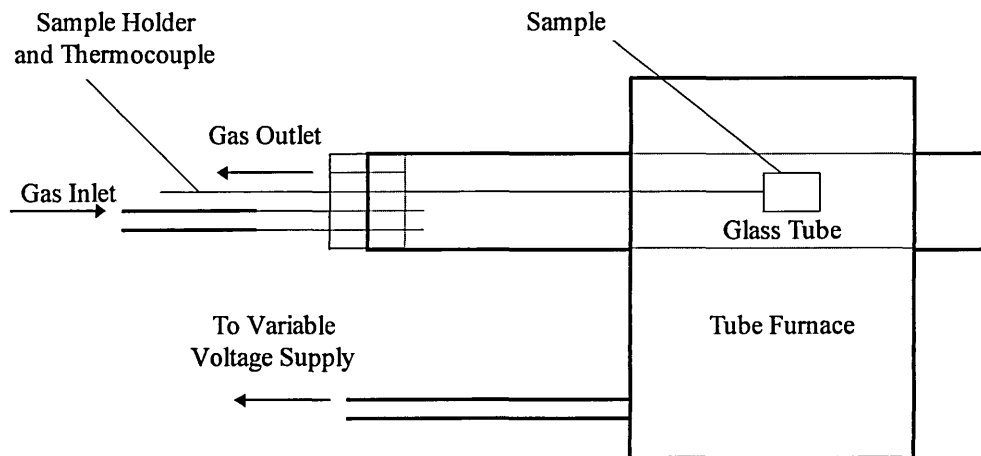


Figure 5.10. Diagram of equipment for annealing tinplate samples.

A flow of nitrogen over the samples during the heating was used to prevent oxidation of the samples. The technique used in the heat treatments is simple. With the glass tube and thermocouple held in place the sample can be moved along the tube by means of a length of copper wire through the gas outlet, which is inserted into a small hole in the sample.

This small hole allows the sample to be held in the furnace without it dislodging from the sample holder. Nitrogen gas was permanently flowed through the system and the gas flow was tested by using leak detector spray on the exit hole of the rubber bung.

The samples were mounted on the wire and inserted into the tube. The samples were then held in the cool zone for 3 minutes until the nitrogen gas filled the tube. The sample was then fed along the tube into the hot zone. Care was taken to place the samples in the same position each time and this was done by means of markings on the tube wall. The samples were left at temperature for the required amounts of time and then removed from the hot zone into the cold zone for a further 3 minutes to allow cooling in a nitrogen atmosphere.

Two series of samples were prepared to analyse the formation of intermetallics. They were heat treated and then etched. The first set of samples were all heat treated at 240°C but for varying times of 1, 2, 5 and 10 minutes. This would serve as an indication of how the diffusion of the tin and steel was progressing through time.

The second set of samples used a constant heating time of 2 minutes but a varying temperature of 240°C down to 190°C. This would show at what temperatures the diffusion process occurs and would help in the identification of the lower detection limit of CEMS as once the limit is identified, using CEMS, ICP-MS can be used to find the concentration of tin atoms on the samples.

### 5.3.4 Etching of Tinplate

Various tinplate etching techniques have been developed and are described in other studies [10,12]. The etching of tinplate during these studies is carried out using the following process similar to that used at the Corus plc Swinden Technology Centre. An etchant solution is produced using 50 g l<sup>-1</sup> sodium hydroxide and 10 g l<sup>-1</sup> potassium iodate. A quantity of the solution is put into a glass beaker, enough to be able to completely immerse the tinplate sample, and the solution is then heated in a fume cupboard to 50 °C. The sample is then immersed in the solution for 2 minutes, during which the surface is visibly darkened as the brighter tin coating is removed. Then the sample is removed and rinsed with de-ionised water and then acetone to remove any traces of etching solution. The sample is then dried in a stream of nitrogen to avoid corrosion product formation. This process has been found to remove the tin without removing the Fe-Sn intermetallics.

### 5.3.5. Carbon Coating

#### 5.3.5.1 Carbon Coating Experimentation

To investigate the sensitivity of the CEMS technique and its suitability for the analysis of commercially produced DWI cans, a carbon coating has been applied in order to help reduce the signal from an uncoated steel substrate. Reduction of substrate signal would theoretically lead to a method of obtaining an improved differentiation of the signal from the very near surface of samples to that from the substrate. This would

occur as the energy of electrons emerging from deeper within the samples is generally less than those arising from the upper area of the samples. Therefore the electrons from lower in the samples would be more easily stopped by an inert coating layer.

However the production of photoelectrons from the coating layer, as a number of previous studies have shown e.g. for coatings such as aluminium [13] and gold [14], initially increases the signal from the substrate. This effect with respect to carbon coatings has been investigated as part of this study and is discussed in section 7.12. The non-resonant electrons have a masking effect that increases with the abundance of heavy elements as the probability of photoelectric interactions increases linearly with  $Z^5$  [15].

The effect of carbon coating was first analysed by coating polished mild steel substrates with various thicknesses of carbon. This was to determine the extent of the effect of photoemissions from the carbon coating. Additional secondary samples with masked off areas were placed next to the primary samples in order to allow determination of carbon thickness by profilometer measurements. The step on the masked off area of the secondary sample would give a typical thickness value for the primary sample.  $^{57}\text{Fe}$  conversion electron Mössbauer spectra were recorded at room temperature for these samples.

Samples of DWI tinplated steel were also analysed to see the effect on analysis of commercial material. The samples were taken from the production line after the drawing and ironing process and before the application of a lacquer coating. These

samples were heat treated in the tube furnace arrangement at 240 °C for 30 seconds under a nitrogen atmosphere in order to promote the growth of small quantities of Fe-Sn intermetallics. These samples were etched in a solution of sodium hydroxide and potassium iodate at 50 °C for 2 minutes to remove metallic tin without affecting any Fe-Sn intermetallics. This etching has the effect of increasing the general signal to noise without altering the relative signals from the Fe substrate or the Fe-Sn intermetallics.

The carbon coating was carried out in an Edwards E306A Coater, figure 5.11, under a vacuum of  $10^{-5}$  mbar. An estimated 20 nm thickness coating of carbon was evaporated onto the DWI sample surfaces and the carbon coat thickness was measured using a profilometer on secondary polished substrate samples coated in the same procedure as the analysed DWI samples.

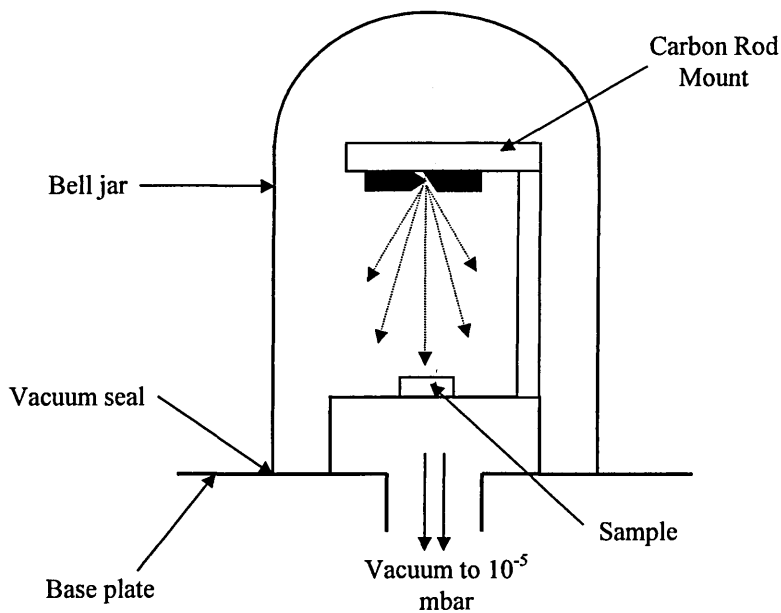


Figure 5.11. Diagram of coater system for carbon coating.

$^{57}\text{Fe}$  conversion electron Mössbauer spectra were recorded at room temperature for these carbon coated samples and the results were compared to the spectra recorded for the samples prior to coating. The spectra fitting was done using Lorentzian site analysis on the Recoil computer software [16].

#### **5.4 Mössbauer Software**

Natural iron samples and the Mössbauer software program, Recoil, are used to calibrate the Mössbauer spectrometer and fit experimental data. It takes a calibration data set and fits Lorentzian lines to the data. These calibration line positions are then used in the processing of experimental data. The data from the experimentation equipment is stored as 512 channels (0 to 511). The data in channels 0 to 255 needs to be folded onto the channels 256 to 511 and the resultant counts need to be averaged. The loss of high accuracy linearity at the extremes of source displacement has to be considered in the final fitting, but the software used does not compensate for the inaccuracies.

The creation of a Mössbauer calibration spectrum is generally automated with user intervention required for identification of peak positions. The peaks are then fitted either automatically or manually. With good strong Lorentzian lineshapes automatic fitting is sufficient, however lower quality data, calibration of low velocity ranges, or deviation from Lorentzian lineshapes can prove to give problematic automatic fitting.

The raw data needs to be folded using the software. For this the raw data file is selected with an appropriate calibration. The software can then identify the correct folding position and produce a folded data set.

The program is then used to fit Lorentzian lines to the data using Lorentzian multiplet analysis [16]. The value of chi squared on the program output gives an indication of the goodness of fit to the data.

## Experimental References

- [1] A. Vértes, L. Korecz, K. Burger, "Mössbauer Spectroscopy", (Elsevier, London, 1979).
- [2] N.N. Greenwood, T.C. Gibb, "Mössbauer Spectroscopy", (Chapman and Hall, London, 1971).
- [3] S. Nasu, High Temperature Materials and Processes, Vol. 17, Nos. 1-2, 1998.
- [4] Mössbauer Driving System 260 Instruction Manual, Wissenschafte Elektronik gmbh.
- [5] J.S. Brooks and S. Thorpe, Hyperfine Interactions 47 (1989) 159-178.
- [6] J.R. Gancedo, M. Gracia, J.F. Marco and J.A. Tabares, Hyperfine Interactions 111 (1998) 83-92.
- [7] D.C. Cook, Hyperfine Interactions 111 (1998) 71-82.
- [8] J.F. Marco, J. Dávalos, M. Gracia, and J.R. Gancedo, Hyperfine Interactions 83 (1994) 111-123.
- [9] J.R. Gancedo, J.F. Marco, M. Gracia, G. Joseph and R.A. Núñez, Hyperfine Interactions 83 (1994) 363-366.
- [10] N.V. Parthasaradhy, Practical Electroplating Handbook, 1989, Prentice Hall.
- [11] D.R. Gabe, Principles of Metal Surface Treatment and Protection, 2<sup>nd</sup> Ed., 1978, Pergamon Press.
- [12] F.A. Lownheim, Modern Electroplating, 3<sup>rd</sup> Edition, 1974, John Wiley and Sons.
- [13] J. L. Davidson PhD Thesis: "<sup>57</sup>Fe Mössbauer Studies of Surface Interactions in a PVD Process", Sheffield Hallam University, (1997).
- [14] M. J. Tricker, L. A. Ash and T. E. Cranshaw, Nucl. Instr. Meth. 143 (1977) 307.
- [15] J. R. Gancedo, J. Z. Dávalos, M. Gracia and J. F. Marco, Hyp. Interact. 110 (1997) 41-50.
- [16] K. Lagarec and D. G. Rancourt, Recoil : Mössbauer Spectral Analysis Software for Windows version 1.0, 1998.

## **6. COMPLEMENTARY ANALYTICAL TECHNIQUES**

### **6.1 Introduction**

A number of different analytical techniques have been used in this study to complement the Mössbauer spectroscopy work. These techniques include SEM, XRD, and GDOES. In most cases no significant sample preparation was required apart from the cleaning of the samples in order to remove surface contaminants. This procedure usually involved cleaning the surface with acetone and distilled water. Such preparation does not damage or contaminate the sample. In some cases however the samples have been prepared in such a way as to alter the structure of the samples. This was done in particular in some of the SEM and XRD work where samples had been etched to remove the tin from the sample surfaces.

### **6.2 Scanning Electron Microscopy (SEM)**

The scanning electron microscope is used to image the surface of a sample and build up a topographical or elemental map of that surface. The SEM uses an electron beam to scan the surface of the specimen in a raster pattern. When the beam impinges on the specimen, some electrons are backscattered, others knock out low energy secondary electrons from the outer shells of atoms, while others produce X-rays. One or more of these can be detected as the signal. Each position of the beam corresponds to a point on the screen of a cathode-ray tube. The scan of the specimen is synchronised with the scan on the screen and the signal is used to control the brightness of the display. The

magnification is determined by the ratio of the picture point size to the beam point size. Since the beam size can be varied from 10 nm to 1  $\mu\text{m}$ , an SEM can produce an enormous range of magnifications from 15 to  $10^5$  times. The highest resolving power is about 10 nm. The SEM has a large depth of field, which means that the range of object distances for which the image is in focus is large compared to other techniques such as optical microscopy. As a result the SEM produces an almost three-dimensional effect.

The Philips XL40 scanning electron microscope was used to determine microscopic integrity of the samples. This SEM incorporates a conventional tungsten filament thermionic gun at a potential of 20 kV and provides videoprint images of the sample surfaces. The images that were produced enabled determination of the quality of the samples as well as providing additional information on sample composition. Specimens are required to be conducting to avoid charging effects. Non-conducting materials must be coated with metal prior to analysis. Since these samples are conducting they were prepared by simply bonding the substrates to stainless steel stubs.

Two different types of SEM images can be produced. The first are secondary electron (SE) images. Secondary electron emissions form topographical contrast images. These images are formed from electrons leaving the surface with velocities corresponding to energies less than 50 eV, a small fraction of the incident energy. These electrons have a range limited to a few nanometres and are reflected at large angles from the incident

beam path. Due to the small interaction volume determined by the limited range secondary imaging is a relatively high resolution mode.

The second type of image that is produced is from back-scattered electron (BSE) scans. These images are formed from electrons leaving the sample surface at high angles with respect to the incident electron beam and are considered to be reflected, rather than re-emitted. The velocity of such electrons corresponds to a significant proportion of the incident energy. Due to these larger energy values the interaction volume is correspondingly larger at about a third of the range, which is in itself between 10  $\mu\text{m}$  and 100  $\mu\text{m}$ , depending on the sample composition. Compositional information arises from the fact that electron yields vary as a function of the atomic number of the scattering element, which for lower atomic number materials ( $Z < 30$ ) is approximately in direct proportion to  $Z$ . Due to the larger range, materials (particularly of higher atomic numbers) can be detected below the sample surface.

Using the Philips XL40 X-ray analysis can also be carried out. Thus the constituent elements of a SE or BSE plot can be identified. In the analysis of the DWI samples the steel can material is identified, but only as iron, with no identification of the other steel material components. This is most likely down to the relatively small quantities of any other elements other than iron and tin in the samples analysed.

## **6.3 X-Ray Diffraction**

### **6.3.1 X-ray Diffraction Techniques**

X rays, like light, may be diffracted. The field of X-ray crystallography deals with the coherent scattering of X-radiation by atomic aggregates constituting matter. When such arrays are highly regular, as is the case in crystals, it is possible to interpret the intensities of the scattered (diffracted) rays directly in terms of the atomic arrays constituting the crystal structure.

The X-ray source provides polychromatic radiation from a copper target tube. The monochromator positioned in front of the detector is tuned to select only the  $\text{CuK}\alpha$  emission line from the source. The system can then be viewed as operating with a monochromatic source.

Two different geometries are used in this study, Bragg-Brentano and glancing angle. In Bragg-Brentano the sample is maintained at an angle  $\theta$  and the counter at an angle  $2\theta$  respectively to the incident X-ray beam, as shown in figure 6.1.

The sample is rotated about the axis normal to its centre. Initially the source, the surface of the sample and the detector are in a line across the diameter of the diffractometer circle. As a scan proceeds, the detector is rotated through an angle of  $2\theta$  degrees per minute while the sample is rotated about its plane through an angle of

$\theta$  degrees per minute. This geometry is maintained throughout and thus only planes parallel to the surface diffract.

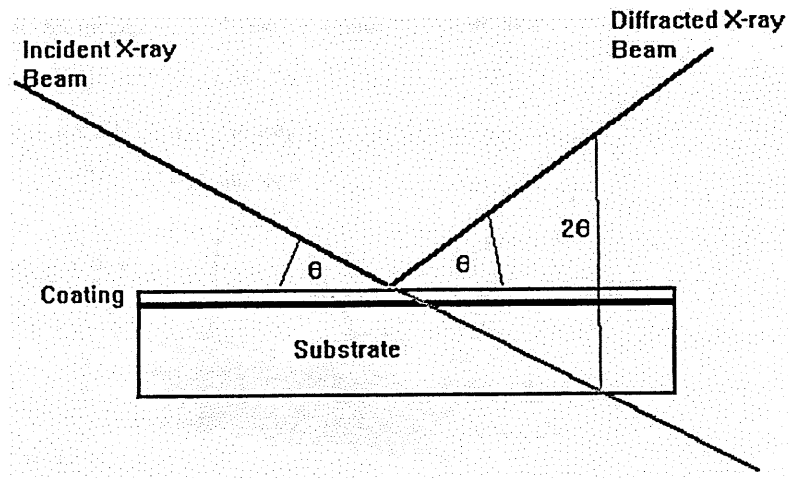


Figure 6.1. Schematic representation of the Bragg-Brentano technique

With glancing angle geometry the angle of incidence of the X-ray beam remains fixed at a low angle ( $0.5^\circ$  to  $5^\circ$ ) as shown in figure 6.2. The sample is therefore held static and the detector is driven. The diffracting planes are at an angle  $\theta - \alpha$  to the sample surface.

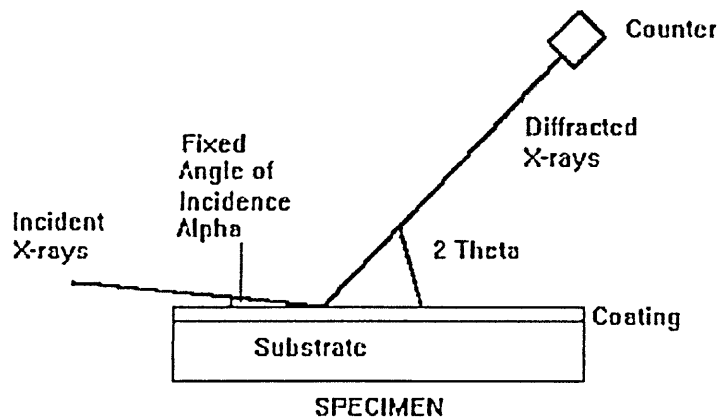


Figure 6.2. Schematic representation of the glancing angle technique.

In these X-ray diffraction techniques, the X-rays detected from the sample surface have been reflected, according to Bragg's law, by families of planes. Whenever a reflection is obtained this condition applies. This reflection provides a semi-focusing action for the reflected and detected X-rays. As the scan proceeds, X-rays are detected only when the angular relationship between the source, sample and detector matches the condition for a Bragg reflection. Therefore, the various Bragg reflections provided by the specimen are detected at the correct angles ( $2\theta$  values) throughout the scan.

### 6.3.2 X-Ray Diffraction Experimental Detail

Analysis of the samples was undertaken at room temperature using a Philips X-ray powder diffractometer. The system consisted of a type PW 3710 controller, type PW 1830 X-ray generator fitted with a long, fine-focus copper tube with an irradiated area of  $12\text{mm} \times 0.4\text{mm}$  which varies through diffraction angle and type PW 1820 goniometer with graphite monochromator. The whole arrangement is housed in a shielded casing to prevent exposure to X-radiation. The analysis and data collection processes were controlled by Philips automated powder diffraction software (APD) version 3.6.

One set of Bragg-Brentano results were obtained along with two sets of glancing angle data, one with incident angle  $\alpha = 1^\circ$  and a second with incident angle  $\alpha = 5^\circ$ . The samples to be analysed had surfaces with average roughness values,  $R_a$ , ranging from 0.008 to 0.500  $\mu\text{m}$ . The samples could be directly mounted on the diffractometer specimen holder without further sample preparation. Diffraction data traces were then

obtained by increasing the generator voltage to 40 kV and slowly bringing the generator current up to 55 mA allowing  $\text{CuK}\alpha$  radiation to be incident on the sample.

The computer connected to the system was then used to set up the type of measurement, range of measurement, time of measurement and other parameters. The detector was set to scan continuously through the  $2\theta$  range 10 to  $100^\circ$  with a step size of 0.040 and the time step was set to 4 seconds. A  $1^\circ$  divergence slit was also defined.

The diffraction produced a series of sharp peaks of high intensity on the diffraction traces. Using the APD software the diffraction angles ( $2\theta$  angles), and their corresponding d-spacing values were obtained enabling analysis and interpretation of the traces. For each peak the software enabled one to determine the peak width, peak intensity, background intensity, relative intensity and its significance.

The constituent materials of the samples could be identified by comparison with the standard data of the JCPDS Powder Diffraction File. With knowledge of the possible major constituents of the samples a number of relevant powder diffraction files were obtained.

There are some problems that arise when comparing experimental results to the standard JCPDS X-ray powder diffraction data. It should be noted that in most cases the standard of equipment has changed since the JCPDS data was taken. However sample preparation has not altered substantially, in fact basic sample preparation is actually quite minimal. All that is required of the sample is that it has a smooth

surface. It should also be noted that the JCPDS data is compiled from the results from one particular sample.

The samples contain several different identified elements and compounds, which were checked against standard data. The JCPDS data however does not quote any theoretical results, and therefore since samples are always different in some way, there will be inevitable discrepancies.

A possible area for discrepancies to arise is in sample preparation. Although, undoubtedly the samples and the standard JCPDS samples possessed the requisite smooth surface, they will have both been processed in different ways. Standard samples are prepared in a variety of different ways. So whatever alterations to the crystalline materials lattice the various drawing procedures produce will be highlighted by inconsistencies in the two sets of results. Such inconsistencies may manifest themselves as peak position and peak height changes.

The standards are usually produced by experimentation on samples at an assumed constant temperature. The experimentation on these samples was not carried out at a constant temperature. The temperature fluctuation was less than 2° C over the whole of the experimental analysis. Therefore further experimental result dissimilarities may have arisen from this difference in experimental procedure.

Modern equipment has advantages over some of the older equipment that has been used to obtain some of the standard data. Some of the older equipment was unable to

resolve very closely positioned peaks. If there are several peaks positioned at each peak point for the standard, then often an average of those peaks is given. Modern equipment is able, to some degree, to resolve between these different lines.

Another potential problem arises from the mounting of the sample. The instrument is calibrated to accept reflections from a specified level. It is, however, difficult to mount samples at an exact height. As a result the reflections obtained may be from slightly higher or slightly lower  $2\theta$  angles. Thus, in subsequent analysis, the corresponding d-spacing values may not accurately match those that could be expected for a particular material. Therefore there may be some deviation from the standard powder diffraction file data. Any sample curvature (especially with the DWI material) can also cause deviation from the standard d-spacing values.

## **6.4 Glow Discharge Optical Emission Spectroscopy (GDOES)**

### **6.4.1 GDOES Theory**

Glow Discharge Optical Emission Spectroscopy (GDOES) is capable of providing compositional depth profiling of conductive samples. Identification of sample constituents in GDOES is done through the identification of photoemissions originating from the excitation and subsequent relaxation of atoms from the sample under study.

Atoms in the sample can be excited when an atom is provided with enough energy to raise an electron to a higher energy level. The excited state is inherently unstable and so for the atom to become more stable an electron moves from a higher energy level into the now vacant lower energy level. In this process excess energy is removed from the system by the emission of a photon of energy  $E$  with corresponding wavelength  $\lambda$ .

Since the energy levels differ from elemental atom to elemental atom, the energy released in a transition is different for each elemental atom and thus each atom has its own distinct characteristic spectral lines. From these spectral lines each atom can be uniquely identified. For quantification of the elements present the intensity of the produced spectral lines is used as the intensity is proportional to the number of emitted photons and thus the elemental concentration in the sample.

This atomic identification can only take place if the atoms are in gaseous form as when in solid form excitation produces a continuum of energy emission due to lattice vibrations and thermal radiation. Thus the sample must be evaporated into an evacuated chamber. For the evaporation of the sample GDOES uses a glow discharge plasma. This is a highly stable excitation source that provides a flat uniform sputter spot on the sample surface which makes GDOES an ideal technique for depth profiling. The technique requires little sample preparation for bulk solids.

## 6.4.2 GDOES Experimental Detail

The LECO GDS-750 QDP Glow Discharge Spectrometer was used for the analysis of the tinplated steel samples. A water cooled Grimm type [1,2] glow discharge source is used in the GDS-750 QDP, as shown in figure 6.3. The analysis chamber has a small vacuum chamber with a hollow cylindrical anode of 8 mm in diameter running through the centre. The sample forms the cathode at one end sealed with an o-ring and the other end of the chamber is sealed by the use of a photon transparent lens. The chamber is evacuated and then a controlled argon pressure is applied across the sample surface. The transmitted photons are detected and analysed by a classical Paschen-Runge configured spectrometer. Typical operating conditions used are 500 to 1500 V at 20 to 200 mA, which gives a sputter rate of the order of 10 to 100 nm per second.

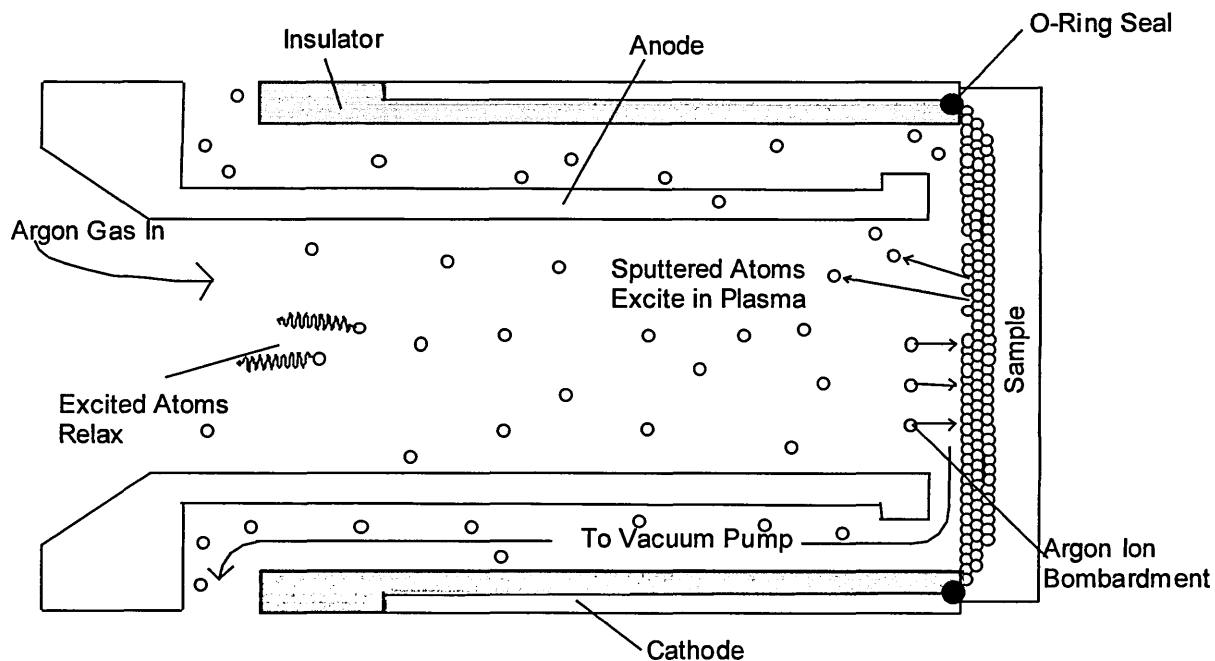


Figure 6.3. Schematic of sputtering in a glow discharge source [3].

The cathodic sputtering process is created by applying a suitable controlled voltage across the anode and cathode. This causes a breakdown of the argon gas. The ions produced are accelerated towards the cathode. On impact neutral cathode atoms are sputtered from the surface along with secondary electrons. The secondary electrons, which are rapidly accelerated towards the anode, collide with the argon atoms causing ionisation allowing the discharge to be sustained. The cathode atoms, which have been sputtered, diffuse into the negative glow region and undergo ionisation by collisions with argon ions or excitation by collisions with secondary electrons. Subsequent relaxation of the excited cathode atoms leads to the emission of photons characteristic of the cathode atom.

Beyond the glow discharge source the spectrometer instrumentation contains a 20 $\mu$ m entrance slit which provides a narrow optical image. The emitted photons are focused by the focussing lens and pass through this entrance slit into a Rowland circle [4]. A concave holographic grating provides first-order diffraction of the incident light. 50 $\mu$ m exit slits around the Rowland circle isolate particular spectral wavelengths. 44 photomultiplier tubes behind the exit slits detect and convert the light into an appropriate electrical signal suitable for processing by the microprocessor. The photomultipliers have a spectral range of 150 - 456nm. The sputtered depth can be found from the sputter times and etch rates of the elements, and quantification of the data is done by analysing the emission line intensities.

## **6.5 Inductively Coupled Plasma Mass Spectrometry (ICP-MS)**

Inductively coupled plasma mass spectrometry (ICPMS) is an analytical technique that requires the sample to be introduced into high-temperature argon plasma, which dissociates molecules and ionizes atoms. Preparation of samples requires lengthy dissolution processing which may be incomplete and can also potentially introduce contamination to the sample. There are interference species produced by the interaction of water and acid species with the argon plasma, however the technique, given careful solution preparation, gives accurate information on elemental concentration.

In the analysis of material in this study 0.25 g of each sample was sectioned for dissolution. With the sample placed in a clean glass beaker 3 ml of nitric acid ( $\text{HNO}_3$ ) and 9 ml of hydrochloric acid (HCl) were introduced and the sample in solution heated to 60 °C for 10 minutes, which allowed the sample to be completely dissolved in solution. The solution was then diluted with de-ionised water to 250 ml.

The sample solution is introduced into high-temperature argon plasma, which dissociates molecules and ionizes atom. The ions are then passed into vacuum via a sample and skimmer cone interface, where a lens stack focuses the ion beam into a quadrupole mass spectrometer. Here, the ions are sorted by mass and detected using a scanning electron multiplier, detecting ions at each mass/charge ratio in rapid sequence. That information is then converted from the electrical signals produced into

digital information that is used to indicate ion intensity and subsequently element concentration.

## **6.6 Talysurf**

The talysurf is used to analyse surface topography. The talysurf used in this study was a Taylor Hobson laser form talysurf 120L. The apposite standards for the measurement of surface topography are ISO 4287/1 and ISO 11562.

The talysurf is a stylus instrument enabling two dimensional tracing of the sample surfaces. The stylus is traversed normal to the surface at constant speed. In the instrument used for this study an arcuate (pivoted beam) 6 mm range 60 mm stylus arm is fitted with a standard conisphere diamond tip (112/2033-327) giving a resolution of 10 nm at the 6 mm range.

Parameters are usually defined over the sampling length or evaluation length, the evaluation length being comprised of a number of sampling lengths. An average parameter estimate is calculated by taking the arithmetic mean of the parameter estimates from all the individual sampling lengths. For roughness profile parameters the standard number of sampling lengths is six.

Of particular interest in this study is the parameter  $R_a$ , which is the average roughness, defined as the arithmetic average of the absolute values of the roughness profile ordinates. The average roughness values are complemented by the values  $R_p$  and  $R_v$ .

$R_p$  is the height of the highest profile peak of the roughness calculated over the evaluation length.  $R_v$  is the depth of the deepest profile valley of the roughness calculated over the evaluation length. The sum of  $R_p + R_v$  is the single roughness depth  $R_t$  and is therefore the maximum difference between the highest profile peak and the deepest profile valley over the whole evaluation length incorporating all sample sections. In this study a 0.8 mm sample filter is used with an evaluation length of 5.6 mm comprising six sections of sampling each of 0.8 mm. The small sample filter helps to reduce the effects of waviness within the samples. The effect of sample curvature is taken care of by fitting the acquired data to concave or convex base lines.

## Complementary Analytical Techniques References

- [1] W. Grimm, *Spectrochimica Acta B* **23** (1968) 443.
- [2] R. Payling, D. Jones and A. Bengtson, *Glow Discharge Optical Emission Spectrometry*, John Wiley & Sons (1997).
- [3] J. L. Davidson, PhD Thesis : “<sup>57</sup>Fe Mössbauer Studies of Surface Interactions in a PVD Process”, Sheffield Hallam University, (1997).
- [4] J. F. James and R. S. Steraberg, *The Design of Optical Spectrometers*, Chapman and Hall, London (1969).

## **7. RESULTS AND DISCUSSION**

Mössbauer experiments have been carried out on many samples to try to identify the Fe-Sn intermetallics. All of the Mössbauer experiments within the individual sections of these results ran for the same length of time and with the detector positioned in the same place for each experiment to provide the best basis for comparison between results. All calculated Mössbauer isomer shifts are given relative to  $\alpha$ -Fe and have an error of  $\pm 0.02 \text{ mm s}^{-1}$ . Calculated values of the magnetic hyperfine field have an error of  $\pm 0.2 \text{ T}$ . Other analytical techniques have been used to complement the Mössbauer analysis and the relevant analysis has been included here.

### **7.1. Analysis of Steel Sheet**

In order to fully understand the effects of DWI processing it was prudent to analyse the sheet steel from the production line before any electrodeposition or DWI processing. Sections of the sheet steel were randomly chosen and analysed.

#### **7.1.1 $^{57}\text{Fe}$ CEMS Analysis of Steel Sheet**

The first Mössbauer experiments were carried out on the steel sheet which is used as the basis for the can blank prior to electrodeposition of tin and subsequent can processing. A clear  $\alpha$ -Fe signal,  $H = 33.0 \pm 0.2 \text{ T}$ ,  $\delta = 0.00 \pm 0.02 \text{ mm s}^{-1}$ , was obtained with a typical relative intensity for peaks 2 and 5 of 6.6 %. A single sextet is seen in the spectra as shown in the example given in figure 7.1. The parameters from

the fitting of this spectrum are shown in table 7.1. These are the exact parameters by which the Recoil data fitting software gave the lowest chi squared ( $\chi^2$ ) value. This particular spectrum was recorded using a 7 mCi source over a 72 hour time period and thus the spectrum is noisy, which is to be expected with such a weak source. The spectrum shows no deviation from the parameters expected for just  $\alpha$ -Fe. Though it is known that there is a small carbon content in the steel there is no indication of any cementite ( $\text{Fe}_3\text{C}$ ) in the spectrum ( $H = 20.8 \text{ T}$ ,  $\delta = 0.19 \text{ mm s}^{-1}$  [1]). Likewise there is no indication of any other alloys present in the sheet material.

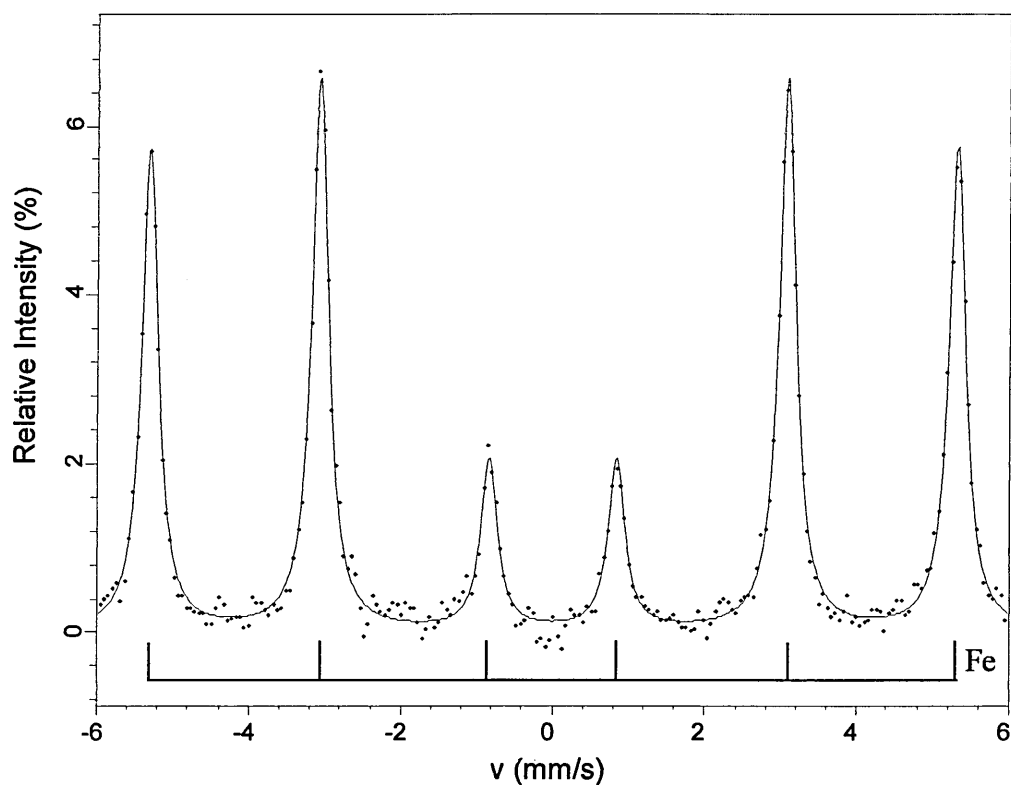


Figure 7.1. Steel can blank.

Sample Description	Figure No.	Mössbauer parameters, relative to $\alpha$ -Fe, at 295 K ( $\pm 0.02 \text{ mm s}^{-1}$ )			Magnetic Hyperfine Field ( $\pm 0.2 \text{ T}$ )	Phase Identified	Relative Phase Area %	Peak 2 and 5 Relative Intensity %	$\chi^2$
		$\delta$	$\Delta$	$\Gamma/2$	H				
Steel can blank	7.1	0.00	0.00	0.13	33.0	$\alpha$ -Fe	100	6.60	0.426

Table 7.1. Parameters for steel can blank analysis.

### 7.1.2 SEM Analysis of Sheet Steel

Analysis using Scanning Electron Microscopy (SEM) reveals further information about the surface of the steel sheet. A number of steel sheets were analysed on both sides and typical images are shown in figures 7.2 and 7.3. There was no discernible difference between different sides of sheets or between different sheets.

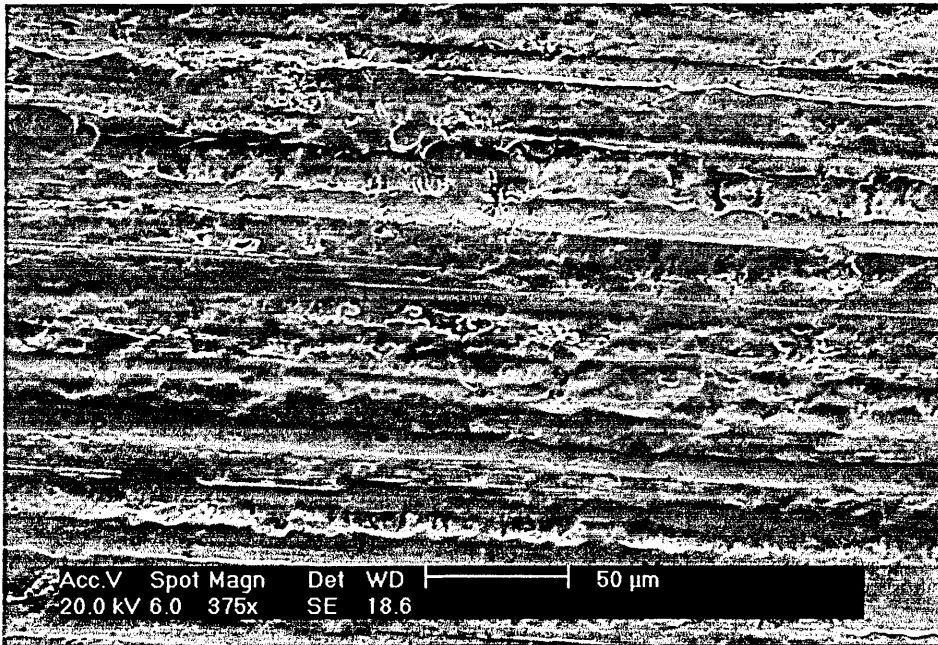


Figure 7.2. Secondary electron image of steel can blank.

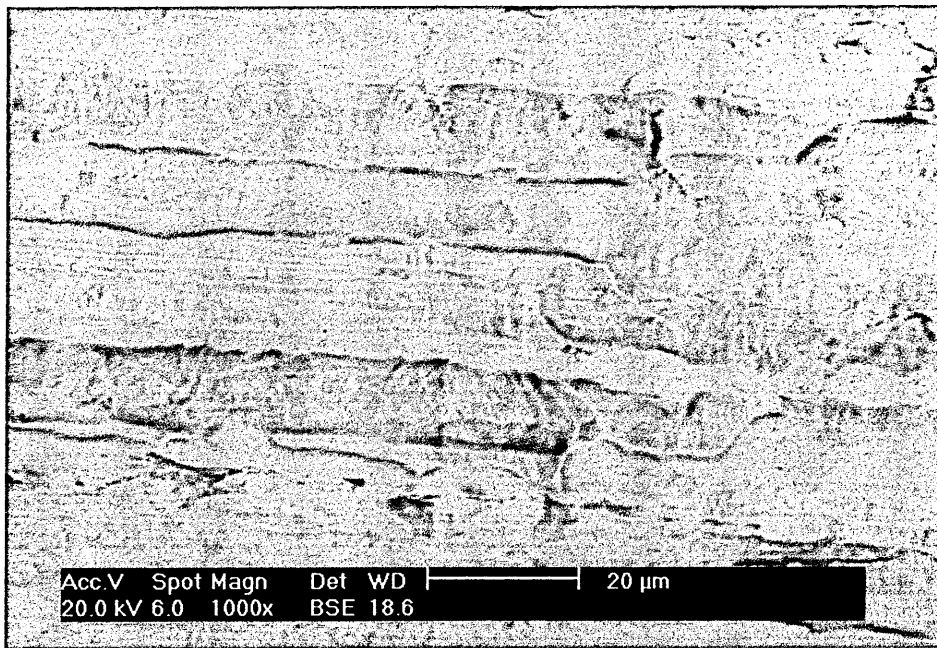


Figure 7.3. Back-scattered electron image of steel can blank.

Figure 7.2 shows a Secondary Electron (SE) image and figure 7.3 shows a Back-Scattered Electron (BSE) image. The SE images generally show topographic detail, whereas the BSE images are used to give further information relating to elemental composition. However both of these images show only the steel sheet with a grooved surface as there is no tin coating applied yet that would provide contrast for the BSE image. The different types of SEM images are discussed in more detail in section 6.2 and with respect to other experimental results in section 7.2 where there is a more varied elemental composition in the samples. The BSE image itself is at higher magnification than the SE image in order to show more clearly the detail of the grooved surface. There are two reasons for doing this when looking at the sheet steel. Firstly the range of backscattered electrons is much greater than that of the electrons detected in the SE mode and this increase in electron range gives an extended diameter of the interaction volume. This extended interaction volume limits resolution and

results in a lack of detail for images obtained at low magnification in BSE mode. Secondly the lack of contrast resulting from the uniformity of material composition reduces image quality, or more precisely image clarity and higher magnifications can help identify any features on the sample surface. X-ray analysis using the Philips XL-40 showed a strong signal arising from the iron but no other elements were identified including carbon, which is known to be present at low levels in the sheet steel material.

The SEM images show the grooves and pits left from processing the steel sheet when rolling to reduce the sheet thickness. The grooves generally have widths in the region of 10  $\mu\text{m}$ , though over the surface of the sheet grooves of up to 50  $\mu\text{m}$  width were observed. This leaves an uneven surface to electroplate with tin so that the thickness of tin will not be entirely uniform over the surface and the overall material thickness will be variable over the surface. Drawing of this material into cans will therefore inevitably lead to uneven distribution of tin on the sample surface.

## **7.2. Analysis of DWI Timplated Steel Cans**

After the initial analysis of the uncoated steel material, a selection of DWI cans were taken from the production line directly after the wall ironing process and before the washing and lacquering procedures, the reasons for which are discussed fully in sections 7.7 and 7.8, but it is enough here to say that both procedures introduce Mössbauer inert layers which severely reduce the signal obtained when using CEMS. Sections of the DWI timplated steel can were taken from the can wall for analysis.

### 7.2.1 $^{57}\text{Fe}$ CEMS Analysis of DWI Tinplated Steel Cans

For the Mössbauer analysis samples were taken from the top and bottom of the can wall and unaltered prior to analysis. Again  $\alpha\text{-Fe}$  signals were obtained as expected, but possibly due to low signal to noise ratios, no intermetallics were identified. Spectra obtained from these experiments are shown in figures 7.4 to 7.7. Parameters for these spectra are summarised in table 7.2.

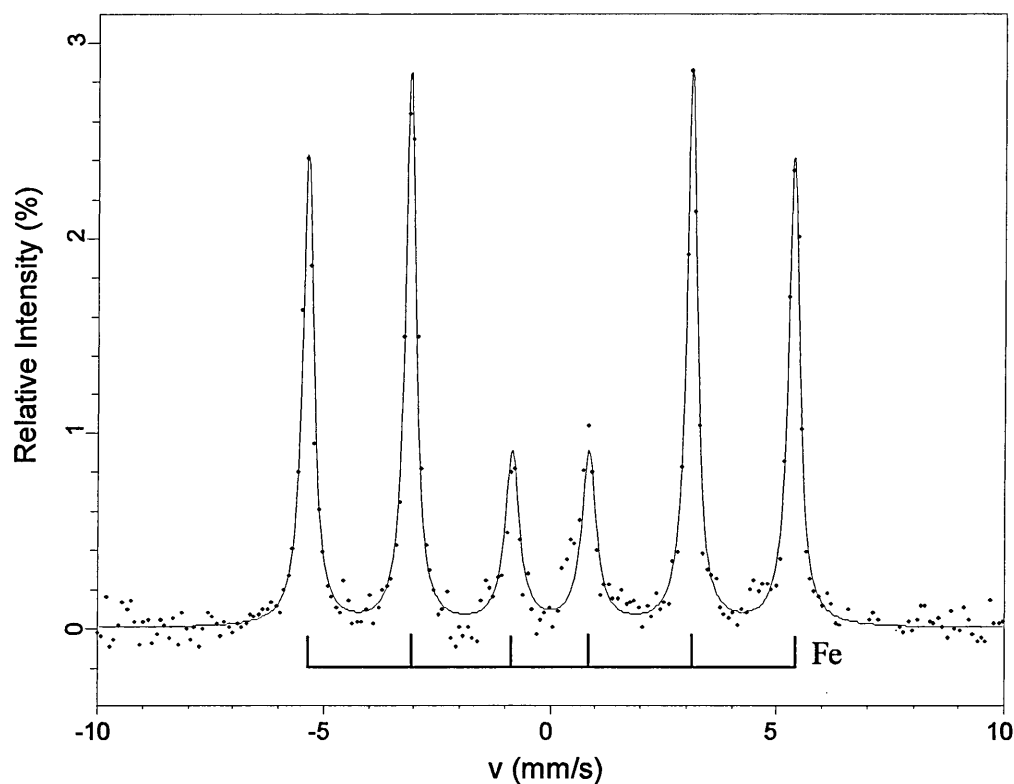


Figure 7.4. Outside top of as-produced DWI can.

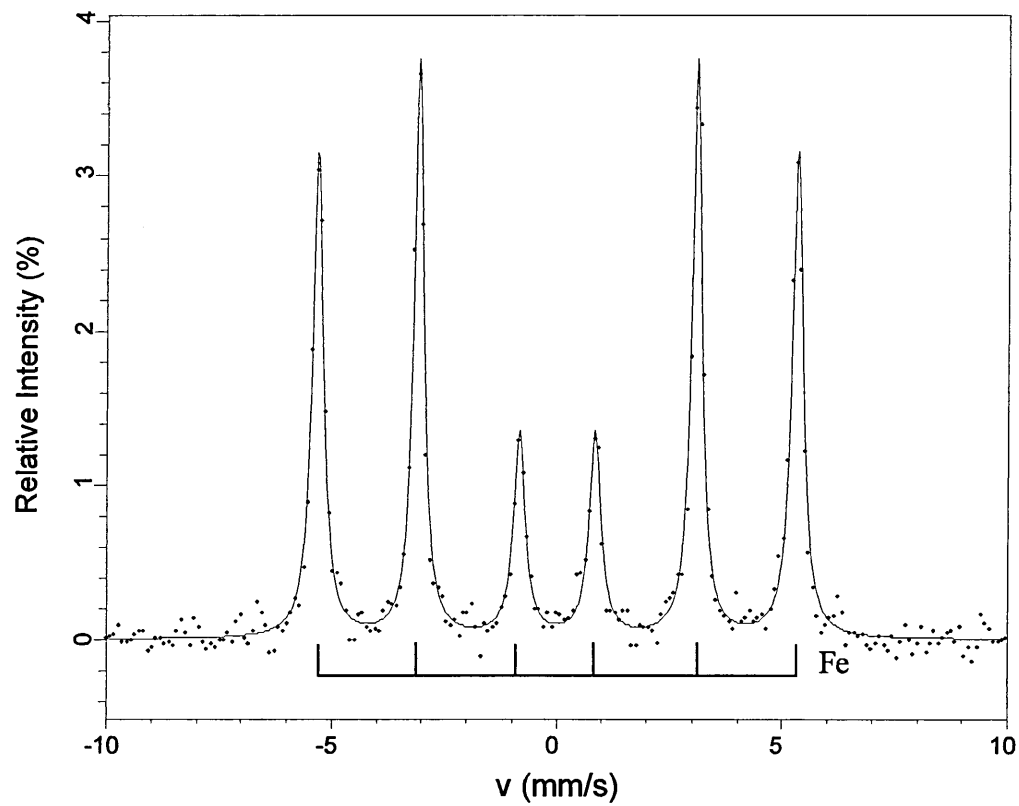


Figure 7.5. Outside bottom of as-produced DWI can.

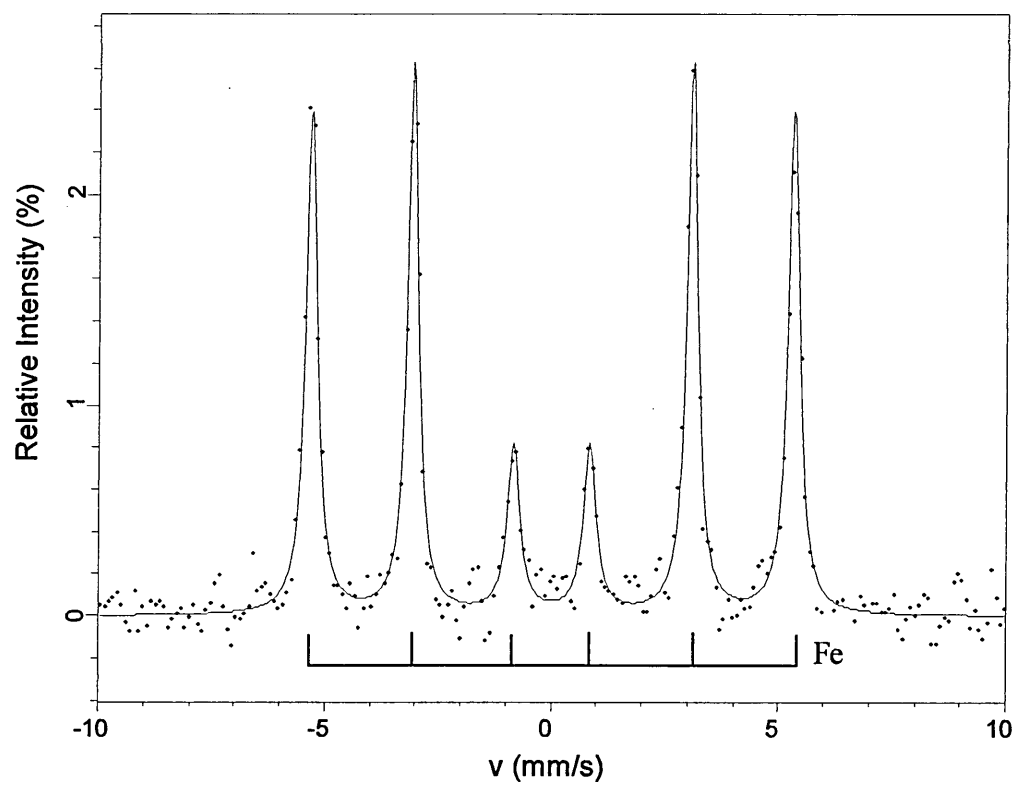


Figure 7.6. Inside top of as-produced DWI can.

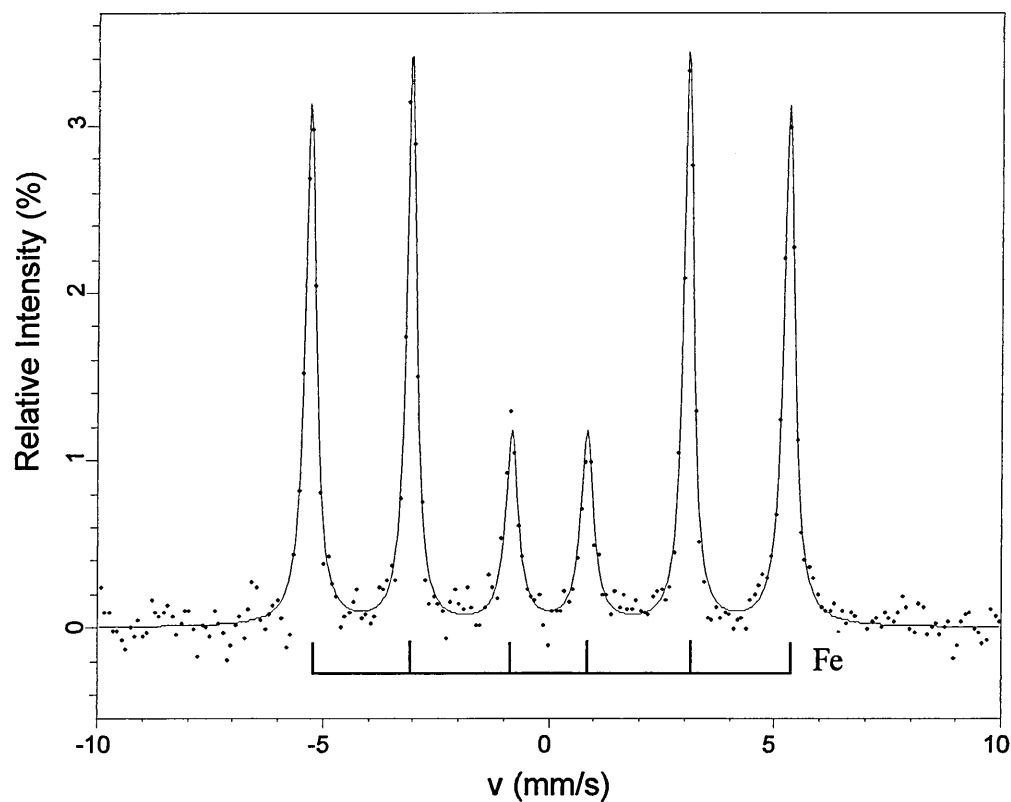


Figure 7.7. Inside bottom of as-produced DWI can.

Sample Description	Figure No.	Mössbauer parameters, relative to $\alpha$ -Fe, at 295 K ( $\pm 0.02 \text{ mm s}^{-1}$ )			Magnetic Hyperfine Field ( $\pm 0.2 \text{ T}$ )	Phase Identified	Relative Phase Area %	Peak 2 and 5 Relative Intensity %	$\chi^2$
		$\delta$	$\Delta$	$\Gamma/2$	H				
Outside top of DWI can	7.4	0.00	0.00	0.15	33.3	$\alpha$ -Fe	100	2.85	0.824
Outside bottom of DWI can	7.5	0.00	0.00	0.14	33.0	$\alpha$ -Fe	100	3.75	1.133
Inside top of DWI can	7.6	0.00	0.00	0.15	33.0	$\alpha$ -Fe	100	2.60	0.638
Inside bottom of DWI can	7.7	0.00	0.00	0.15	32.8	$\alpha$ -Fe	100	3.40	0.661

Table 7.2. Parameters for as-produced can analysis.

From these preliminary experiments the analysis of the as-produced DWI tinplated steel can provides no discernible evidence of the Fe-Sn intermetallics of any form, the two most expected being FeSn and FeSn<sub>2</sub>. The observed  $\alpha$ -Fe signal corresponding to the substrate vary on the different areas of the can wall. The greatest signal, denoted by greater relative intensities of the  $\alpha$ -Fe peaks, was found on the bottom of the can wall when analysing the outside of the can. The spectrum for this area, figure 7.5, shows a relative intensity for peaks 2 and 5 of 3.7 %. It is assumed therefore that there is least tin on this area of the can to mask the  $\alpha$ -Fe signal. The spectrum for analysis of the inside bottom of the can wall, figure 7.7, then showed the next greatest signal. For this area there is a reduction of signal compared to the analysis of the outside bottom of the can wall, giving a relative intensity value for peaks 2 and 5 of 3.4 %. Since the two greatest signals were obtained from the bottom of the can this analysis suggests that within the DWI process the bottom of the can has more tin removed from the surface.

The least signal was observed with the inside of the top of the can, figure 7.6, though this signal was observed to be very similar to that found when analysing the outside of the top of the can, figure 7.4. The slightly greater signal is observed when analysing the outside of the can wall. These values are tabulated in table 7.2. The relevance of this slight differentiation between inner and outer can surfaces depends on the variation of coating weight on the two surfaces of the tinplate before DWI processing. Equal initial weighting would suggest that tin is generally removed more from the outer can surface, possibly onto the die surface rather than onto the punch on the inside of the can. In the case of the DWI tinplate used to form these cans the coating weights for both surfaces

are set equal at  $2.8 \text{ g cm}^{-2}$  and thus tin has been removed more from the outer can surface.

### 7.2.2 $^{119}\text{Sn}$ Mossbauer Analysis of DWI Tinplated Steel Cans

$^{119}\text{Sn}$  Mössbauer experiments on the as-produced can have been carried out by Prof. Friedrich E. Wagner at the Technische Universität München, Germany. Subsequent analysis was carried out using the Recoil software package at Sheffield Hallam University. Figures 7.8 and 7.9 show two different fits of a single spectrum, recorded using transmission geometry at 4.2 K, resulting from the analysis of a sample from the outside top of the as produced DWI can wall. Parameters from the analysis are summarised in table 7.3.

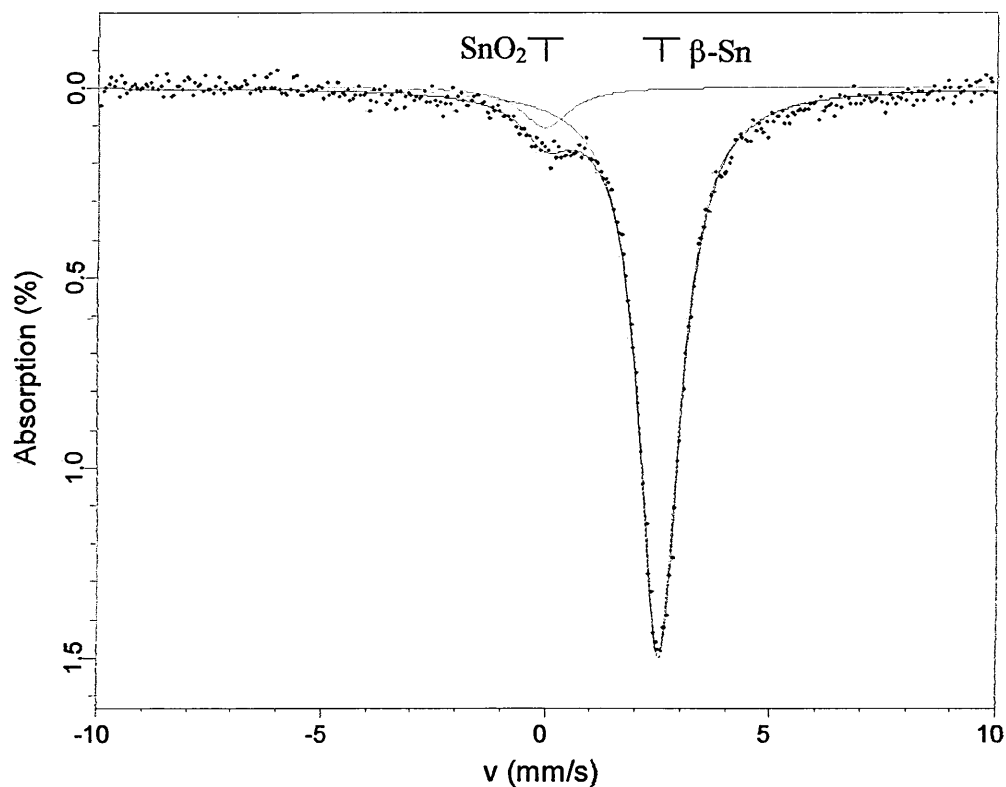


Figure 7.8.  $^{119}\text{Sn}$  analysis of as produced DWI can.

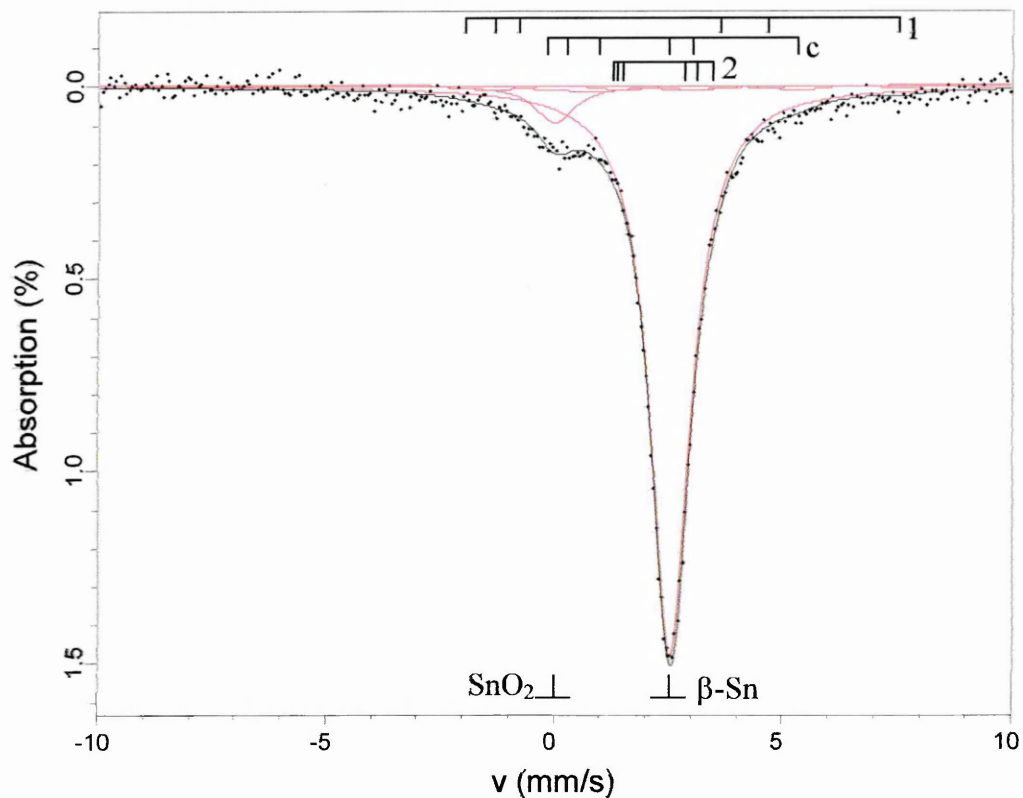


Figure 7.9.  $^{119}\text{Sn}$  analysis of as produced DWI can with  $\text{FeSn}_2$  fitted.

Sample Description	Figure No.	Mössbauer parameters, relative to $\text{BaSnO}_3$ , at 4.2 K ( $\pm 0.02 \text{ mm s}^{-1}$ )			Magnetic Hyperfine Field ( $\pm 0.1 \text{ T}$ ) H	Phase Identified	Relative Phase Area %	$\chi^2$
		$\delta$	$\Delta$	$\Gamma/2$				
$^{119}\text{Sn}$ DWI can analysis	7.8	2.54	0.00	0.55	0.0	$\beta\text{-Sn}$	92.0	1.116
		-0.02	0.00	0.66	0.0	$\text{SnO}_2$	8.0	
$^{119}\text{Sn}$ DWI can analysis with $\text{FeSn}_2$ fitted	7.9	2.53	0.00	0.53	0.0	$\beta\text{-Sn}$	87.8	1.082
		-0.01	0.00	0.53	0.0	$\text{SnO}_2$	5.7	
		2.30	0.86	0.55	6.7	$\text{FeSn}_2$ (1)	1.9	
		2.30	0.86	0.55	0.4	$\text{FeSn}_2$ (2)	1.5	
		2.30	0.86	0.55	3.3	$\text{FeSn}_2$ (c)	3.1	

Table 7.3. Parameters for  $^{119}\text{Sn}$  analysis of DWI cans.

The spectra for the  $^{119}\text{Sn}$  analysis of the as produced DWI can, figure 7.8, shows metallic tin ( $\beta\text{-Sn}$ ), relative intensity 1.50%, and tin oxide ( $\text{SnO}_2$ ), relative intensity

0.11%, with little evidence of any other compounds identifiable beyond the background noise. There is some deviation from the background level at either side of the tin and oxide peaks and the fit in figure 7.9 is fitted with fixed values of  $\text{FeSn}_2$  to check for the intermetallic that is observed in some of the later  $^{57}\text{Fe}$  analysis of etched DWI (see section 7.3).

Three major components to the spectra for  $\text{FeSn}_2$  have been previously identified at 4.2 K using  $^{119}\text{Sn}$  Mössbauer Spectroscopy [2,3] and the parameters for the three observed components are,  $H = 6.65 \pm 0.1$  T with  $\delta = 2.30 \pm 0.02$   $\text{mm s}^{-1}$  and  $\Delta = 0.86 \pm 0.02$   $\text{mm s}^{-1}$ ,  $H = 0.4 \pm 0.1$  T with  $\delta = 2.30 \pm 0.02$   $\text{mm s}^{-1}$  and  $\Delta = 0.86 \pm 0.02$   $\text{mm s}^{-1}$  and  $H = 3.25 \pm 0.1$  T with  $\delta = 2.30 \pm 0.02$   $\text{mm s}^{-1}$  and  $\Delta = 0.86 \pm 0.02$   $\text{mm s}^{-1}$  denoted as 1, 2 and c respectively, creating a complex spectra as shown in figure 7.10. This data was used for the fit of the as-produced can spectra in figure 7.9 with linewidths fixed at  $0.550$   $\text{mm s}^{-1}$ . The data for  $\text{FeSn}_2$  was also fitted using the area ratios quoted by Venturini et al. [2] of 29:23:48 for sites 1:2:c.

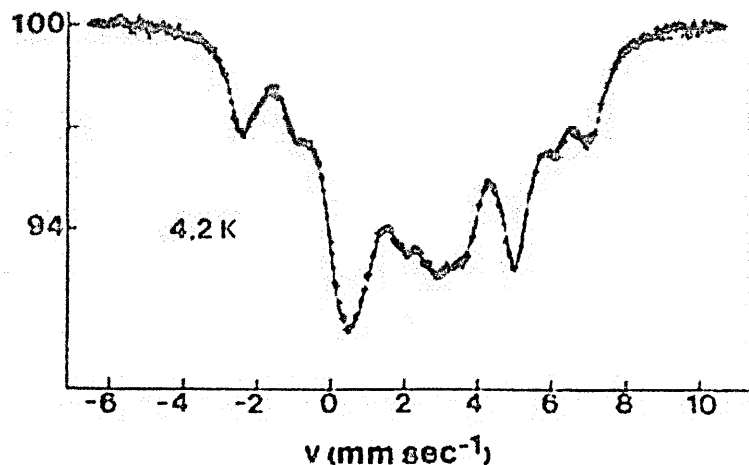


Figure 7.10.  $^{119}\text{Sn}$  spectra of  $\text{FeSn}_2$  [2].

The fit of the  $^{119}\text{Sn}$  data has a slightly lower  $\chi^2$  value for the fit with  $\text{FeSn}_2$  included however the fixing of the  $\text{FeSn}_2$  parameters means that the  $\chi^2$  value obtained is distorted. Freeing the parameters for the  $\text{FeSn}_2$  components causes the fitting to fail, possibly due to the large metallic tin peak covering the velocity range of the individual components and the complexity of the overall  $\text{FeSn}_2$  signal, and so this particular fitting of the data for the as produced DWI analysis should be treated with caution. It is however thought that the slight deviation from the background level either side of the metallic tin and tin oxide peaks is most likely to be due to the presence of  $\text{FeSn}_2$ .

### 7.2.3 SEM Analysis of DWI Tinplated Steel Cans

Analysis using SEM reveals further information about the surface of the can wall. Four areas of the as-produced DWI tinplated steel can have been analysed in the SEM corresponding to the four areas analysed using  $^{57}\text{Fe}$  CEMS analysis, namely, the outside top and bottom and inside top and bottom areas.

There are two types of images displayed here in figures 7.11 to 7.16, which are of the outside of the as-produced can, namely, Back-Scattered Electron (BSE) and Secondary Electron (SE) images. BSE images are favoured for displaying compositional data as the intensity displayed on the computer screen is proportional to the atomic number of the element in question. Areas of higher atomic number elements show brighter than lower atomic number elements. Here we have iron and tin as the main elements involved. Iron has an atomic number of 26 whereas tin is much higher at 50. If the elements present are close together it may be difficult to resolve them successfully,

however these two elements are distinct in the images. So the bright areas in the BSE images are tin and the darker areas are iron. SE images are mainly used to show topographical data but do display some compositional data also. BSE images do show some topographical data but are not as useful in this respect as SE images.

It is difficult to tell from the SEM images whether there is a significant difference in tin concentration between the top and bottom of the can. The problem arises because of the adjustments to the equipment required due to the non-flat surface of the can. The focus, brightness and contrast all had to be adjusted between samples and this causes the contrast in different images to be varied.

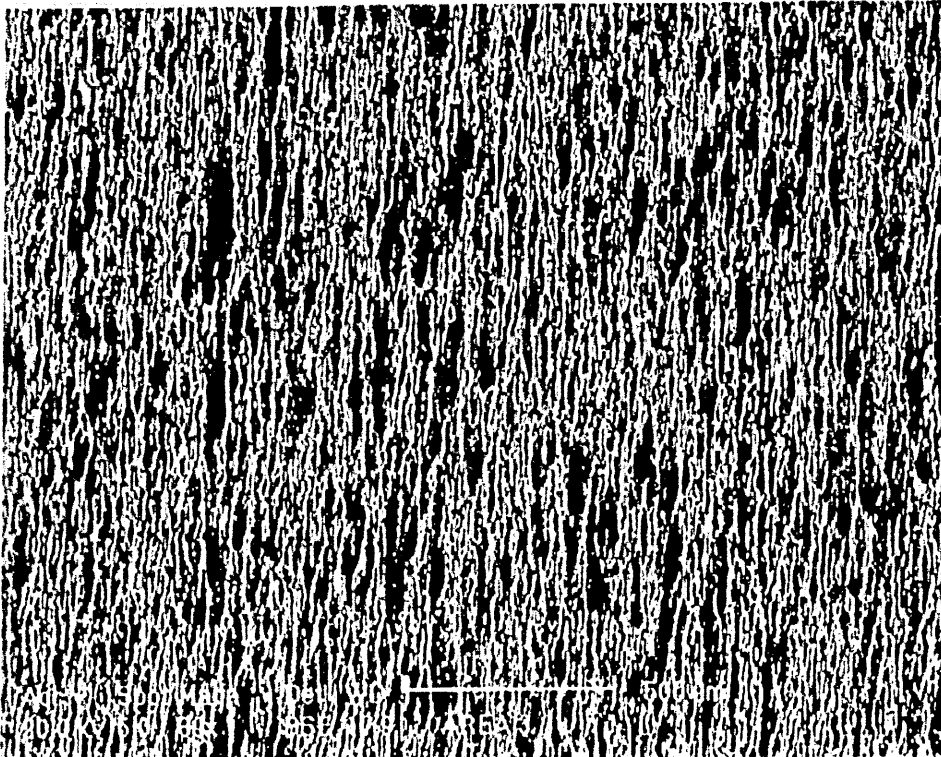


Figure 7.11. Low magnification BSE image of the outside top of the as-produced DWI can.



Figure 7.12. High magnification BSE image of the outside top of the as-produced DWI can.



Figure 7.13. High magnification SE image of the outside top of the as-produced DWI can.

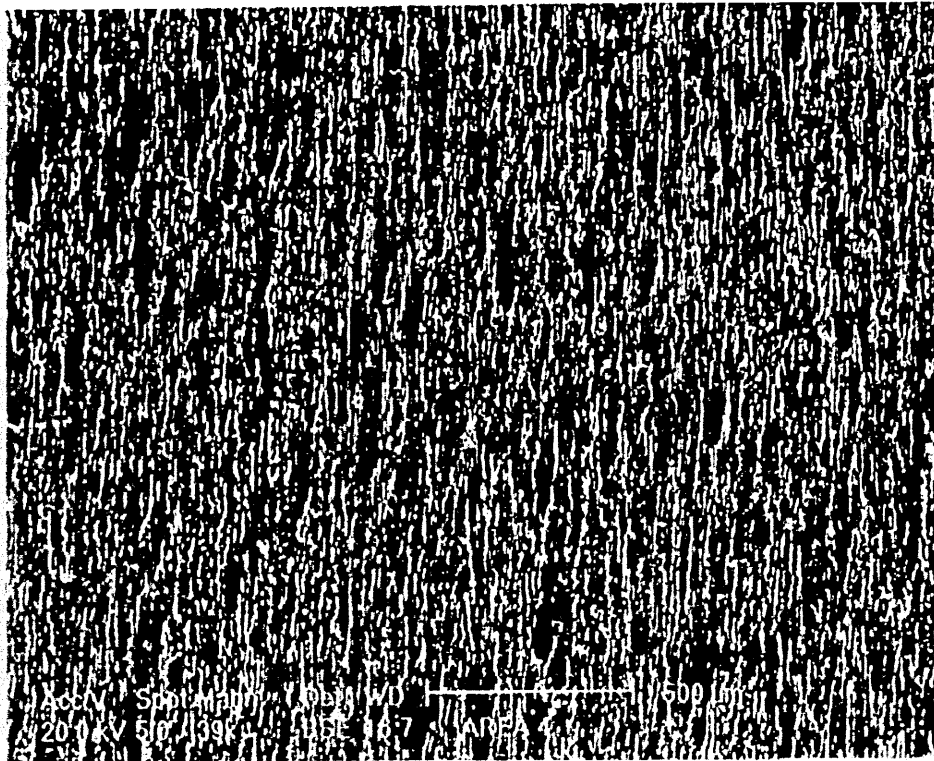


Figure 7.14. Low magnification BSE image of the outside bottom of the as-produced DWI can.

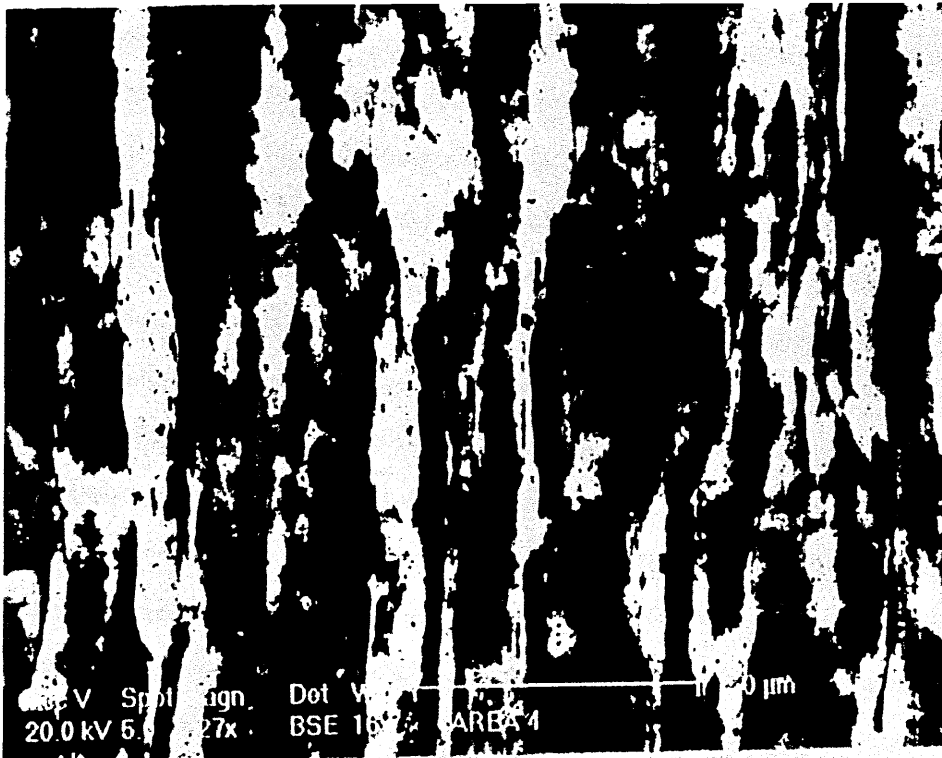


Figure 7.15. High magnification BSE image of the outside bottom of the as-produced DWI can.

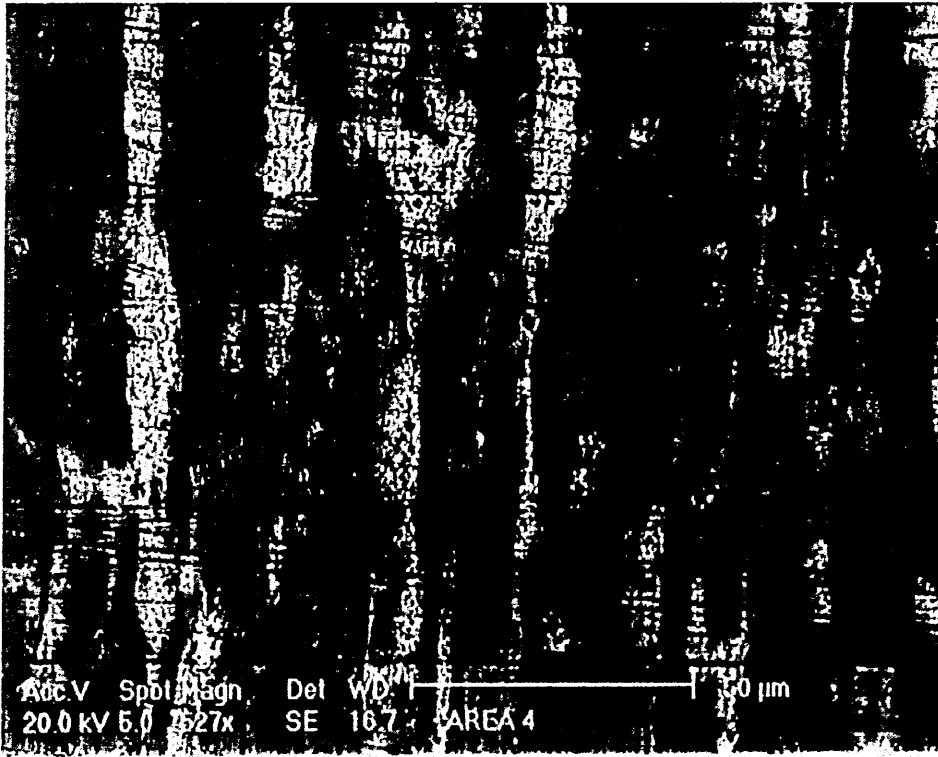


Figure 7.16. High magnification SE image of the outside bottom of the as-produced DWI can.

From the low magnification BSE images in figures 7.11 and 7.14 it appears that the top of the can, figure 7.11, has the greatest concentration of tin, which is in agreement with the initial Mössbauer experiments. However at higher magnification, such as in figures 7.12 and 7.15, the difference is not observed as clearly, as would be expected when imaging such a small sample of the surface. At higher magnifications contrast differences between images is not as significant. A previous SEM study of DWI cans [4] also found that there was a variation in tin concentration on the can wall. It was postulated in that study that during the initial two cupping operations of the DWI process [5] the difference in diameter reduction that the wall material at different heights had undergone produced the variation in tin concentration on the can wall.

There were also some small areas on the sample surfaces that were darker than the identified iron areas. These were analysed using X-ray microanalysis and were found to be carbon, possibly due to handling of the can post production or the carbon deposits may have been introduced during can production. Traces of oxygen were also present and are probably due to the presence of oxides.

The SE images in figures 7.13 and 7.16 show scoring of the can surface perpendicular to the drawing direction of the can wall. This is presumed to be general marking from the production process and subsequent handling of the can. Areas of tin are still shown as lighter areas on a background of iron and seem to be more heavily scored than the iron areas. This could be partly due to the contrast in the images but also due to the hardness of iron compared to tin. Much of the defects in the surface area are also found in the tin areas, some may be due to areas of tin being dragged from the surface either during or post production.

The X-ray microanalysis (EDX) images show the elements present in two analysed areas of the can wall. The first image, figure 7.17, is of the light region identified by the SEM. The largest peaks correspond to tin, however some iron content is also present, this shows that the layer of tin is covering the iron but is not thick enough to completely mask the iron, the X-ray signal arising from up to 1  $\mu\text{m}$  into the sample (the range of the electrons at 20 keV in iron). The signal from the iron is much less in this image than it is in the second image, figure 7.18, where the dark region was imaged. In the analysis of the dark area there is no tin identified and therefore little or no tin present in these areas.

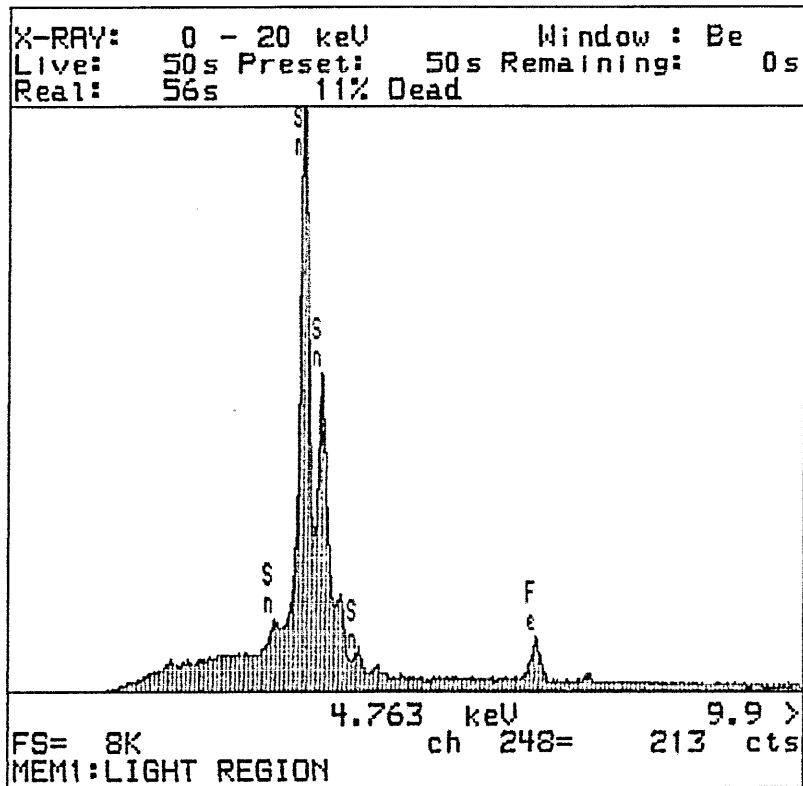


Figure 7.17. EDX spectrum acquired from light coloured region of BSE image.

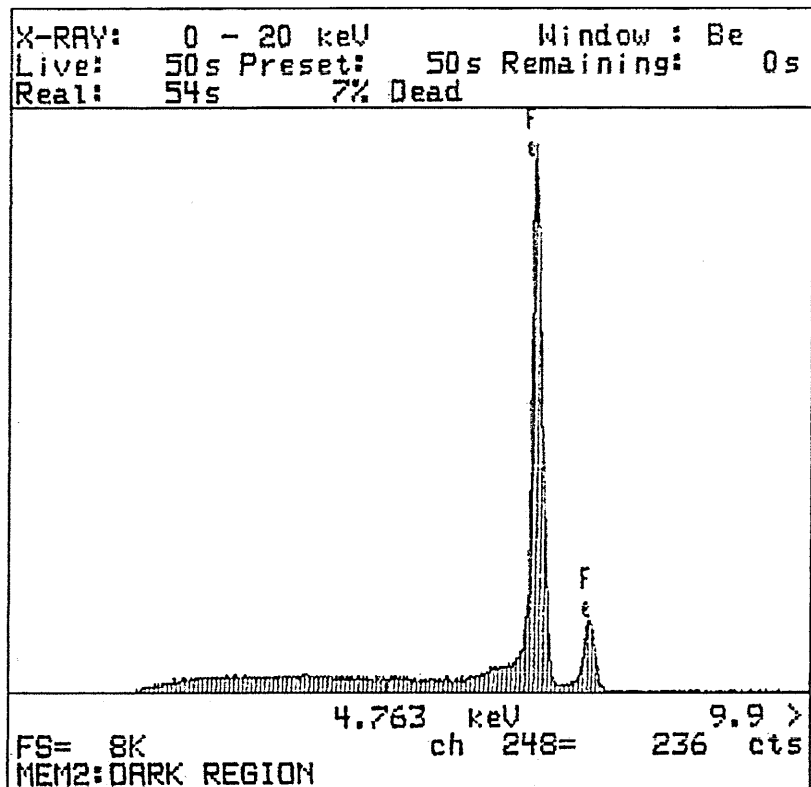


Figure 7.18. EDX spectrum acquired from dark coloured region of BSE image.

Figures 7.19 - 7.24 show the inside of the as-produced DWI can and again the images are of both BSE and SE scans. As with the images of the outside of these areas, it is difficult to observe differences between the top and bottom of the can wall. The difference in tin coverage was best observed at lower magnifications using BSE scans, however the difference was not as marked as it was with the outside of the can wall, this is due to the velocity of the wall material in contact with the punch being approximately zero during formation of the can.

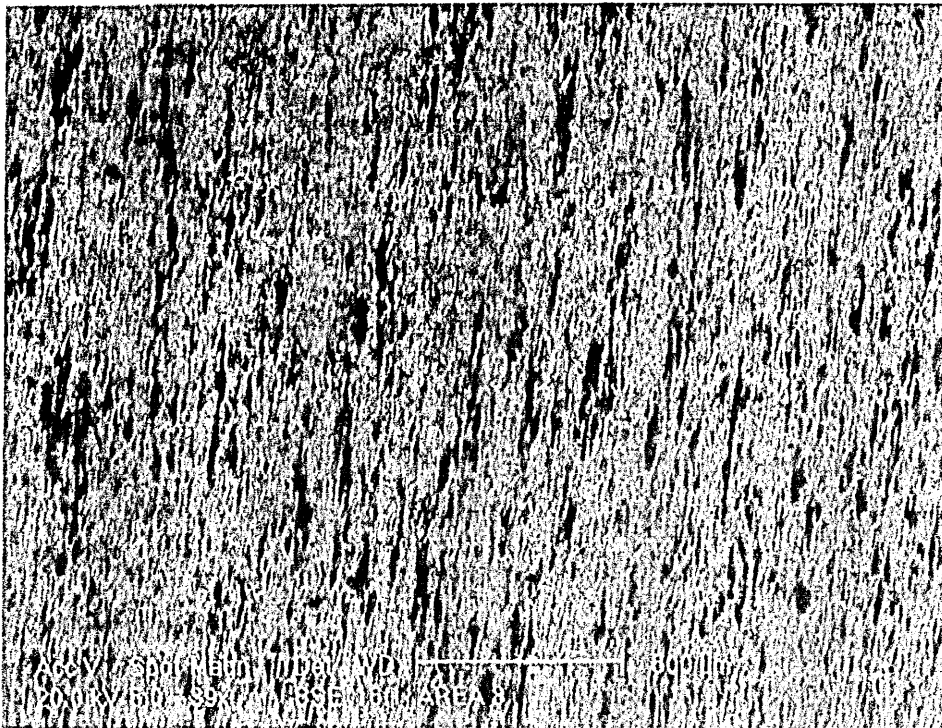


Figure 7.19. Low magnification BSE image of the inside top of the as-produced DWI can.



Figure 7.20. High magnification BSE image of the inside top of the as-produced DWI can.

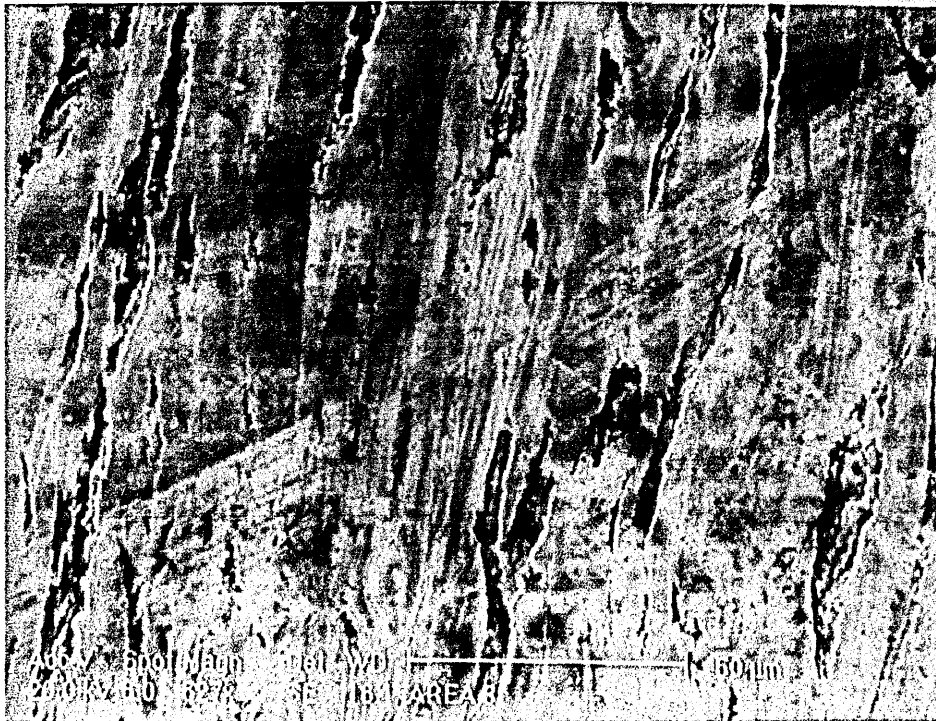


Figure 7.21. High magnification SE image of the inside top of the as-produced DWI can.

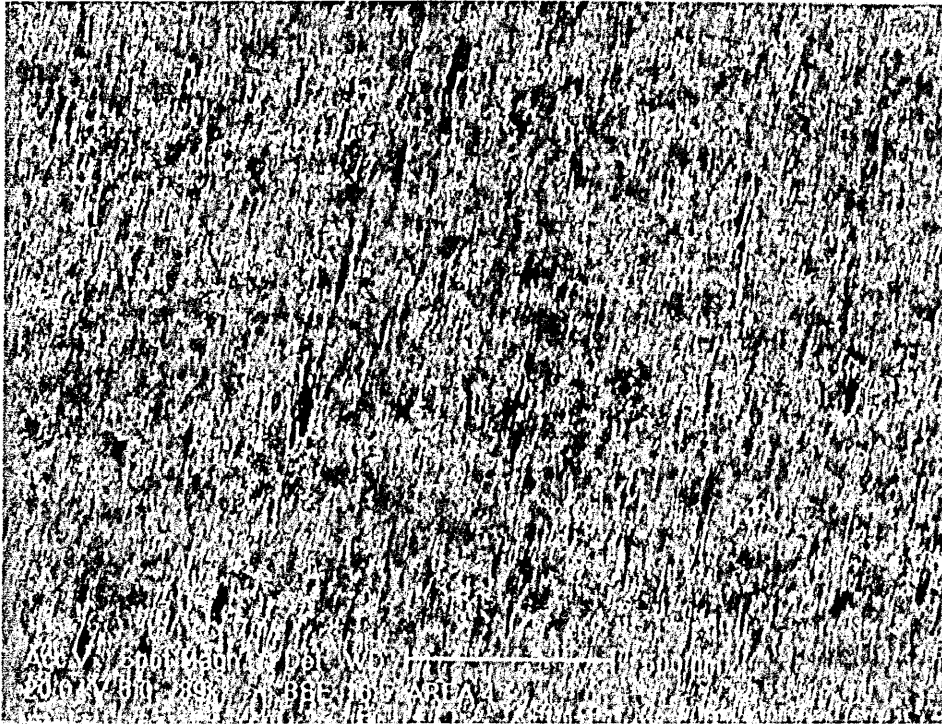


Figure 7.22. Low magnification BSE image of the inside bottom of the as-produced DWI can.



Figure 7.23. High magnification BSE image of the inside bottom of the as-produced DWI can.

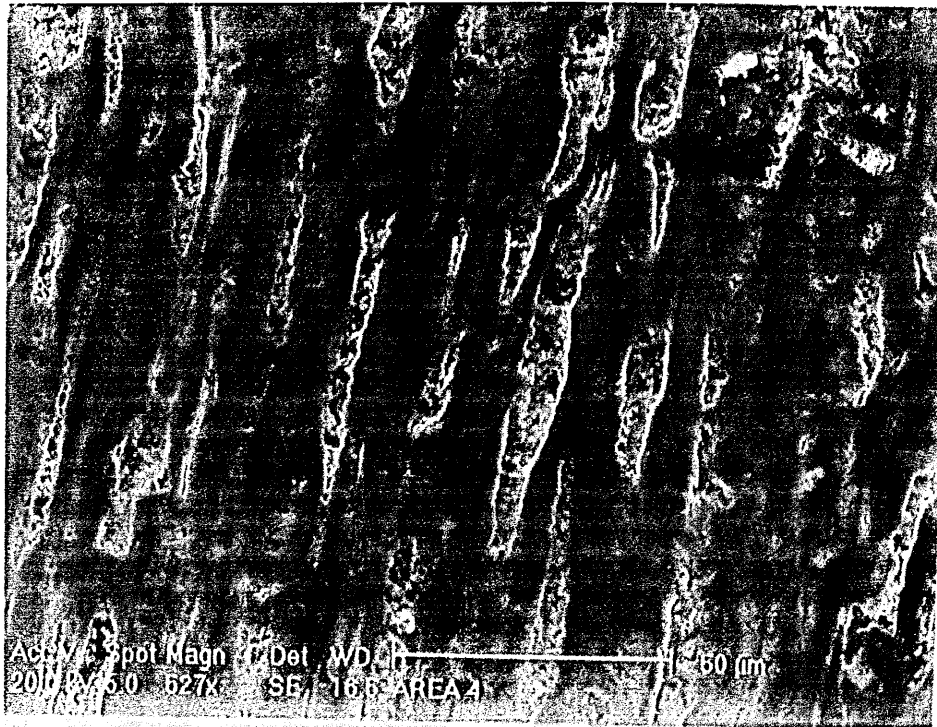


Figure 7.24. High magnification SE image of the inside bottom of the as-produced DWI can.

Figure 7.21 shows scoring typical of the top area of the inside of the can wall. Around the can perimeter the scoring is in all directions with no preferred direction unlike the outside of the can, figure 7.13, where the scoring ran perpendicular to the tin filled grooves. On the bottom of the outer can wall, figure 7.16, similar scoring is observed to that found at the top of the outer can wall, figure 7.13. In contrast the bottom of the can wall on the inside is relatively free of scoring, figure 7.24, though there tend to be more tin free vertical grooves than any other area of the can. These grooves are similar to those seen on the sheet steel before processing and may be remnants of those surface undulations, which are not significantly altered by the DWI process. Again as the punch and inside can wall do not have a significant velocity differential the inside can surface is expected to be less deformed by the DWI process than the outside of the can wall.

#### 7.2.4 GDOES Analysis of DWI Tinplated Steel Cans

The final work done on the as-produced DWI can was a GDOES analysis, shown in figure 7.25. Unfortunately the clarity of the trace is not ideal. However it can be seen that after the initial surface contamination (oxygen, nitrogen and carbon), which occurs in the top 20 nm there is a gradual decrease in tin and a corresponding increase in iron. Tin at the near surface contributes almost 80% of the signal decreasing rapidly to 50% at about 60 nm depth and falling to around 2 % by a depth of 500 nm.

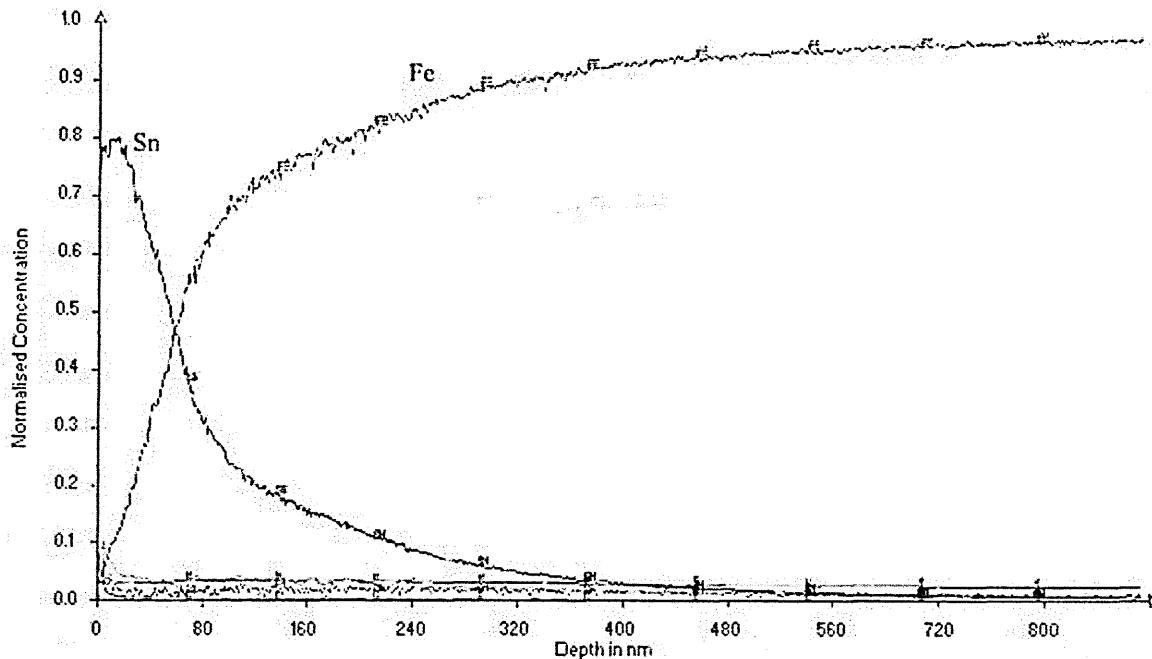


Figure 7.25. GDOES trace of as-produced DWI can.

The rate of decrease then slows with tin still being identified at the maximum depth analysed of 800 nm, though only at very low percentages (<1%). The unevenness of

the substrate will contribute to the gradual decrease in tin rather than a specific cut off depth as the tin inhabits the valleys in the substrate surface.

#### 7.2.5 Summary of Analysis of DWI Tinplated Steel Cans

Thus the as-produced DWI can shows no evidence of intermetallic formation when analysed using CEMS. The tin layer is found to be uneven due to the processing of the can with tin occupying vertical valleys in the steel substrate. These valleys are most likely formed due to the uneven nature of the base sheet steel and the forces on the material during the drawing and ironing phases. From the CEMS analysis (figures 7.4 to 7.7) the tin appears to be more prevalent on the inside of the can wall and is more concentrated at the top of the wall, though SEM analysis proves inconclusive in this respect. X-ray analysis does show some carbon on the sample surfaces at low concentration though only in certain areas. X-ray analysis of the light and dark areas (figures 7.17 and 7.18) indicated that across the can surface there were tin-free areas with exposed steel substrate.  $^{119}\text{Sn}$  Mössbauer analysis shows some  $\text{SnO}_2$  that has formed on the tin. GDOES analysis showed a gradual falloff of tin at the surface and this was attributed to be unevenness of the sample surface with the tin occupying unknown depth valleys in the steel substrate. The tin signal in the GDOES analysis is relatively insignificant below a depth of 500 nm.

### 7.3. Analysis of Etched DWI Tinned Steel Cans

The analysis of the as-produced DWI cans raised the question of whether the material contained any identifiable intermetallics or whether the spectrometer was not sensitive enough to identify any intermetallics that may be present on the DWI cans. A number of samples were etched to remove the tin overlayer in order to analyse any underlying intermetallics more easily.

#### 7.3.1 $^{57}\text{Fe}$ CEMS Analysis of Etched DWI Tinned Steel Cans

To help evaluate the use of this Mössbauer spectrometer, in the analysis of the cans, a batch of samples were etched to remove the tin overlayer. This etching procedure does not remove the intermetallics but removes the  $^{57}\text{Fe}$  Mössbauer inert tin layer which leads to improved signal to noise for any identifiable compounds allowing for easier identification of any intermetallics. The procedure in section 5.3.4 was used, but with an etch time of 90 seconds (originally specified in the Corus plc procedure). The effect of this will be discussed shortly. Spectra obtained from these experiments are shown in figures 7.26 to 7.29. Parameters for these spectra are summarised in table 7.4.

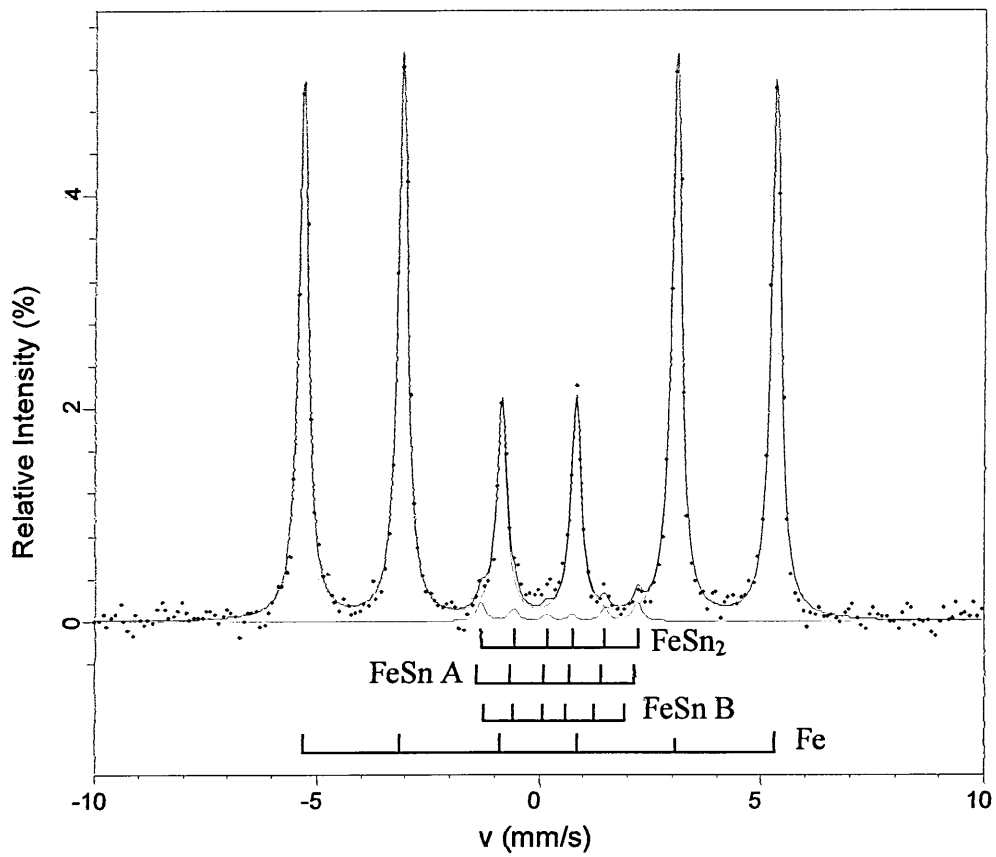


Figure 7.26. Outside top of etched DWI can.

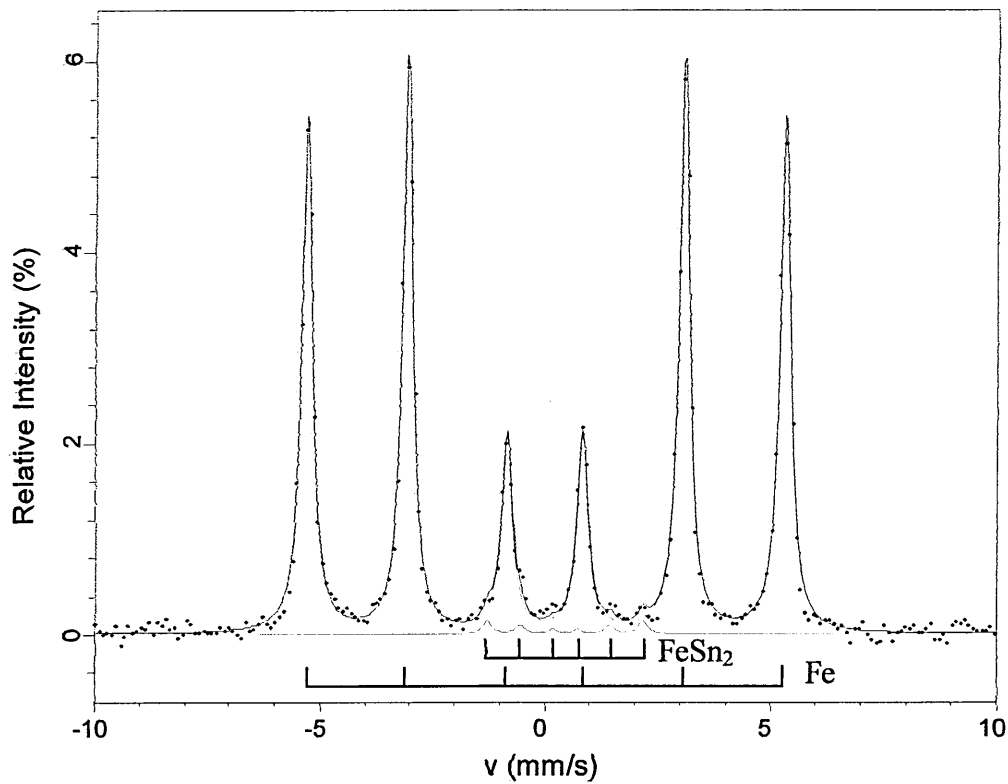


Figure 7.27. Outside bottom of etched DWI can.

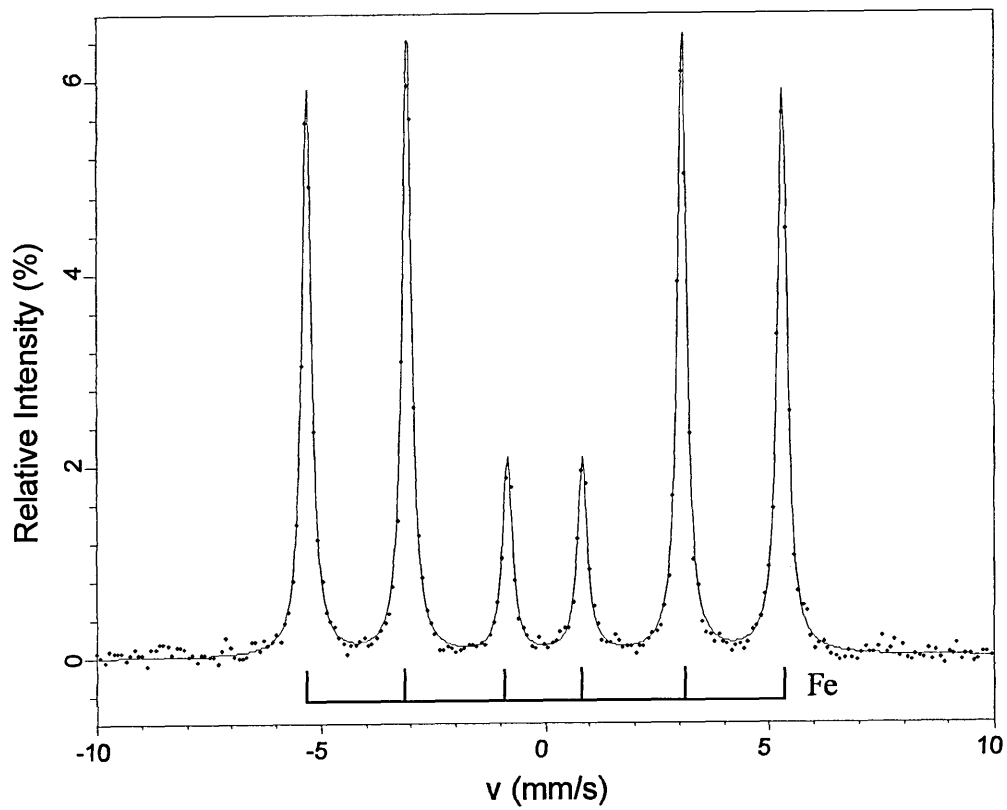


Figure 7.28. Inside bottom of etched DWI can.

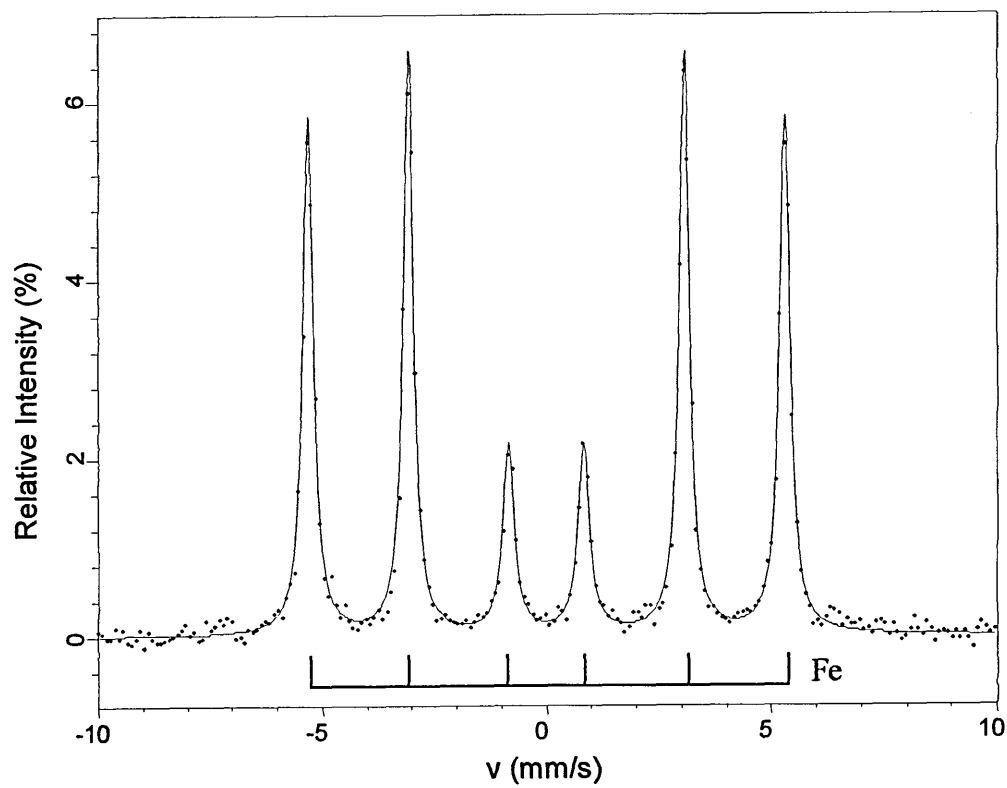


Figure 7.29. Inside top of etched DWI can.

Sample Description	Figure No.	Mössbauer parameters, relative to $\alpha$ -Fe, at 295 K ( $\pm 0.02 \text{ mm s}^{-1}$ )			Magnetic Hyperfine Field ( $\pm 0.2 \text{ T}$ )	Phase Identified	Relative Phase Area %	Peak 2 and 5 Relative Intensity %	$\chi^2$
		$\delta$	$\Delta$	$\Gamma/2$					
Outside top of etched DWI can	7.26	0.00	0.00	0.13	33.0	$\alpha$ -Fe	97.6	5.40	0.708
		0.47	0.00	0.11	10.9	FeSn <sub>2</sub>	2.4	0.10	
Outside bottom of etched DWI can	7.27	0.00	0.00	0.14	32.9	$\alpha$ -Fe	98.3	6.10	0.899
		0.47	0.00	0.11	10.7	FeSn <sub>2</sub>	1.7	0.10	
Inside bottom of etched DWI can	7.28	0.00	0.00	0.13	32.9	$\alpha$ -Fe	100	6.40	1.014
Inside top of etched DWI can	7.29	0.00	0.00	0.14	32.9	$\alpha$ -Fe	100	6.60	0.998

Table 7.4. Parameters for etched can analysis.

These samples provided spectra with greater % effect signals and better signal to noise ratios than found with the unetched samples (table 7.2). Some distortion of the spectra (figures 7.26 and 7.27) shows possible Fe-Sn intermetallics on the outside of the can wall but with such low levels, just above the noise threshold, distinguishing which of the intermetallics are present is difficult. Both FeSn and FeSn<sub>2</sub> could be present at very low levels and are able to fit to the data, with FeSn<sub>2</sub> being slightly preferable (as fitted in the spectra in figures 7.26 and 7.27. Marker bars are shown for both FeSn and FeSn<sub>2</sub> in figure 7.26). The analysis of the inside of the cans shows much less significant distortion and the spectra can only be fitted with parameters for  $\alpha$ -Fe. Thus it is possible that the outside of the can experiences the greater frictional forces inducing heat, which may lead to intermetallic formation.

With the tin removed it was expected that the signals obtained from the etched samples would be very similar to the base steel material. This is the case with the two inside samples (figures 7.28 and 7.29), which have relative intensities for peaks 2 and 5 of 6.4 % and 6.6 % compared to 6.6 % for the sheet steel.

On the outside wall of the etched can samples (figures 7.26 and 7.27), where the intermetallics are observed, there is a significant decrease in the observed peak intensities. The sample with intermetallics from the top of the can (figure 7.26) has the greatest reduction in  $\alpha$ -Fe peak intensity compared to the sheet steel counterpart, shown in figure 7.1. The relative intensity of peaks 2 and 5 for this etched sample is 5.4 % compared to 6.6 % for the sheet steel. The sample with identified intermetallics from the bottom of the can (figure 6.27) has a relative intensity for peaks 2 and 5 of 6.1 % compared to 6.6 % for the sheet steel.

The outside top of the can (figure 7.26) has the greatest amount of identified  $\text{FeSn}_2$ , being 2.4 % of the overall signal. The sample with intermetallics from the bottom of the can (figure 7.27) has only 1.7 %  $\text{FeSn}_2$  identified.

### 7.3.2 $^{119}\text{Sn}$ Mössbauer Analysis of Etched DWI Tinplated Steel Cans

Further analysis using  $^{119}\text{Sn}$  Mössbauer spectroscopy has been carried out and figures 7.30 and 7.31 show two different fits of a single spectrum, generated at 4.2 K using transmission geometry, resulting from the analysis of a sample from the outside top of the etched DWI can wall. Parameters from the analysis are summarised in table 7.5.

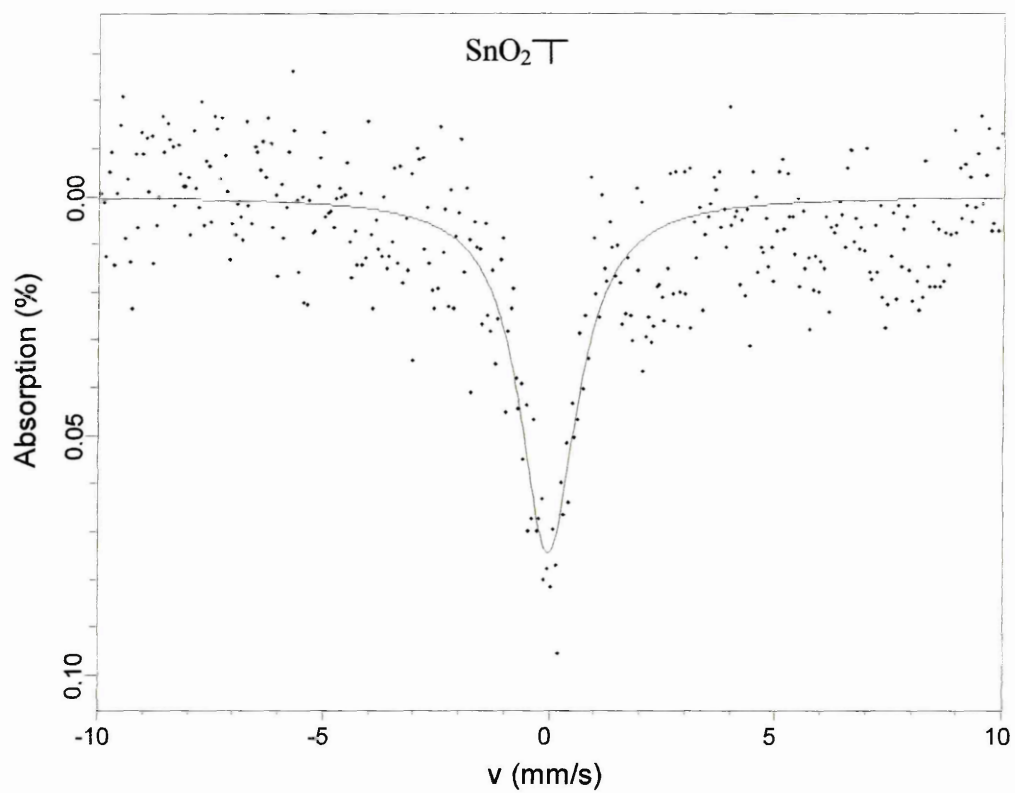


Figure 7.30.  $^{119}\text{Sn}$  analysis of etched DWI can.

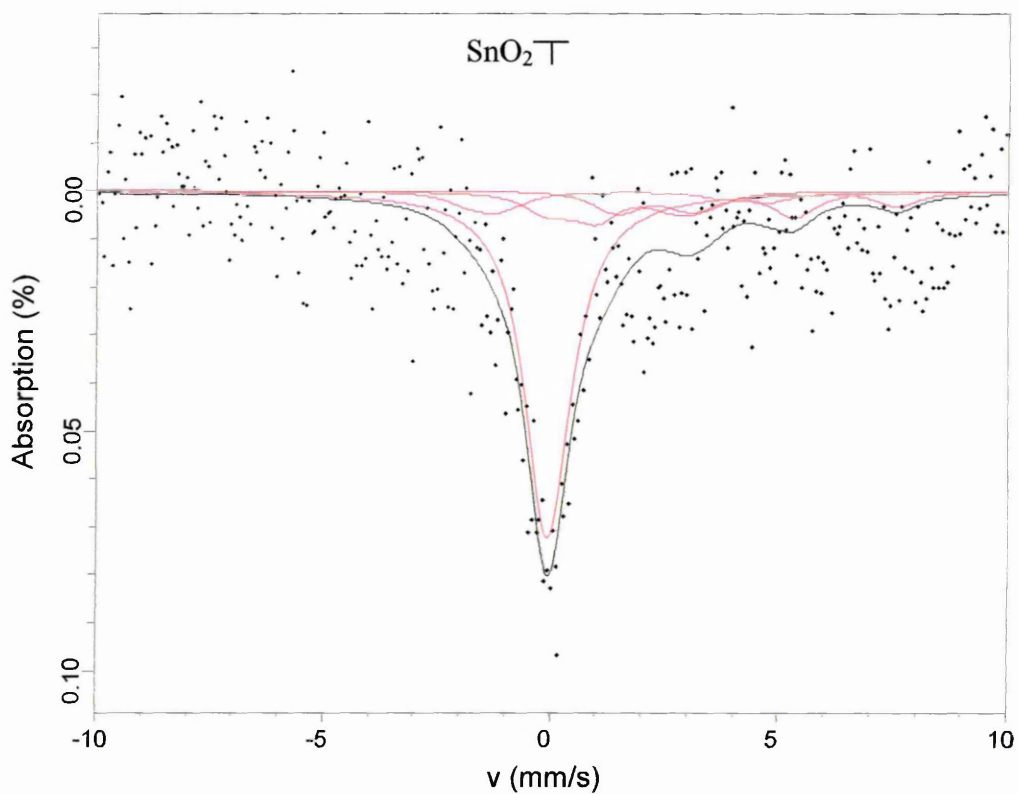


Figure 7.31.  $^{119}\text{Sn}$  analysis of etched DWI can with  $\text{FeSn}_2$  fitted.

Sample Description	Figure No.	Mössbauer parameters, relative to $\alpha$ -Fe, at 295 K ( $\pm 0.02 \text{ mm s}^{-1}$ )			Magnetic Hyperfine Field ( $\pm 0.2 \text{ T}$ )	Phase Identified	Relative Phase Area %	$\chi^2$
		$\delta$	$\Delta$	$\Gamma/2$	H			
$^{119}\text{Sn}$ Etched DWI can	7.30	-0.04	0.00	0.77	0.0	$\text{SnO}_2$	100	1.111
$^{119}\text{Sn}$ Etched DWI can with $\text{FeSn}_2$ fitted	7.31	-0.06	0.00	0.61	0.0	$\text{SnO}_2$	64.8	1.035
		2.30	0.86	0.55	6.7	$\text{FeSn}_2$ (1)	10.2	
		2.30	0.86	0.55	0.4	$\text{FeSn}_2$ (2)	8.1	
		2.30	0.86	0.55	3.3	$\text{FeSn}_2$ (c)	16.9	

Table 7.5. Parameters for  $^{119}\text{Sn}$  analysis of etched DWI can.

The etched DWI can analysed does not show any discernible  $\text{FeSn}_2$  peaks as identified in previous studies of  $\text{FeSn}_2$  [6], visible above the background noise. By fitting low levels of  $\text{FeSn}_2$  with half the peak intensities of the unetched spectra, shown in figure 7.9, the  $\chi^2$  value of the fit can be reduced as seen in figure 7.31. This particular fitting of the data with  $\text{FeSn}_2$  included should be treated with caution, as the level of  $\text{FeSn}_2$  obtained in the fit is not really significant compared to the background noise level.

The etched DWI can contains a similar amount of  $\text{SnO}_2$  to the unetched can, as it is observed on the etched can spectrum with a relative peak intensity of 0.08% compared to 0.11% on the unetched as produced can, thus showing that the oxide is not completely removed during the 90 second etching, which is an unexpected result as it was expected that the  $\text{SnO}_2$  would be formed on the exposed surface of the tin layer and therefore removed prior to removal of the metallic tin during the etching. Metallic tin however seems to be completely absent from the etched spectrum, showing that the etching procedure was highly successful in its removal. Subsequent samples were etched for 2 minutes and were shown later by the use of XRD to not contain any  $\text{SnO}_2$ .

### 7.3.3 SEM Analysis of Etched DWI Tinned Steel Cans

Analysis using SEM reveals further information about the surface of the can wall. The first of these samples, shown in figure 7.32, was taken from the top of the can wall. The second of these samples, shown in figure 7.33, was taken from the bottom of the can wall. Only the outer surfaces of these areas were studied in depth.

Both samples were from a DWI can that had been etched.  $^{119}\text{Sn}$  analysis has shown that the tin is completely removed (see section 7.3.2). SEM BSE images do not show any contrast, as there is no tin on the samples, therefore these images are not included here. On the SEM images there is certainly not the contrast, which was found on the outer surfaces of the as-produced DWI can.

These SE images show the topography of the etched can and clearly show the valleys that had tin embedded in them prior to etching. These valleys generally run in a vertical direction on the can wall and do not follow the grooves created by the rolling of the original sheet steel. This is as expected as the forces involved in the reduction of the wall thickness in the ironing process will dictate the final material topography.

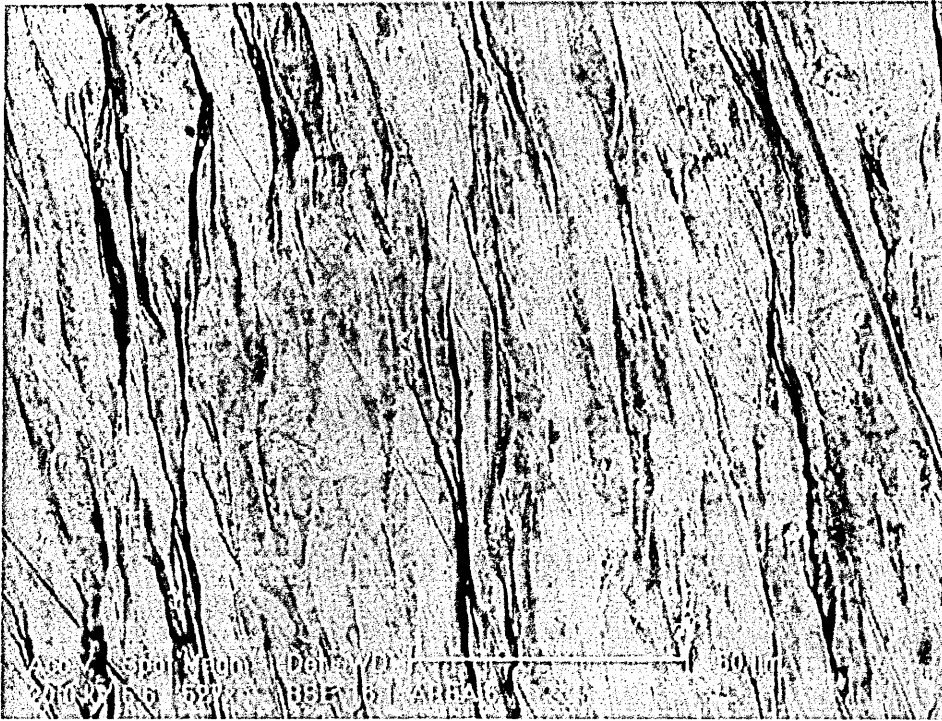


Figure 7.32. High magnification SE image of the outside top of the etched DWI can.

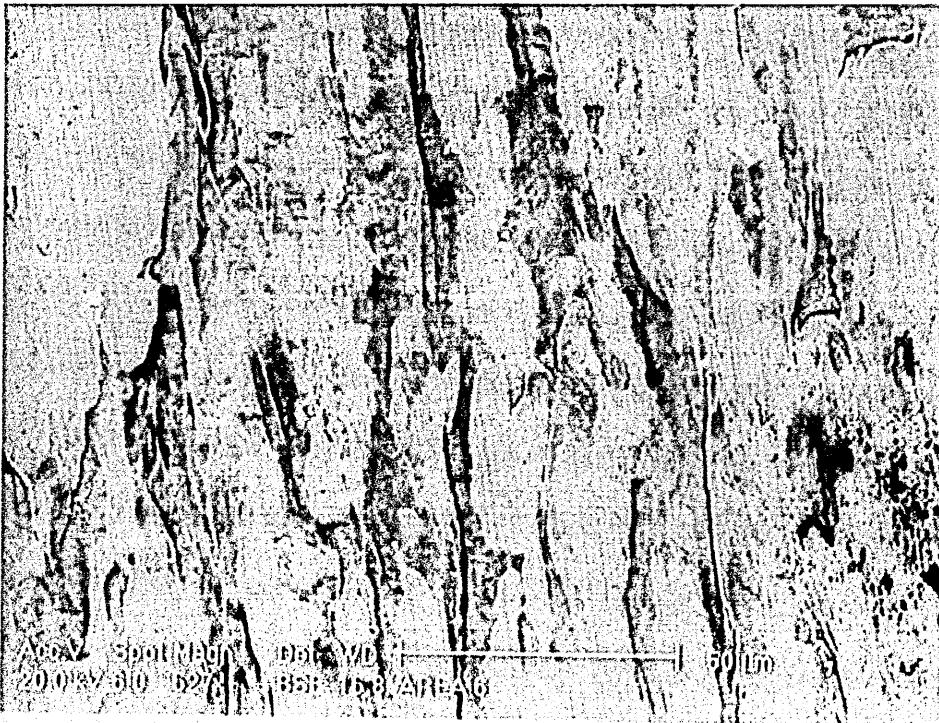


Figure 7.33. High magnification SE image of the outside bottom of the etched DWI can.

#### 7.3.4 Summary of Analysis of Etched DWI Tinplated Steel Cans

Etching the tin overlayer had the effect of revealing slight distortions in the  $^{57}\text{Fe}$  CEMS signals particularly on the outer surfaces of the cans. Such distortions have been fitted and found to be in good agreement with the  $\text{FeSn}_2$  parameters obtained from various literature sources. Analysis using  $^{119}\text{Sn}$  Transmission Mössbauer, of the etched material, only revealed a low level of  $\text{SnO}_2$  because of an inadequate etch, which was subsequently lengthened in time. SEM analysis revealed in further detail the topography of the steel can with vertical valleys formed from the high friction drawing and ironing procedure of the already uneven base material.

#### 7.4. Results of Analysis of Can Bases

The DWI can processing procedure causes high frictional forces on the can wall from which it is possible that temperatures reached coupled with the mechanical forces involved has lead to the formation of intermetallics as can be seen from the analysis of the etched DWI can wall in section 7.3. The can bases are not drawn and ironed, as the wall of the can is, but do undergo some mechanical working when compressed during bottom forming and so analysis of the can bases gives an indication of whether these compressive forces can influence intermetallic formation.

### 7.4.1 $^{57}\text{Fe}$ CEMS Analysis of DWI Tinplated Steel Can Bases

Both as-produced and etched can bases were analysed using  $^{57}\text{Fe}$  CEMS, the resultant spectra of which are shown in figures 7.34 and 7.35. The outsides of the can ends have been analysed. Parameters for the spectrum of a typical can base sample are summarised in table 7.6.

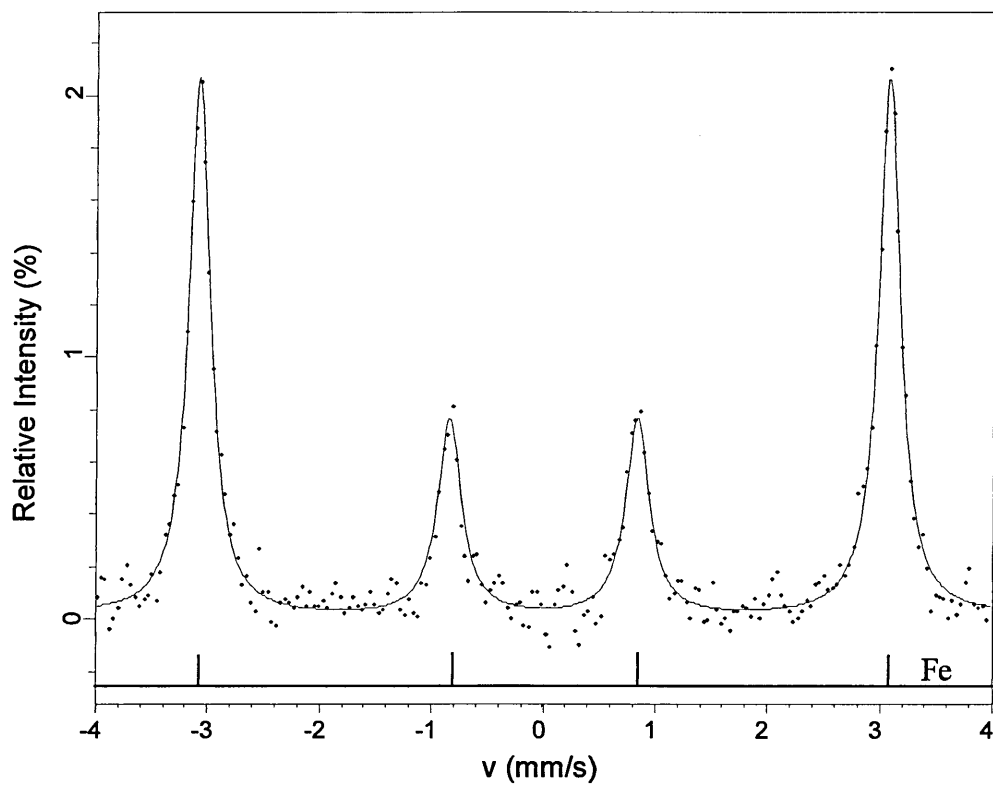


Figure 7.34. As-produced DWI can base.

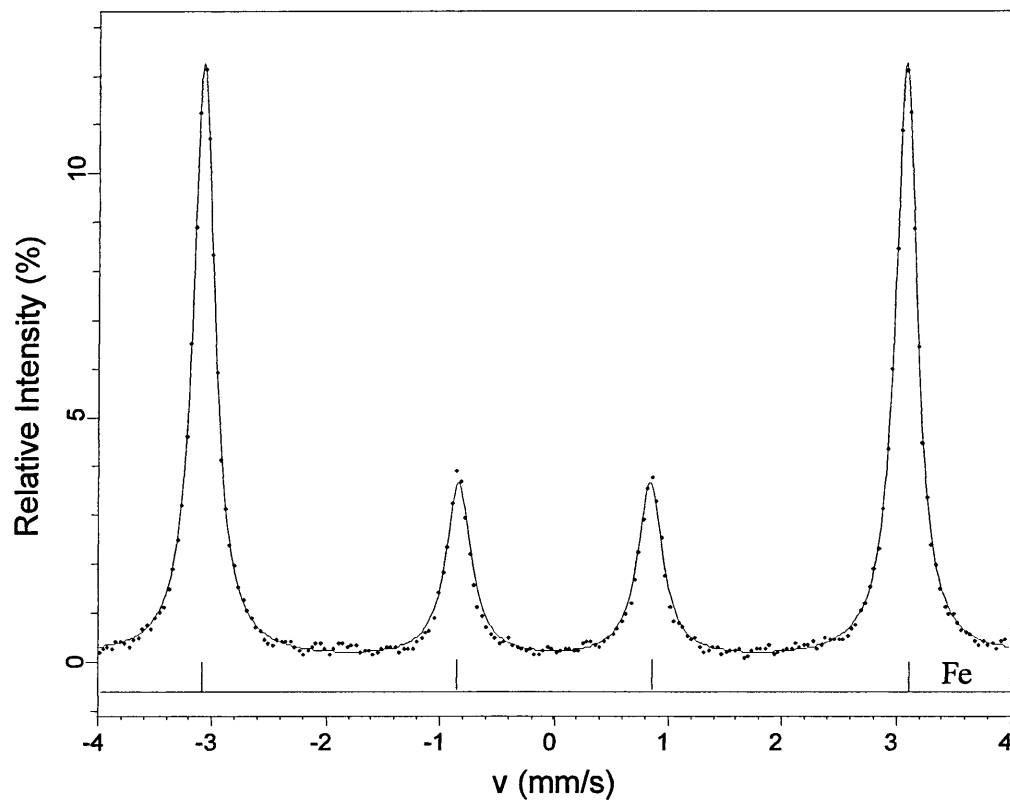


Figure 7.35. Etched DWI can base.

Sample Description	Figure No.	Mössbauer parameters, relative to $\alpha$ -Fe, at 295 K ( $\pm 0.02 \text{ mm s}^{-1}$ )			Magnetic Hyperfine Field ( $\pm 0.2 \text{ T}$ )	Phase Identified	Relative Phase Area %	Peak 2 and 5 Relative Intensity %	$\chi^2$
		$\delta$	$\Delta$	$\Gamma/2$	H				
As-produced DWI can base	7.34	0.00	0.00	0.12	33.0	$\alpha$ -Fe	100	2.05	0.620
Etched DWI can base	7.35	0.00	0.00	0.12	33.0	$\alpha$ -Fe	100	12.20	0.945

Table 7.6. Parameters for analysis of can base.

Samples prior to etching have noisy signals due to the amount of tin present on the samples. It is worth noting that the tin coating is not sufficient to stop the identification of the substrate. By etching away the tin layer, the signals obtained from these can base

samples can be fitted more accurately and gives the possibility of identifying any intermetallics present. However there is no evidence of intermetallics on the can bases even when etched.

It was expected that the can wall would be exposed to the greatest forces and heat production during processing and this is reflected in the detection of intermetallics on the can wall and their absence on the can bases.

#### 7.4.2 SEM Analysis of DWI Tinplated Steel Can Bases

Analysis of the as-produced DWI can ends using SEM shows the topography resulting from can end processing compared to can wall processing. Figure 7.36 shows a 250× magnification SE image of the base of a typical DWI can.

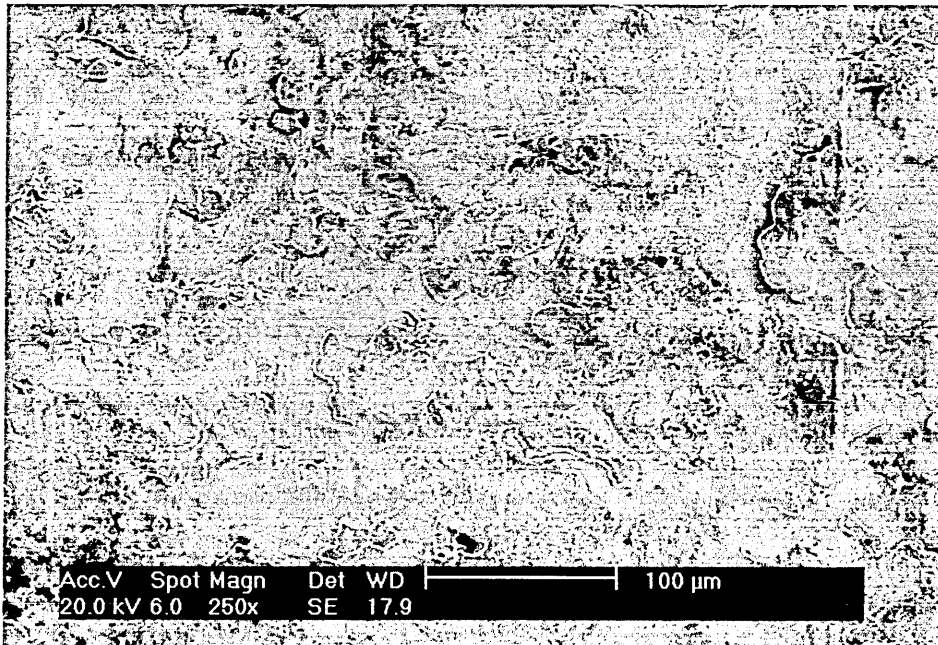


Figure 7.36. SE image of a typical DWI can base.

Closer inspection of the can base with the SEM, figure 7.37, shows the surface to be more homogeneously covered with tin compared to the can walls. Figure 7.38 shows an X-ray analysis of the sample surface shown in figure 7.37. This trace is typical of those found on the whole can base. BSE imaging results in fairly uniform tin distribution as shown in figure 7.39.

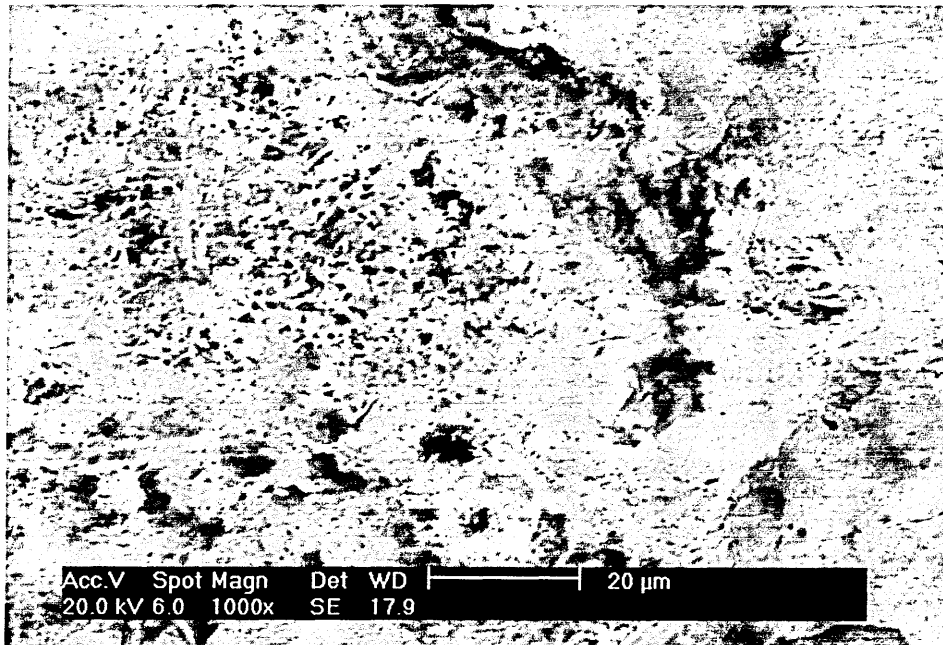


Figure 7.37. High magnification SE image of a typical DWI can base.

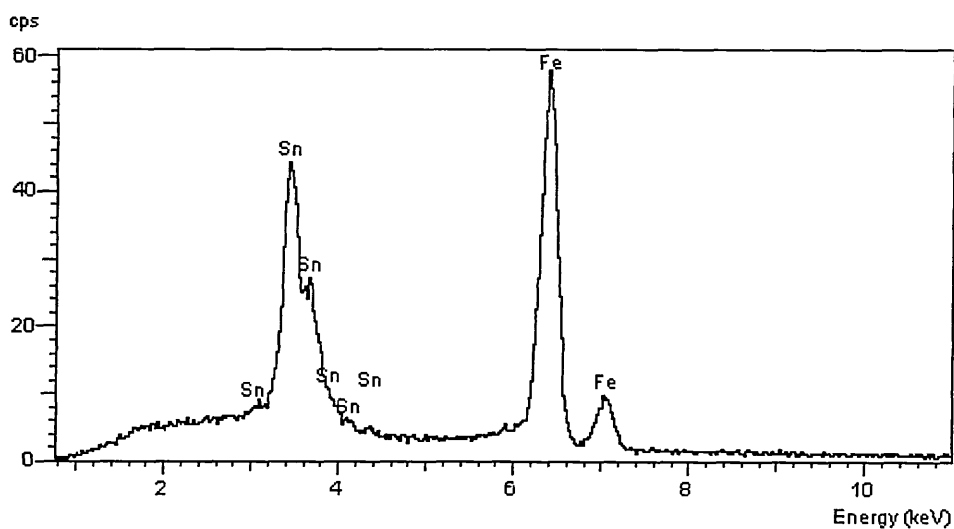


Figure 7.38. EDX analysis of can base shown in figure 7.37.

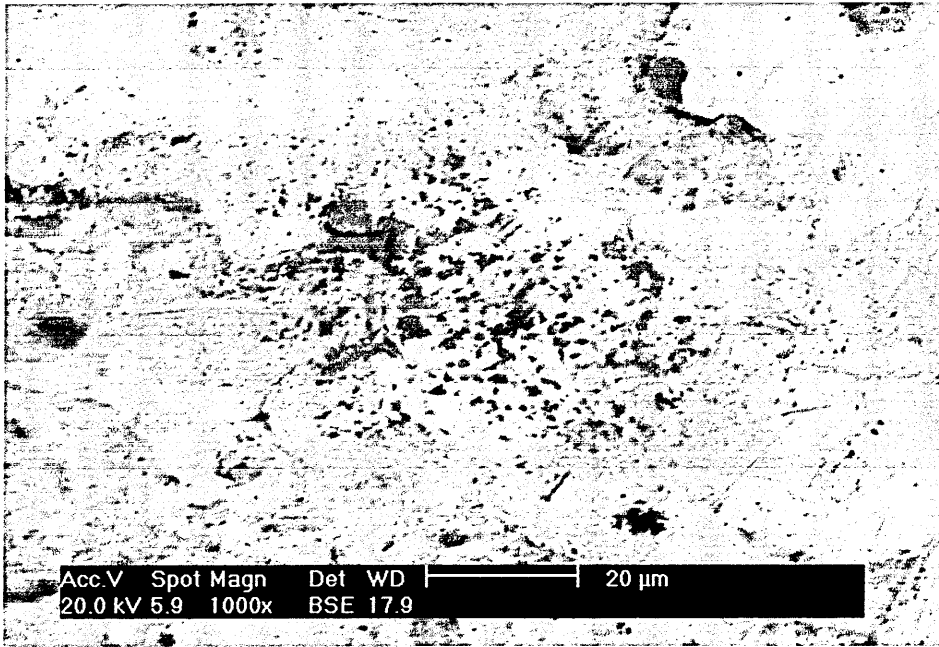


Figure 7.39. High magnification BSE image of a typical DWI can base.

These SEM images do not show the grooved surfaces found on the can wall, which is an expected result as the major force used to form the can bases is compressive and not one which would deform the material in such a way to form the surface striations. The tin is observed as islands covering most of the can base, some dark areas are observed on the BSE image, figure 7.39, and there are some obvious holes shown on the SE image. Over the whole surface of the can base similar X-ray analysis results were obtained, this result was repeated when taking the X-ray spectrum from the low magnification image area shown in figure 7.36. The dark “sputtered” areas observable on both images of the can base shown at high magnification were unable to be identified as no other element was present in the X-ray analysis. It is presumed that this is some surface marking from the bottom forming process but is too insubstantial to be identified beyond the background signal.

### 7.4.3 Summary of Analysis of DWI Tinned Steel Can Bases

The can bases are observed to have a more uniform tin coating which is much thicker than that found on the can walls, which is expected as the can base does not have such an overall reduction in thickness. There is also no evidence of intermetallics on these DWI can base samples, giving further indication that the intermetallic signal observed at low levels on the can walls is due to the drawing and ironing of the material.

### 7.5. Preliminary Analysis of Flowbrightened Tinplate

It was evident, from the work on etched samples of the DWI can wall, that the amount of intermetallics on the DWI tinned steel cans was very small. In order to analyse the hyperfine parameters of some possible intermetallics present on commercially produced tinplate, samples of flowbrightened tinplate were obtained from Corus plc. and analysed both in the as-produced (figure 7.40) and etched (figure 7.41) states. Parameters for these spectra are summarised in table 7.7.

Sample Description	Figure No.	Mössbauer parameters, relative to $\alpha$ -Fe, at 295 K ( $\pm 0.02 \text{ mm s}^{-1}$ )			Magnetic Hyperfine Field ( $\pm 0.2 \text{ T}$ )	Phase Identified	Relative Phase Area %	Peak 2 and 5 Relative Intensity %	$\chi^2$
		$\delta$	$\Delta$	$\Gamma/2$	H				
As-produced flowbrightened tinplate	7.40	0.00	0.00	0.13	33.0	$\alpha$ -Fe	84.4	1.00	0.664
		0.54	0.00	0.16	10.9	FeSn <sub>2</sub>	15.6	0.12	
Etched flowbrightened tinplate	7.41	0.00	0.00	0.12	33.0	$\alpha$ -Fe	82.1	2.95	0.619
		0.49	0.00	0.16	10.9	FeSn <sub>2</sub>	17.9	0.40	

Table 7.7. Parameters for flowbrightened tinplate.

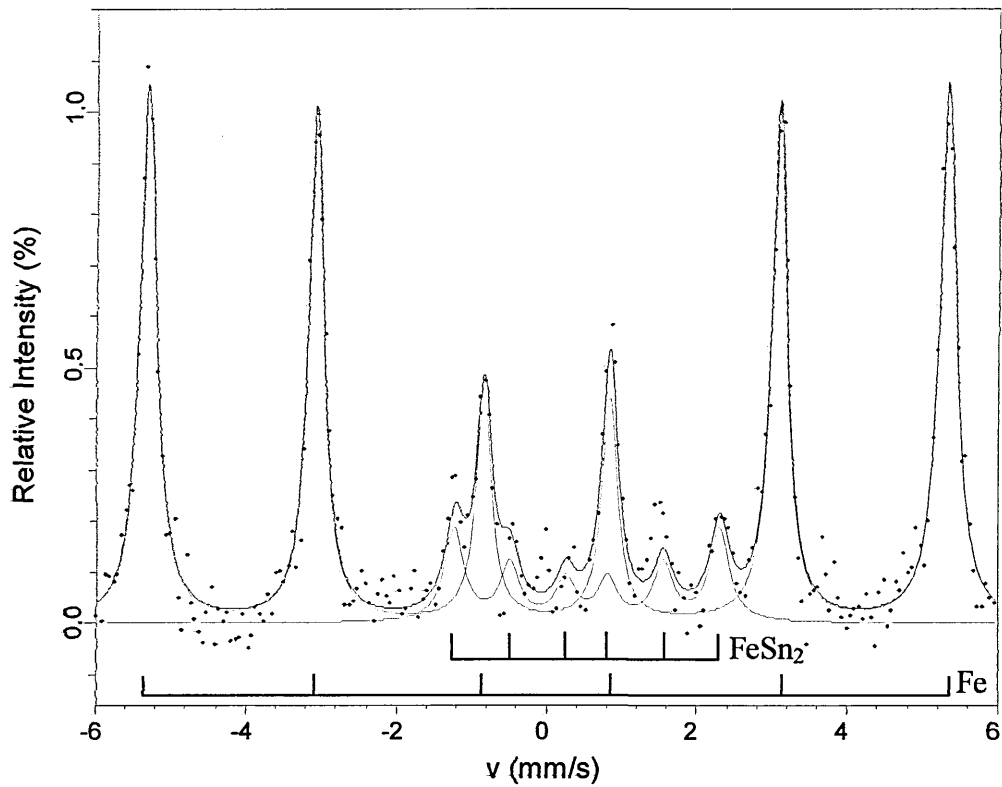


Figure 7.40. As-produced flowbrightened tinplate.

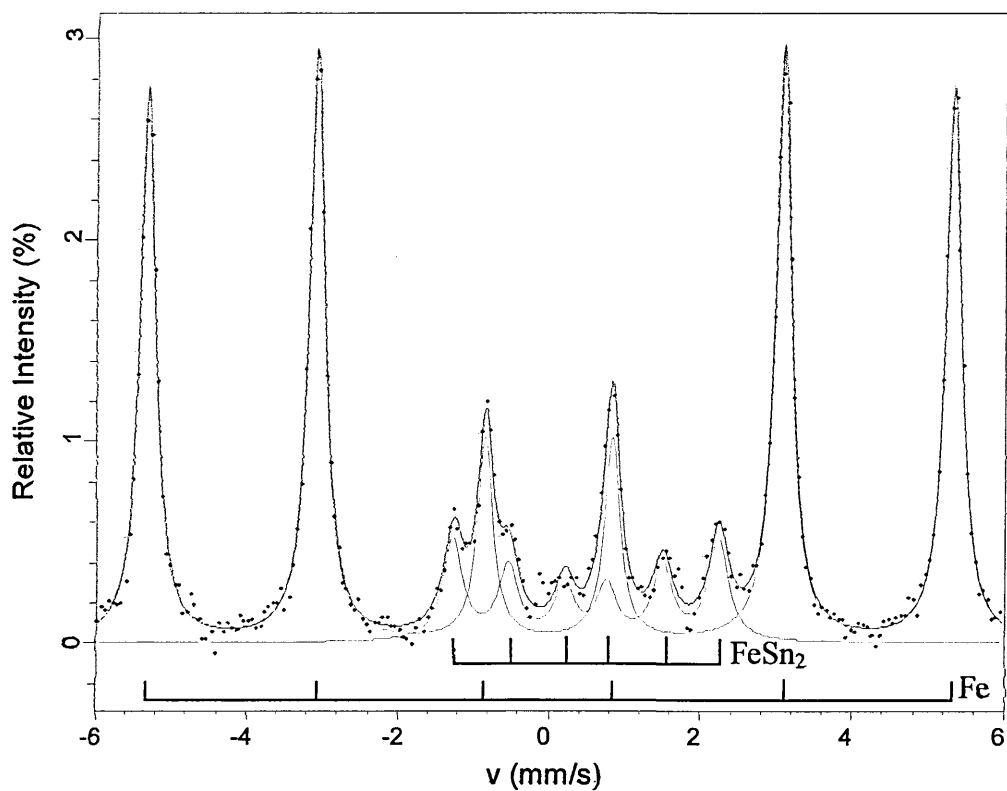


Figure 7.41. Etched flowbrightened tinplate.

From the resulting spectra it is clearly evident that there is at least one additional sextet signal with a significantly lower field than the  $\alpha$ -Fe. Fitting with free parameters for the Mössbauer hyperfine parameters produced the results as shown in table 7.7. The parameters obtained were most closely related to those of FeSn<sub>2</sub> [6,7,8,9]. These tinplate samples had undergone the flowbrightening process whereby the tin, once deposited on the steel substrate, is reflowed over the steel surface. This involves temperatures that are high enough to melt the tin coating and promote intermetallic growth.

Before etching, the signal from the tinplate is low but is still able to be fitted using the Recoil software program. Identified in the spectrum are an  $\alpha$ -Fe component and an FeSn<sub>2</sub> component. After etching the signals became more evident as noise in the spectrum was significantly reduced.

This commercially produced flowbrightened tinplate material shows clear evidence of FeSn<sub>2</sub>. DWI cans for the beverage industry are however made from matte tinplate (i.e. non-flowbrightened) and so intermetallics would have to be formed by the heat and pressure induced in the press during drawing and wall ironing. Matte tinplate is analysed and compared to flowbrightened tinplate in section 7.9.

## **7.6. Preliminary Heat Treatment Studies**

To look at the effect of heat applied to the DWI tinplated steel cans a number of samples were heat-treated in the basic system shown in figure 7.42. Two samples were

taken from the top of a can wall and two from the bottom of the can wall. A flow of nitrogen over the samples during the heating was used to help prevent oxidation of the samples. The hotplate was heated to approximately 240 °C and the samples were exposed to the elevated temperature for 10 minutes.

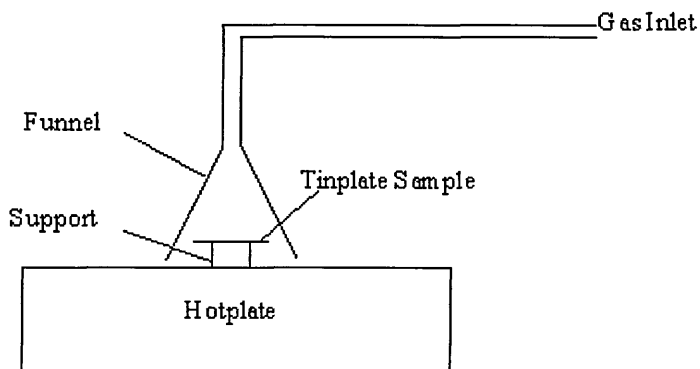


Figure 7.42. Basic heat-treatment system.

The first two samples, one from the top of the can wall and one from the bottom of the can wall, were annealed while in direct contact with the hotplate. The samples turned blue after this process.

### 7.6.1 $^{57}\text{Fe}$ CEMS Analysis of Heat-Treated DWI Tinplated Steel Cans

Subsequent fitting of the Mössbauer experimental data showed evidence of at least a third sextet with a higher field, probably due to the presence of oxides formed during annealing. The Mössbauer spectrum of the first sample, which was taken from the top of the can wall and is shown in figure 7.43, fitted to an  $\alpha\text{-Fe}$  phase, a  $\text{FeSn}_2$  phase and a third phase, X, with  $H = 51.3 \pm 0.2$  T and  $\delta = 0.48 \pm 0.02$  mm s<sup>-1</sup>. The second sample, taken from the bottom of the can wall but not shown here, was almost

identical, with the Mössbauer spectrum fitting to an  $\alpha$ -Fe phase, a  $\text{FeSn}_2$  phase and a third phase, X, with  $H = 50.8 \pm 0.2$  T and  $\delta = 0.49 \pm 0.02$   $\text{mm s}^{-1}$ . This third phase is assumed to be the same as the third phase on the first sample. Though this third unknown phase has a field corresponding to  $\alpha$ - $\text{Fe}_2\text{O}_3$  the centre shifts obtained whilst fitting are found to be  $0.1$   $\text{mm s}^{-1}$  greater than for that oxide phase at 300 K [10]. Although a small proportion of this difference may be attributed to differences in temperature, it is possible that a second oxide phase, likely to be  $\text{Fe}_3\text{O}_4$ , may be present as fitted in figure 7.44 for the first sample, this corrects most of the shift. The same results for the fitting of the second sample were found. These two samples are likely to have been heated to the same temperature as the hotplate ( $240$   $^\circ\text{C}$ ) and also been exposed to air in the heating arrangement which has led to these oxides being formed.

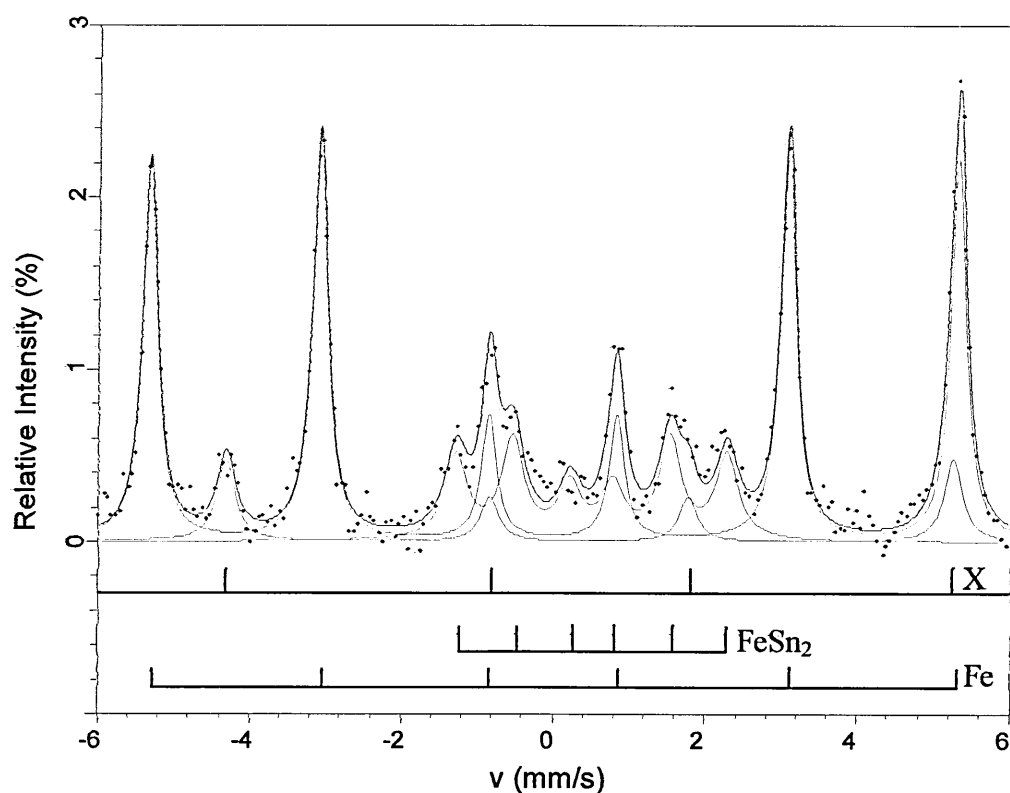


Figure 7.43. Outside top of heat-treated DWI can.

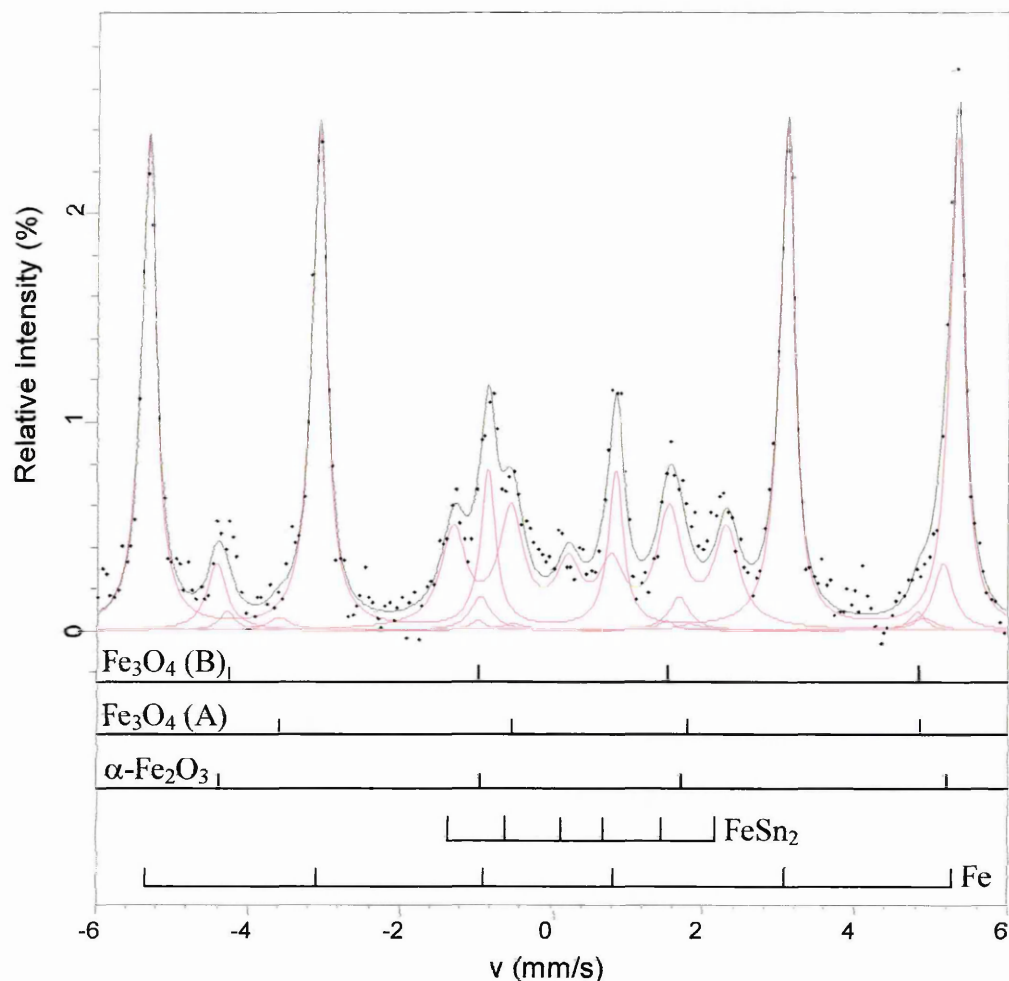


Figure 7.44. Outside top of heat-treated DWI can fitted with multiple oxides.

The third and fourth selected areas were heat treated while mounted on a glass support within the heating arrangement and no colour changes were observed. The third sample was from the top of the can wall and the fourth from the bottom of the can wall. These samples were then etched to provide clearer signals. The resulting Mössbauer experimental data provided at least two sextets, which have been successfully fitted with  $\alpha$ -Fe and FeSn<sub>2</sub> values (figure 7.45 for the third sample and figure 7.46 for the fourth sample). These DWI can sections are likely to have been heated to a lower temperature than the first two samples as there was no direct contact with the hotplate. This is reflected in the lower level of intermetallics formed.

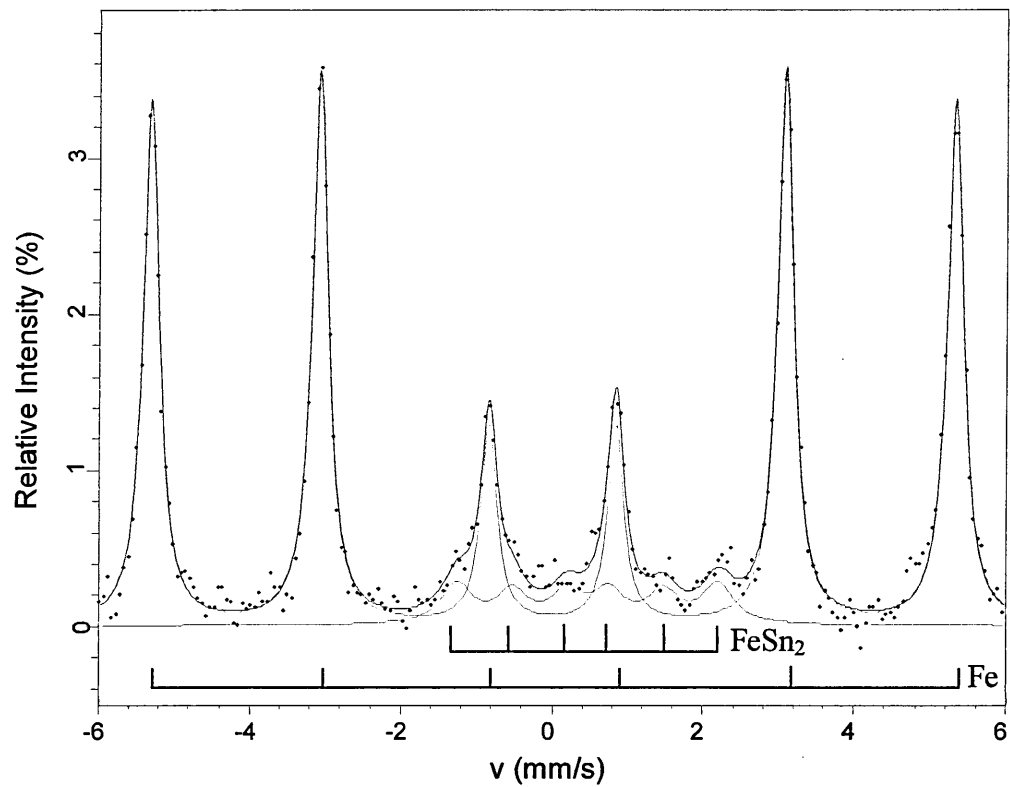


Figure 7.45. Outside top of heat-treated and etched DWI can.

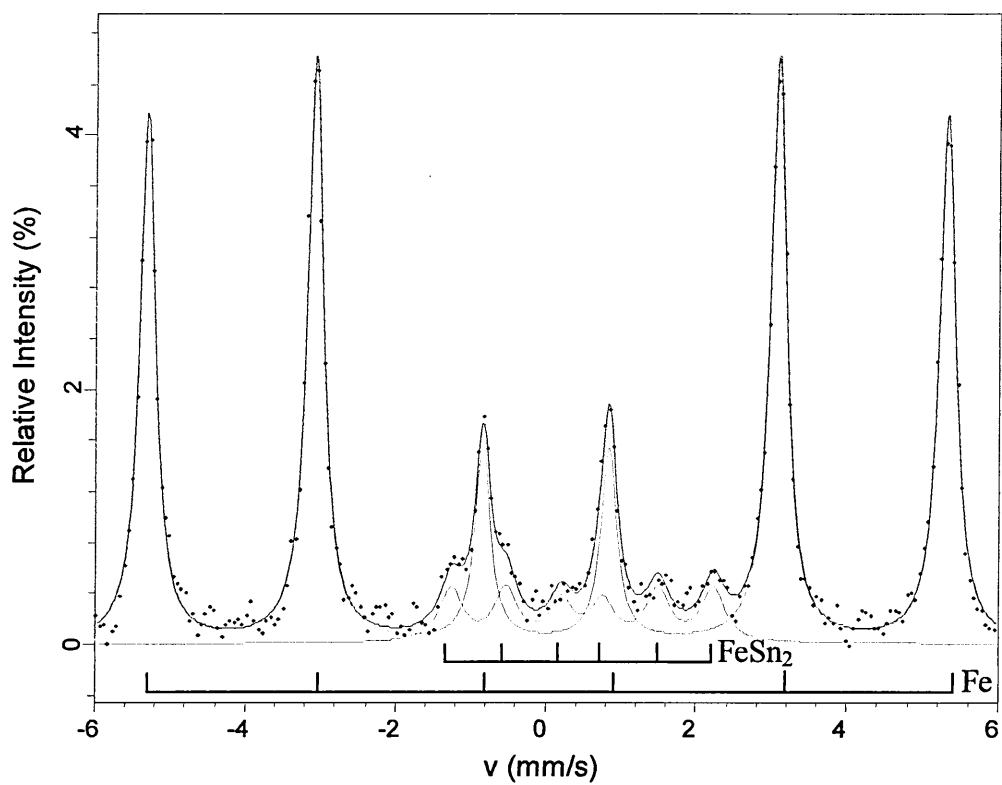


Figure 7.46. Outside bottom of heat treated and etched DWI can.

The samples would also have been exposed to less air than the previously heated samples due to them being in closer proximity to the jet of nitrogen in the funnel of the heating arrangement thus no significant oxidation occurred.

The fourth heat-treated DWI sample was then analysed using transmission  $^{57}\text{Fe}$  Mössbauer spectroscopy, the resulting spectrum is shown in figure 7.47. This shows the same area analysed as in figure 7.46, however the intermetallic signal identified using  $^{57}\text{Fe}$  CEMS was not identified because the bulk is analysed when using the transmission geometry to detect  $\gamma$ -ray absorption rather than the surface when using CEMS. Only an  $\alpha$ -Fe signal,  $H = 32.97 \pm 0.2 \text{ T}$ ,  $\delta = 0.00 \pm 0.02 \text{ mm s}^{-1}$  is observed.

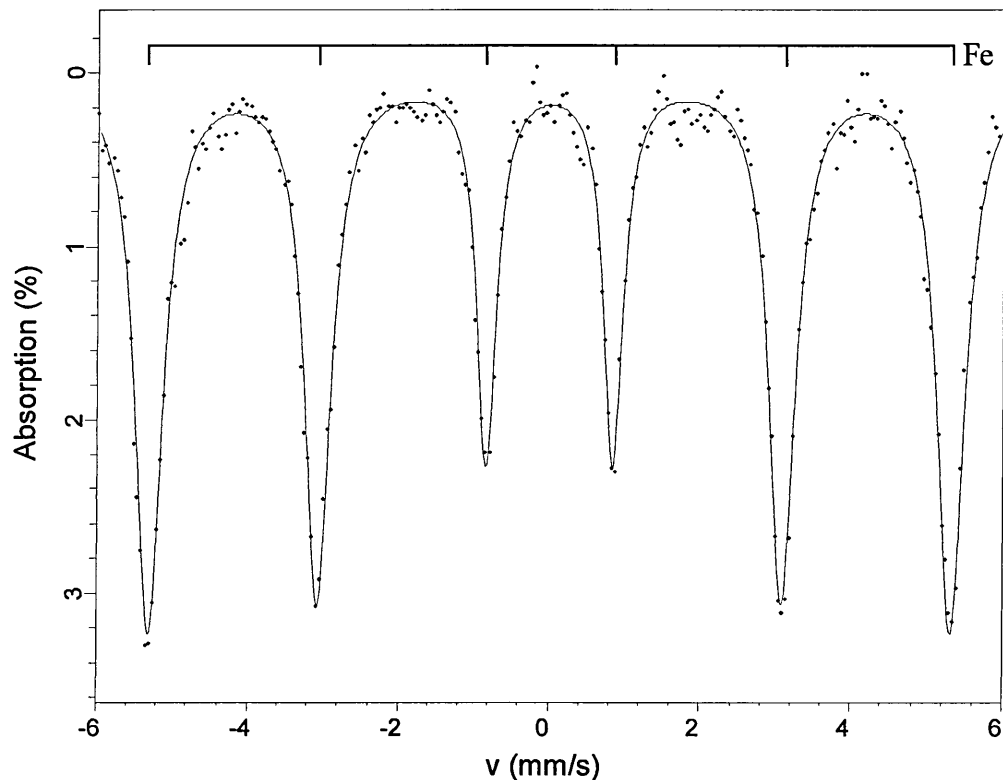


Figure 7.47. Transmission spectra of outside bottom of heat-treated and etched DWI can.

Thus, since transmission experiments are not surface sensitive, whereas CEMS experiments are, transmission studies are shown to be of little use in this study of the intermetallics on the sample surfaces. Parameters for these spectra of the heat-treated samples are summarised in table 7.8.

Sample Description	Figure No.	Mössbauer parameters, relative to $\alpha$ -Fe, at 295 K ( $\pm 0.02 \text{ mm s}^{-1}$ )			Magnetic Hyperfine Field ( $\pm 0.2 \text{ T}$ )	Phase Identified	Relative Phase Area %	Peak 2 and 5 Relative Intensity %	$\chi^2$
		$\delta$	$\Delta$	$\Gamma/2$	H				
Outside top of heat-treated DWI can (blue colouration - one unknown component fitted)	7.43	0.00	0.00	0.12	33.0	$\alpha$ -Fe	52.6	2.40	0.615
		0.50	0.00	0.18	11.1	FeSn <sub>2</sub>	20.0	0.65	
		0.48	0.00	0.14	51.3	Unknown	27.4	0.50	
Outside top of heat-treated DWI can (blue colouration - three oxides fitted)	7.44	0.00	0.00	0.12	33.0	$\alpha$ -Fe	57.9	2.45	0.715
		0.50	0.00	0.20	11.1	FeSn <sub>2</sub>	22.8	0.50	
		0.37	0.00	0.16	51.3	$\alpha$ -Fe <sub>2</sub> O <sub>3</sub>	13.5	0.32	
		0.66	0.00	0.17	45.5	Fe <sub>3</sub> O <sub>4</sub> (A)	2.7	0.04	
		0.27	0.00	0.12	48.7	Fe <sub>3</sub> O <sub>4</sub> (B)	3.1	0.05	
Outside top of heat-treated and etched DWI can	7.45	0.00	0.00	0.13	33.0	$\alpha$ -Fe	86.6	3.60	0.671
		0.47	0.00	0.25	10.7	FeSn <sub>2</sub>	13.4	0.25	
Outside bottom of heat treated and etched DWI can	7.46	0.00	0.00	0.13	33.0	$\alpha$ -Fe	86.0	4.60	0.654
		0.49	0.00	0.19	10.8	FeSn <sub>2</sub>	14.0	0.40	
Outside top of heat-treated and etched DWI can (transmission)	7.47	0.00	0.00	0.16	33.0	$\alpha$ -Fe	100	3.10	0.586

Table 7.8. Parameters for preliminary heat treated can analysis.

Heat-treatment of the DWI tinplate causes the formation of more Fe-Sn intermetallics and with subsequent etching of these samples the signals obtained from the CEMS analysis clearly show the sextet of the FeSn<sub>2</sub> intermetallics. These samples were able to

be fitted using  $\text{FeSn}_2$  parameters showing that the flowbrightening process and simple heat treatment processes under nitrogen atmosphere carried out here lead to the formation of the same intermetallic phase. These preliminary heat treatment studies led to the more in depth analysis of temperature dependence of intermetallic formation in section 7.11.

#### 7.6.2 XRD Analysis of Heat-Treated DWI Tinplated Steel Cans

XRD was used to analyse the crystallographic structure of the DWI can wall that was taken from the top of the can wall, heat-treated and the etched, as shown in figure 7.45. Three different X-ray diffraction traces were taken of the same sample with different angles of incidence for the X-ray beam. Using the X-ray diffractometer with Bragg-Brentano geometry the diffraction trace in figure 7.48 was obtained. The peak fitting data is shown in tables 7.9, 7.10 and 7.11. The intensities of the peaks relative to the largest peak in the sample are given for each peak as 'RI %'. For simplicity of comparison to the standard data, compounds or elements not containing the largest peak in the trace are also given 'adjusted RI %' figures in the table, which are the relative intensities of each peak to the largest peak of that compound or element.

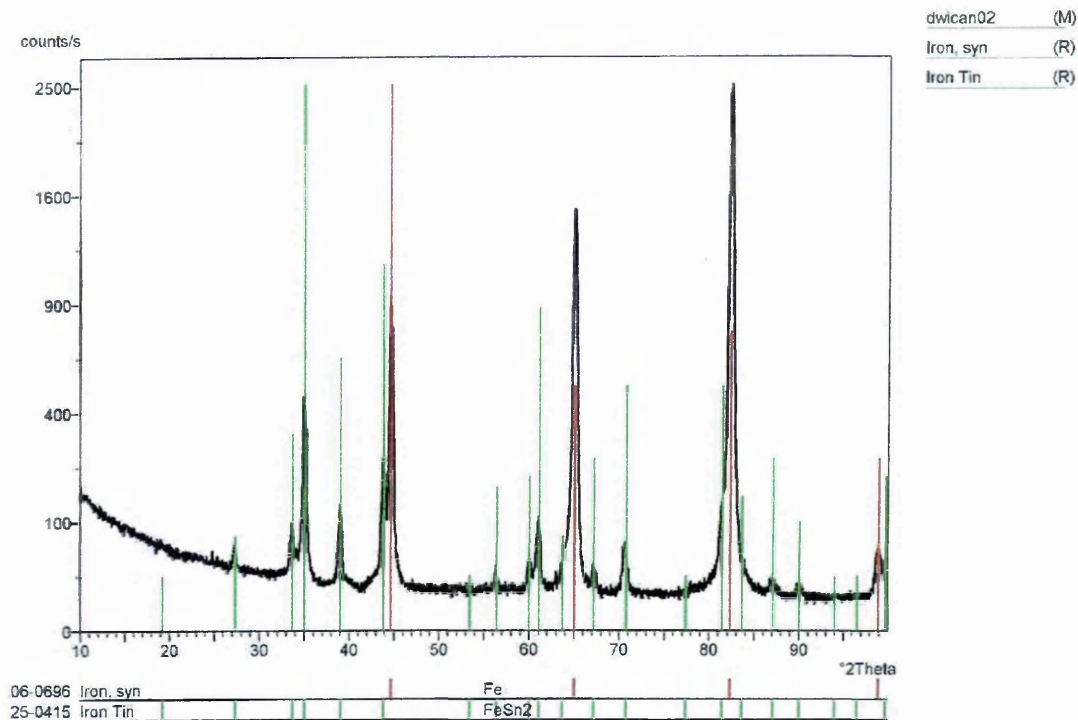


Figure 7.48. Diffraction trace of DWI can obtained using Bragg-Brentano geometry.

There are eight of the  $\text{FeSn}_2$  peaks missing from the sample data (table 7.9), a number of which are listed as having relative intensities of 1 or less in the standard and so these can easily be lost in noise, this is the case with 5 of these peaks. Two peaks, with relative intensities of 3 and 6 in the standard are unidentified due to their close proximity to strong Fe peaks which have made identification of the much weaker  $\text{FeSn}_2$  peaks more difficult for the software. The last peak is unidentified both due to its close proximity to an Fe peak and the cut off  $2\theta$  angle. The adjusted relative intensities are useful for comparisons to the relevant standard. The trace relative intensity is the data as given for the whole trace encompassing all identified compounds.

FeSn <sub>2</sub> Standard				Sample				
d / Å	2θ / °	RI %	h k l	d / Å	2θ / °	RI %	Adjusted RI %	d Diff. / Å
4.610	19.2365	1	1 1 0					
3.260	27.3333	3	2 0 0	3.2747	27.2083	1	5.5	0.0147
2.656	33.7164	13	0 0 2	2.6663	33.5822	3	16.5	0.0103
2.556	35.0774	100	2 1 1	2.5688	34.8970	18.2	100.0	0.0128
2.304	39.0612	25	1 1 2	2.3113	38.9328	4.8	26.4	0.0073
2.063	43.8465	45	2 0 2	2.0679	43.7372	9.2	50.5	0.0049
1.713	53.4424	<1	3 2 1					
1.629	56.4371	7	3 1 2	1.6331	56.2828	0.6	3.3	0.0041
1.540	60.0215	8	3 3 0	1.5401	60.0172	1	5.5	0.0001
1.515	61.1167	35	2 1 3	1.5183	60.9697	3.6	19.8	0.0033
1.460	63.6826	3	4 2 0					
1.392	67.1930	10	4 0 2	1.3932	67.1274	0.7	3.8	0.0012
1.330	70.7795	20	0 0 4	1.332	70.6573	2.2	12.1	0.002
1.232	77.3942	1	2 0 4					
1.181	81.4156	20	4 1 3	1.1824	81.2989	4.2	23.1	0.0014
1.155	83.6539	6	5 1 2					
1.118	87.0947	10	3 1 4	1.1186	87.0362	0.5	2.7	0.0006
1.089	90.0314	4	6 0 0	1.0887	90.0630	0.3	1.6	-0.0003
1.053	94.0215	<1	4 3 3					
1.032	96.5532	1	4 0 4					
1.0073	99.7549	8	3 3 4					

Table 7.9. Peak fitting data for FeSn<sub>2</sub>.

A surprising result is that no tin oxide is observed which is contrary to the result obtained from <sup>119</sup>Sn Mössbauer spectroscopy analysis in section 7.3 where the SnO<sub>2</sub> was not entirely removed. In fact none of the subsequent analysis by the XRD technique provided any evidence of SnO<sub>2</sub> in any etched sample and so it can only be assumed that the etch of the can sample analysed using <sup>119</sup>Sn Mössbauer spectroscopy as shown in section 7.3 was incomplete in some way leaving the tin oxide present.

Fe Standard				Sample			
d / Å	2θ / °	RI %	h k l	d / Å	2θ / °	RI %	d Diff. / Å
2.0268	44.6714	100	1 1 0	2.0317	44.5579	37.2	0.0049
1.4332	65.0182	20	2 0 0	1.4338	64.9877	60.4	0.0006
1.1702	82.3286	30	2 1 1	1.17	82.3458	100	-0.0002
1.0134	98.9399	10	2 2 0	1.0148	98.7552	1.7	0.0014

Table 7.10. Peak fitting data for Fe.

The Fe is identified fully in this sample with all four peaks clearly visible in the trace (table 7.10). Comparing to the standard data the relative intensities do not follow the trend associated with Fe. The diffraction from the (211) plane is the strongest in this instance as compared to the strongest in the standard, which is the (110) plane.

Sample Unidentified Peaks			
Peak no.	d / Å	2θ / °	RI %
1	2.5507	35.1526	12.9
2	1.5889	57.9947	0.1
3	1.3348	70.4870	1.9
4	1.1724	82.1408	92.1

Table 7.11. Sample unidentified peaks.

There at first appear to be four unidentified peaks in this trace as shown in table 7.11, but they are either noise or have arisen because of the APD software fitting a number of narrow peaks to what is in effect a single broader peak. The latter is due to the peaks being not entirely symmetrical and this is the case with peaks numbered 1 and 3, which are part of FeSn<sub>2</sub> peaks and peak 4, which is part of an Fe peak. Peak 2 is of low intensity and is considered to be noise. The relative intensities given for these unidentified peaks are relative to the strongest peak in the trace.

Using the X-ray diffractometer with glancing angle geometry, with an angle of incidence of the X-ray beam of  $5^\circ$ , the diffraction trace in figure 7.49 was obtained. The peak fitting data is shown in tables 7.12, 7.13 and 7.14.

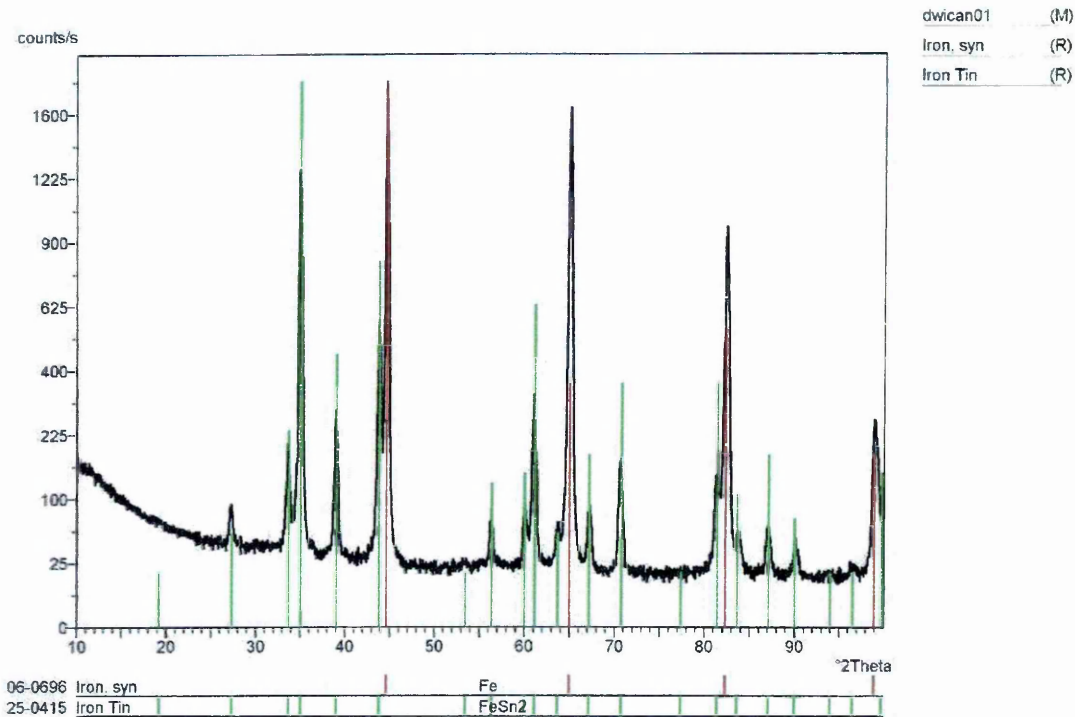


Figure 7.49. Diffraction trace of DWI can obtained using glancing angle geometry at  $5^\circ$  incidence.

There are four of the  $\text{FeSn}_2$  peaks missing from the sample data, the first three of which are listed as having relative intensities of 1 or less in the standard and so these can easily be lost in noise (table 7.12). There are no  $\text{FeSn}_2$  peaks masked by the close proximity of Fe peaks, as was the case when using Bragg-Brentano geometry, as the  $\text{FeSn}_2$  is more intense compared to the Fe signal in the glancing angle trace. The last peak of the  $\text{FeSn}_2$  data is unidentified as it is close to the cut off  $2\theta$  angle making identification by the APD software difficult.

FeSn <sub>2</sub> Standard				Sample				
d / Å	2θ / °	RI %	h k l	d / Å	2θ / °	RI %	Adjusted RI %	d Diff. / Å
4.610	19.2365	1	1 1 0					
3.260	27.3333	3	2 0 0	3.2729	27.2235	2.6	3.7	0.0129
2.656	33.7164	13	0 0 2	2.6586	33.6824	8.5	12.2	0.0026
2.556	35.0774	100	2 1 1	2.5634	34.9729	69.8	100.0	0.0074
2.304	39.0612	25	1 1 2	2.3048	39.0470	13.4	19.2	0.0008
2.063	43.8465	45	2 0 2	2.0654	43.7929	30.2	43.3	0.0024
1.713	53.4424	<1	3 2 1	1.7156	53.3550	0.2	0.3	0.0026
1.629	56.4371	7	3 1 2	1.6313	56.3504	3.5	5.0	0.0023
1.540	60.0215	8	3 3 0	1.5396	60.0387	4	5.7	-0.0004
1.515	61.1167	35	2 1 3	1.5169	61.0320	17.1	24.5	0.0019
1.460	63.6826	3	4 2 0	1.4607	63.6485	2.4	3.4	0.0007
1.392	67.1930	10	4 0 2	1.391	67.2477	3.9	5.6	-0.001
1.330	70.7795	20	0 0 4	1.333	70.5964	8	11.5	0.003
1.232	77.3942	1	2 0 4					
1.181	81.4156	20	4 1 3	1.1833	81.2241	6.8	9.7	0.0023
1.155	83.6539	6	5 1 2	1.1543	83.7161	1.8	2.6	-0.0007
1.118	87.0947	10	3 1 4	1.1182	87.0752	2.6	3.7	0.0002
1.089	90.0314	4	6 0 0	1.0891	90.0208	1.9	2.7	0.0001
1.053	94.0215	<1	4 3 3					
1.032	96.5532	1	4 0 4	1.0329	96.4413	0.4	0.6	0.0009
1.0073	99.7549	8	3 3 4					

Table 7.12. Peak fitting data for FeSn<sub>2</sub>.

Fe Standard				Sample			
d / Å	2θ / °	RI %	h k l	d / Å	2θ / °	RI %	d Diff. / Å
2.0268	44.6714	100	1 1 0	2.0285	44.6319	100	0.0017
1.4332	65.0182	20	2 0 0	1.4353	64.9114	85.8	0.0021
1.1702	82.3286	30	2 1 1	1.1708	82.2773	53.1	0.0006
1.0134	98.9399	10	2 2 0	1.0143	98.8210	12.5	0.0009

Table 7.13. Peak fitting data for Fe.

The four Fe peaks in the range of 2θ angles analysed are again identified fully in this sample with all four peaks clearly visible in the trace (table 7.13). Again, as with the Bragg-Brentano geometry, a comparison of the experimentally obtained relative intensities to the standard data shows a difference for the various planes. In this particular case the (110) plane is most intense as in the standard, however the (200)

and (211) planes are reversed in terms of their intensities, and are both more intense than would be expected from the values of the relative intensities for the Fe standard diffraction data.

Sample Unidentified Peaks			
Peak no.	d / Å	2θ / °	RI %
1	1.1671	82.5950	29.3

Table 7.14. Sample unidentified peak.

There at first appears to be an unidentified peak in the trace, shown in table 7.14. However this peak has arisen because of the APD software fitting two narrow peaks to what is in effect a single Fe peak, which is asymmetrical. The relative intensity given for this peak is relative to the strongest peak in the trace.

Using the X-ray diffractometer with glancing angle geometry, with an angle of incidence of the X-ray beam of 1°, the diffraction trace in figure 7.50 was obtained. The peak fitting data is shown in tables 7.15, 7.16 and 7.17.

There are five of the FeSn<sub>2</sub> peaks missing from the sample data, four have relative intensities in the standard data of 1 or less and so these can easily be lost in noise (table 7.15). The last peak of the FeSn<sub>2</sub> data is also unidentified as it is close to the cut off 2θ angle and also close to an Fe peak making identification by the APD software difficult.

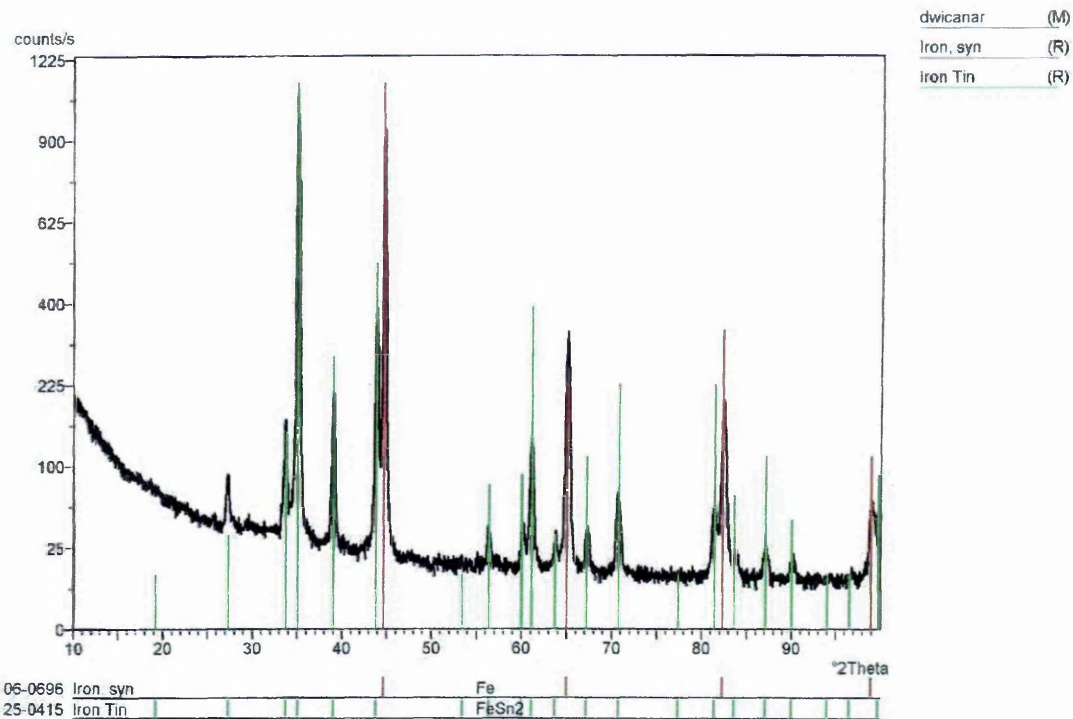


Figure 7.50. Diffraction trace of DWI can obtained using glancing angle geometry at 1° incidence.

FeSn <sub>2</sub> Standard				Sample			
d / Å	2θ / °	RI %	h k l	d / Å	2θ / °	RI %	d Diff. / Å
4.610	19.2365	1	1 1 0				
3.260	27.3333	3	2 0 0	3.2647	27.2932	4.6	0.0047
2.656	33.7164	13	0 0 2	2.662	33.6381	12.1	0.006
2.556	35.0774	100	2 1 1	2.5599	35.0222	100	0.0039
2.304	39.0612	25	1 1 2	2.3048	39.0470	16.9	0.0008
2.063	43.8465	45	2 0 2	2.0639	43.8264	32.6	0.0009
1.713	53.4424	<1	3 2 1				
1.629	56.4371	7	3 1 2	1.6317	56.3354	2.4	0.0027
1.540	60.0215	8	3 3 0	1.54	60.0215	2.7	0
1.515	61.1167	35	2 1 3	1.5152	61.1078	11.2	0.0002
1.460	63.6826	3	4 2 0	1.4583	63.7656	1.8	-0.0017
1.392	67.1930	10	4 0 2	1.391	67.2477	2.4	-0.001
1.330	70.7795	20	0 0 4	1.3314	70.6939	5.4	0.0014
1.232	77.3942	1	2 0 4				
1.181	81.4156	20	4 1 3	1.1815	81.3739	4	0.0005
1.155	83.6539	6	5 1 2	1.1544	83.7072	1.2	-0.0006
1.118	87.0947	10	3 1 4	1.1184	87.0557	1.7	0.0004
1.089	90.0314	4	6 0 0	1.0881	90.1262	0.9	-0.0009
1.053	94.0215	<1	4 3 3				
1.032	96.5532	1	4 0 4	1.029	96.9285	0.3	-0.003
1.0073	99.7549	8	3 3 4				

Table 7.15. Peak fitting data for FeSn<sub>2</sub>.

Fe Standard				Sample				
d / Å	2θ / °	RI %	h k l	d / Å	2θ / °	RI %	Adjusted RI %	d Diff. / Å
2.0268	44.6714	100	1 1 0	2.0246	44.7226	85.5	100	-0.0022
1.4332	65.0182	20	2 0 0	1.4337	64.9928	28.4	33.2	0.0005
1.1702	82.3286	30	2 1 1	1.17	82.3458	17.4	20.4	-0.0002
1.0134	98.9399	10	2 2 0	1.0129	99.0061	4.9	5.7	-0.0005

Table 7.16. Peak fitting data for Fe.

As with the examination of this sample using the other two geometries, all four peaks of the Fe diffraction trace in this range are identified and are shown in table 7.16. The intensity ratios observed using the geometry with an incident X-ray beam at an angle of 1° are the closest of the three observed sets of data to the standard data. Again as with the other two examinations of the sample the relative intensities do not correlate with those from the standard. In this case the (200) and (211) planes diffract with intensities corresponding to the other plane. This trace has an Fe signal that does not include the most intense peak in the trace and so adjusted relative intensities are given in table 7.16 alongside the experimentally observed values for the whole trace.

Sample Unidentified Peaks			
Peak no.	d / Å	2θ / °	RI %
1	7.8588	11.2493	3.2
2	3.0320	29.4334	0.5
3	1.1664	82.6555	10.1

Table 7.17. Sample unidentified peaks.

There are three unidentified peaks on this trace as shown in table 7.17. These peaks were unidentified by the APD software, however they are either noise or have arisen through two peaks being fitted to one broader asymmetrical one. Peaks 1 and 2 when observed on the trace appear to be of low intensity and are most likely to be noise.

Peak 3 is part of an Fe peak fitted due to the asymmetry in the peak. The relative intensities given for these peaks are relative to the strongest peak in the trace.

This preliminary heat treatment study used the DWI can as a basis for the analysis itself and therefore unfortunately contains an uneven substrate. Nevertheless the heat treatment applied at approximately 240 °C is enough to promote the growth of FeSn<sub>2</sub> within the samples. Annealing in the basic furnace described led to some problems with oxide formation, which led to the development of the second furnace arrangement. XRD analysis of the samples without identified oxides also showed clear evidence of FeSn<sub>2</sub> and no other intermetallic product. The glancing angle XRD analysis was better at identifying the surface dwelling FeSn<sub>2</sub>.

## **7.7. Analysis of Lacquer Coated DWI Tinned Steel Cans**

Although the cans analysed in this study are not lacquer coated it is interesting to see what effect such a coating has on the analysis of the DWI cans.

### **7.7.1 <sup>57</sup>Fe CEMS Analysis of Lacquer Coated DWI Tinned Steel Cans**

The data from the lacquer coated cans was found to be difficult to fit as it was of poor quality due to the absorption of conversion electrons in the protective lacquer coating. Figure 7.51 shows the spectrum resulting from the analysis of the outer wall of an area from the top of one of the lacquered DWI cans.

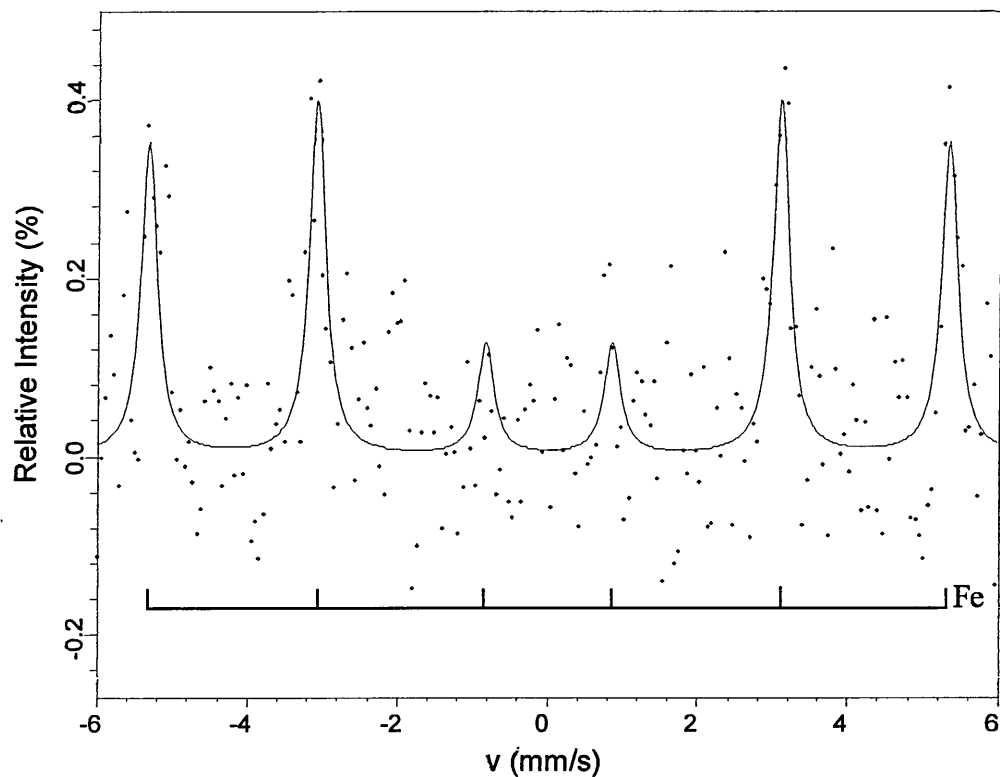


Figure 7.51. DWI can with lacquer coating.

Sample Description	Figure No.	Mössbauer parameters, relative to $\alpha$ -Fe, at 295 K ( $\pm 0.02 \text{ mm s}^{-1}$ )			Magnetic Hyperfine Field ( $\pm 0.2 \text{ T}$ )	Phase Identified	Relative Phase Area %	$\chi^2$
		$\delta$	$\Delta$	$\Gamma/2$	H			
Lacquer coated DWI	7.51	0.01	0.00	0.13	33.1	$\alpha$ -Fe	100	0.548

Table 7.18. Parameters for DWI can with lacquer coating.

The spectrum is shown fitted with an  $\alpha$ -Fe signal,  $H = 33.1 \pm 0.2 \text{ T}$ ,  $\delta = 0.01 \pm 0.02 \text{ mm s}^{-1}$ . Comparing to a similar area of an as-produced can without lacquer coating (see figure 7.4, section 7.2.1) it is evident that there is a large reduction in the peak intensities from 2.45%, 2.90% and 0.91% for peaks 1, 2 and 3 respectively in the as-produced can to 0.35%, 0.40% and 0.13% for peaks 1, 2 and 3 respectively

for the lacquered can. Thus it was shown that any Mössbauer analysis attempted should be done on non-lacquered cans to allow for easier identification of any iron containing compounds.

### 7.7.2 SEM Analysis of Lacquer Coated DWI Tinplated Steel Cans

SEM analysis of the cans with lacquer coating did not show the iron substrate with tin on the surface. Instead the layer of lacquer was seen. With the microscope set at 20 kV this surface lacquer was easily destroyed. This is seen in the SEM image, figure 7.52, where a square hole is seen in the centre where the microscope has been focused at higher magnification and the scanning electron beam has disrupted the coating integrity. Switching to 10 kV it was possible to image the surface of this substance but some destruction of the surface layer took place, making the whole sample covered in holes (some of the holes were seen immediately and therefore may be there prior to the electron beam impinging on the sample surface). The EDX analysis included here was taken at 20 kV as the iron and tin are not identified at 10 kV, and so the surface layer is not identified. Attempts to identify the surface layer at 10 kV failed and thus this layer is not formally identified. Therefore the analysis of the lacquer coated cans proved to be inappropriate as the lacquer coating was easily destroyed by the electron beam.

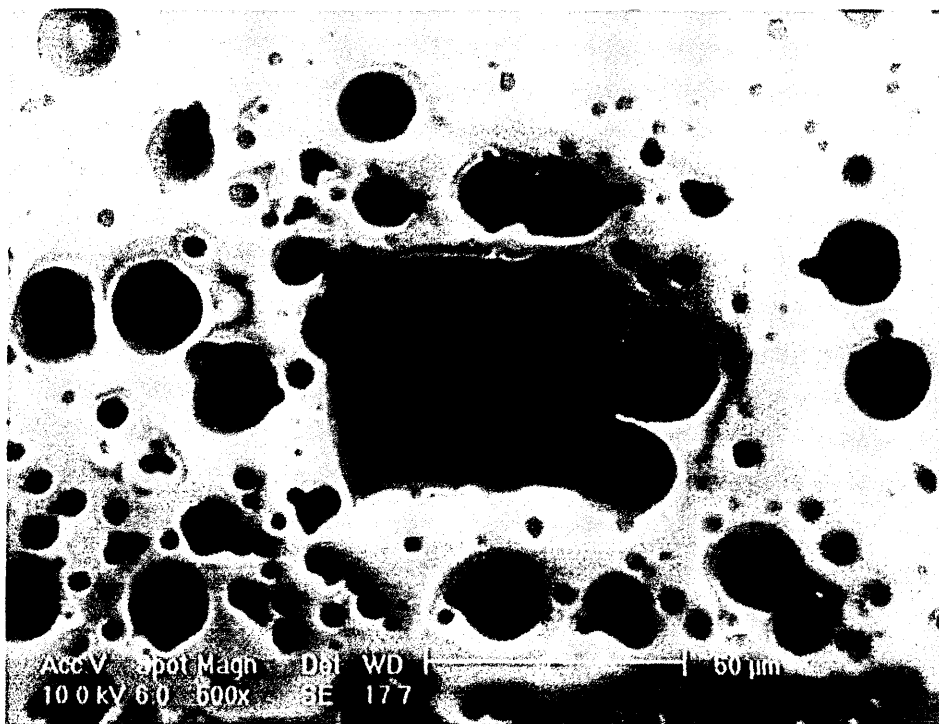


Figure 7.52. SE SEM image of DWI can with lacquer coating.

Figure 7.52 shows a typical image from this series of SEM experiments. X-ray analysis showed the iron and tin components but no other detectable element. Thus analysis of these cans by electron microscopy reveals no further information.

### **7.8. Analysis of Washed and Unwashed DWI Tinplated Steel Cans**

It has also been found that analysis of unwashed cans is preferable to washed cans as the wash process introduces similar difficulties with signal reduction possibly due to an inert layer being formed during the wash process. As is shown in the  $^{119}\text{Sn}$  work in section 7.3, tin oxide layers are not removed on etching and so the wash process may promote  $\text{SnO}_2$  growth, or introduce some other Mössbauer inert layer which would lead to a degradation of the observed signal.

### 7.8.1 $^{57}\text{Fe}$ CEMS Analysis of Washed and Unwashed DWI Tinplated Steel Cans

The reduction in signal observed on the  $^{57}\text{Fe}$  CEMS spectra is quite marked as seen in figures 7.53 and 7.54. Before the wash process the total counts for the spectra above background is almost 4 times that after the wash process both samples being taken from the top of the respective cans and analysed on the outside. Parameters for the spectra of the washed and unwashed samples are summarised in table 7.19.

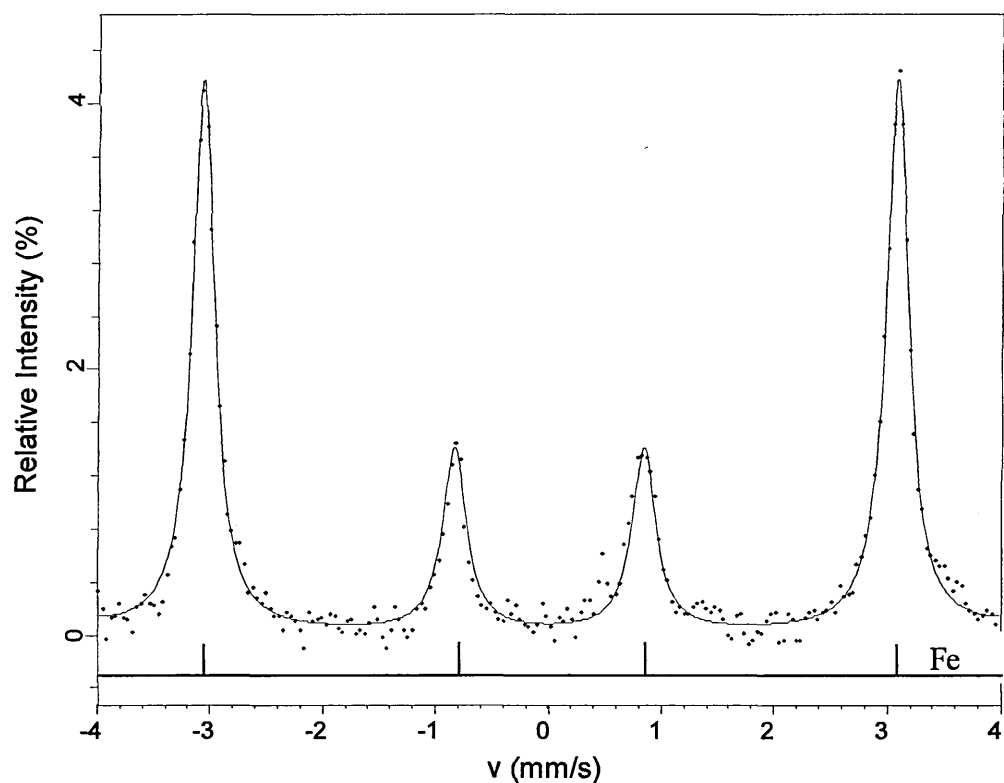


Figure 7.53. DWI can before wash process.

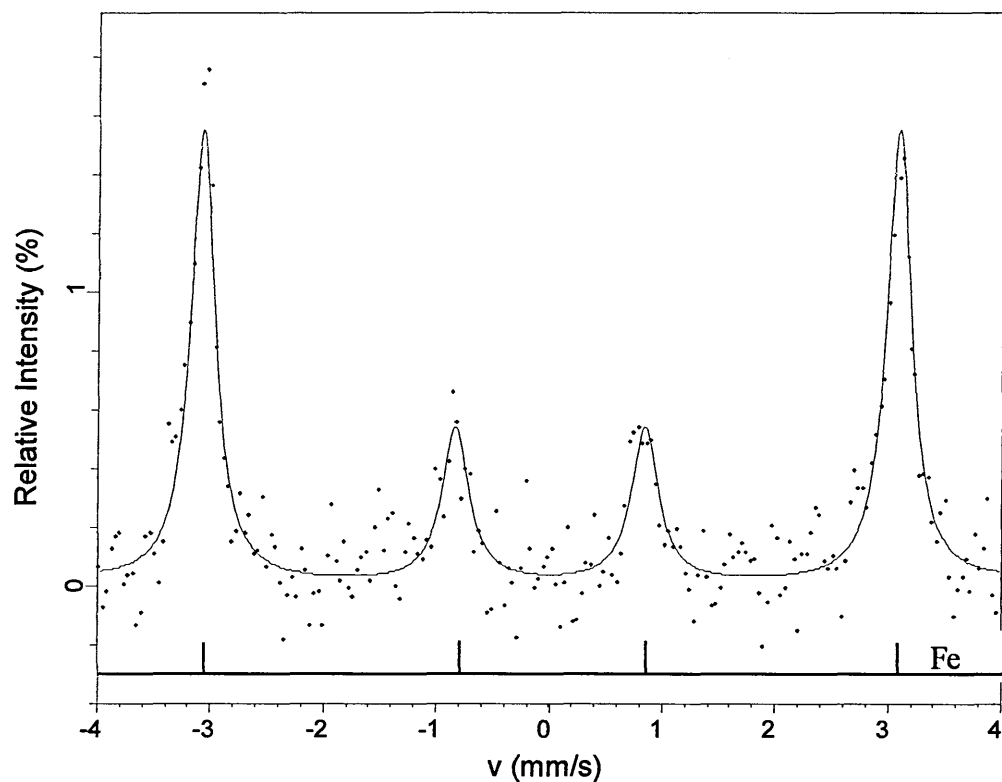


Figure 7.4. DWI can after wash process.

Sample Description	Figure No.	Mössbauer parameters, relative to $\alpha$ -Fe, at 295 K ( $\pm 0.02 \text{ mm s}^{-1}$ )			Magnetic Hyperfine Field ( $\pm 0.2 \text{ T}$ )	Phase Identified	Relative Phase Area %	Peak 2 and 5 Relative Intensity %	$\chi^2$
		$\delta$	$\Delta$	$\Gamma/2$	H				
DWI before wash process	7.53	0.00	0.00	0.12	32.9	$\alpha$ -Fe	100	4.15	0.648
DWI after wash process	7.54	0.00	0.00	0.14	33.0	$\alpha$ -Fe	100	1.55	0.602

Table 7.19. Parameters for washed and unwashed can analysis.

The signal in the  $^{57}\text{Fe}$  CEMS analysis for the washed sample is observed to be much less intense than the unwashed sample. Therefore  $^{57}\text{Fe}$  CEMS analysis for the cans in this study is more easily carried out on unwashed cans.

## 7.8.2 SEM Analysis of Washed and Unwashed DWI Tinplated Steel Cans

Using the SEM to image the surface of the washed and unwashed samples provides no significant clue as to a reason for the vast reduction in the signal from the Mössbauer analysis. Figures 7.55 and 7.56 show the SE and BSE SEM images respectively of the unwashed sample with figure 7.57 being the EDX analysis of the area shown in the two images.

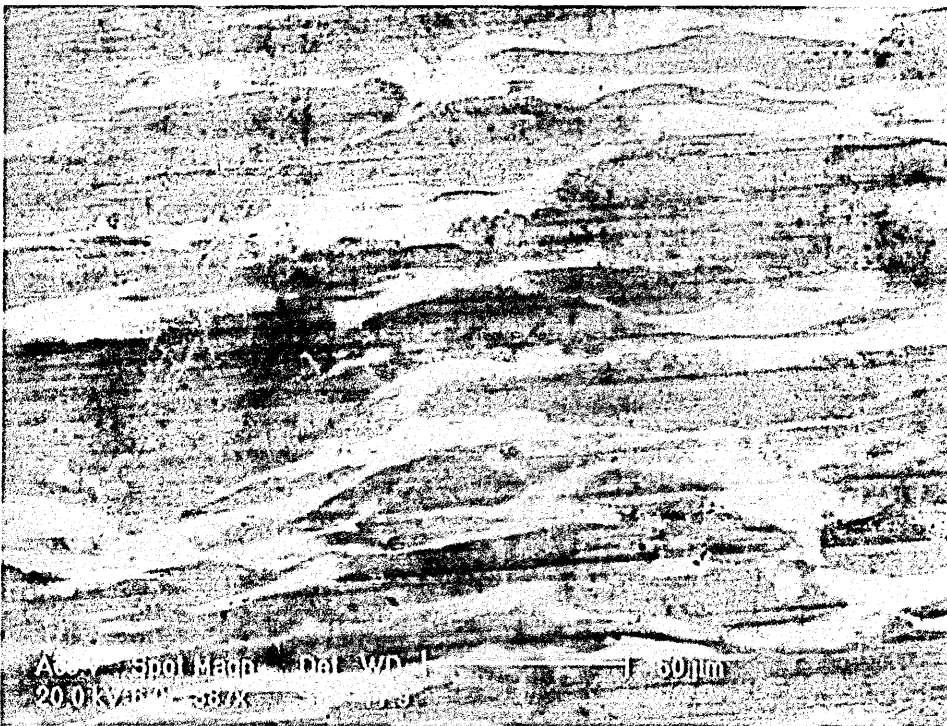


Figure 7.55. SE SEM image of DWI can before wash process.

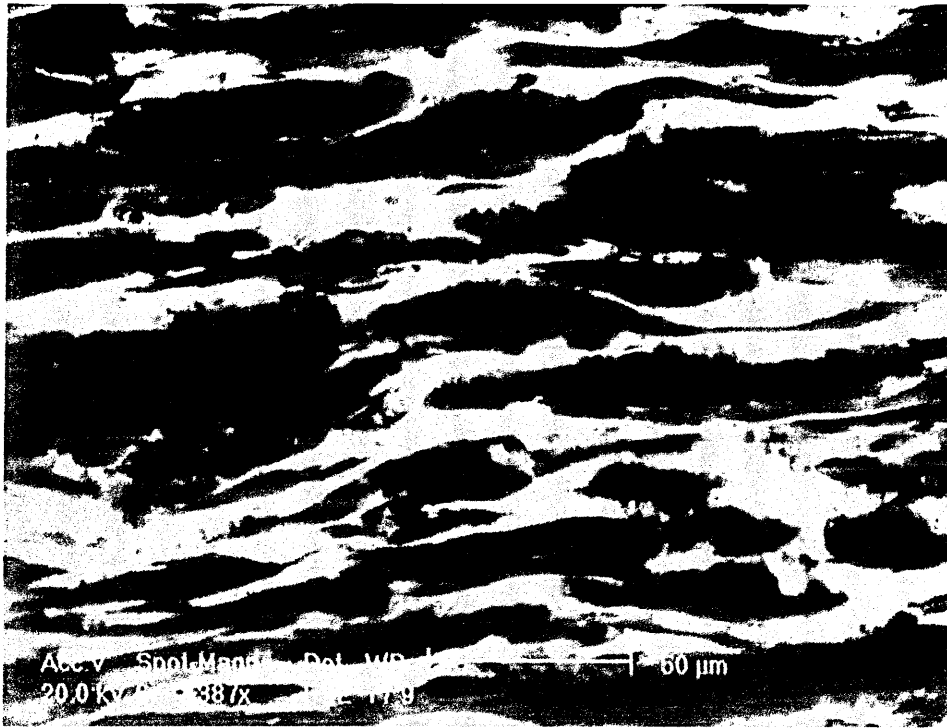


Figure 7.56. BSE SEM image of DWI can before wash process.

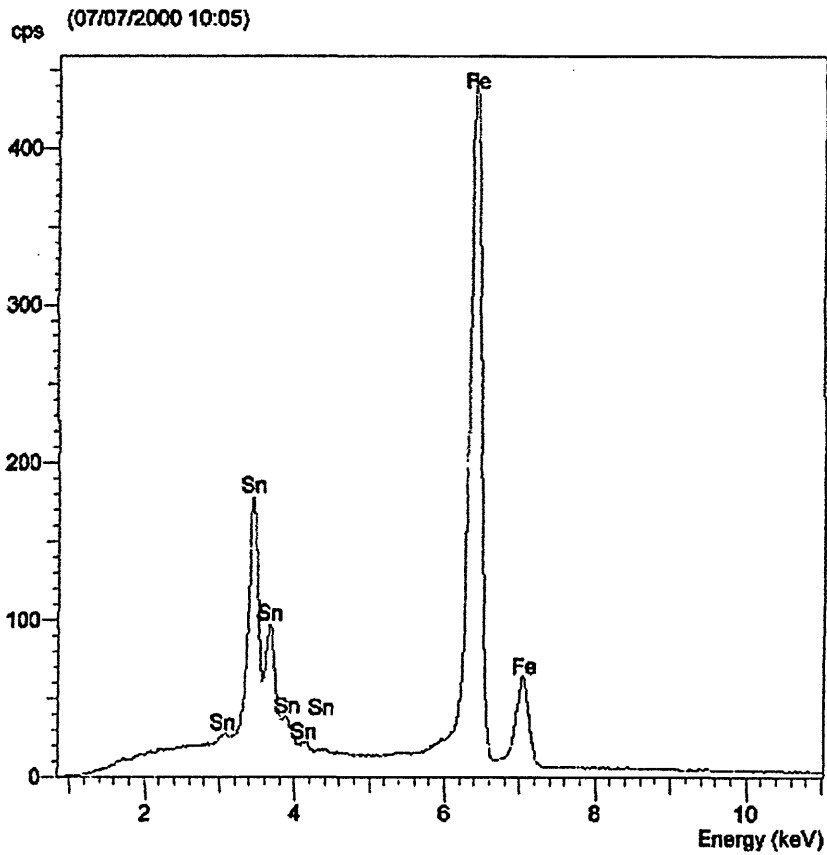


Figure 7.57. EDX analysis of DWI can shown in figures 7.55 and 7.56.

Figures 7.58 and 7.59 show the SE and BSE SEM images respectively of the washed sample with figure 7.60 being the EDX analysis of the area shown in these two images.

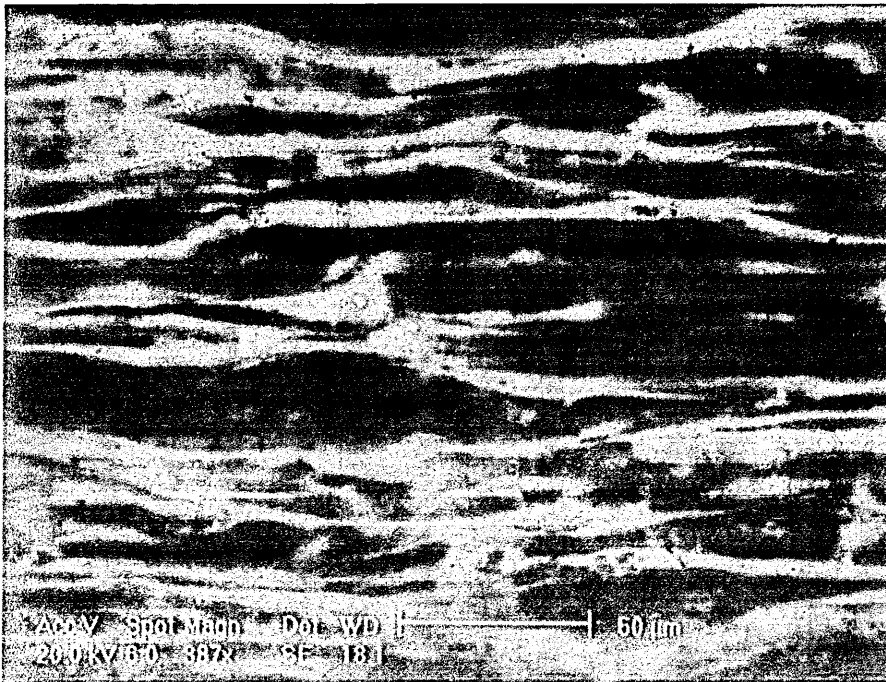


Figure 7.58. SE SEM image of DWI can after wash process.



Figure 7.59. BSE SEM image of DWI can after wash process.

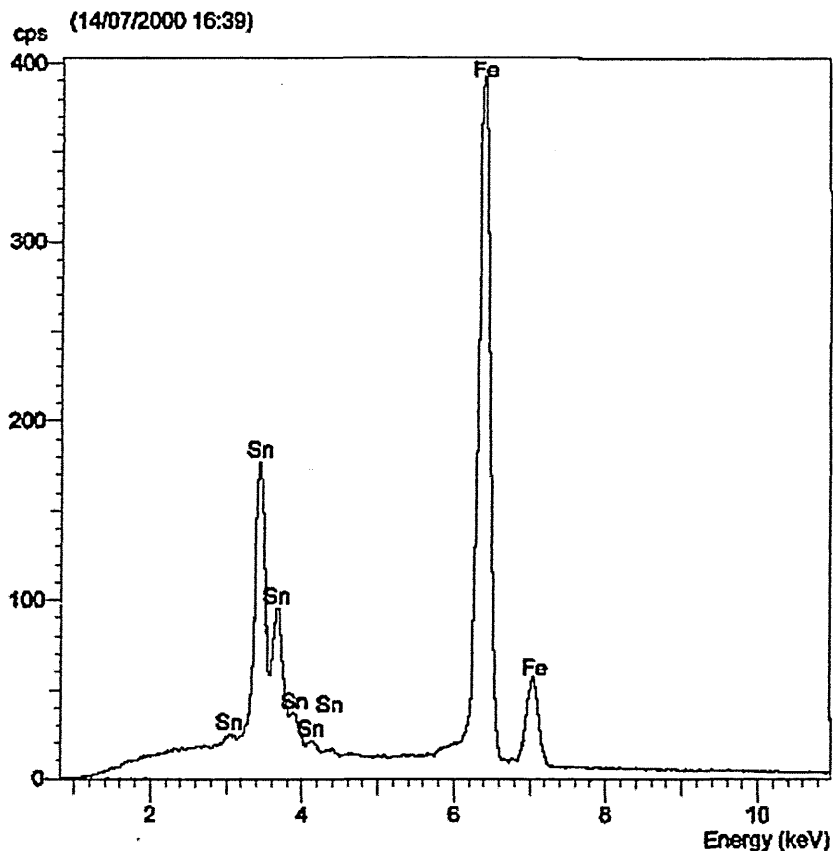


Figure 7.60. EDX analysis of DWI can shown in figures 7.58 and 7.59.

From this SEM and EDX analysis there is only a small difference between the results for the washed and unwashed samples. In particular it is difficult to spot significant differences in the images, both having specks of contamination on the surface. The unwashed sample appears to have slightly more contrast between the iron and tin identified though this could be due to differences in contrast levels set when imaging the separate samples. The EDX analysis shows a slight reduction in iron signal on the washed sample compared to the unwashed sample and with the high surface sensitivity of the Mössbauer technique compared to the EDX analysis this difference could indicate some very thin surface layer enough to affect the Mössbauer signal greatly without affecting the EDX analysis considerably. This surface layer could be non-

crystalline giving no scattering in the EDX analysis whilst still affecting the Mössbauer analysis.

To obtain the maximum information about possible intermetallics the cans analysed should be neither washed nor lacquered as these processes lead to reduced signals. The cans analysed within this study, with the exception of those shown in figures 7.52, 7.58 and 7.59, are not washed or lacquered.

### **7.9. Results of $^{57}\text{Fe}$ CEMS Analysis of Tinplate Sheet Material**

In order to analyse whether the formation of the intermetallics found on the DWI cans was due to the can processing or whether they are formed earlier in the deposition of tin onto the steel substrate surface, sheets of matte and flowbrightened tinplate were analysed. Although the cans in this study are formed from matte sheets, coating weight  $2.8 \text{ g cm}^{-2}$ , the flowbrightened sheets are used in the formation of other containers and are made from heating the matte sheets, and are therefore of some interest. Sheets from a number of different production runs were sampled but were all found to be consistent. The spectra from one sheet of matte, as-produced and etched, and one sheet of flowbrightened, as-produced and etched are shown in figures 7.61 - 7.64. These are the upper sides of the sheets as produced on the production line and are unmarked.

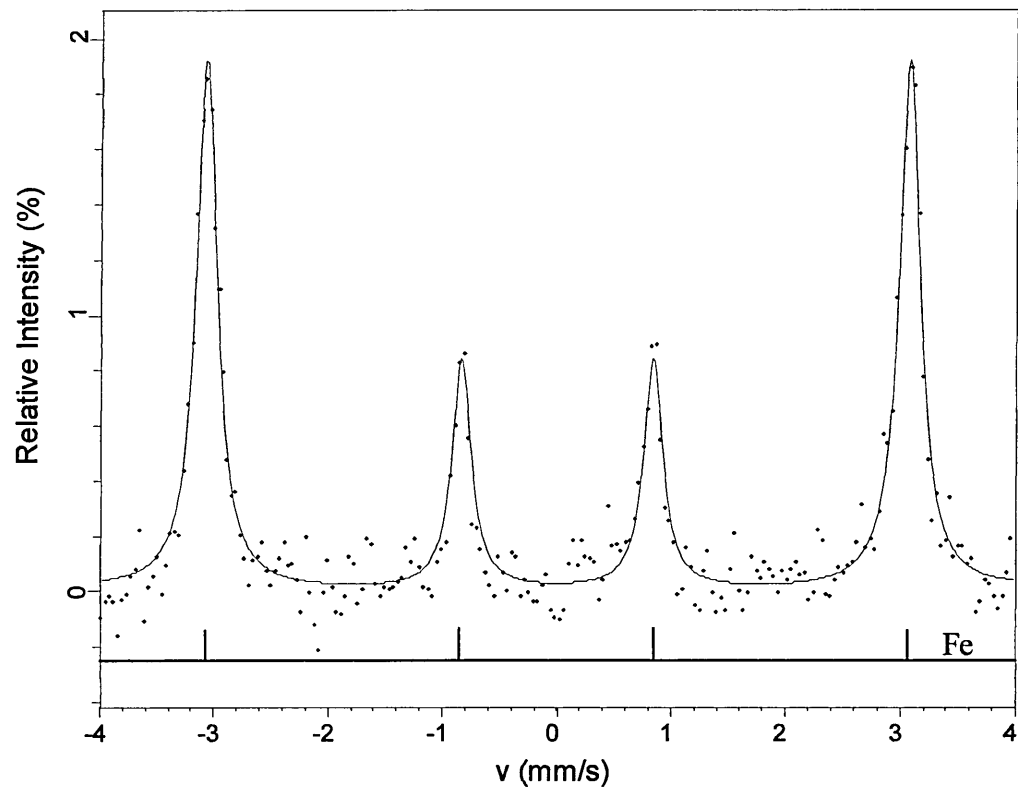


Figure 7.61. Unetched matte tinplate.

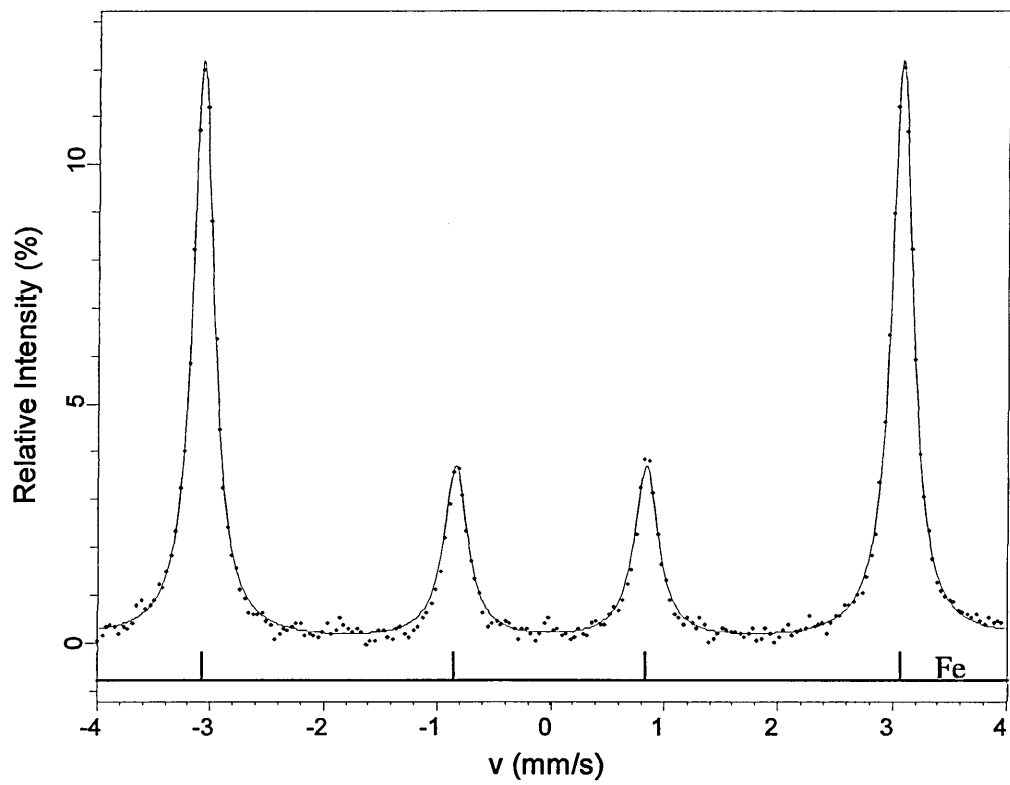


Figure 7.62. Etched matte tinplate.

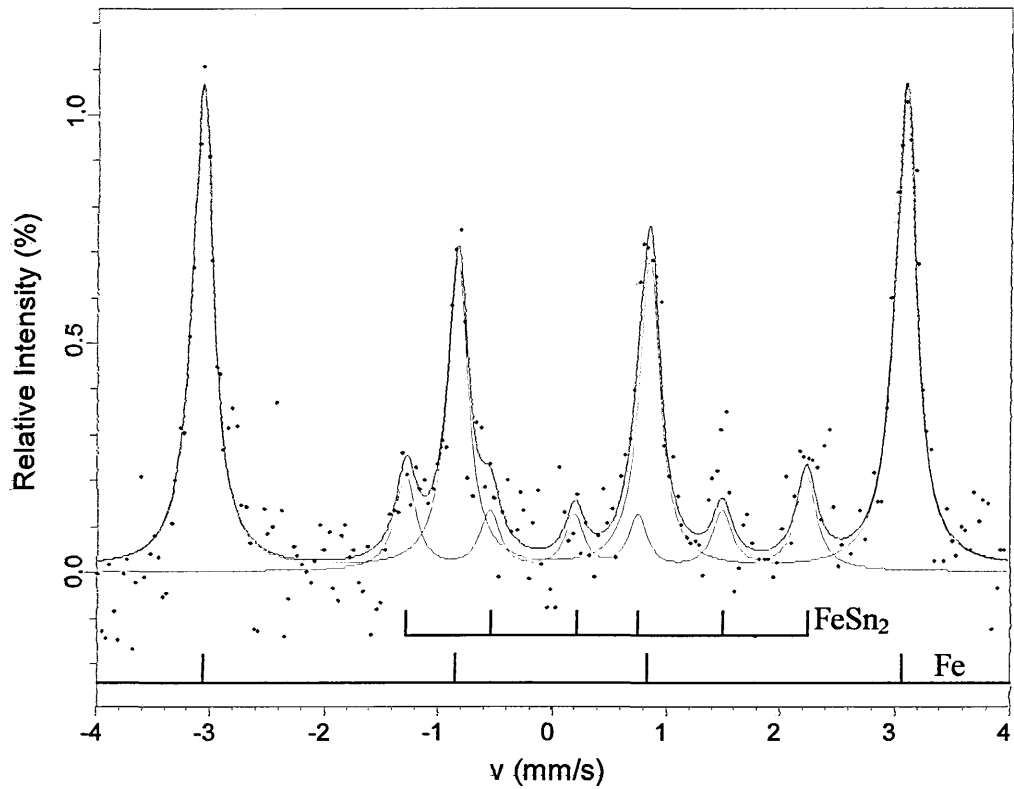


Figure 7.63. Unetched flowbrightened tinplate.

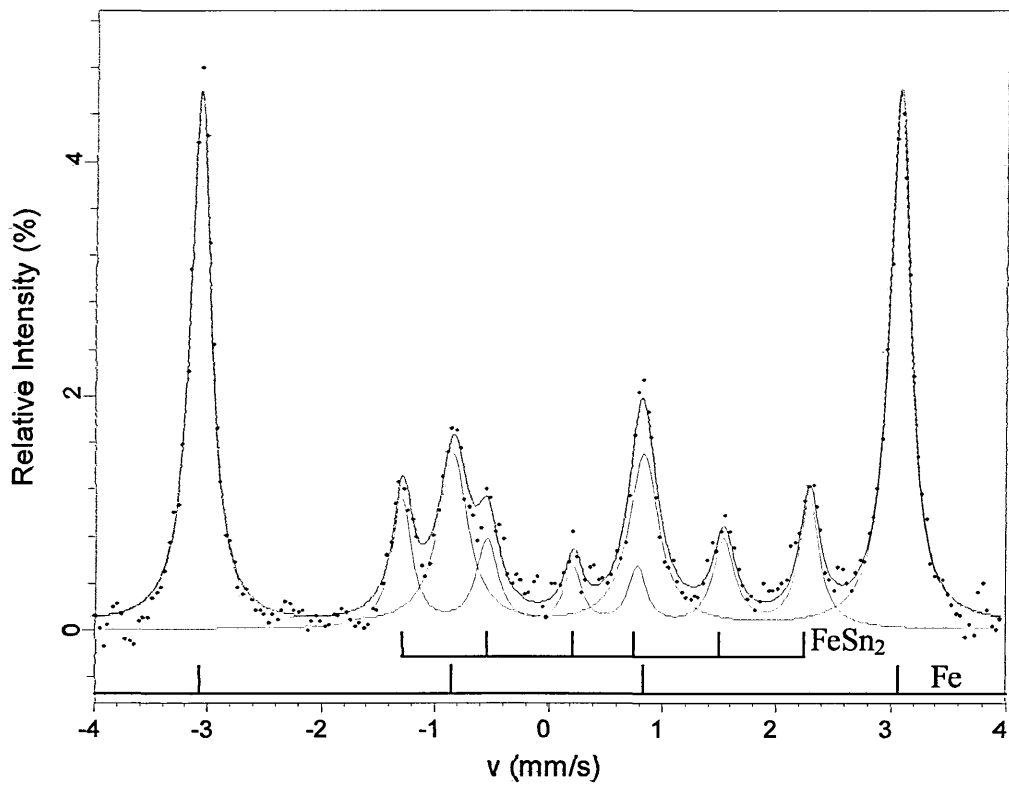


Figure 7.64. Etched flowbrightened tinplate.

The reverse sides of the sheets were also analysed as these would form the opposite side of the can wall when produced, the spectra from the analysis are shown in figures 7.65 - 7.68. The reverse sides of the sheets were at the bottom on the production line and have visible lines running along them where they have been in contact with the rollers on the line. Parameters for the spectra of both sides of the matte and flowbrightened tinplate samples are summarised in table 7.20.

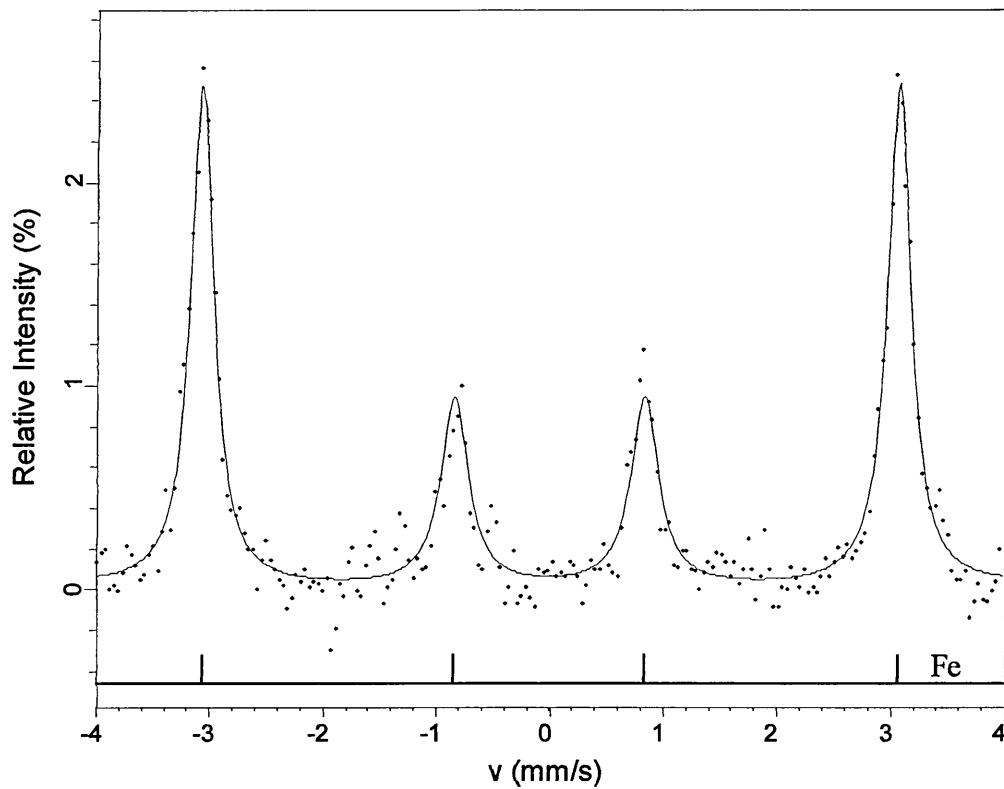


Figure 7.65. Reverse side of unetched matte tinplate.

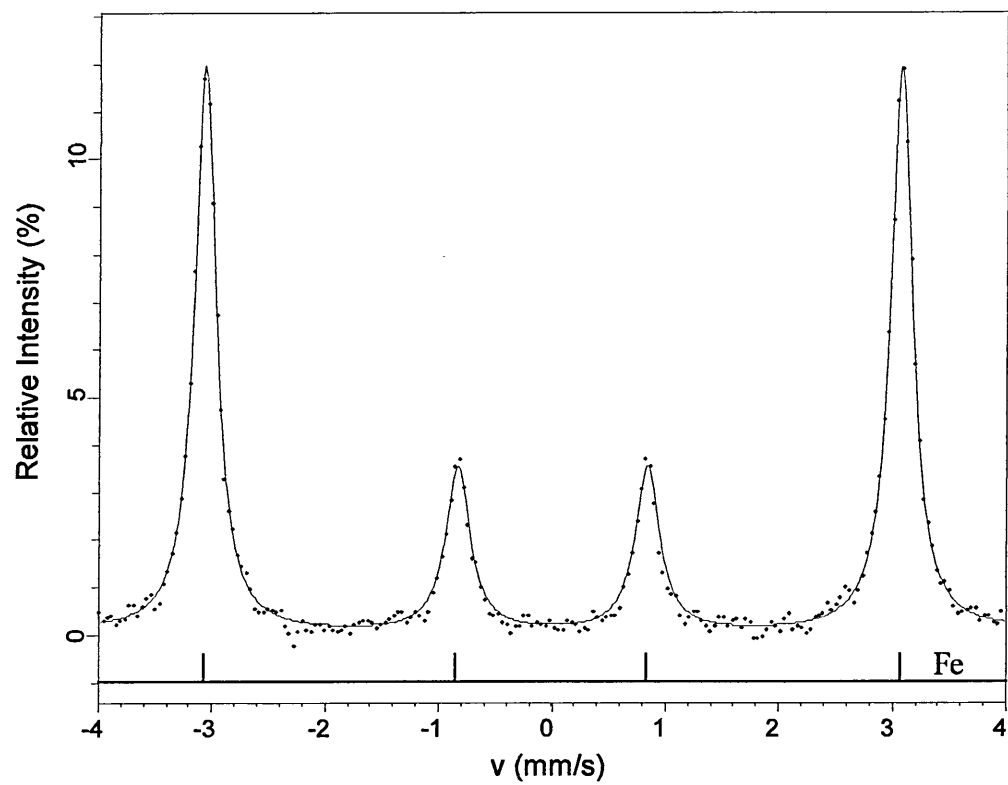


Figure 7.66. Reverse side of etched matte tinplate.

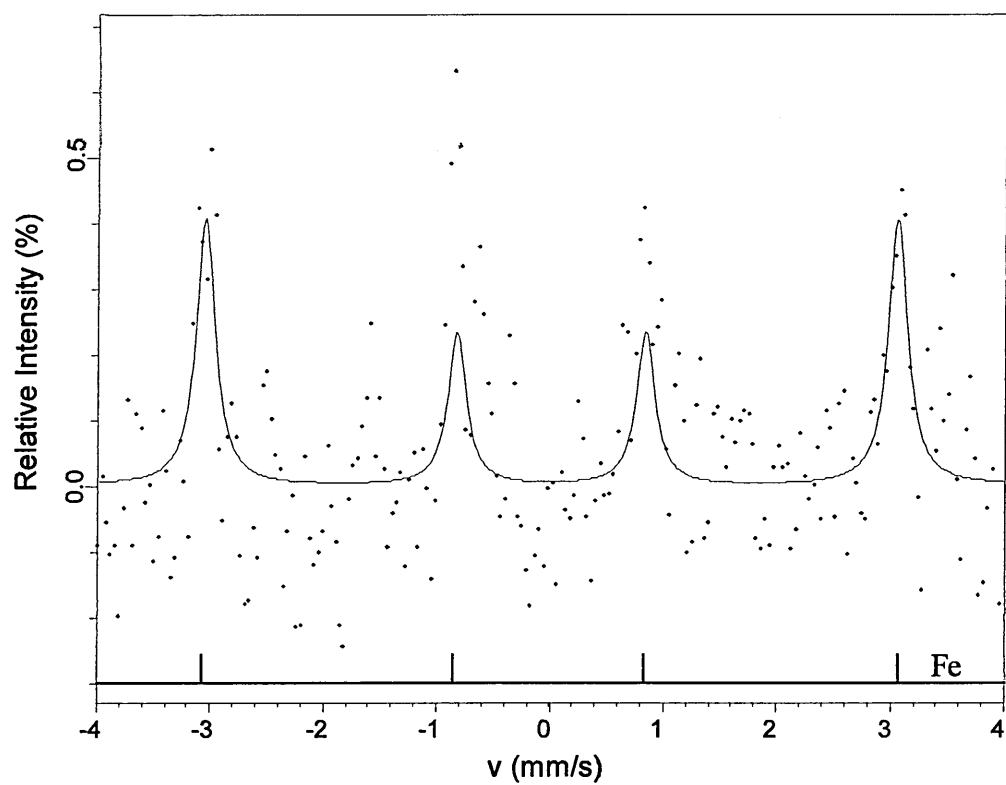


Figure 7.67. Reverse side of unetched flowbrightened tinplate.

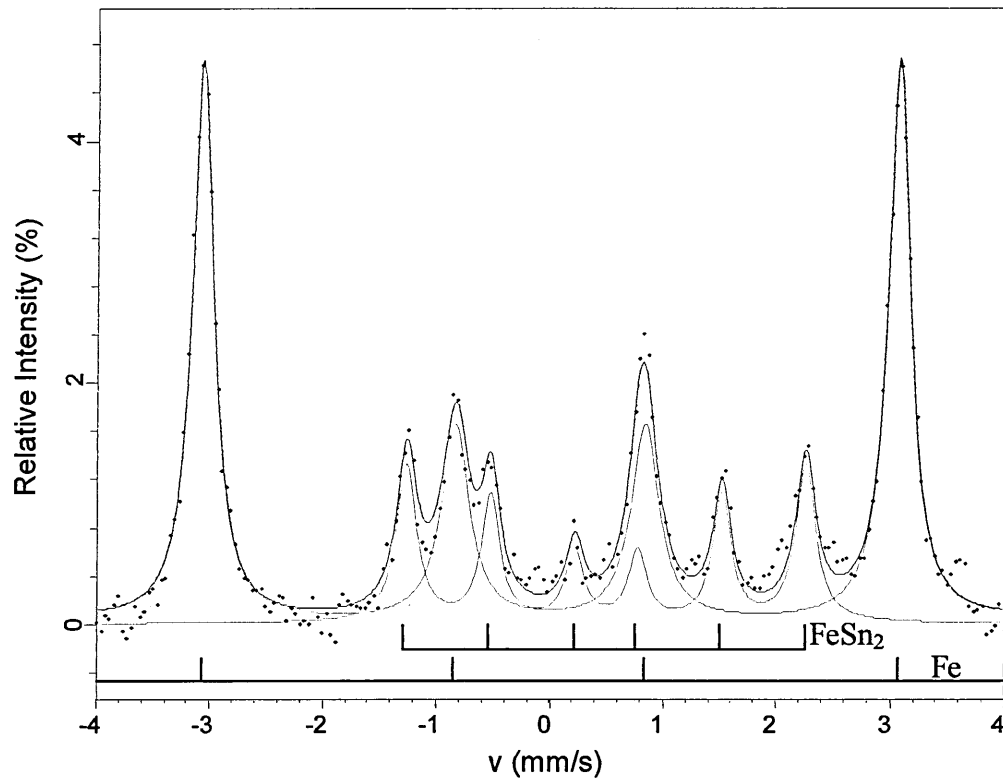


Figure 7.68. Reverse side of etched flowbrightened tinplate.

The matte tinplate analysed here shows no evidence of intermetallics on either side of the sheets, even when etched (figures 7.62 and 7.66). When etched the  $\alpha$ -Fe signal was equal on both sides as would be expected when no intermetallics are present. Unetched, the reverse side of the matte sheets produce a greater signal indicating that the upper surface of the tinplate is coated with a greater thickness of tin. This is in contrast to what was expected as the can material is expected to have coating weight  $2.8 \text{ g cm}^{-3}$  and to be even on both sides. This makes the results of the DWI processed can a little more significant as there was found to be less tin on the outside of the can wall. Initially this was thought to be due to the frictional forces acting on the inner and outer can wall being different. However it cannot be ruled out that the sheets also began with different coating weights on the two sides of the tinplate material.

Sample Description	Figure No.	Mössbauer parameters, relative to $\alpha$ -Fe, at 295 K ( $\pm 0.02 \text{ mm s}^{-1}$ )			Magnetic Hyperfine Field ( $\pm 0.2 \text{ T}$ )	Phase Identified	Relative Phase Area %	Peak 2 and 5 Relative Intensity %	$\chi^2$
		$\delta$	$\Delta$	$\Gamma/2$					
Unetched matte tinplate	7.61	0.00	0.00	0.10	32.9	$\alpha$ -Fe	100	1.90	0.611
Etched matte tinplate	7.62	0.00	0.00	0.13	32.9	$\alpha$ -Fe	100	12.10	1.194
Unetched flowbrightened tinplate	7.63	0.00	0.00	0.11	33.0	$\alpha$ -Fe	86.2	1.07	0.539
		0.47	0.00	0.10	10.9	FeSn <sub>2</sub>	13.8	0.11	
Etched flowbrightened tinplate	7.64	0.00	0.00	0.16	32.9	$\alpha$ -Fe	82.8	4.60	0.944
		0.50	0.00	0.10	11.1	FeSn <sub>2</sub>	17.2	0.80	
Reverse side of unetched matte tinplate	7.65	-0.01	0.00	0.15	33.0	$\alpha$ -Fe	100	2.45	0.655
Reverse side of etched matte tinplate	7.66	0.00	0.00	0.13	32.9	$\alpha$ -Fe	100	12.00	1.178
Reverse side of unetched flowbrightened tinplate	7.67	0.00	0.00	0.10	32.7	$\alpha$ -Fe	100	0.40	0.698
Reverse side of etched flowbrightened tinplate	7.68	0.00	0.00	0.15	32.9	$\alpha$ -Fe	80.8	4.60	0.771
		0.50	0.00	0.10	10.9	FeSn <sub>2</sub>	19.2	1.00	

Table 7.20. Parameters for analysis of matte and flowbrightened tinplate sheets.

The flowbrightened tinplate clearly exhibited evidence of intermetallics on both sides of the sheets of tinplate (figures 7.63 and 7.67). The parameters for the intermetallic sextets are close to those of FeSn<sub>2</sub> and this is therefore the likely phase present. When etched the spectra for both sides of the sheets are very similar with 17.2% of the overall signal area for the upper side being due to the FeSn<sub>2</sub> component and 19.2% FeSn<sub>2</sub> for the reverse side (figures 7.64 and 7.68). The difference in FeSn<sub>2</sub>

concentration is possibly due to either slightly uneven heating or quenching after heating.

The flowbrightened tinplate has a greatly reduced  $\alpha$ -Fe signal compared to the matte tinplate. This is due to the intermetallic layer forming the uppermost layer of the sample and the high surface sensitivity of the CEMS technique, with 75% of the signal coming from the first 100 nm, 90% from the first 200 nm and 92% in the top 300 nm [11]. Thus a thin intermetallic layer as on these tinplate surfaces will be identified whilst the substrate signal is significantly reduced. A comparison of the unetched matte and unetched flowbrightened tinplates on the upper surfaces reveals a reduction in the peak intensities for the  $\alpha$ -Fe signal when flowbrightened of approximately half (figures 7.61 and 7.63). The etched samples (figures 7.62 and 7.64) showed an even more pronounced reduction in  $\alpha$ -Fe signal.

Unetched, the signal for the reverse side of the flowbrightened sheet (figure 7.67) is much lower than that for the upper side (figure 7.63) indicating that the reverse side of the tinplate is coated with more tin, in fact it is not possible to identify intermetallics on the reverse side without etching, whereas they are identified on the upper surface. Thus it is apparent that the tinplate sheet from the matte stage through the flowbrightening stage does not show consistent marking and it cannot be assumed that the phases on the marked side of the matte sheet is the same as the marked side for the flowbrightened sheet.

Clearly from this analysis the matte tinplate material used for the can blanks does not contain identifiable intermetallics, and so the intermetallics identified on the can walls are a product of the subsequent manufacturing process. In this case the cans have only undergone the DWI process and so it is apparent that this process in itself leads to the formation of small amounts of intermetallics, most probably  $\text{FeSn}_2$ .

## **7.10. Results of Analysis of Tinplate With Defects**

To further test the analytical capabilities of CEMS and SEM, tinplate from the tinplate plant, designated as defective by Corus plc., was analysed using these techniques.

### **7.10.1 $^{57}\text{Fe}$ CEMS Analysis of Tinplate With Defects**

Two particular areas of a sheet of tinplate were analysed, using Mössbauer spectroscopy, both unetched and etched, figures 7.69 - 7.72. The first area had dark markings, which were initially thought to be some form of contamination or possible alloy; the second area was without such markings. Both of the tinplate samples were analysed from the same side of the tinplate sheet that contained the marked areas in order to observe any difference between marked and unmarked areas. Parameters for the spectra of the defective tinplate sheet samples are summarised in table 7.21.

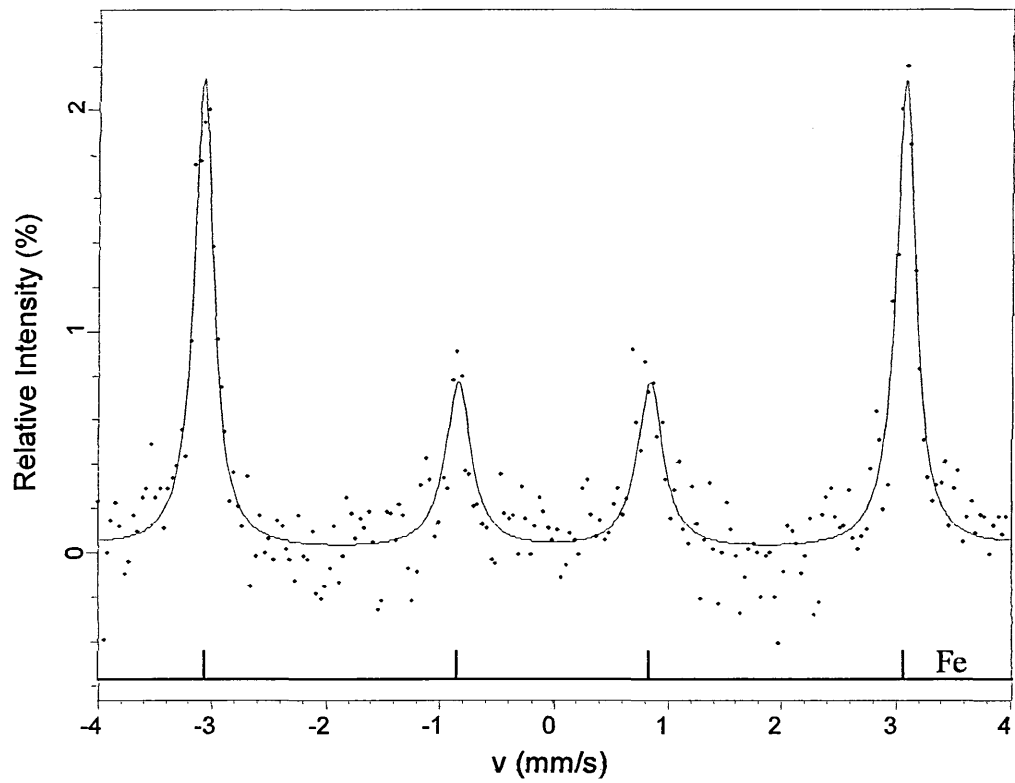


Figure 7.69. Tinplate with dark markings.

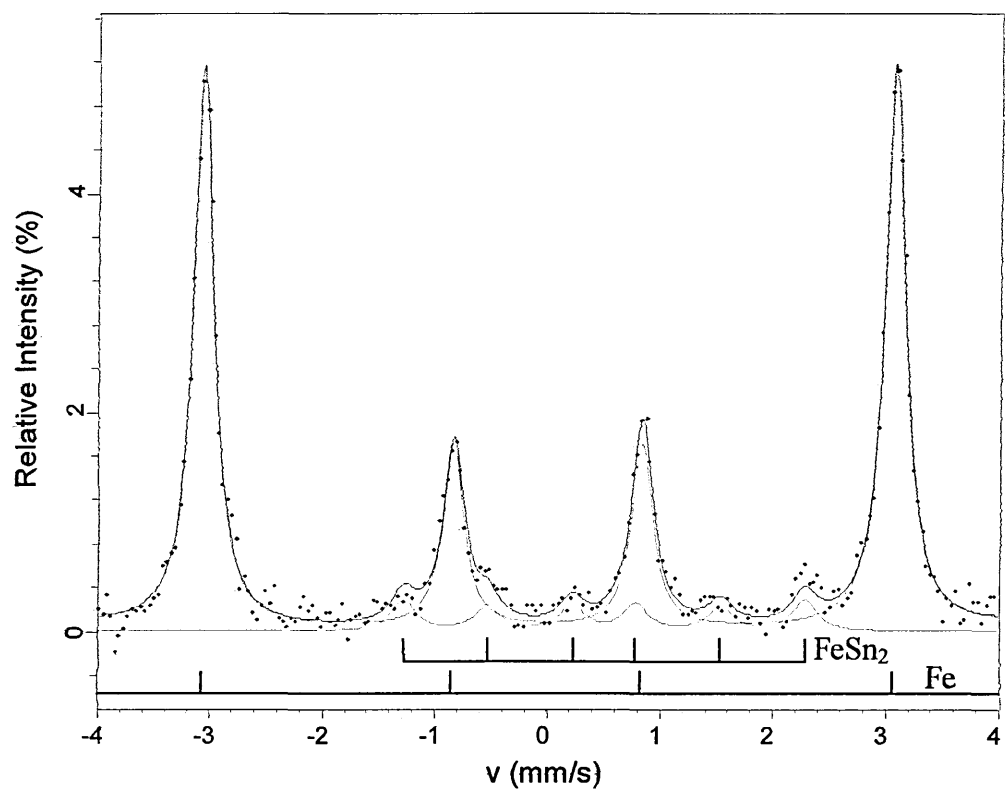


Figure 7.70. Etched tinplate with dark markings.

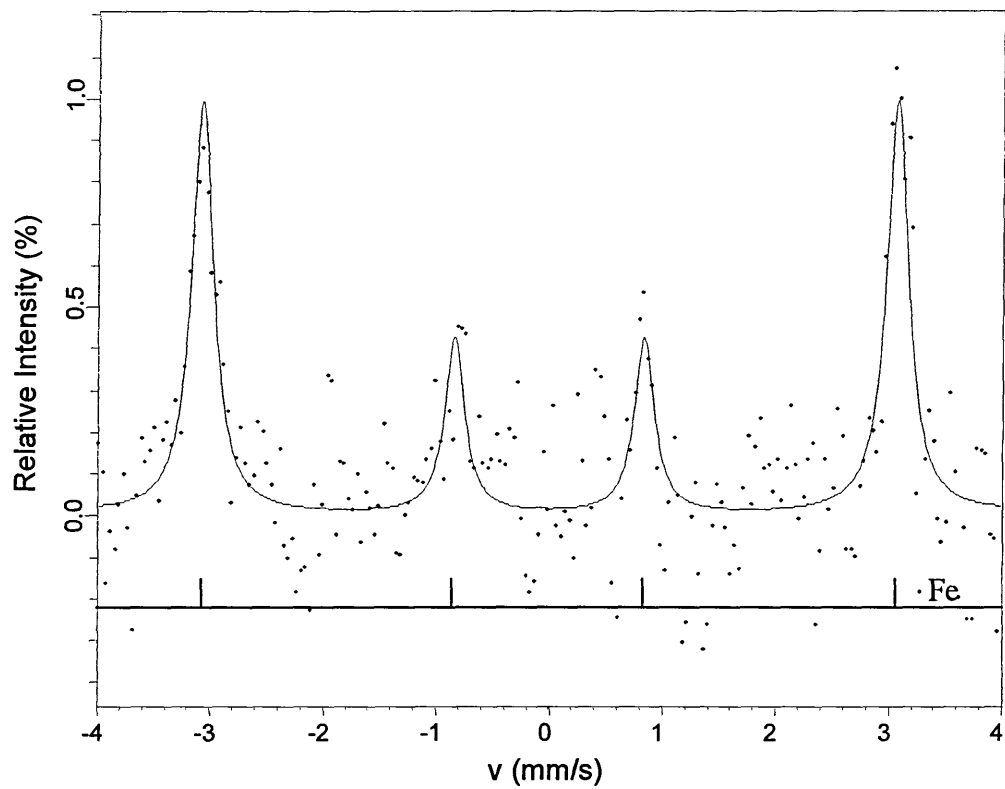


Figure 7.71. Tinplate without dark markings.

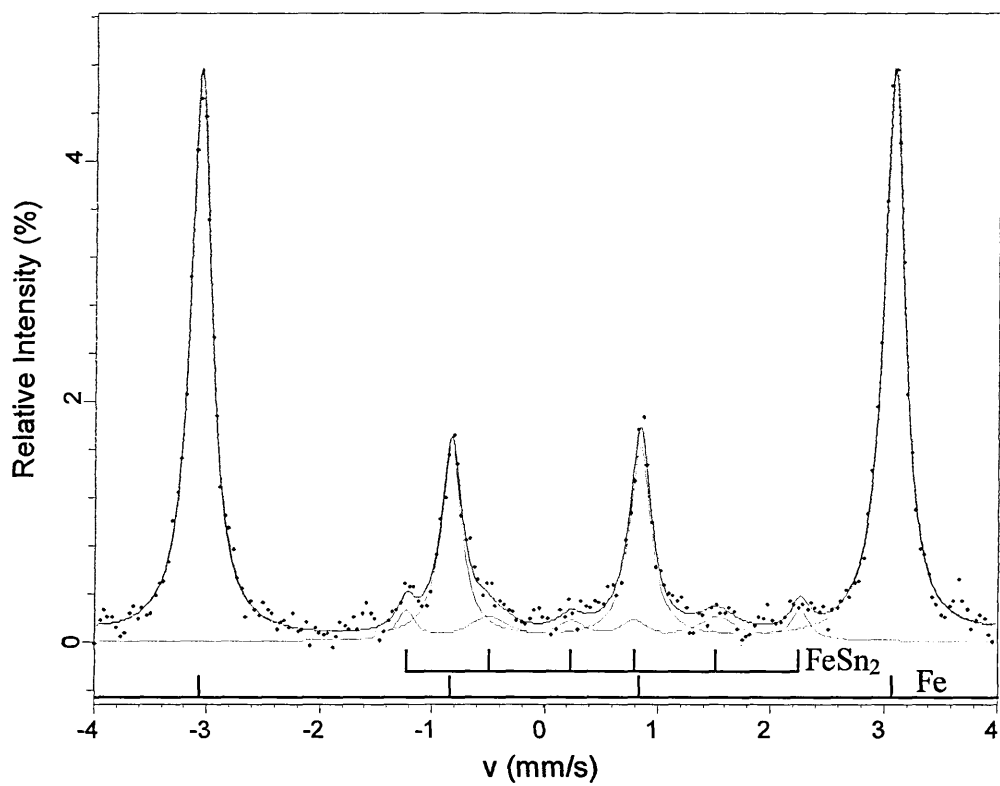


Figure 7.72. Etched tinplate without dark markings.

Sample Description	Figure No.	Mössbauer parameters, relative to $\alpha$ -Fe, at 295 K ( $\pm 0.02 \text{ mm s}^{-1}$ )			Magnetic Hyperfine Field ( $\pm 0.2 \text{ T}$ )	Phase Identified	Relative Phase Area %	Peak 2 and 5 Relative Intensity %	$\chi^2$
		$\delta$	$\Delta$	$\Gamma/2$					
Tinplate with dark markings	7.69	0.00	0.00	0.12	33.0	$\alpha$ -Fe	100	2.10	0.481
Etched tinplate with dark markings	7.70	0.00	0.00	0.11	32.9	$\alpha$ -Fe	93.2	5.20	0.455
		0.50	0.00	0.13	11.1	FeSn <sub>2</sub>	6.8	0.25	
Tinplate without dark markings	7.71	-0.01	0.00	0.11	32.9	$\alpha$ -Fe	100	1.00	0.571
Etched tinplate without dark markings	7.72	0.00	0.00	0.11	32.9	$\alpha$ -Fe	92.8	4.75	0.578
		0.51	0.00	0.15	10.8	FeSn <sub>2</sub>	7.2	0.20	

Table 7.21. Parameters for analysis of defective tinplate.

Both samples prior to etching have noisy signals due to the amount of tin present on the samples. It is worth noting that the tin coating is not sufficient to stop the identification of the substrate. Unetched, the area with dark markings shows a greater  $\alpha$ -Fe signal intensity than the area without dark markings, suggesting that there is less tin on the marked area of tinplate. This could take the form of areas of exposed substrate, especially with rough substrates, or lightly coated areas, from uneven deposition on smooth substrates, which allow the conversion electrons to escape from the substrate virtually unhindered by a coating, leading to a greater  $\alpha$ -Fe signal (table 7.21).

By etching away the tin layer, the signals obtained from these tinplate samples can be fitted more accurately and gives the possibility of identifying any intermetallics present. The etching procedure left the dark markings intact indicating that they were more likely to be markings on the steel substrate or indeed patches of alloyed material

rather than marking or contamination on the surface of the tin layer. If the markings were on the tin surface they would be removed as the underlying tin overlayer is removed. It is observed that, upon analysis, both etched samples of the marked and unmarked areas, as shown in figures 7.70 and 7.72, show the presence of intermetallics in similar proportions. Thus the dark markings observed on the marked area are not likely to be a visual indication of intermetallics.

This means that the dark areas are formed of some other material and either not alloyed with the steel substrate, or alloy at a level below the limit of detection, because no other phase is observed when using CEMS. The dark markings could also be the first signs of corrosion on areas of exposed substrate, at very low levels these may not be detected above the background, however a visible amount of Fe corrosion product on the samples should be detectable in the spectra and so this particular scenario is unlikely.

From the etched tinplate analysis the observed Fe-Sn intermetallics are identified as  $\text{FeSn}_2$ . From the Mössbauer spectra of the tinplate, the  $\text{FeSn}_2$  identified comprises 6.8% and 7.2% of the total spectra areas with and without the dark markings respectively. Thus the dark markings are most likely to be some contamination that prevents the tin from adhering to the steel substrate and therefore inhibit intermetallic formation.

The  $\text{FeSn}_2$  signal from this defect tinplate is much less than on the previously analysed flowbrightened tinplate where the upper side had 17.2%  $\text{FeSn}_2$  and the reverse side

19.2%. On the outside of the can wall (figures 7.26 and 7.27) the intermetallics identified comprise 2.4% and 1.7% of the spectra areas from the top and bottom of the can wall respectively, less than in the defect tinplate. No intermetallics are observed on the inside of the can walls, the can bases or the matte tinplate sheets.

#### 7.10.2 SEM Analysis of Tinplate With Defects

The samples of defect material were analysed using the SEM. Looking at the samples of unmarked material it can be seen from figure 7.73 that the surface of the tinplate is highly irregular. The BSE image, figure 7.74, shows the areas of iron (dark) and tin (light) identified.

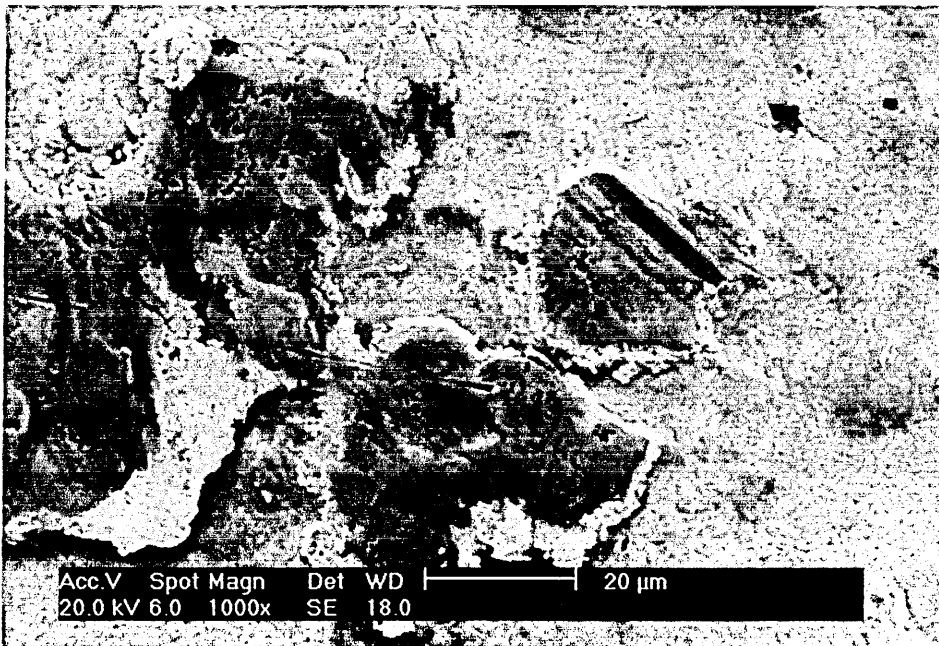


Figure 7.73. SE SEM image of tinplate without dark markings.

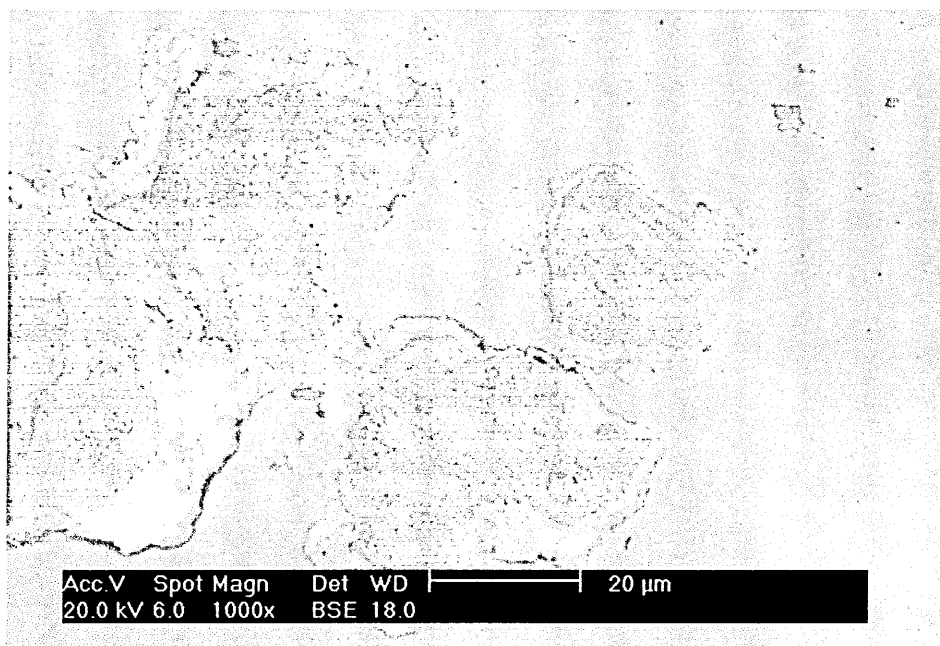


Figure 7.74. BSE SEM image of tinplate without dark markings.

The majority of the area of the tinplate surface without dark markings is coated with tin and having raised areas being composed of iron with some tin at the edges. The raised iron islands are marked with grooves and pits similar to those found on the base sheet steel prior to plating. Thus it is possible that there has been no tin electrodeposited on these areas though in the bath without surface contamination this is unlikely. It is also possible that tin that has been deposited over the entire surface and has been subsequently removed from the raised areas exposing the substrate. This may have occurred during heat treatment, though this is likely to have left some tin in the grooves and pits. A further explanation of the absence of tin on the substrate islands is physical removal of tin as the sheet has traversed the production line, but again this could have left residual tin on the islands. The EDX analysis of this whole area, figure 7.75, shows a fairly equal amount of signal, in terms of counts per second (cps) from both the tin and iron.

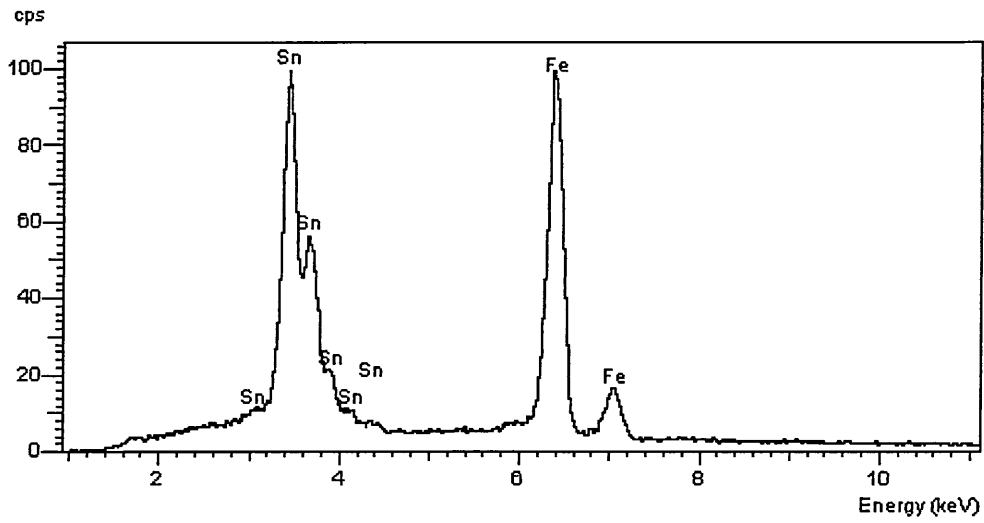


Figure 7.75. EDX analysis of tinplate without dark markings.

For the sample showing dark markings, the SEM SE image, figure 7.76, shows an irregular surface but with the raised areas being composed of tin as shown in the BSE image, figure 7.77.

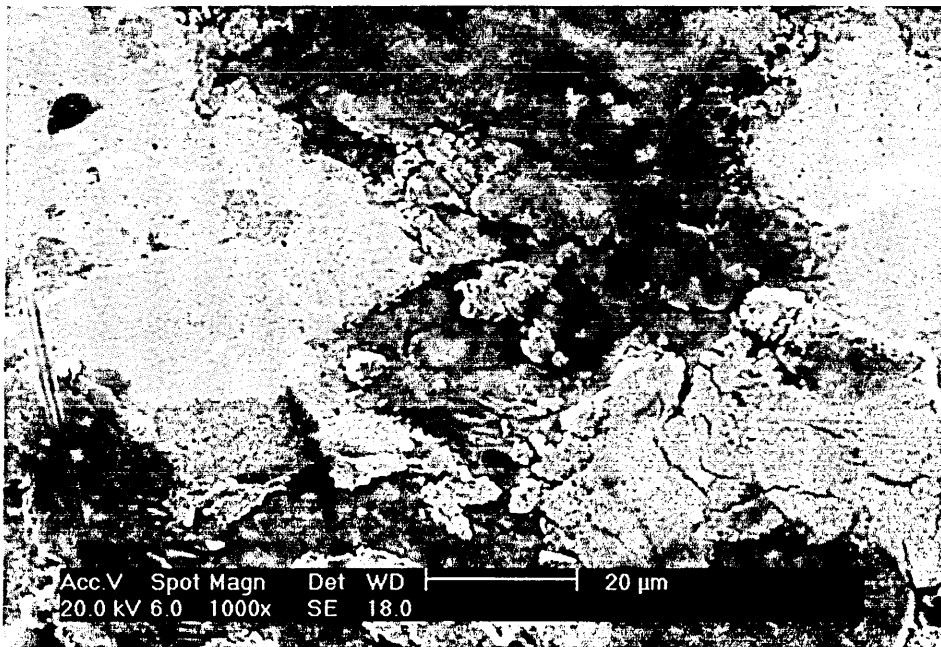


Figure 7.76. SE SEM image of tinplate with dark markings.

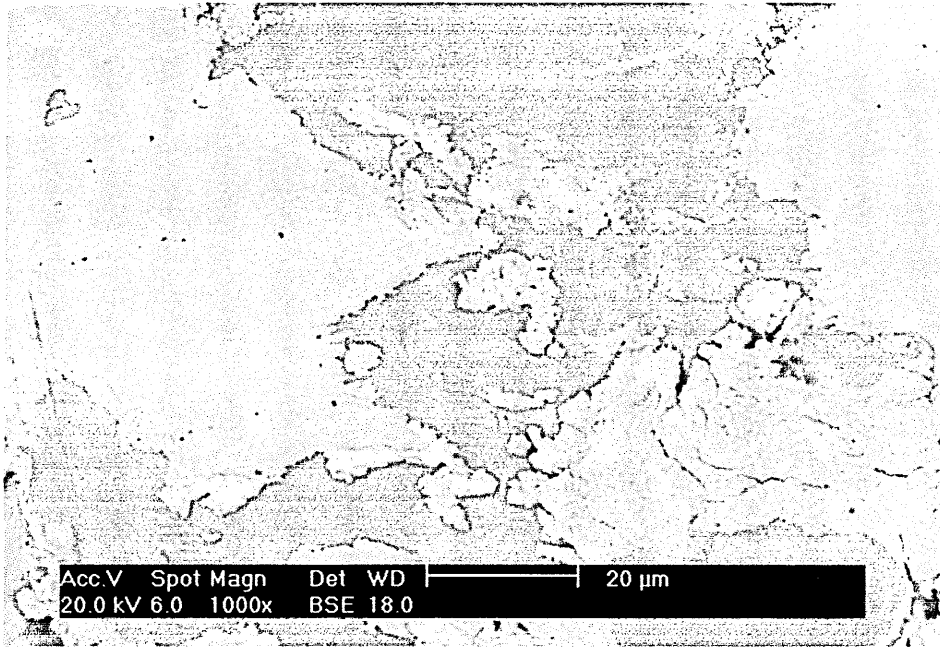


Figure 7.77. BSE SEM image of tinplate with dark markings.

The EDX analysis, figure 7.78, shows that there is no other identified element. These results were repeated over the surface of the samples and were found to be consistently repeatable.

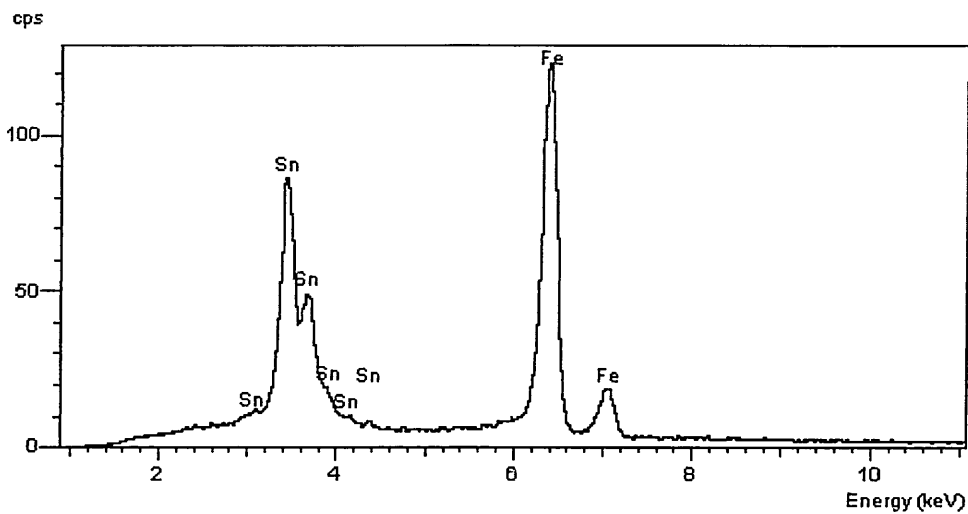


Figure 7.78. EDX analysis of tinplate with dark markings.

Etching the marked material resulted in the removal of tin, shown in the BSE image figure 7.79, with the corresponding SE image still showing a very rough surface, figure 7.80 though generally without the globular features associated with the tin deposits.

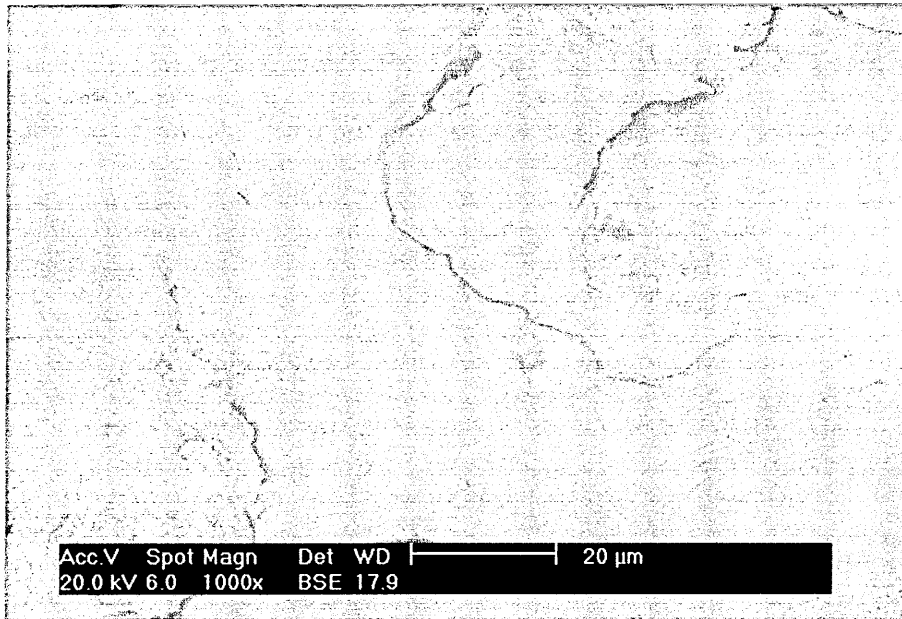


Figure 7.79. BSE SEM image of etched marked tinplate.

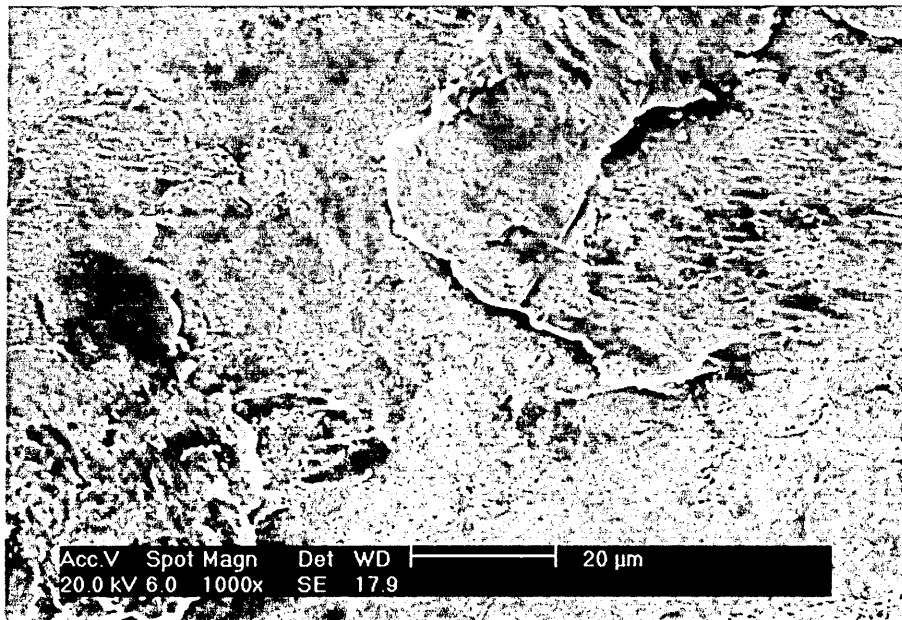


Figure 7.80. SE SEM image of etched marked tinplate.

The EDX analysis, figure 7.81, shows greater iron signal as expected with the overlayer of tin removed and some tin signal probably arising from the FeSn<sub>2</sub> intermetallics as identified using CEMS that are evident on the sample surface.

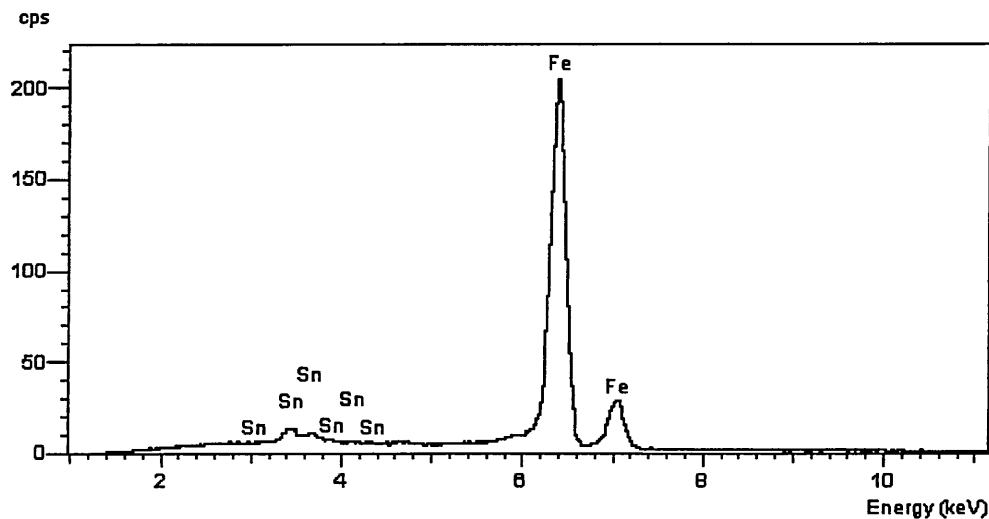


Figure 7.81. EDX analysis of etched marked tinplate.

### 7.10.3 Summary of Analysis of Tinplate With Defects

In conclusion it is difficult to identify the dark markings. CEMS analysis revealed a slightly greater signal for iron in the marked areas prior to etching and again after etching. The area without dark markings exhibited a greater FeSn<sub>2</sub> signal. The SEM analysis showed two very different surfaces with the unmarked area being composed of a tin coated surface with exposed iron islands and the marked area composed of more globular formation of tin on the steel substrate. Thus it appears likely that the dark markings are contamination on the steel substrate prior to plating that prevents tin forming a homogenous layer.

## **7.11. Results of Heat Treatment of Tinplate**

A series of samples were polished and then coated with tin as described in section 5.3.2. This procedure was critical in the investigation of heat treatments as the same weight of tin per unit area and thus the same thickness should be deposited on each sample to permit a direct comparison between the results. Table 7.22 shows the depth of the deposited tin as determined through measurements of the sample weights before and after deposition on ten separate samples. Covered areas are based on having both faces of the sample available for deposition and this area being 2 cm × 2 cm per side.

Sample ID	Mass before g ± 0.0001 g	Mass after g ± 0.0001 g	Mass deposited g ± 0.0002 g	Area m <sup>2</sup> ± 0.0001 m <sup>2</sup>	Depth μm ± 0.15 μm
1	0.6614	0.6740	0.0126	0.0008	2.16
2	0.7010	0.7131	0.0121	0.0008	2.07
3	0.7484	0.7609	0.0125	0.0008	2.14
4	0.7536	0.7665	0.0129	0.0008	2.21
5	0.6899	0.7017	0.0118	0.0008	2.02
6	0.7797	0.7922	0.0125	0.0008	2.14
7	0.6895	0.7011	0.0116	0.0008	1.99
8	0.6708	0.6822	0.0114	0.0008	1.95
9	0.6708	0.6825	0.0117	0.0008	2.00
10	0.6984	0.7095	0.0111	0.0008	1.90

Table 7.22. Table for depths of tin layer in electrodeposition.

Thus a depth of approximately 2 μm of tin was deposited on the substrate surfaces, assuming a compact layer.

### 7.11.1 SEM Analysis of Electrodeposited Tinplate

As can be seen from the SEM results (figures 7.82 and 7.83) the deposited layer is not particularly compact. Therefore the depth of the tin layer will be larger than the calculated 2  $\mu\text{m}$  and have an uneven microtexture.

Most of the surface was covered in globule or crystal like formations with fairly even deposition and very few raised areas where deposition had been more prevalent. Thus the surface is considered to be reasonably uniform. Figure 7.82 shows an area typical of the deposited surface, covered almost entirely with tin except for a few small areas, such as that found in the central top area of the image, shown as a dark patch, where the substrate shows through. Higher magnification, such as in figure 7.83, shows the crystal like formations, which appear to have no preferred orientation.

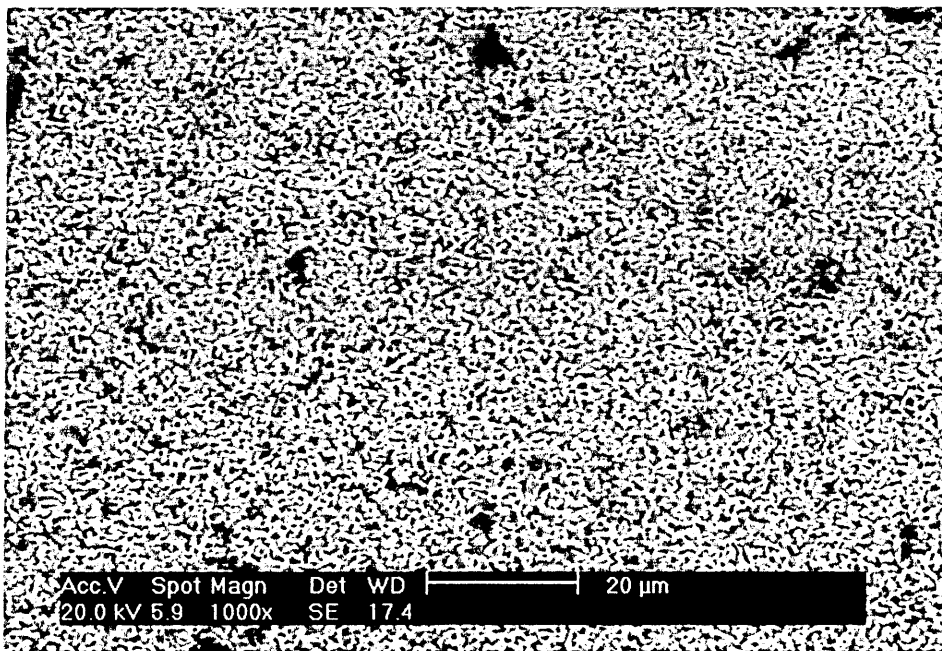


Figure 7.82. SE SEM image of electrodeposited polished substrate.

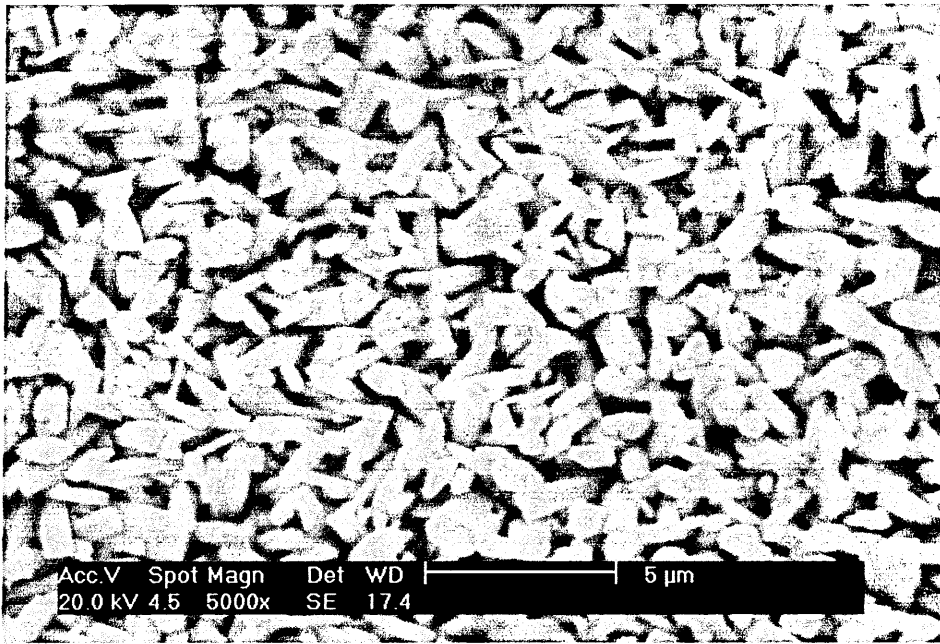


Figure 7.83. SE SEM image of electrodeposited polished substrate at 5000× magnification.

#### 7.11.2 Discussion of Intermetallic Formation During Heat Treatment Process

The heat treatments were a critical part of this experiment. A more efficient and controllable heat treatment system than that previously used (section 7.6) was devised and constructed in order to analyse the intermetallic formation parameters. The heat treatment of the tinplate samples causes the growth of more intermetallics within the samples. Intermetallics are formed in these samples when diffusion between the tin and steel occurs. Studies by Barry and Thwaites [12] found the more rounded form of the crystallites produced by solid phase nucleation and growth (below 232°C) to be more compact, which is thought to be desirable for corrosion resistance.

The different reactions that can take place in metallic binary systems are of two types, eutectic and peritectic. The peritectic type reactions are considered here as they occur

when the components have large differences in melting points as opposed to eutectic type reactions, which occur when the melting points of the components are relatively similar [13]. Two possible reactions then occur depending on the state of the two elemental components. Peritectic reactions are those between a liquid and a solid that result in a new solid phase, whereas a peritectoid reaction is that between two solids to form a new solid phase.

At the extreme of the temperature range reached in the processing here, which is 240 °C, only FeSn and FeSn<sub>2</sub> can be formed peritectically as the tin is molten whilst the steel remains in solid form. However a number of studies have shown FeSn<sub>2</sub> to form below the melting point of tin [7,12] but have not quantified the lower limits or particularly analysed the time for intermetallics to form. The other intermetallics cannot be formed as the temperatures are not conducive to their production nor is the constitution of the boundary between the iron and tin suitable for the reactions to take place.

The alloy formed then depends on temperature and concentration of elements at the boundary. In the cases described here at the interface the weight percentage of tin at the interface is regarded as ~100%. Thus FeSn<sub>2</sub> is preferentially formed early in any heat induced diffusion as can be seen from the phase diagrams in figures 4.5 and 4.6. Heat treatment above 500 °C gives rise to production of FeSn at the interface as shown in a previous study [7], however these temperatures are not reached in this study.

During the heating procedure diffusion occurs such that the new phase effectively coats the solid Fe so that it is insulated from further reaction [14] and slows any diffusion. Although with an intermetallic layer present the diffusion is slowed it is not stopped and further diffusion will occur giving rise to a slowly increasing intermetallic layer thickness. Longer heat treatments may give rise to FeSn being formed as the effective composition of the surface layer is such that the weight percentage of tin to  $\alpha$ -Fe at the interface is no longer 100% and may reach the condition for FeSn formation. Ujihira [7] found FeSn to form at 400 °C for a 30 minute heat treatment, but again neither this temperature or length of heat treatment are used in this study. Therefore FeSn<sub>2</sub> is the intermetallic that would be expected to form from the heat treatments in this study.

The heat treatments were carried out according to the procedure set out in section 5.3.3 using the furnace arrangement shown in figure 5.10. A series of samples was heat treated at 240 °C for 1, 2, 5 and 10 minutes to investigate the intermetallic formation with time. A second set of samples was heat treated for 2 minutes at temperatures between 190°C and 240°C to investigate the amount of intermetallics formed over the temperature range. This would also help in the identification of the lower detection limit of CEMS by comparing to complementary ICP-MS studies. It is known that in the DWI process the ironing ring temperature peak is around 200 °C [15] and thus it is desirable to have an indication of whether FeSn<sub>2</sub> is formed at this temperature. The samples once heat treated were then etched as in the procedure described in section 5.3.4 to remove all excess tin.

### 7.11.3 $^{57}\text{Fe}$ CEMS Analysis of Varying Time of Heat Treatment

The CEM spectra recorded for the analysis of intermetallic formation with different heat treatment times are shown in figures 7.84 to 7.87. Parameters for the spectra are shown in table 7.23.

All CEM spectra are fitted with sextets for  $\alpha\text{-Fe}$  and  $\text{FeSn}_2$ . The comparison of intermetallics to substrate signal is observed most easily by analysing the relative % area of the sextets calculated from the counts under the respective sextets (table 7.24) the outer peaks of the sextets being fitted by the Recoil fitting program to have mean linewidth and a fixed ratio between them and peaks 2 and 5.

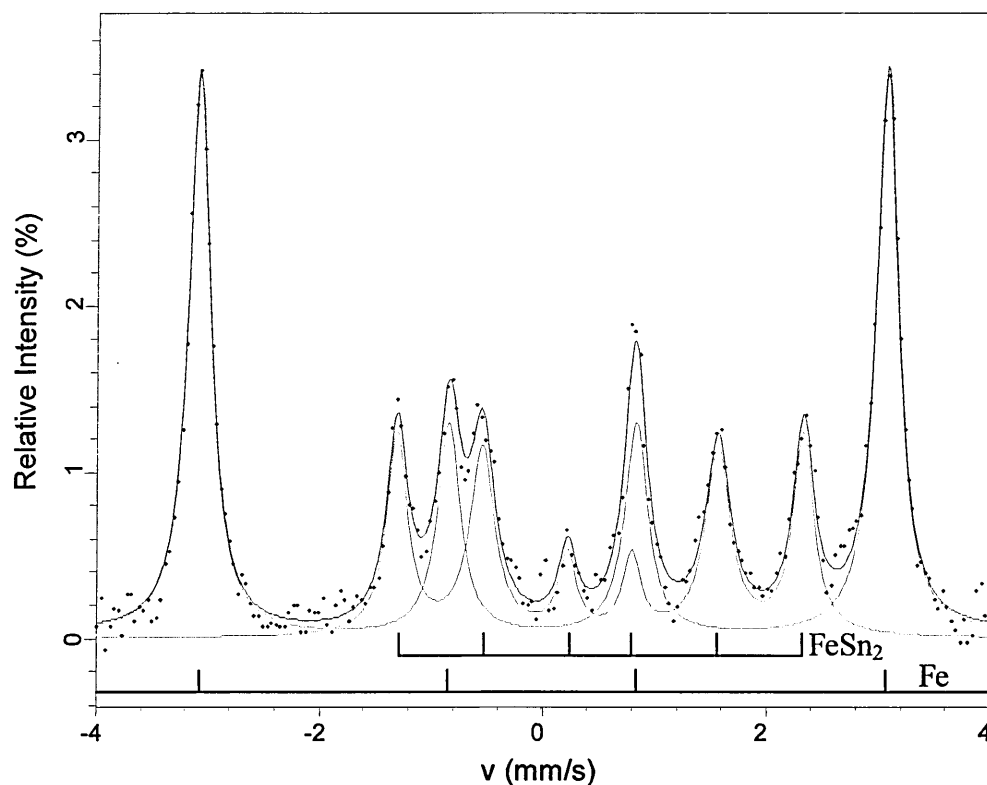


Figure 7.84.  $^{57}\text{Fe}$  CEMS spectrum of sample heated for 1 minute at 240 °C.

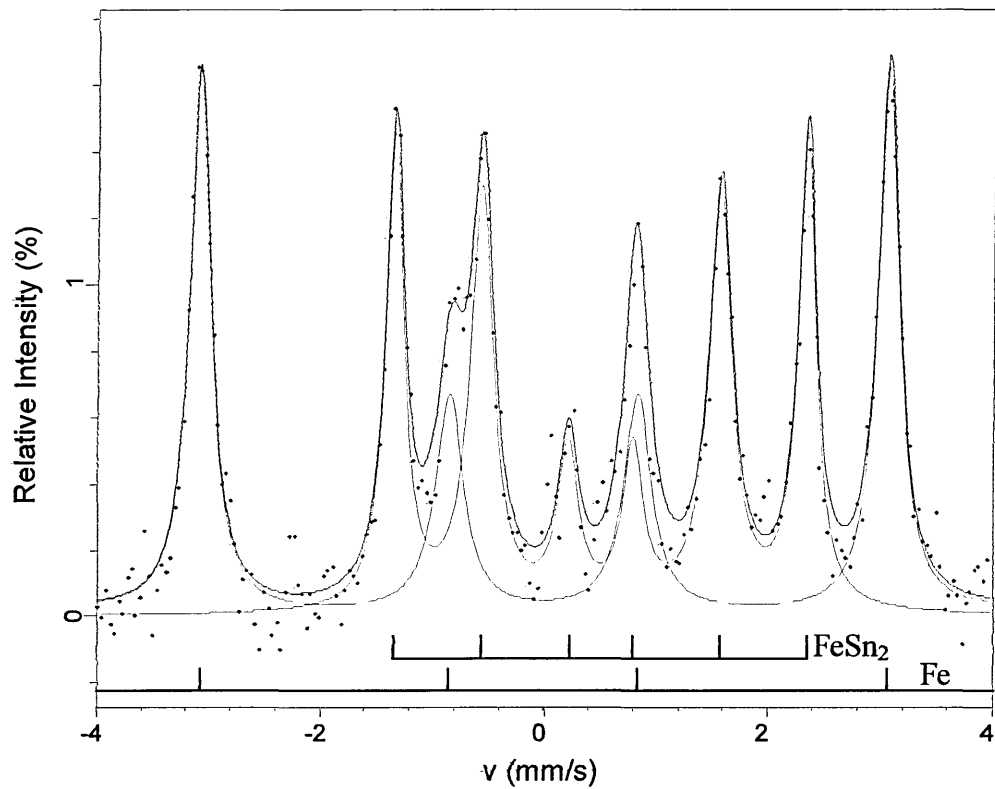


Figure 7.85.  $^{57}\text{Fe}$  CEMS spectrum of sample heated for 2 minutes at 240 °C.

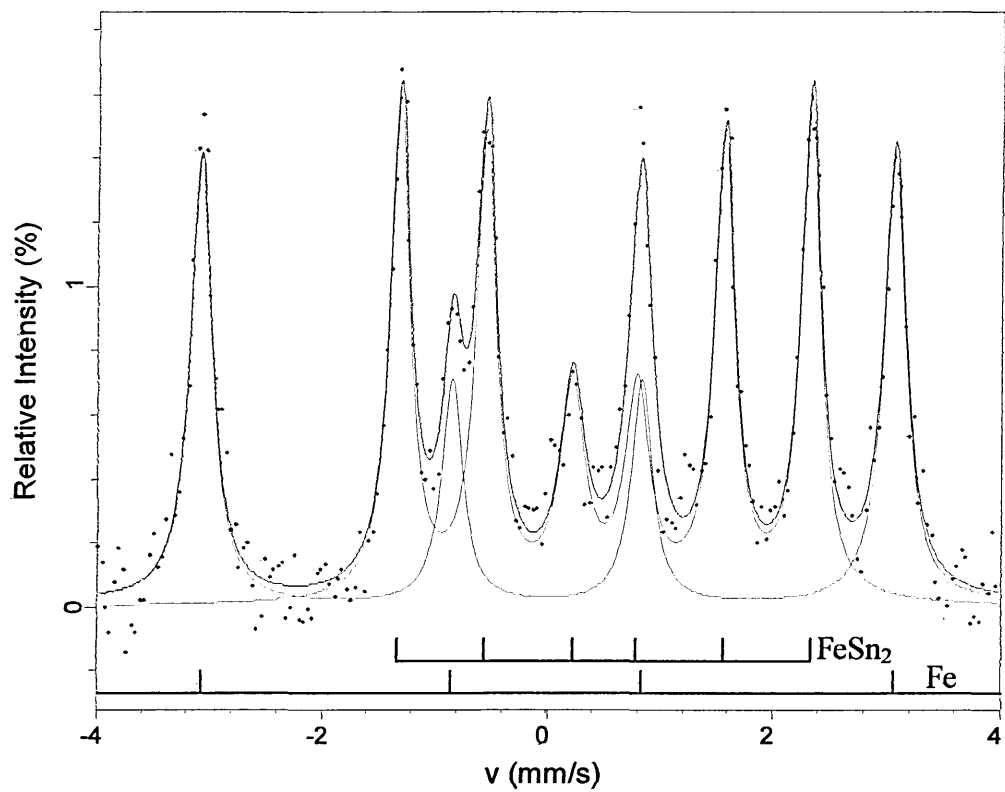


Figure 7.86.  $^{57}\text{Fe}$  CEMS spectrum of sample heated for 5 minutes at 240 °C.

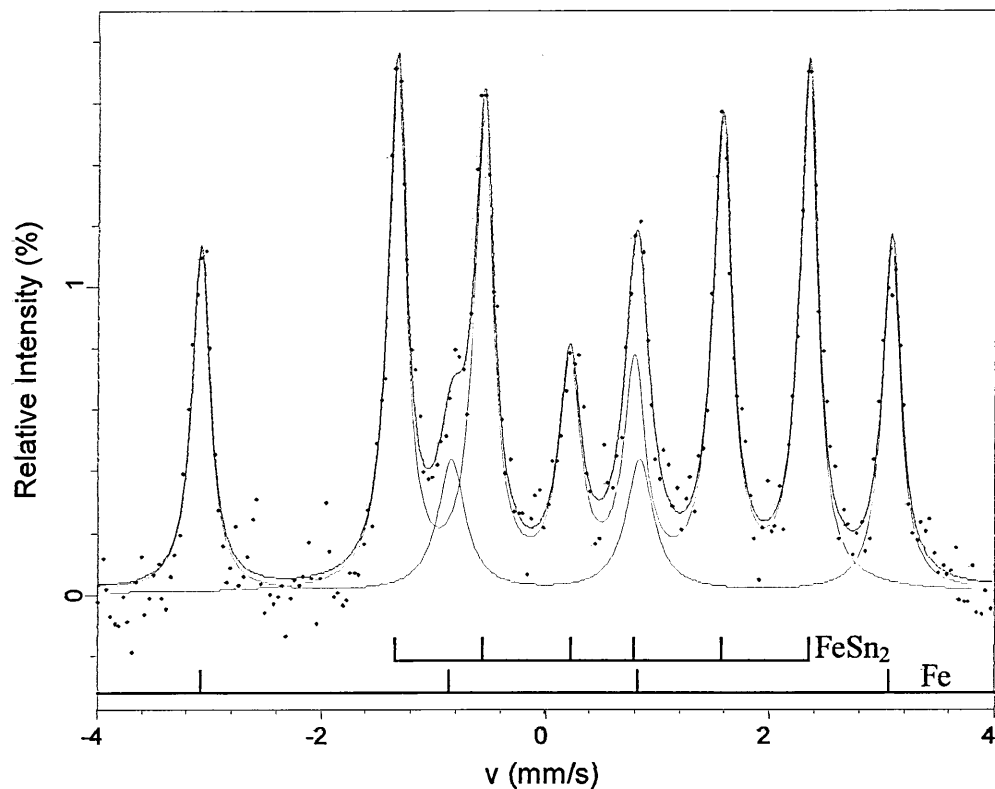


Figure 7.87.  $^{57}\text{Fe}$  CEMS spectrum of sample heated for 10 minutes at 240 °C.

Sample Description	Figure No.	Mössbauer parameters, relative to $\alpha\text{-Fe}$ , at 295 K ( $\pm 0.02 \text{ mm s}^{-1}$ )			Magnetic Hyperfine Field ( $\pm 0.2 \text{ T}$ )	Phase Identified	Peak 2 and 5 Relative Intensity %	$\chi^2$
		$\delta$	$\Delta$	$\Gamma/2$	H			
1 minute at 240 °C	7.84	0.00	0.00	0.12	33.0	$\alpha\text{-Fe}$	3.40	0.709
		0.51	0.00	0.11	11.3	$\text{FeSn}_2$	1.15	
2 minutes at 240 °C	7.85	-0.01	0.00	0.13	33.0	$\alpha\text{-Fe}$	2.65	0.638
		0.50	0.00	0.11	11.4	$\text{FeSn}_2$	1.30	
5 minutes at 240 °C	7.86	-0.01	0.00	0.12	32.9	$\alpha\text{-Fe}$	1.40	0.614
		0.50	0.00	0.11	11.3	$\text{FeSn}_2$	1.50	
10 minutes at 240 °C	7.87	0.00	0.00	0.13	33.0	$\alpha\text{-Fe}$	1.10	0.457
		0.50	0.00	0.11	11.4	$\text{FeSn}_2$	1.55	

Table 7.23. Parameters from analysis of intermetallic formation with different heat treatment times.

The decrease in the rate of increase of intermetallic signal area with increasing time of heat treatment, figure 7.88, shows that the intermetallic layer is increasing whilst the

substrate signal is decreasing. However at 240 °C it is clear from the series of spectra that the actual increase in intermetallics over time is very small whilst the decrease in iron signal from the substrate is comparatively large, especially in the 1 to 2 minute range.

There are two interlinked factors which contribute to a slow down of intermetallic production, firstly the FeSn<sub>2</sub> intermetallic layer forms a barrier to further diffusion, as discussed previously, and therefore further intermetallic production, and secondly the free tin is used up to form the FeSn<sub>2</sub> which leaves less to form further intermetallics. Given a very thin initial tin layer, the resultant intermetallic layer will be limited by the small amount of tin present, thicker tin layers will allow for greater intermetallic thickness.

It is reasonable to assume that after 1 minute at 240 °C the intermetallic production has reached a plateau, most likely due to intermetallic barrier formation since the initial tin layer is reasonably thick at 2 µm. The high surface sensitivity of the CEMS technique would explain the large decrease in the substrate (bulk) signal for a correspondingly small increase in intermetallic (surface) signal. The % areas of the two contributing components of each of the spectra are shown in table 7.24.

Heat Treatment Time (Minutes)	Figure	FeSn <sub>2</sub> Signal %	α-Fe Signal %
1	7.84	25.4	74.6
2	7.85	40.6	59.4
5	7.86	49.0	51.0
10	7.87	56.7	43.3

Table 7.24. Results for varying heat treatment times.

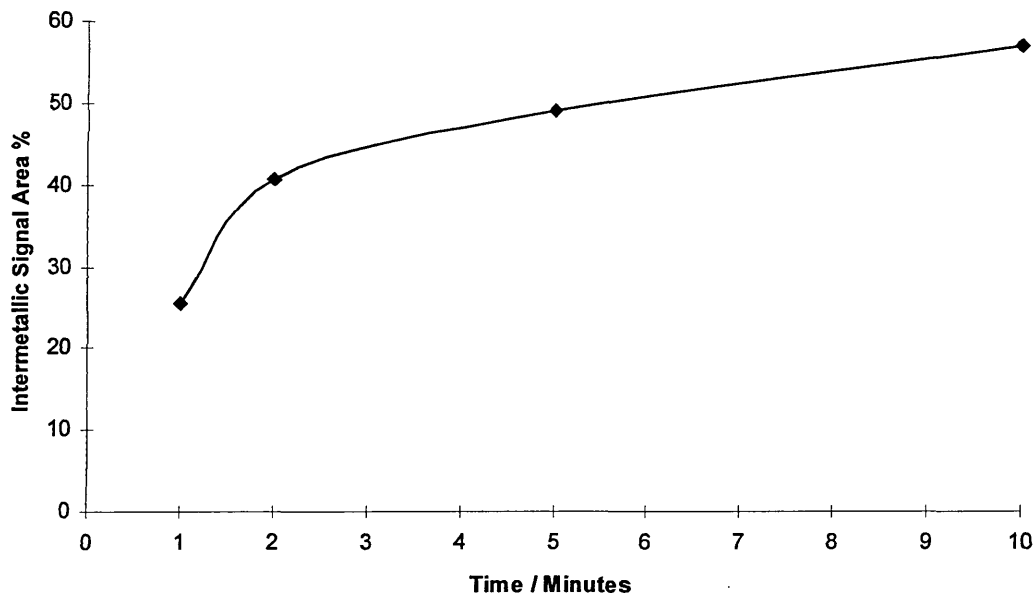


Figure 7.88. Variation of intermetallic signal area for different heating times at 240 °C.

#### 7.11.4 $^{57}\text{Fe}$ CEMS Analysis of Varying Temperature of Heat Treatment

The second set of samples used a constant heating time of 2 minutes but a varying temperature of 190°C to 240°C. This would show at what temperatures the diffusion process occurs and would help in the identification of the lower detection limit of CEMS as once the limit is identified, using CEMS, ICP-MS can be used to find the concentration of tin atoms on the samples and the two results compared to find the sensitivity of the CEMS technique for this particular intermetallic.

The CEM spectra recorded for the analysis of intermetallic formation with different heat treatment temperatures are shown in figures 7.89 to 7.93. Parameters for the spectra are shown in table 7.25.

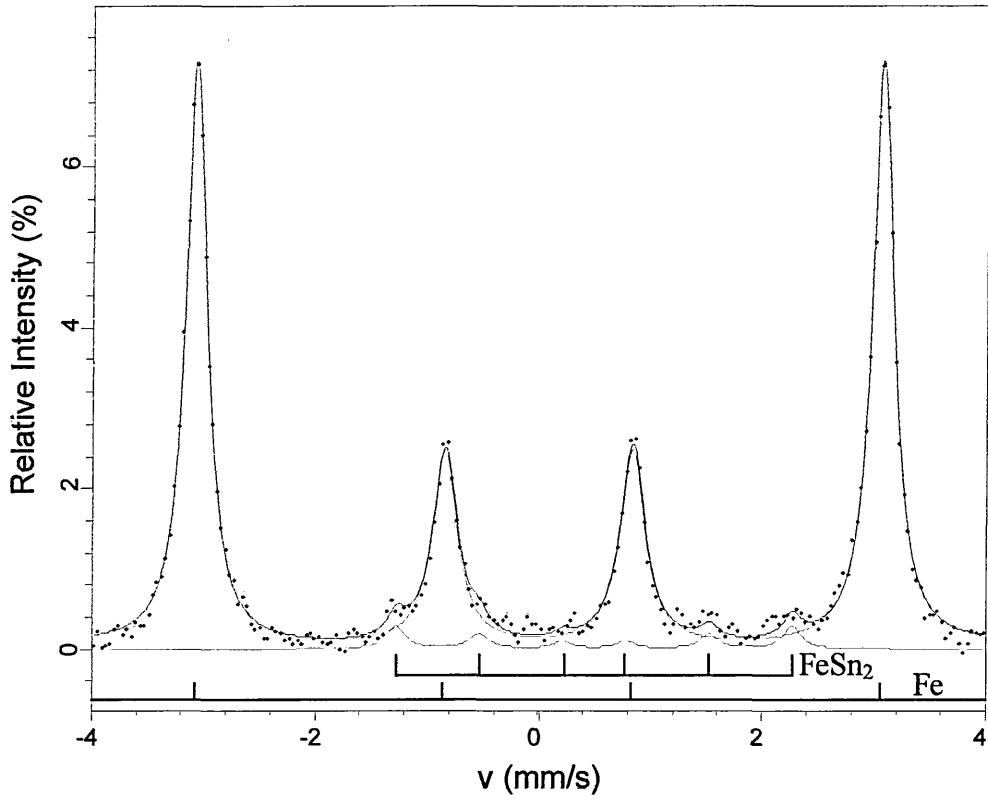


Figure 7.89.  $^{57}\text{Fe}$  CEMS spectrum of sample heated at 190 °C for 2 minutes.

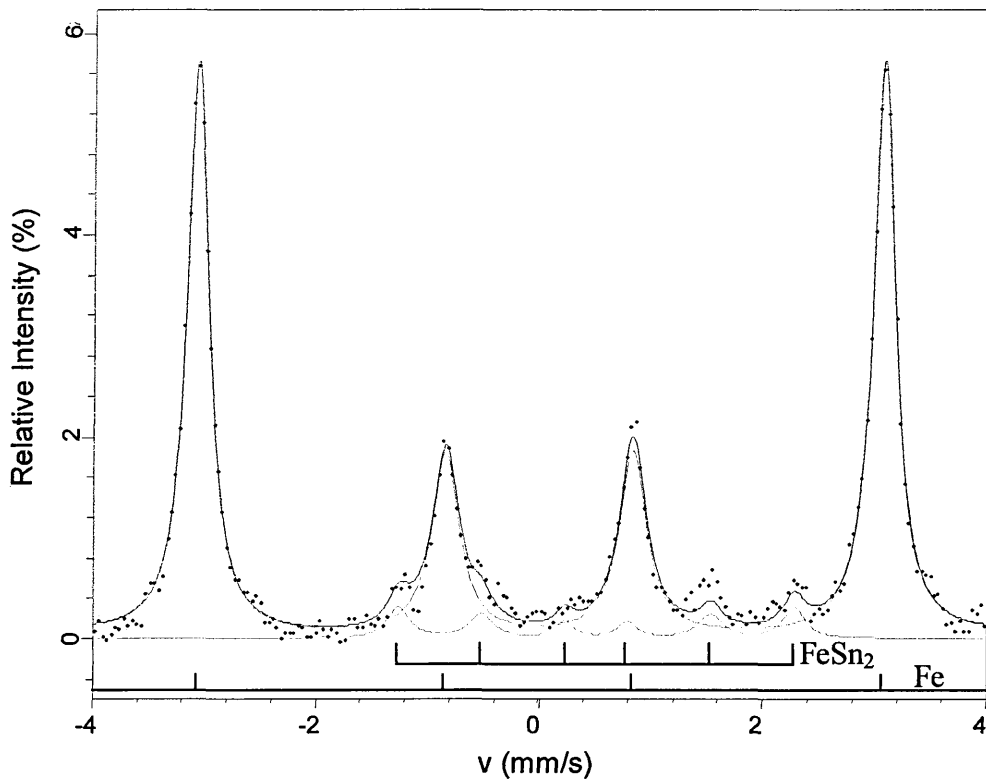


Figure 7.90.  $^{57}\text{Fe}$  CEMS spectrum of sample heated at 200 °C for 2 minutes.

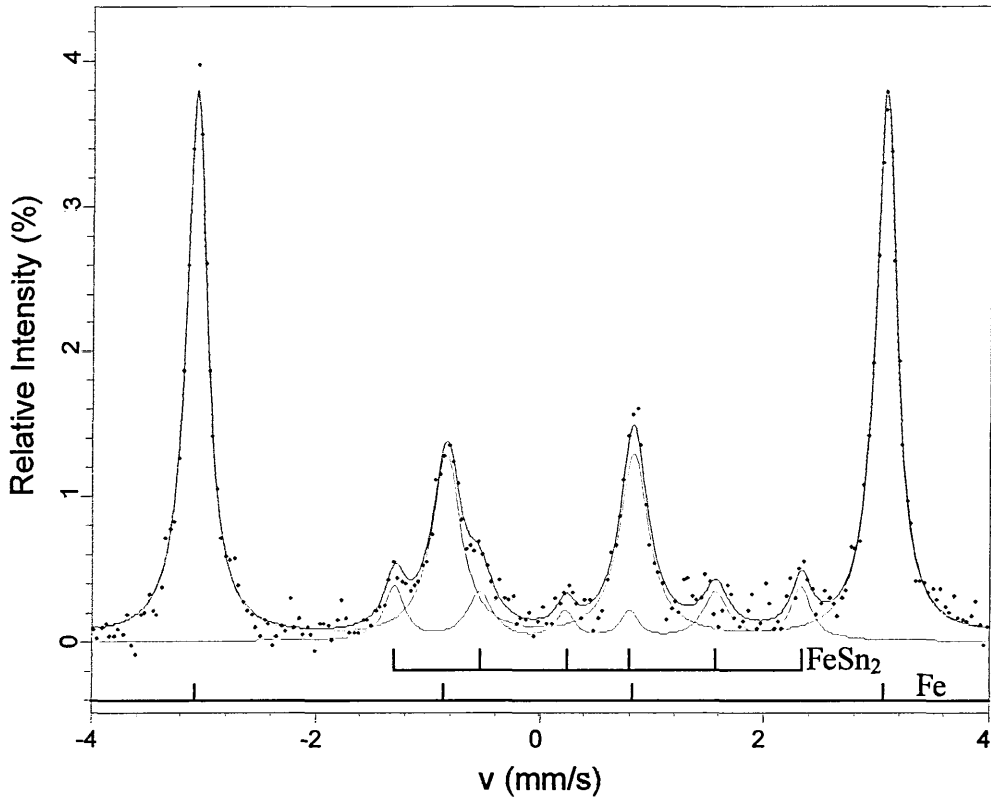


Figure 7.91.  $^{57}\text{Fe}$  CEMS spectrum of sample heated at 210 °C for 2 minutes.

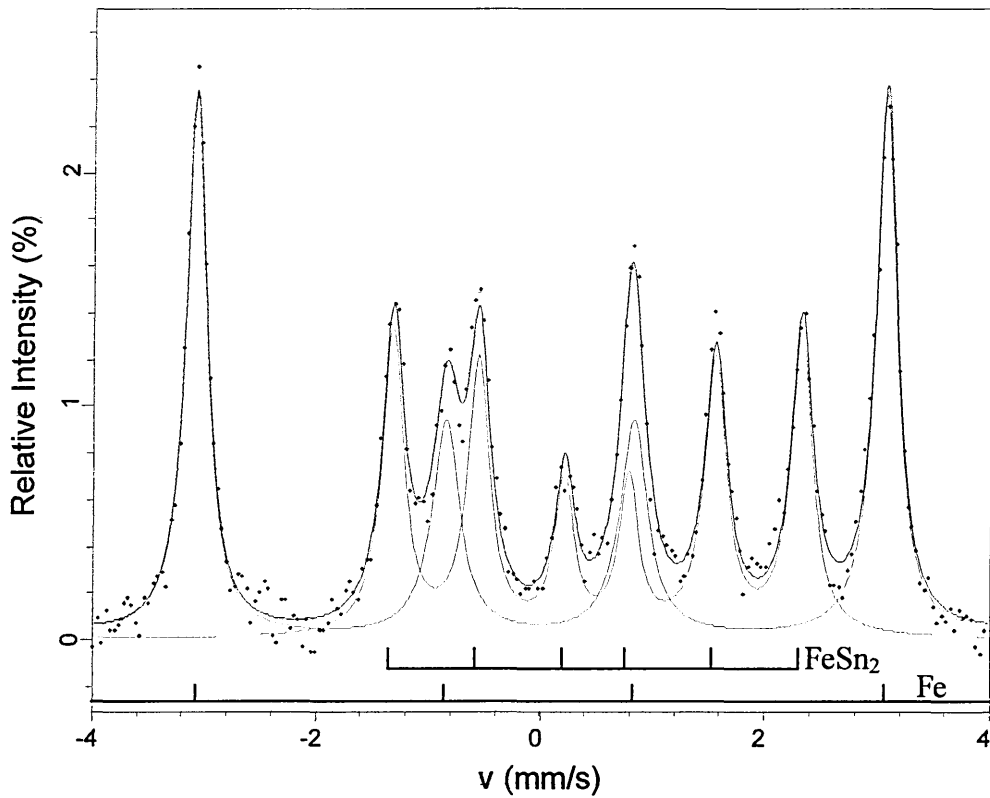


Figure 7.92.  $^{57}\text{Fe}$  CEMS spectrum of sample heated at 220 °C for 2 minutes.

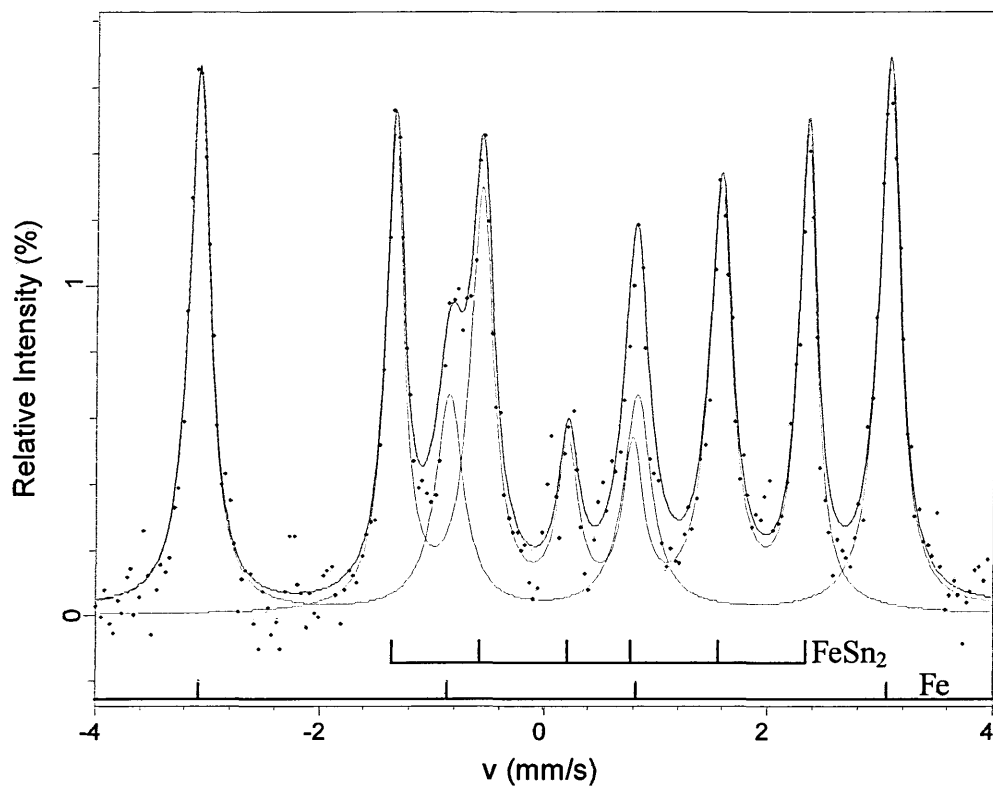


Figure 7.93.  $^{57}\text{Fe}$  CEMS spectrum of sample heated at 240 °C for 2 minutes.

Sample Description	Figure No.	Mössbauer parameters, relative to $\alpha\text{-Fe}$ , at 295 K ( $\pm 0.02 \text{ mm s}^{-1}$ )			Magnetic Hyperfine Field ( $\pm 0.2 \text{ T}$ )	Phase Identified	Peak 2 and 5 Relative Intensity %	$\chi^2$
		$\delta$	$\Delta$	$\Gamma/2$	H			
2 minutes at 190 °C	7.89	0.00	0.00	0.12	33.0	$\alpha\text{-Fe}$	7.30	1.385
		0.50	0.00	0.11	11.0	$\text{FeSn}_2$	0.20	
2 minutes at 200 °C	7.90	0.00	0.00	0.13	32.9	$\alpha\text{-Fe}$	5.75	0.931
		0.51	0.00	0.11	11.0	$\text{FeSn}_2$	0.25	
2 minutes at 210 °C	7.91	0.00	0.00	0.13	32.9	$\alpha\text{-Fe}$	3.80	0.688
		0.52	0.00	0.12	11.3	$\text{FeSn}_2$	0.35	
2 minutes at 220 °C	7.92	0.00	0.00	0.13	33.0	$\alpha\text{-Fe}$	2.35	0.716
		0.50	0.00	0.11	11.3	$\text{FeSn}_2$	1.20	
2 minutes at 240 °C	7.93	-0.01	0.00	0.13	33.0	$\alpha\text{-Fe}$	2.65	0.638
		0.50	0.00	0.11	11.4	$\text{FeSn}_2$	1.30	

Table 7.25. Parameters from analysis of intermetallic formation with different heat treatment temperatures.

Figure 7.89 shows that the diffusion of tin and steel substrate occurs down to temperatures as low as 190 °C where the percentage of the FeSn<sub>2</sub> sextet is only 2.7 % and only just distinguishable from the background. Figure 7.94 shows the variation of intermetallic signal area with temperature of heat treatment. The % areas of the two contributing components of each of the spectra are shown in table 7.26.

Heat Treatment Temperature (°C)	Figure	FeSn <sub>2</sub> Signal %	α-Fe Signal %
190	7.89	2.7	97.3
200	7.90	4.9	95.1
210	7.91	9.2	90.8
220	7.92	34.1	65.9
240	7.93	40.6	59.4

Table 7.26. Results for varying heat treatment temperatures.

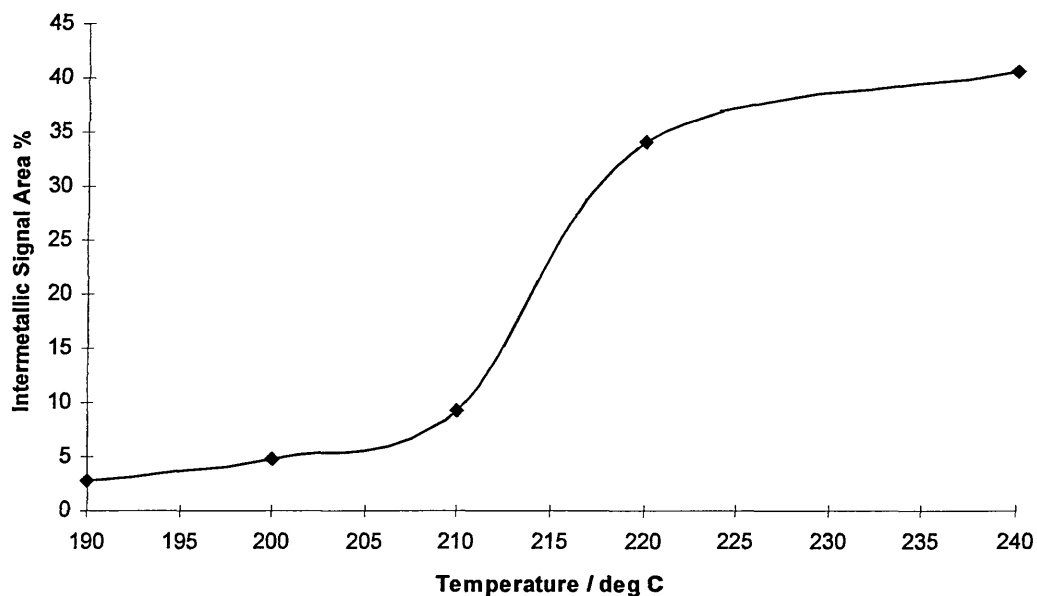


Figure 7.94. Variation of intermetallic signal areas for different heating temperatures, for 2 minute heat treatments.

Much more intermetallic formation occurs at temperatures near the melting point of tin, and it decreases significantly below 220 °C. The decrease in rate of production of intermetallics above 220 °C shows that the diffusion of the tin into the steel substrate is beginning to reach a plateau. As described previously the slow down of intermetallic production is due to the barrier to diffusion that the FeSn<sub>2</sub> intermetallic layer forms and the reduction in free tin on the surface leaving less to form further intermetallics.

#### 7.11.5 ICP-MS Analysis of Heat Treated Samples

Inductively Coupled Plasma Mass Spectrometry (ICP-MS) was then used to find the concentration of tin in the etched samples. By using the Inductively Coupled Plasma Mass Spectrometer the atomic constituents of samples can be identified. Although this does not reveal detailed compositional data such as the presence of intermetallics or oxides it gives an accurate multi-element analysis of a sample that is acid digested in solution. The low detection limit of the ICP-MS means that it is ideally suited to analysing the tinned steel samples that have been etched to leave just the steel substrates and any intermetallics. Since the etching procedure has been shown to remove all metallic tin whilst leaving intermetallics it can be assumed that tin atoms identified by ICP-MS are due to the intermetallics and any SnO<sub>2</sub> that may have subsequently formed on the sample, and since SnO<sub>2</sub> forms on the surface of the tin it is most likely that the majority of the oxide will be removed along with the tin, indeed the XRD studies of similar samples with 2 minute etch treatments showed no tin oxides. This then gives some indication of the detection limit of the CEMS spectrometer. By taking a sample of etched tinned steel that has been previously heat treated to the

point where the intermetallics are just identifiable using CEMS we can analyse the sample, using ICP-MS, to identify the number of tin atoms per million compared to the number of iron atoms per million in the solution.

Three samples were chosen to show this CEMS detection limit. Samples A, B and C were chosen from a series of heat treated and etched tinned steel samples. All samples were heat treated for 2 minutes but at different temperatures. These samples were then all dissolved into solution and then analysed, by using the process identified in section 6.5.

Table 7.27 shows the results from ICP-MS analysis and details of the samples. The values quoted are,  $x$ , the  $\text{mg l}^{-1}$  value detected by the ICP-MS technique and  $s$ , the standard deviation associated with that value.

Sample Identification	Sample Parameters	$x$ (Sn) $\text{mg l}^{-1}$	$s$ (Sn)	$x$ (Fe) $\text{mg l}^{-1}$	$s$ (Fe)
Sample A	240°C for 2 Minutes	21.35	0.211	709	3.02
Sample B	200°C for 2 Minutes	19.24	0.183	776	1.42
Sample C	190°C for 2 Minutes	18.75	0.210	766	1.23

Table 7.27. ICP-MS results.

As the samples had been etched for two minutes following the heat treatments, all of the tin present in the ICP-MS results is presumed to arise from the tin contained within the intermetallics. Resolving these results into percentages of tin and iron it is seen that the samples follow a trend that is expected in that the level of tin identified reduces as

the temperature of heat treatment reduces and thus the level of intermetallics formed reduces. For sample A, which was heat treated at 240 °C - beyond the melting point of tin, 2.92% of the sample was identified as tin and 97.08% as iron. The CEMS spectrum for this sample shows an easily identifiable sextet corresponding to FeSn<sub>2</sub> and an equally clear sextet corresponding to the steel substrate.

It has been shown in this study that at 220 °C the sextet for FeSn<sub>2</sub> is still easily identifiable and thus this sample was not analysed using ICP-MS. At 210 °C the FeSn<sub>2</sub> sextet becomes much more difficult to see immediately and at 200 °C that sextet is less than 8% of the total signal, still identifiable, but somewhat convoluted by background noise. This heat treatment temperature of 200 °C corresponds to sample B where ICP-MS has identified 2.42% tin and 97.58% iron.

That is a decrease of 0.5% (or a 14% decrease in total tin) from 240 °C to 200 °C and such a decrease in tin concentration reduced the FeSn<sub>2</sub> component of the CEMS spectra from 43.4% to 7.1%. At 190°C, as shown with sample C, the FeSn<sub>2</sub> sextet contributes approximately 3% of the total signal which has been arbitrarily set as the low level of detection. This corresponds to a 2.39% tin signal and 97.61% iron signal in the ICP-MS. With a heat treatment below 190 °C the signal is unidentifiable from the background.

### 7.11.6 GDOES Analysis of Heat Treated Samples

The depth of the intermetallic layers are not known and so it cannot be ascertained what amount of the intermetallic signal comes from which depth into the sample. Depth profiling using GDOES was carried out to try to provide information on the thickness of intermetallic layers.

GDOES was carried out on a sample which was electrodeposited with tin as described in section 5.3.2 to give a 2  $\mu\text{m}$  coating of tin, heat treated at 240  $^{\circ}\text{C}$  for 2 minutes and then etched to remove the metallic tin not subsumed into the intermetallic layer.

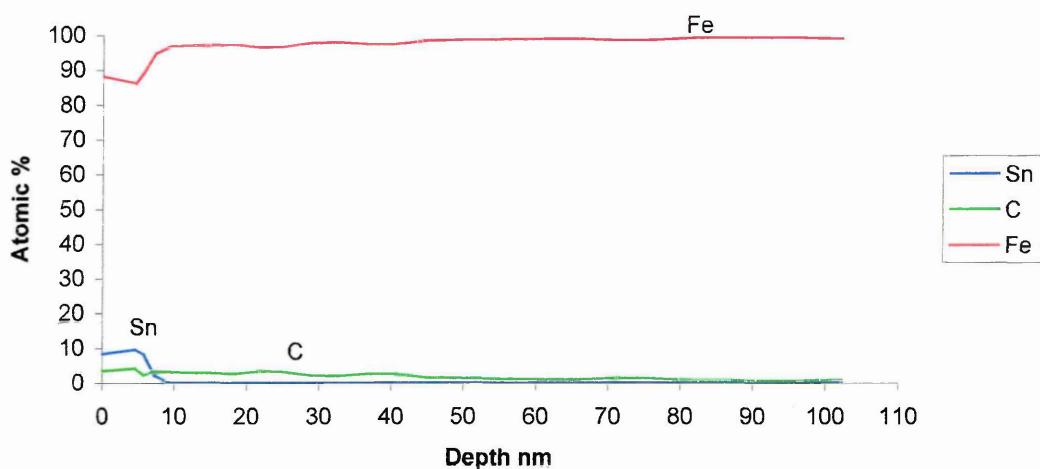


Figure 7.95. GDOES trace of electrodeposited sample heat treated at 240 $^{\circ}\text{C}$  for 2 minutes and then etched.

The GDOES trace in figure 7.95 shows a small amount of tin indicating a thin layer of intermetallic, assuming a minimum of unremoved tin oxide, though with varying sputter rate dictated by the rough sample surface, the value of the thickness determined

(approximately 10 nm) is not to be taken as an extremely accurate intermetallic layer depth reading. The diffusion of the tin into the substrate may have developed this range for which tin could be detected and so the value is not unreasonable for this sample. The amount of carbon near the surface however seems unexpectedly high, some will be due to contamination and some to the content in the steel substrate. It is possible that carbon deposits at the surface due to contamination may have been inadvertently absorbed into the steel surface during heat treatment and this may have diffused further into the substrate.

#### 7.11.7 $^{119}\text{Sn}$ and $^{57}\text{Fe}$ Mössbauer Analysis of Heat Treated DWI Can

A sample of heat treated DWI can taken from the top of the can wall was analysed on the outside using  $^{57}\text{Fe}$  CEMS. The sample was heat treated, using the basic furnace arrangement shown in figure 7.42, at 240 °C for 30 seconds, but not etched. Analysis of the same area of this heat treated DWI sample using  $^{119}\text{Sn}$  Mössbauer spectroscopy was then carried out by Prof. Friedrich E. Wagner at the Technische Universität München, Germany. Figure 7.96 shows the  $^{57}\text{Fe}$  CEMS spectrum and figures 7.97 and 7.98 show two different fits of a single spectrum, obtained using  $^{119}\text{Sn}$  Mössbauer spectroscopy recorded using transmission geometry at 4.2 K. Parameters from the  $^{57}\text{Fe}$  analysis are summarised in table 7.28 and parameters from the  $^{119}\text{Sn}$  analysis are summarised in table 7.29.

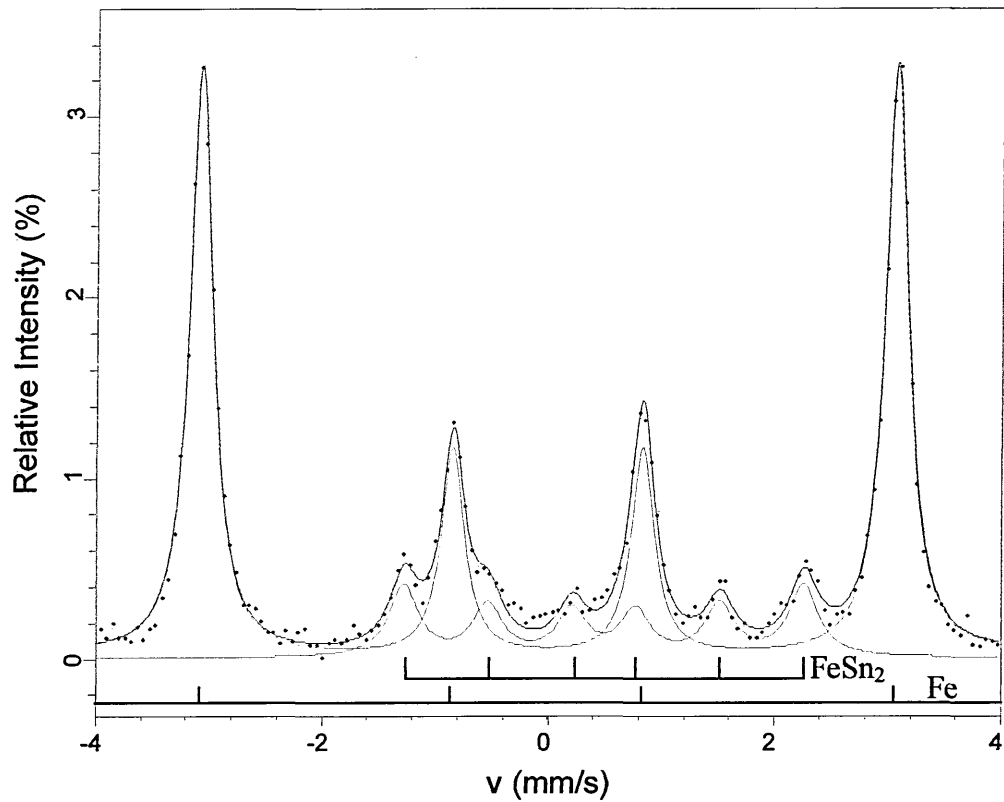


Figure 7.96.  $^{57}\text{Fe}$  CEMS analysis of heat treated DWI can.

Sample Description	Figure No.	Mössbauer parameters, relative to $\alpha\text{-Fe}$ , at 295 K ( $\pm 0.02 \text{ mm s}^{-1}$ )			Magnetic Hyperfine Field ( $\pm 0.2 \text{ T}$ )	Phase Identified	Relative Phase Area %	Peak 2 and 5 Relative Intensity %	$\chi^2$
		$\delta$	$\Delta$	$\Gamma/2$	H				
Heat-treated DWI can	7.96	0.00	0.00	0.12	32.9	$\alpha\text{-Fe}$	86.7	3.30	0.814
		0.50	0.00	0.16	11.0	$\text{FeSn}_2$	13.3	0.35	

Table 7.28. Parameters for  $^{57}\text{Fe}$  CEMS analysis of heat treated DWI can.

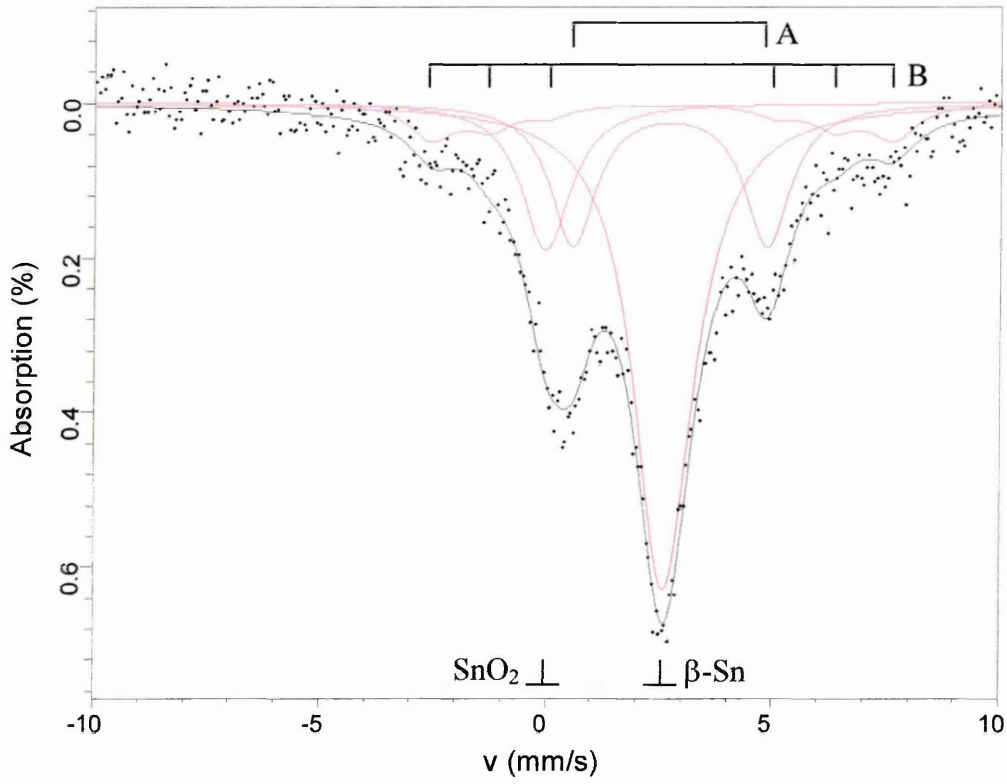


Figure 7.97.  $^{119}\text{Sn}$  Mössbauer analysis of heat treated DWI can.

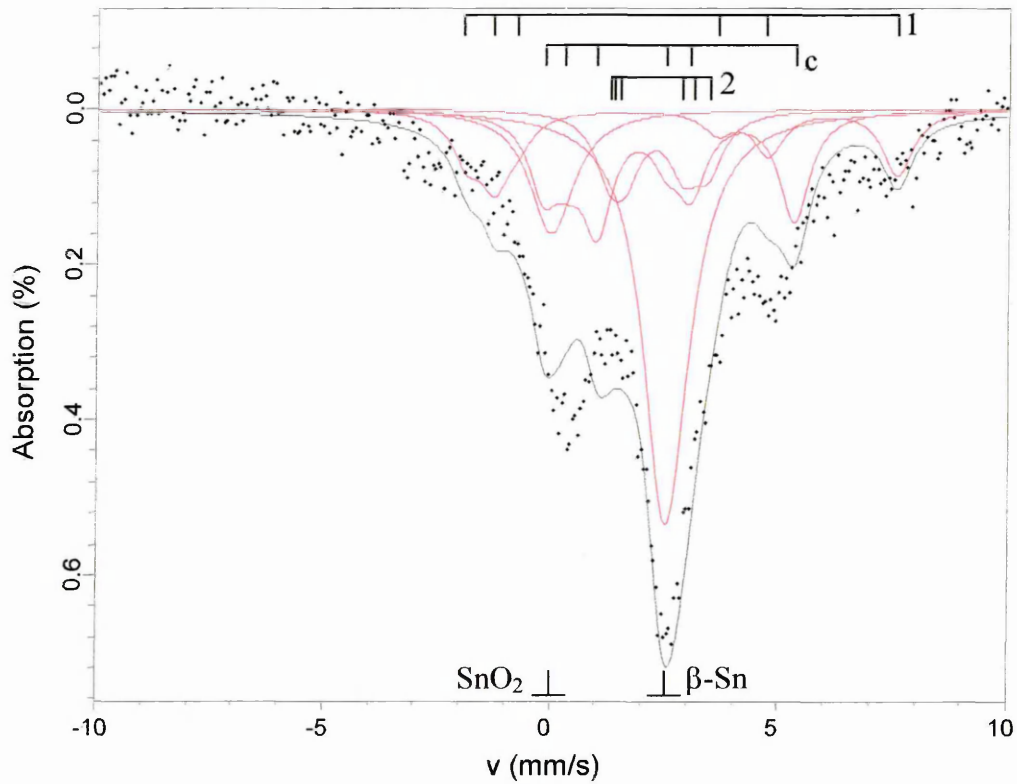


Figure 7.98.  $^{119}\text{Sn}$  Mössbauer analysis of heat treated DWI can with  $\text{FeSn}_2$  fitted.

Sample Description	Figure No.	Mössbauer parameters, relative to $\alpha$ -Fe, at 295 K ( $\pm 0.02 \text{ mm s}^{-1}$ )			Magnetic Hyperfine Field ( $\pm 0.2 \text{ T}$ )	Phase Identified	Relative Phase Area %	$\chi^2$
		$\delta$	$\Delta$	$\Gamma/2$	H			
Heat- treated DWI can	7.97	2.61	0.00	0.79	0.0	$\beta$ -Sn	52.1	1.066
		-0.02	0.00	0.66	0.0	SnO <sub>2</sub>	13.2	
		2.72	4.29	0.61	0.0	Unknown A	23.3	
		2.43	0.00	0.61	7.7	Unknown B	11.4	
Heat- treated DWI can with FeSn <sub>2</sub> fitted	7.98	2.57	0.00	0.69	0.0	$\beta$ -Sn	36.2	2.072
		0.00	0.00	0.48	0.0	SnO <sub>2</sub>	10.9	
		2.30	0.86	0.55	6.7	FeSn <sub>2</sub> (1)	15.4	
		2.30	0.86	0.55	0.4	FeSn <sub>2</sub> (2)	12.1	
		2.30	0.86	0.55	3.3	FeSn <sub>2</sub> (c)	25.4	

Table 7.29. Parameters for <sup>119</sup>Sn Mössbauer analysis of heat treated DWI can.

At 295 K the <sup>119</sup>Sn parameters for FeSn<sub>2</sub> are quoted in literature as being simple, comprising a single sextet having a field of 2.5 T with signs of a small quadrupole interaction and an isomer shift of 2.1 mms<sup>-1</sup> [16]. However the spectrum from the heat treated DWI sample analysed by <sup>119</sup>Sn Mössbauer spectroscopy in this study was taken at 4.2 K where FeSn<sub>2</sub> comprises three components [2], the parameters of which are quoted in section 7.2, creating a more complex spectrum.

The as-produced cans analysed in section 7.2 have very little distortion to the spectra above background that would have indicated clearly the presence of intermetallics and in particular FeSn<sub>2</sub>. Etching the cans as in section 7.3 resulted in spectra, which in some cases indicated a very low level of FeSn<sub>2</sub>. Both unetched and etched cans contained a detectable of SnO<sub>2</sub>, which was not significantly removed during a 90 second etching however metallic tin was completely removed from the etched sample and it has been subsequently observed that etching at 2 minutes removes the SnO<sub>2</sub>.

Heat treating the DWI can form  $\text{FeSn}_2$  as has been previously shown. Thus the heat-treated sample  $^{119}\text{Sn}$  spectrum was expected to show  $\text{FeSn}_2$ . However the spectrum is difficult to interpret. Metallic tin is easily observed with approximately half of the relative peak intensity of the as-produced sample and there is increased  $\text{SnO}_2$  compared to the as-produced sample when analysed using  $^{119}\text{Sn}$  Mössbauer spectroscopy. The increased  $\text{SnO}_2$  is probably formed during the heat-treatment process, which was carried out prior to the development and construction of the furnace arrangement used for the other heat treatments here. There are certainly other components in the spectrum, of which at least some must be due to  $\text{FeSn}_2$ , and no other Fe-Sn intermetallic, when considering the results from  $^{57}\text{Fe}$  analysis, which showed  $\text{FeSn}_2$  as the only Fe-Sn intermetallic present.

The best fit to the  $^{119}\text{Sn}$  data acquired comes from fitting a single sextet and a doublet along with the singlets for  $\beta\text{-Sn}$  and  $\text{SnO}_2$ , though there are possibly more complex components at lower levels. Fitting with parameters from the analysis by Venturini et al. does not provide a particularly good fit as seen in figure 7.98. Even by varying the relative peak intensities, linewidths and component areas the fit does not fit well to the data.

Observed on the spectrum is a large component or combination of components contributing to a peak at around  $5 \text{ mm s}^{-1}$  and there is further significant distortion across the velocity range of the three main observed peaks in the spectrum, which is most clearly observed at the outer extents of the spectrum at  $-2.5 \text{ mm s}^{-1}$  and  $7.5 \text{ mm s}^{-1}$ .

#### 7.11.8 Summary of Analysis of Heat Treatment of Tinfoil

The heat treatments of the tin electrodeposited steel substrates have shown that the formation of FeSn<sub>2</sub> occurs down to 190 °C where the resolution of the CEMS spectrometer is such that this is determined to be the minimum amount of intermetallics observable. This is lower than the temperature observed in DWI processing but is for a length of time much longer than such processing. However this analysis of heat treatment parameters has shown that temperatures observed in the can processing are certainly high enough to form intermetallics, and a small amount will be formed even with short heating times, which will then subsequently affect the mechanical and chemical properties of the cans. GDOES showed the depth range of any tin in the samples to be 10 nm, this would be in the form of FeSn<sub>2</sub>.

#### 7.12. Results of Carbon Coating

In order to investigate the possibility of carbon coatings being suitable for distinguishing between layers and improving surface sensitivity, information regarding photoemission production in this type of coating was required. To this end a series of polished mild steel samples were coated with various thickness coatings of carbon.

A number of polished steel samples were produced and coated with different layers of carbon using the procedure in section 5.3.5. Previous studies of such systems using aluminium [17], copper [18] and gold [19] coatings showed the opposite of what was expected in that the substrate signal actually initially increased due to the production of

photoelectrons in the coating layer adding to the signal observed. After a certain coating thickness, which depends on coating material, the signal begins to decrease as the photoelectron production becomes less significant compared to the dampening effect of the inert layer.

This analysis using carbon would show how significant photoelectron production is compared to the dampening effect of carbon. The carbon coating would then be applied to multilayer systems to see if improved signal differentiation between near surface layer and substrate could be observed.

Thickness approximations were calculated from the mass of carbon evaporated in the coater as shown in Appendix 1. The carbon is sputtered from the carbon source, which consists of a pointed carbon rod forced against a second rod with a 45° angle surface. The travel of this rod can be fixed so that a certain amount of carbon is evaporated.

#### 7.12.1 Profilometer Measurements of Carbon Thickness

When coating the respective polished steel samples with carbon, a second sample was coated with a masked off area at the same time within close proximity of the first. Using a profilometer the step in the surface from the polished steel to the carbon, produced at the mask interface, can be measured. The profilometer detects the phase of a reflected laser beam and a dedicated software program calculates the different distances observed across the surface of a specimen.

Figures 7.99 to 7.102 show the results from the profilometer with varying carbon thicknesses corresponding to carbon rod travels during deposition of 3, 4, 5 and 6 mm respectively.

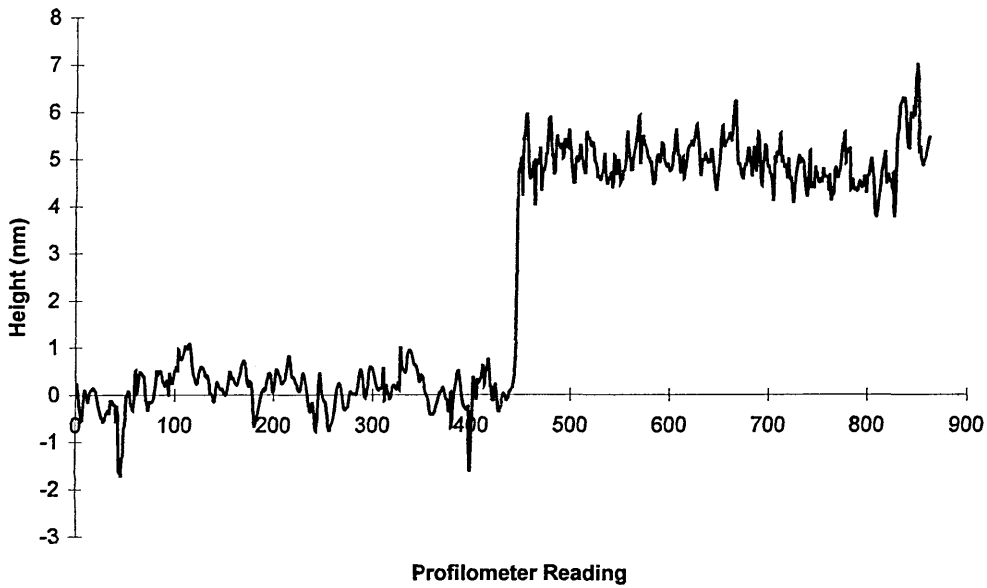


Figure 7.99. Profilometer graph showing interface between uncoated and carbon coated surfaces for 3mm carbon rod travel.

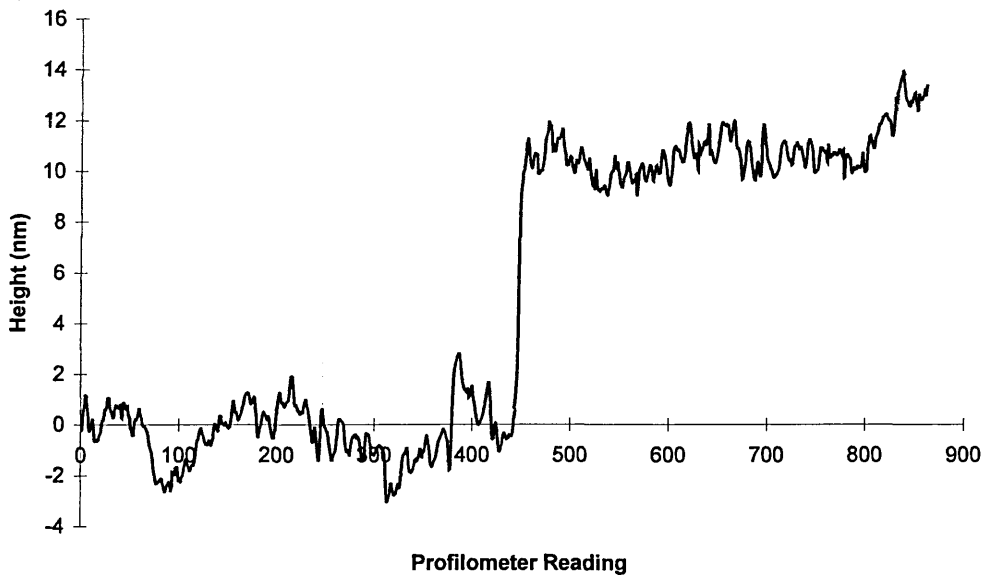


Figure 7.100. Profilometer graph showing interface between uncoated and carbon coated surfaces for 4mm carbon rod travel.

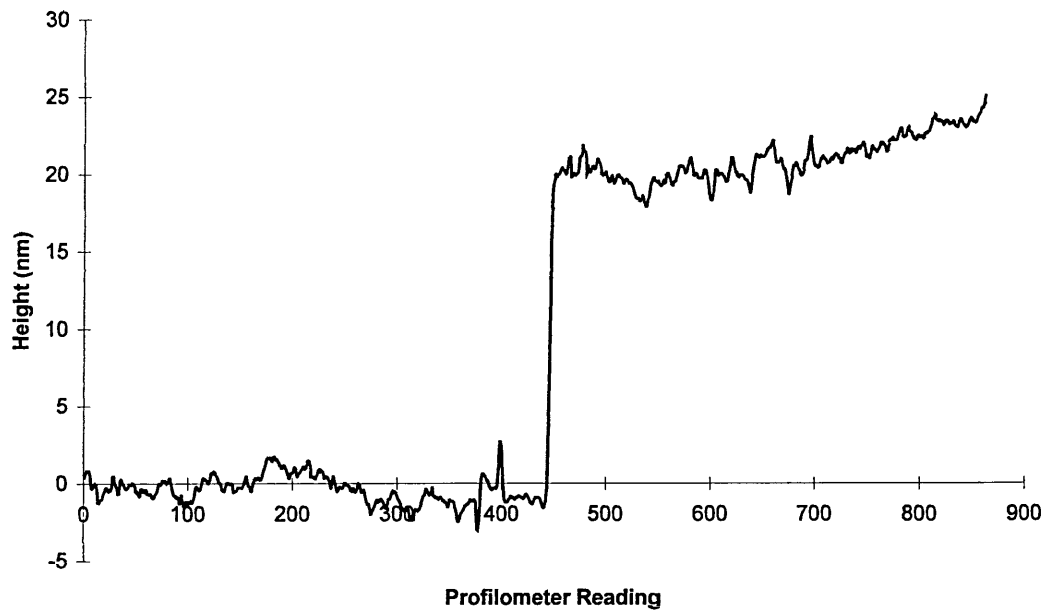


Figure 7.101. Profilometer graph showing interface between uncoated and carbon coated surfaces for 5mm carbon rod travel.

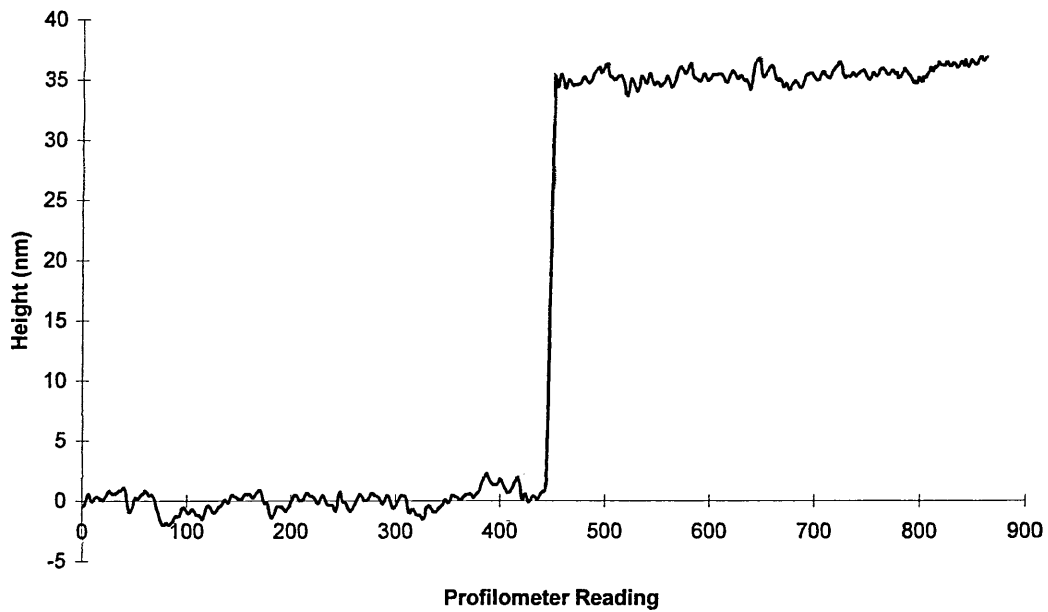


Figure 7.102. Profilometer graph showing interface between uncoated and carbon coated surfaces for 6mm carbon rod travel.

The roughness on the surface is due to some roughness in the polished mild steel surface and also the roughness of the evaporated carbon coating. The samples are not entirely flat so away from the interface the thickness appears to increase in a number of the samples, particularly evident in 7.101. However this is due to slight curvature of the steel substrates.

A deposited carbon thickness of approximately 5.0 nm is observed at the interface of the first sample, 10.3 nm at the interface of the second sample, 19.9 nm on the third sample and 35.1 nm on the fourth sample. These values were calculated as the average of the first two hundred profilometer readings after the carbon interface, which reduces any effect from sample curvature whilst giving a reasonable sample range.

These measured values differ from the calculated values because as the carbon is deposited on the samples the dynamics of the evaporation changes, the contact area increases as the sharpened rod decreases giving rise to more evaporation of carbon onto the samples but also elsewhere including back onto the rods. Thus the calculations above are likely to overestimate the carbon thickness values for larger carbon rod travels. The values taken from both the calculations and the experimentally derived values must be considered to be estimates as no direct measurement of the carbon thickness on the samples was found to be possible. Using GDOES to attempt thickness calculations proved to be of no practical use since the results were of lower resolution than those obtained from the profilometer on the control samples.

### 7.12.2 $^{57}\text{Fe}$ CEMS Analysis of Carbon Coated Polished Steel Samples

The effect of the photoemissions from the carbon coating can be seen from the series of Mössbauer spectra in figures 7.103 to 7.107 and the graphs in figures 7.108 and 7.109, which show the variation of percent effect and sextet area as the coating thickness increases. Parameters for the spectra fitting are shown in table 7.30.

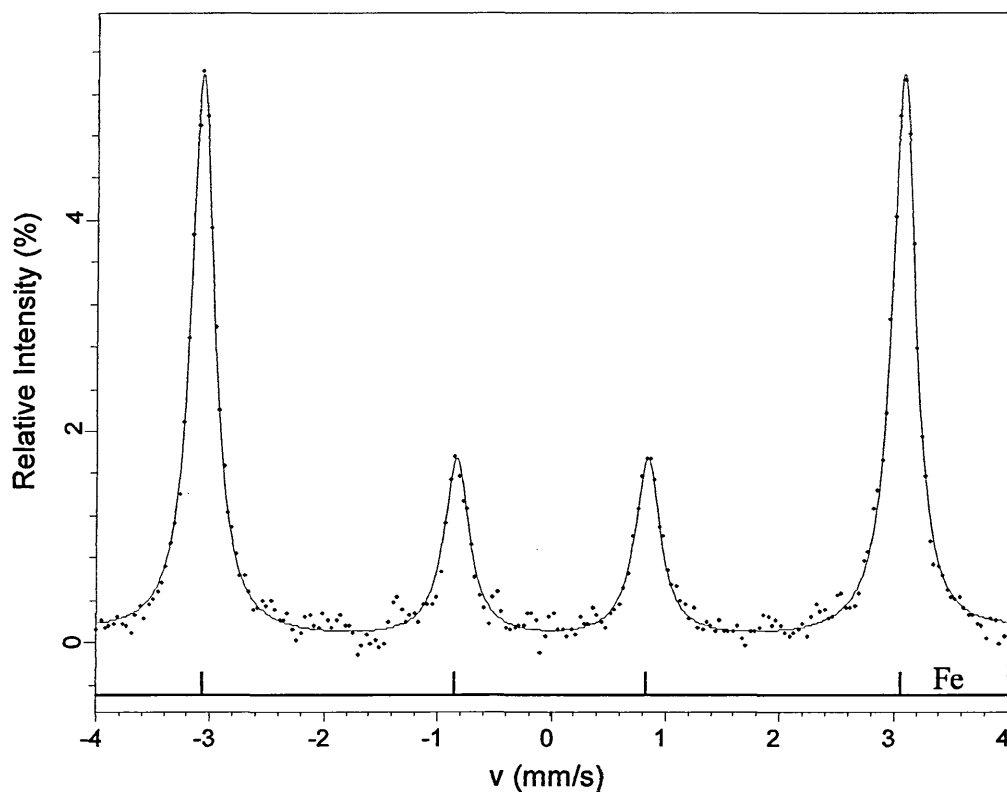


Figure 7.103. Mössbauer spectrum of the polished steel substrate with no carbon coating.

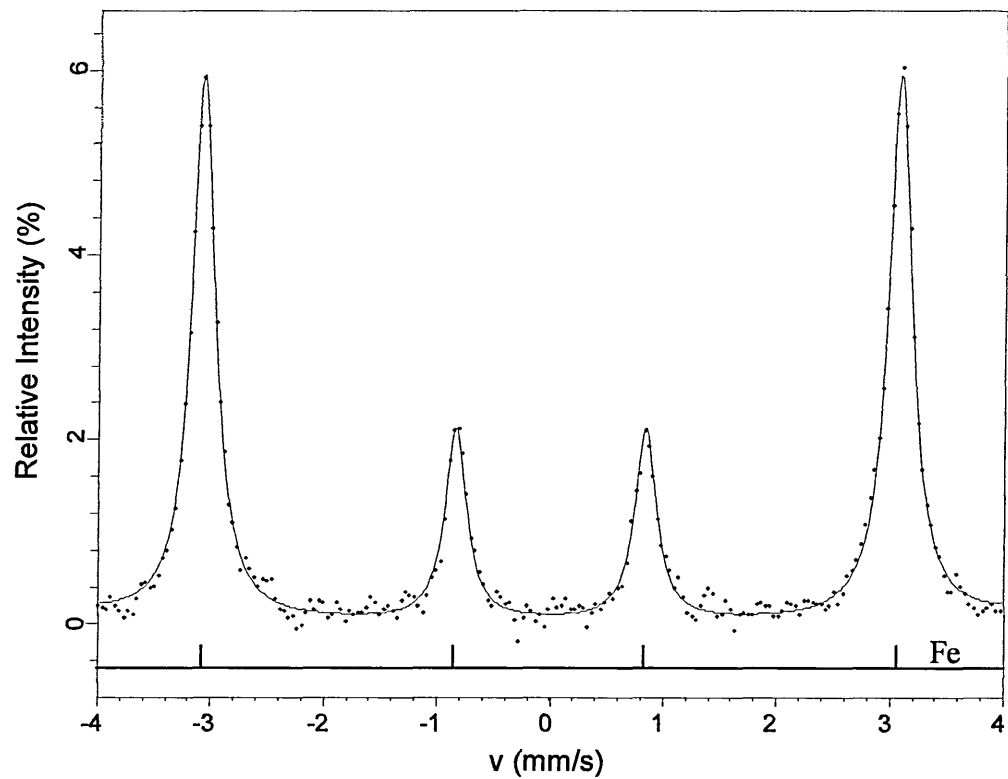


Figure 7.104. Mössbauer spectrum of the polished steel substrate with 5.0 nm carbon coating.

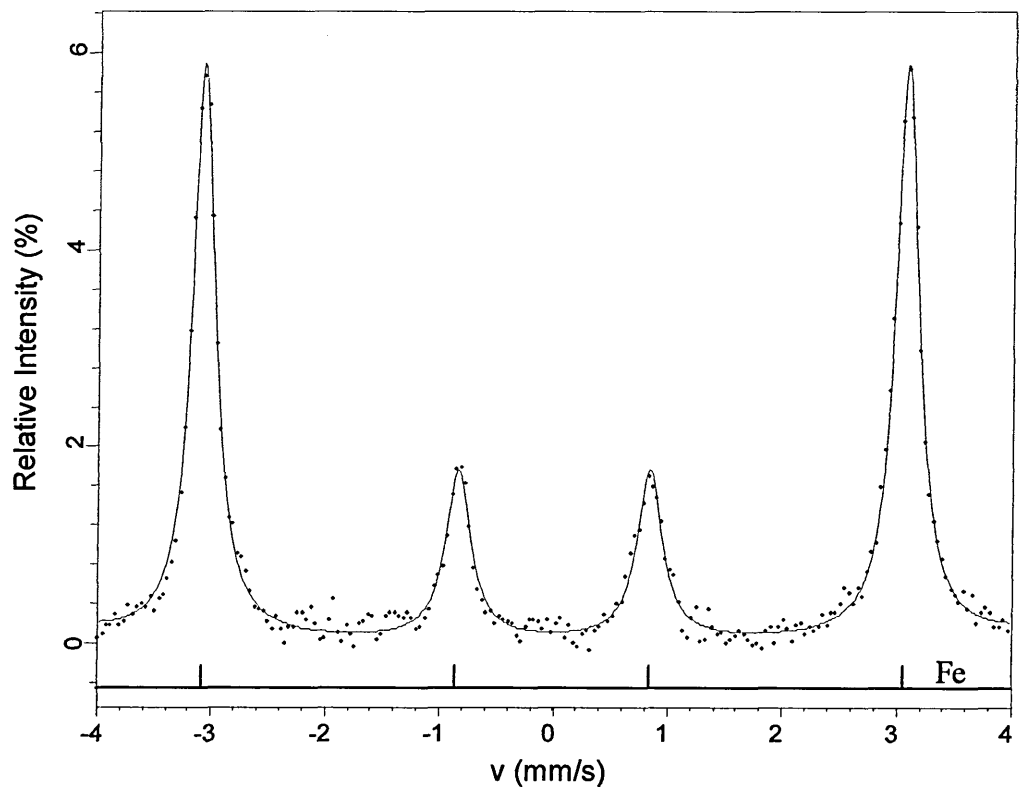


Figure 7.105. Mössbauer spectrum of the polished steel substrate with 10.3 nm carbon coating.

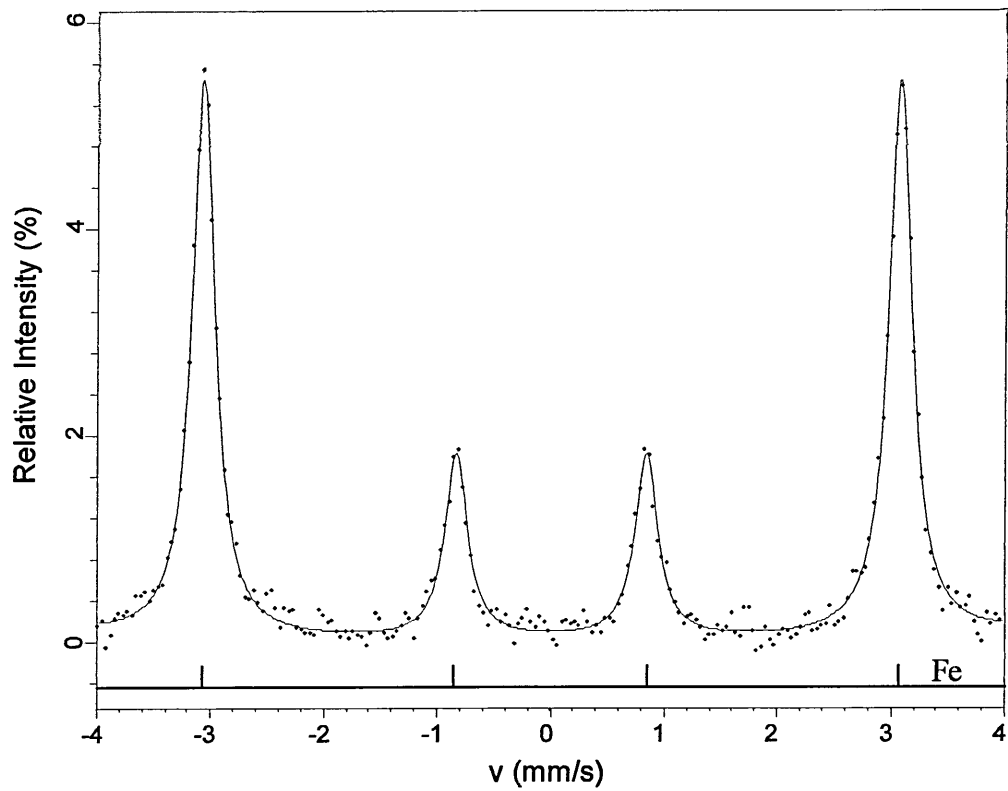


Figure 7.106. Mössbauer spectrum of the polished steel substrate with 19.9 nm carbon coating.

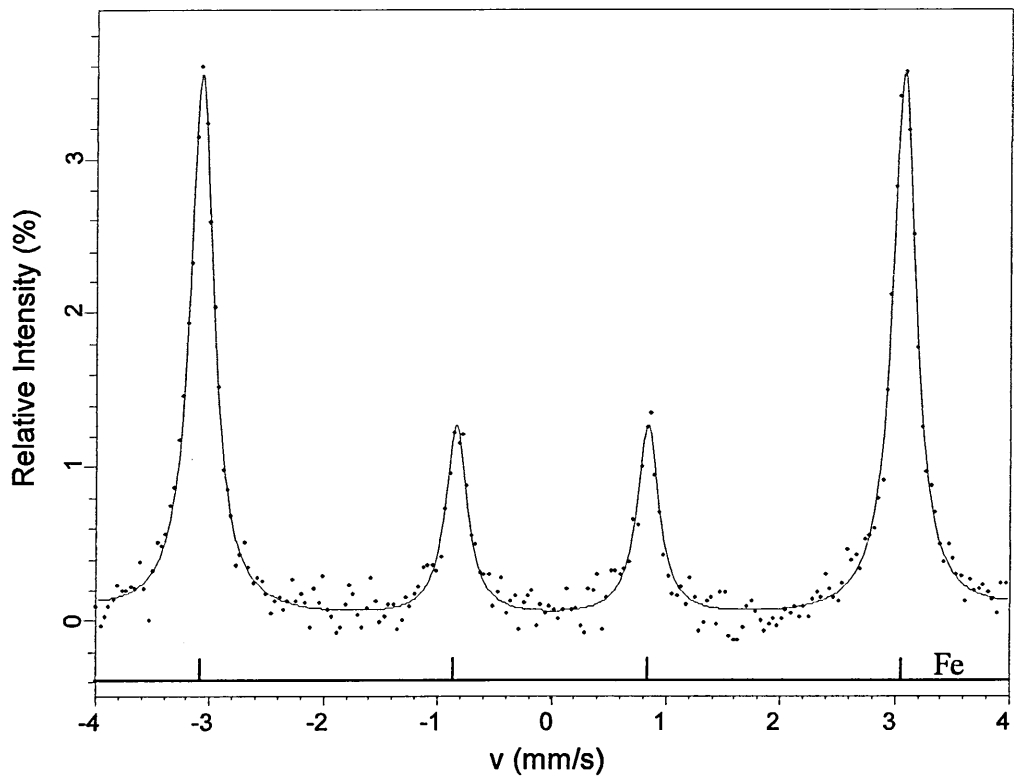


Figure 7.107. Mössbauer spectrum of the polished steel substrate with 35.1 nm carbon coating.

Sample Description	Figure No.	Mössbauer parameters, relative to $\alpha$ -Fe, at 295 K ( $\pm 0.02 \text{ mm s}^{-1}$ )			Magnetic Hyperfine Field ( $\pm 0.2 \text{ T}$ )	Phase Identified	Relative Phase Area %	Peak 2 and 5 Relative Intensity %	$\chi^2$
		$\delta$	$\Delta$	$\Gamma/2$					
No carbon coating	7.103	-0.02	0.00	0.13	33.0	$\alpha$ -Fe	100	5.40	0.629
5.0 nm carbon coating	7.104	0.00	0.00	0.12	33.0	$\alpha$ -Fe	100	5.95	0.626
10.3 nm carbon coating	7.105	0.00	0.00	0.13	33.0	$\alpha$ -Fe	100	5.90	0.721
19.9 nm carbon coating	7.106	0.00	0.00	0.12	32.9	$\alpha$ -Fe	100	5.45	0.627
35.1 nm carbon coating	7.107	0.00	0.00	0.12	32.9	$\alpha$ -Fe	100	3.55	0.536

Table 7.30. Parameters for carbon coated steel samples.

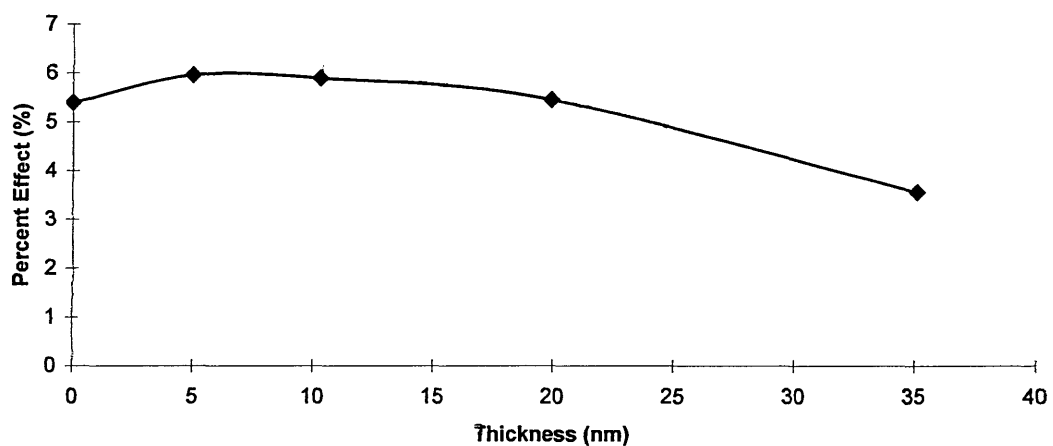


Figure 7.108. Variation of percent effect as a function of deposited carbon thickness.

From the graph of percent effect (of peaks 2 and 5) against carbon thickness, figure 7.108, there is an observed increase in signal strength as the coating is initially increased from zero to approximately 7nm, however this increase is limited to a maximum of 0.5% over the uncoated sample whereas for example aluminium was

shown to increase the signal to 8% more than without an overlayer. Then as the dampening effect of the coating absorbing conversion electrons from the substrate becomes more dominant the effect of the photoemissions becomes less and less significant.

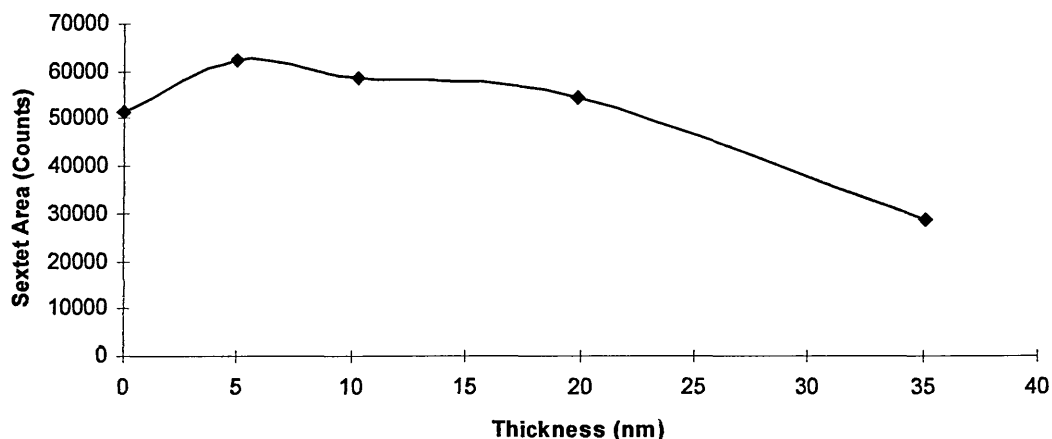


Figure 7.109. Variation of sextet area as a function of deposited carbon thickness.

There is a similar trend observed in the graph of sextet areas against carbon thickness, figure 7.109. From this graph it is seen that the area of the sextets observed begin to decrease more rapidly after 20 nm.

### 7.12.3. <sup>57</sup>Fe CEMS Analysis of Carbon Coated DWI Tinplate Samples

Since the carbon coating was shown to have much less photoelectron production and emission than surface sensitivity analysis experiments with other coatings have shown [17,18,19] it was prudent to see what effect the carbon coat would have on the substrates with intermetallics present on the surface. A 20 nm thickness of carbon was

chosen as being most suitable from the earlier experiments into photoemission from the carbon layer, this was chosen from the area where overall signal was decreased compared to the uncoated substrate.

By applying a carbon coating to multilayer samples it was hoped that some preferential reduction of substrate signal would be observed. Reduction of substrate signal would theoretically lead to a method of obtaining an improved differentiation of the signal from the very near surface of the sample to that from the substrate.

Basic exponential attenuation of the emitted electron flux is usually used to describe the attenuation of electrons through materials [18,20]. Such an attenuation description is suitable for single material systems or multilayered systems, which are composed of Mössbauer active layers, in experiments where electrons are not separated in energy. This however does not describe adequately the electron energy distribution at the exit point of the material surface. A number of studies have used the Mössbauer inert coatings to attempt to reduce the electron energies from the material. Since electrons originating from lower in the material will exit with statistically lower energies than those originating from nearer the surface, a coating would be expected to preferentially reduce the number of electrons from lower in the material. However as it has already been described, these coatings introduce further emitted electrons since photoelectrons are emitted when X-rays, produced throughout the material, interact with atoms in the overlayer. Since the number of X-rays produced by a small near surface layer is less than the bulk, the overall effect would be to increase the substrate signal compared to overlayer signal and this has been observed experimentally [19]. This effect depends

on the  $Z^5$  relationship [21] and thus carbon is an ideal material to use, but has yet to be examined in any study. Given the results above for carbon layers of different thickness there is still some photoelectron production. The following experimental analysis aimed to ascertain whether the photoelectron production or the emergent electron energy reduction dominates in the system.

Figure 7.110 shows the Mössbauer spectra of a sample of heat treated DWI before carbon coating. The heat treatment was conducted in the tube furnace at 240 °C for 30 seconds, followed by an etch procedure to remove the tin. Easily identifiable are the inner four lines of the sextet for the  $\alpha$ -Fe and the sextet for FeSn<sub>2</sub>, both relative to  $\alpha$ -Fe. An estimated 5mm carbon coat travel was used on the surface sensitivity samples corresponding to a carbon thickness of approximately 20nm. Figure 7.111 shows the same two sextets for the sample once coated in carbon and shows different relative peak counts and relative areas for the two sextets to those from the non-coated sample. The parameters for these carbon coated samples are shown in table 7.31. The differences between the two spectra in terms of sextet areas and peak intensities can be found using the Recoil software package and are tabulated in table 7.32.

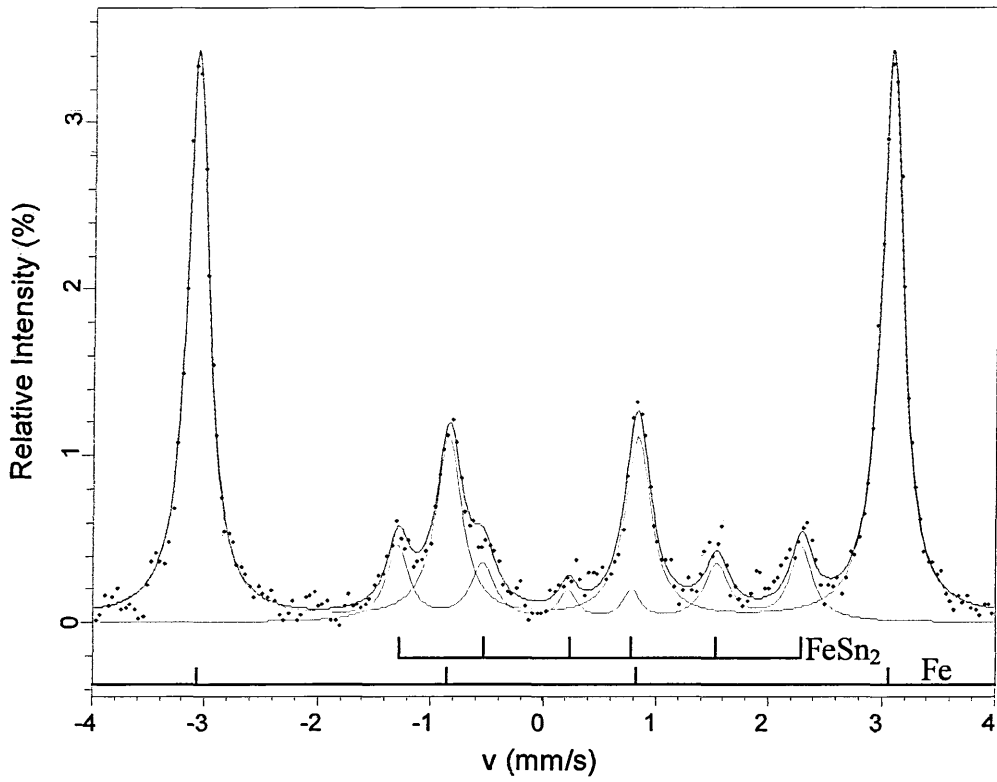


Figure 7.110. Mössbauer spectrum of the heat treated DWI sample before carbon coating.

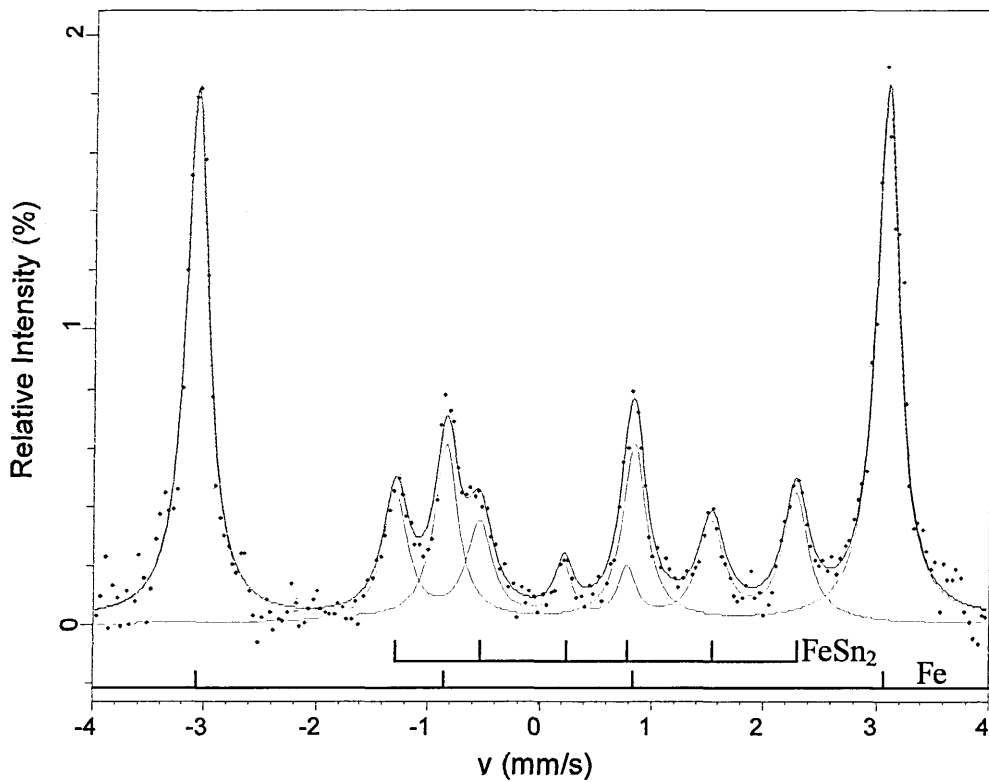


Figure 7.111. Mössbauer spectrum of the the heat treated DWI sample after carbon coating.

Sample Description	Figure No.	Mössbauer parameters, relative to $\alpha$ -Fe, at 295 K ( $\pm 0.02 \text{ mm s}^{-1}$ )			Magnetic Hyperfine Field ( $\pm 0.2 \text{ T}$ )	Phase Identified	$\chi^2$
		$\delta$	$\Delta$	$\Gamma/2$	H		
Heat treated DWI sample before coating	7.110	0.00	0.00	0.13	33.0	$\alpha$ -Fe	0.720
		0.50	0.00	0.12	11.1	FeSn <sub>2</sub>	
Heat treated DWI sample after coating	7.111	0.00	0.00	0.13	33.0	$\alpha$ -Fe	0.543
		0.50	0.00	0.12	11.1	FeSn <sub>2</sub>	

Table 7.31. Parameters for carbon coated and non-carbon coated DWI.

	Non-Coated DWI	Coated DWI
Peak counts (%) for peaks 2 and 5 of $\alpha$ -Fe	3.43	1.82
Peak counts (%) for peaks 3 and 4 of $\alpha$ -Fe	1.11	0.61
Peak counts (%) for peaks 1 and 6 of FeSn <sub>2</sub>	0.46	0.45
Peak counts (%) for peaks 2 and 5 of FeSn <sub>2</sub>	0.35	0.35
Peak counts (%) for peaks 3 and 4 of FeSn <sub>2</sub>	0.20	0.20
Relative area (%) for $\alpha$ -Fe	88.3	79.8
Relative area (%) for FeSn <sub>2</sub>	11.7	20.2

Table 7.32. Comparison of peak counts and relative sextet areas for carbon coated and non-carbon coated DWI.

Clearly the carbon coat has had an effect on the  $\alpha$ -Fe signal from the substrate, reducing the peak counts of peaks 2 and 5 to 53% of the value prior to coating, whereas the signal from the intermetallics is not significantly reduced being 98% of the value prior to coating. The relative area of the  $\alpha$ -Fe is reduced when carbon coated from 88.3% to 79.8% and the relative area of the FeSn<sub>2</sub> is increased from 11.7% to 20.2%. In the case of samples such as these, with low levels of Fe-Sn intermetallics on a substrate of Fe (in the form of mild steel), the CEMS technique shows the

intermetallics on the sample surface more clearly after the application of a carbon coating of suitable thickness. This experiment was consistently repeatable and although it does not increase the intermetallic signal it preferentially decreases the signal from lower in the sample (in this case the steel substrate), making intermetallic identification easier.

Although not explicitly analysed within this study it is assumed that the tin coatings on the DWI lead to increased substrate signals due to the production of photoelectrons in the tin layer adding to the signal observed, much as that found in previous studies of gold and aluminium coatings. Much as with those other coatings, after a certain coating thickness, the substrate signal would begin to decrease as the photoelectron production became less significant compared to the dampening effect of the tin layer. Thus the removal of the tin layer in these studies helps to remove this significant problem when trying to detect the intermetallics present.

In conclusion this technique proves to be a simple and non-destructive way of making the CEMS technique using a gas-flow proportional counter more surface sensitive without any equipment alteration. In terms of viewing intermetallics in the DWI material this may prove to be a useful technique for future analysis.

### **7.13. Sample Roughness Effects in Mössbauer Spectroscopy**

Another area of work that has been examined is the roughness of sample surfaces and their effect on the formation and detection, by CEMS, of intermetallics on these sample surfaces.

#### **7.13.1 Roughness Measurements of Substrates**

To analyse the effect of sample surface roughness on the signals obtained from CEMS a series of ground steel samples with an FeSn<sub>2</sub> intermetallic layer were produced. The sample production involved four stages. Grinding to define various roughness levels, electrodeposition of tin onto the rough substrates, heat treatments of the samples to form intermetallics and etching to remove excess tin.

The samples were ground using the technique already described in section 5.3.2.1. However instead of polishing down to a mirrored finish with 1µm diamond paste, the samples were prepared to different roughness using various grit papers, and are identified by the final grinding or polishing stage as 1 µm, 6 µm, P1200, P600, P240 and P120. These samples were analysed using a Taylor Hobson 120L laser form talysurf to check, prior to tinplating, the actual roughness of the sample surfaces. Three separate traces were taken for each sample on various areas of the sample surfaces all perpendicular to the direction of the visible striations on the surfaces.

Typical traces for the six roughness samples are shown in figures 7.112 to 7.117. The average results of the talysurf measurements for each sample are collated in table 7.33.

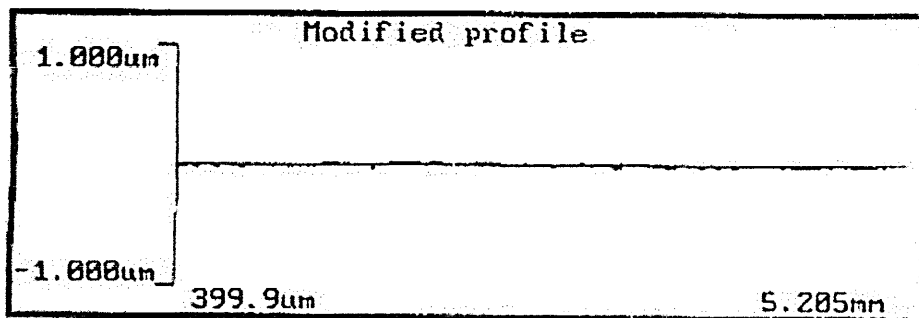


Figure 7.112. Talysurf trace of the sample 1 μm.

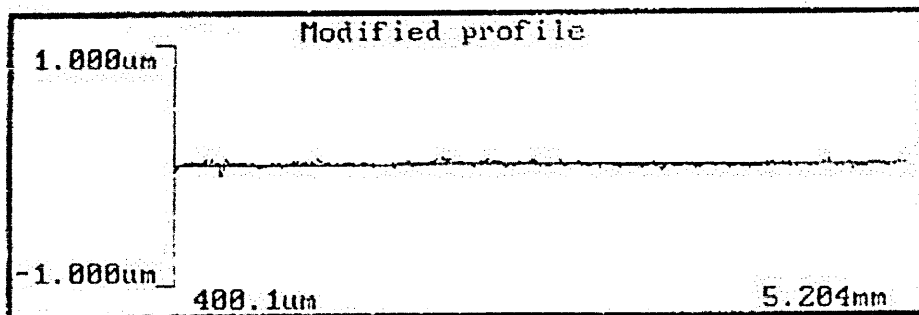


Figure 7.113. Talysurf trace of the sample 6 μm.

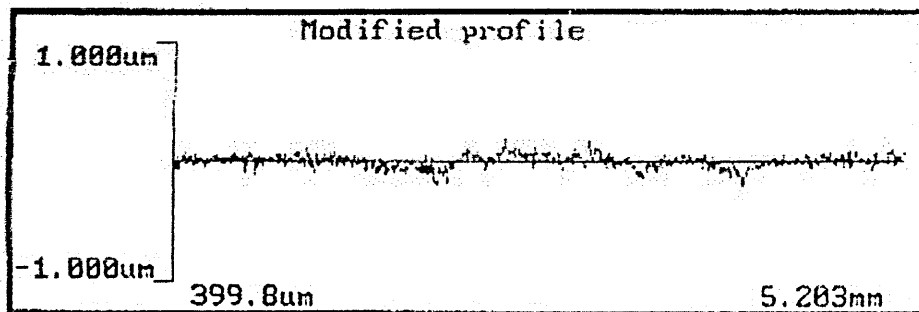


Figure 7.114. Talysurf trace of the sample P1200.

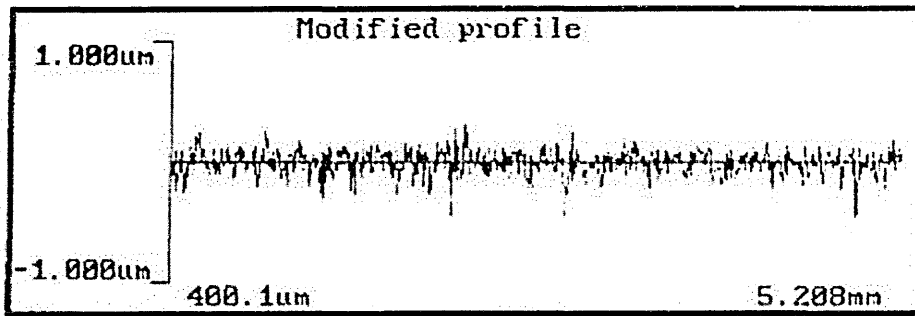


Figure 7.115. Talysurf trace of the sample P600.

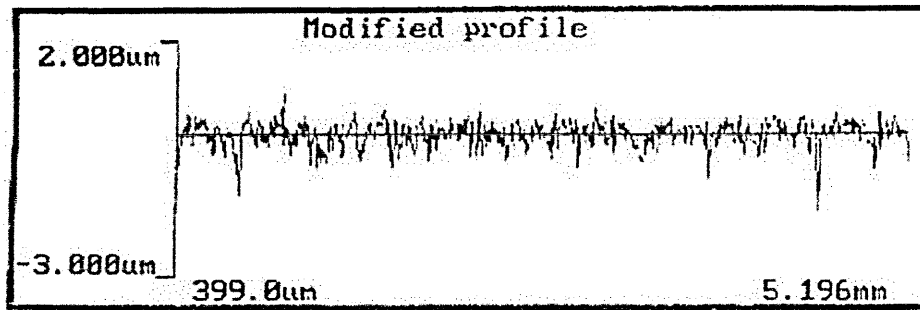


Figure 7.116. Talysurf trace of the sample P240.

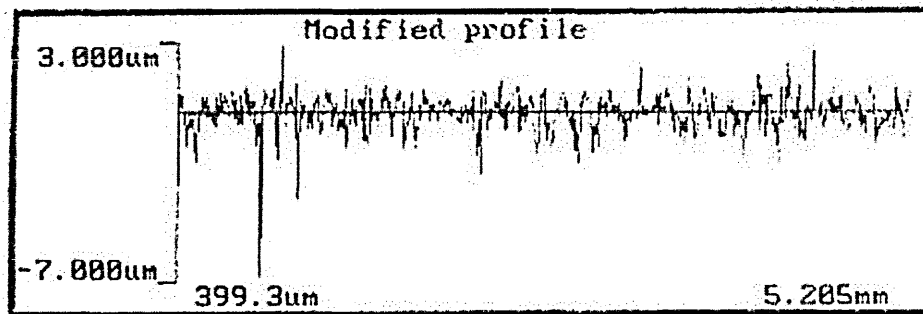


Figure 7.117. Talysurf trace of the sample P120.

Sample Identification	Figure no.	Average Roughness ( $R_a$ ) / $\mu\text{m}$	Average Deviation of Results from Mean / $\mu\text{m}$	Max. Peak to Valley Distance ( $R_t$ ) / $\mu\text{m}$
1 $\mu\text{m}$	7.112	0.008	0.002	0.066
6 $\mu\text{m}$	7.113	0.018	0.005	0.143
P1200	7.114	0.060	0.013	0.693
P600	7.115	0.064	0.008	0.764
P240	7.116	0.219	0.009	2.658
P120	7.117	0.500	0.045	7.574

Table 7.33. Talysurf Results

The talysurf results show a general progression in roughness as the final polishing stage roughness increases from an average roughness of 0.008  $\mu\text{m}$  with 1  $\mu\text{m}$  diamond paste polishing to 0.5  $\mu\text{m}$  with P120 grit paper. The average roughness,  $R_a$ , is an average calculated from the three sample traces each of which consists of six sample lengths. It is defined as the arithmetic average of the absolute values of the roughness profile ordinates.

The average deviation of results from the mean is a measure of how different the three sample traces for a particular roughness formation are. The P1200 sample has an average deviation of 0.013  $\mu\text{m}$  meaning that the three traces have an average roughness 0.013  $\mu\text{m}$  from the mean of the three samples. From the average deviation parameter the polished samples are seen to be the most consistent and the roughest sample, ground with P120 graded paper, gives the most inconsistent average roughness values.

The P1200 sample has a larger deviation than expected and therefore may have an area on the sample that has greater roughness than the remainder of the sample. This could have arisen if the final grinding stage had not removed all the marks left by the

previous P600 grinding stage or the P1200 grade paper was not consistent over its surface.

The maximum peak to valley distance,  $R_t$ , is the maximum found on the three sample traces and is the distance from highest peak to lowest valley over the six sample lengths of the particular sample trace. Thus this is a further indicator of roughness but is unfortunately affected by extreme peaks and valleys. This is observed in particular in the P120 trace where there is an extreme valley and to lesser extent in all sample traces.

Despite any minor inconsistencies from extreme peaks and valleys, the series of traces show the general trend in increasing roughness. The P1200 and P600 results for average roughness and maximum peak to valley distance are similar and would therefore be expected to lead to similar CEMS results.

#### 7.13.2 Sample Preparation and SEM Analysis of Electrodeposited Coatings

The roughness samples were analysed using the SEM prior to electrodeposition and SE SEM images are shown in figures 7.118, 7.119 and 7.120 showing the 1 $\mu$ m diamond pasted polished sample along with the samples ground with P600 and P120 graded papers for the final grinding stage.

The increasing roughness is observed on these SE SEM images with the polished sample showing virtually no grooves at high magnification. The grooving of the

surface is evident when using P600 and P120 papers, with the groove width and depth increasing at the paper roughness increases.

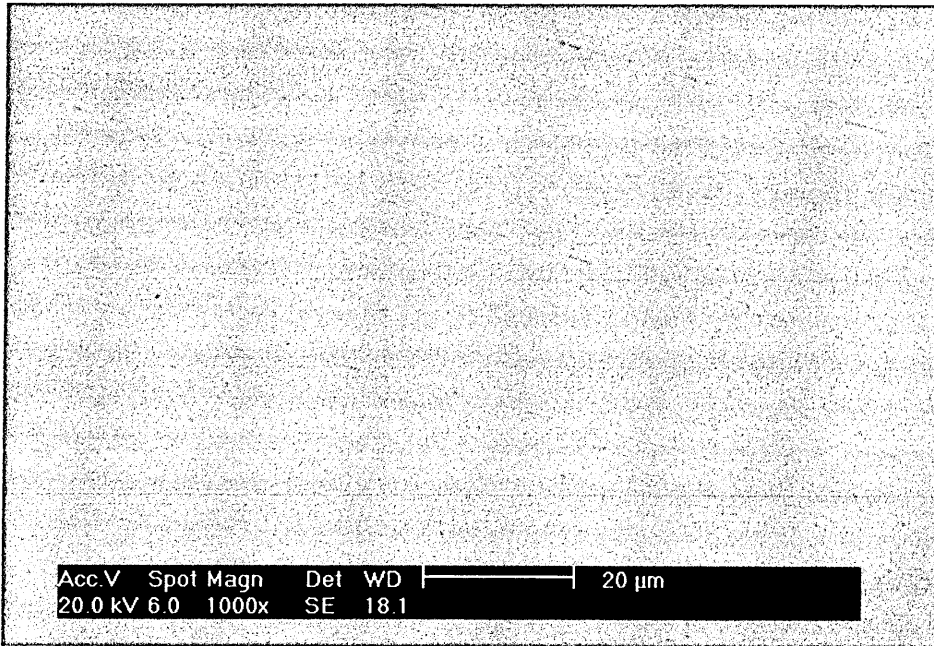


Figure 7.118. SE SEM image of the 1µm polished sample.

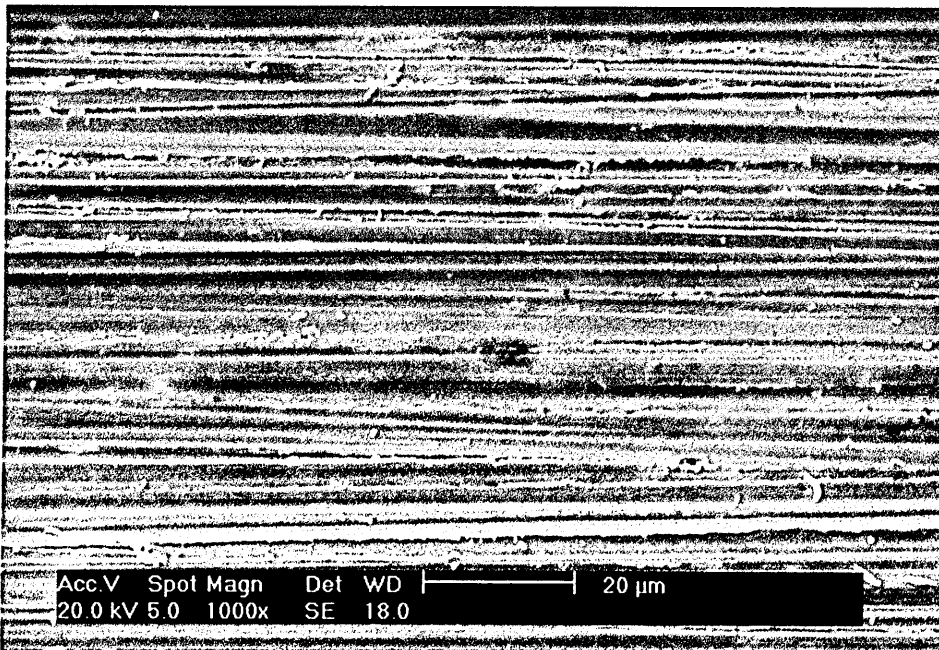


Figure 7.119. SE SEM image of the P600 sample.

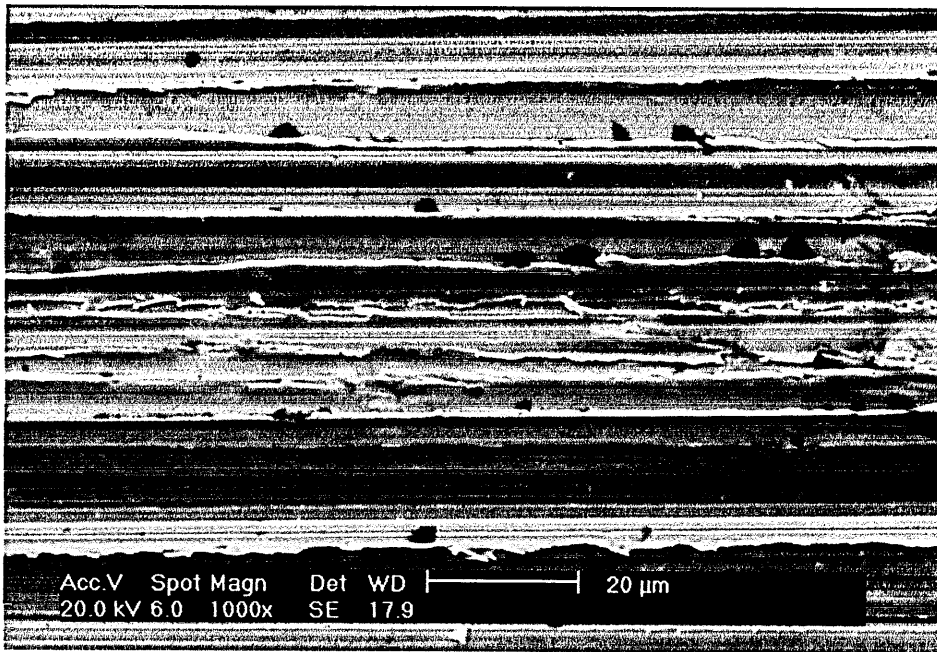


Figure 7.120. SE SEM image of the P120 sample.

The roughness samples were then coated with tin as described in section 5.3.2 to deposit a 2 μm coating of tin. This procedure was critical in the investigation as the same weight of tin per unit area and thus the same average thickness should be deposited on each sample to minimise the errors in the results.

Table 7.34 shows the depth of the deposited tin as determined through measurements of the sample weights before and after deposition on a set of six roughness samples. Covered areas are based on having both faces of the sample available for deposition and this area being 2 cm × 2 cm per side.

Sample ID	Mass before g ± 0.0001 g	Mass after g ± 0.0001 g	Mass deposited g ± 0.0002 g	Area m <sup>2</sup> ± 0.0001 m <sup>2</sup>	Depth μm ± 0.15 μm
1 μm	0.7588	0.7711	0.0123	0.0008	2.10
6 μm	0.7028	0.7143	0.0115	0.0008	1.97
P1200	0.7751	0.7871	0.0120	0.0008	2.05
P600	0.7605	0.7719	0.0114	0.0008	1.95
P240	0.6690	0.6809	0.0119	0.0008	2.04
P120	0.6618	0.6739	0.0121	0.0008	2.07

Table 7.34. Table for depths of tin layer in electrodeposition for roughness analysis.

A set of roughness samples were analysed using scanning electron microscopy after the electrodeposition procedure. The samples where the surface is least rough show similar morphology to that of the polished steel samples previously analysed after the electrodeposition procedure. The surface contains an array of crystal like formations without preferred orientation.

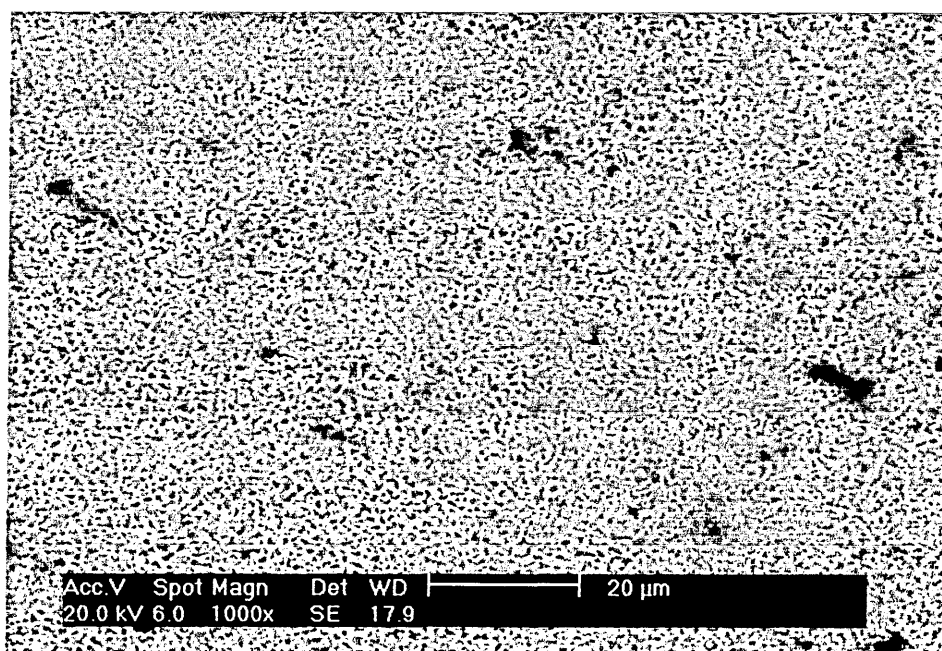


Figure 7.121. SE SEM image of the 1μm polished sample electrodeposited with tin at 1000× magnification.

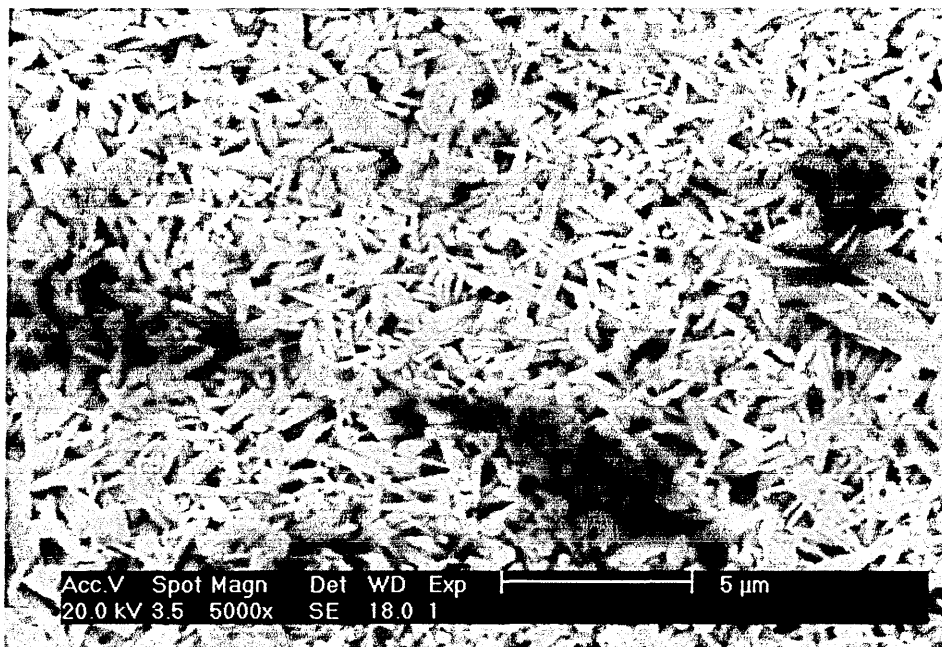


Figure 7.122. SE SEM image of the 1µm polished sample electrodeposited with tin at 5000× magnification.

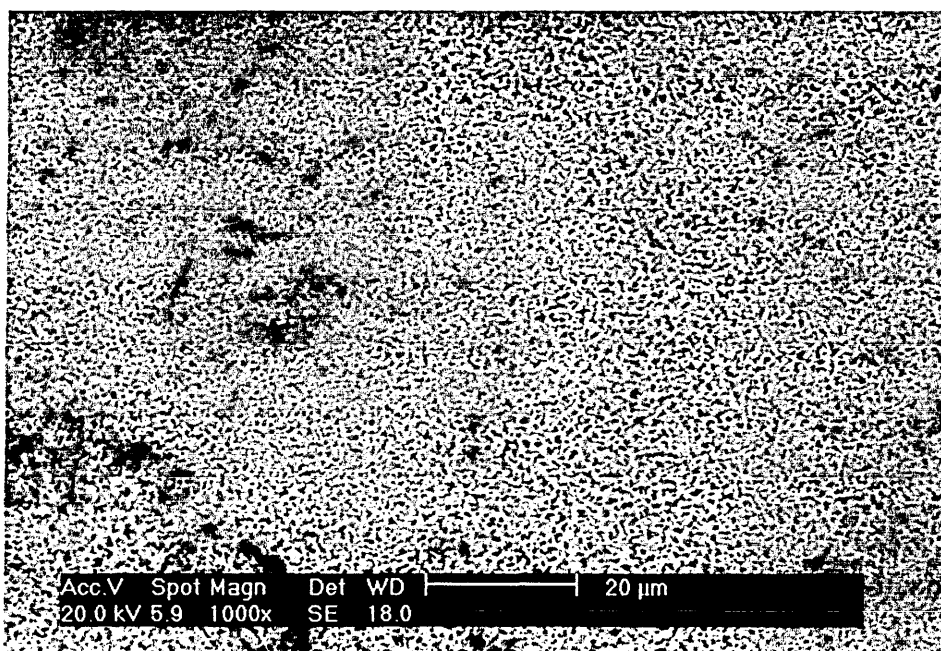


Figure 7.123. SE SEM image of the P1200 ground sample electrodeposited with tin at 1000× magnification.

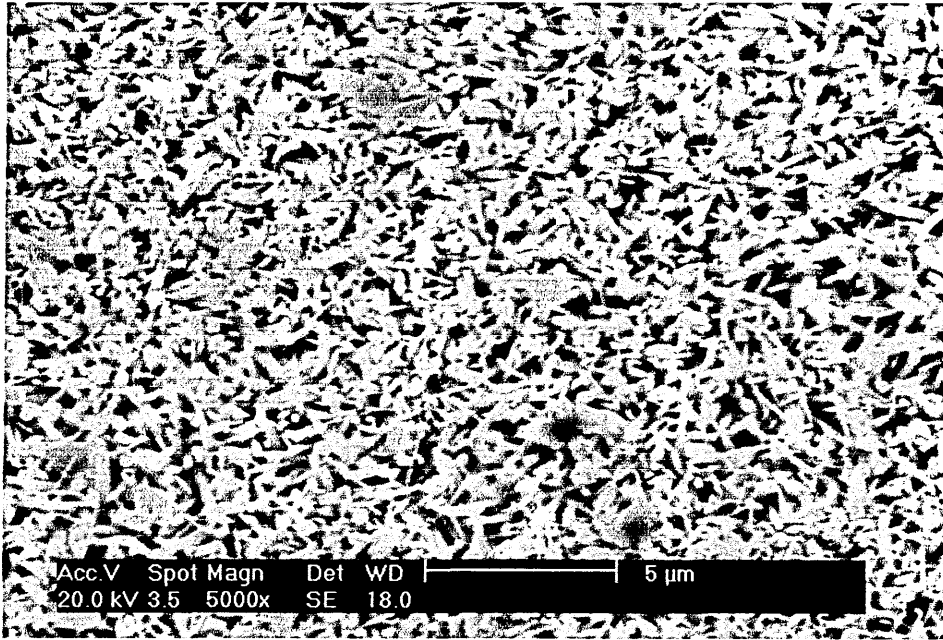


Figure 7.124. SE SEM image of the P1200 ground sample electrodeposited with tin at 5000× magnification.

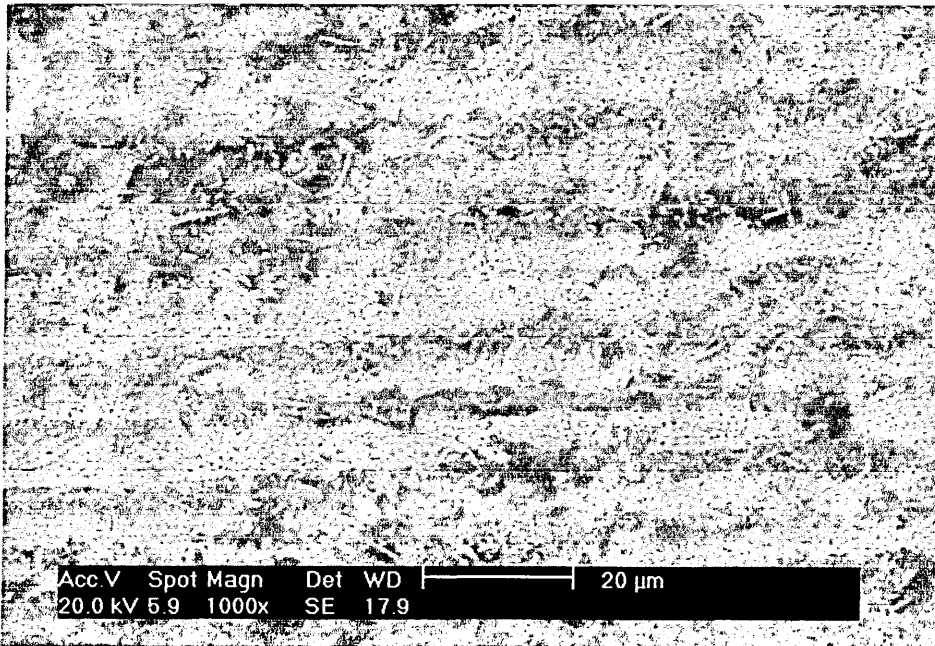


Figure 7.125. SE SEM image of the P240 ground sample electrodeposited with tin at 1000× magnification.

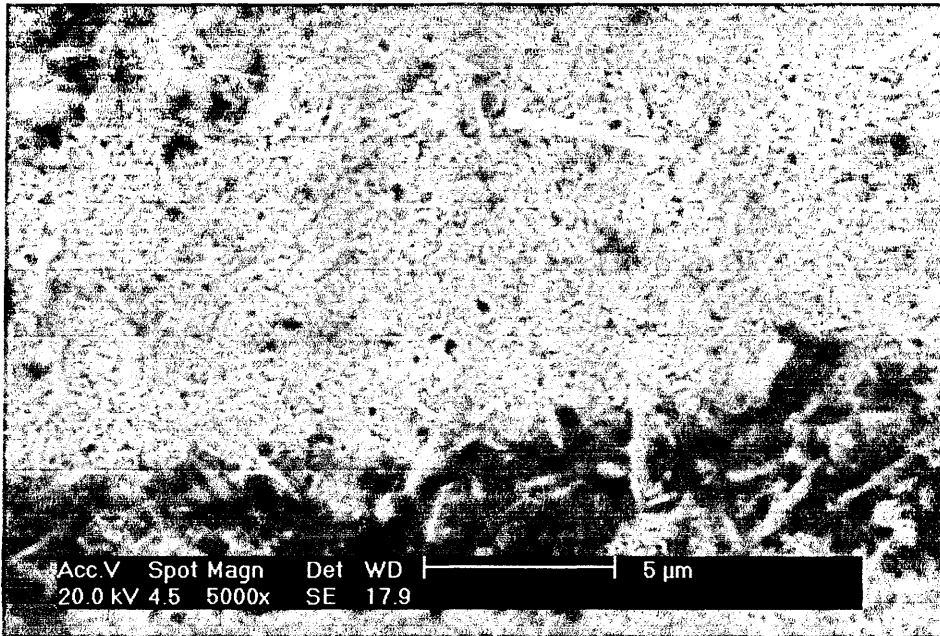


Figure 7.126. SE SEM image of the P240 ground sample electrodeposited with tin at 5000× magnification.

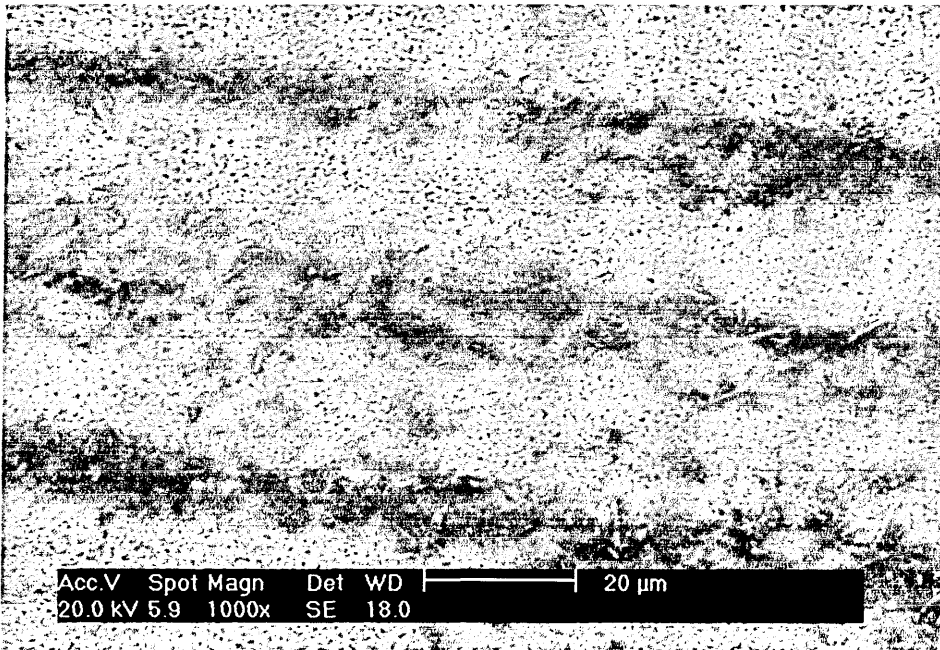


Figure 7.127. SE SEM image of the P120 ground sample electrodeposited with tin at 1000× magnification.

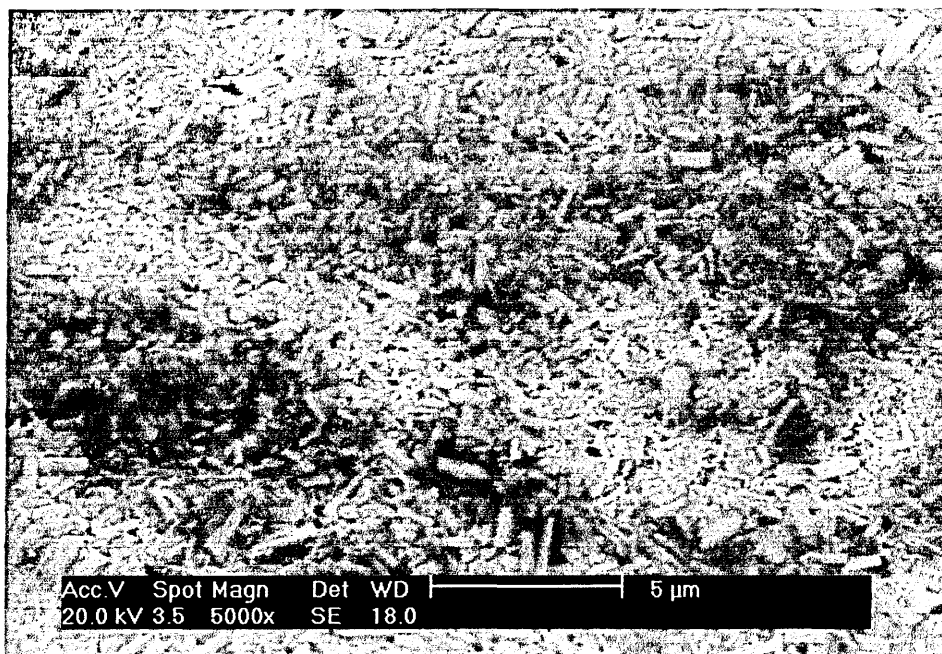


Figure 7.128. SE SEM image of the P120 ground sample electrodeposited with tin at 5000× magnification.

The series of SEM images in figures 7.121 to 7.128 show how the electrodeposition alters with increasing roughness. It would appear that the crystal formation on the surfaces depends on the substrate surface undulations. Without undulation the crystals formed are uniform over the surface and large in size approximating to 1 to 3 μm in length and less than 0.5 μm in width. As the roughness increases as shown in figures 7.123 and 7.124 the crystals begin to form with similar uniformity but less than half of the dimensions for the individual crystals.

Increasing roughness further it is seen that the underlying substrate roughness shows through, figure 7.125, with dark streaks where the substrate is showing through the deposited tin. It is difficult from this image and the other rough sample image at 1000× magnification, figure 7.127, to tell whether the areas of substrate showing are the peaks

or valleys. At higher magnifications, figures 7.126 and 7.128, the decrease in crystal size continues to be observed to the point where most of the crystals are sub-micron size.

After the electrodeposition of the 2  $\mu\text{m}$  coating of tin these samples were then heat treated in the tube furnace under nitrogen for 10 minutes at 240 °C. The heat treatments were also a critical part of this experiment, they were carried out according to the procedure set out in section 5.3.3 and care was taken to ensure that each sample was exposed to the same temperature in the furnace for the same amount of time. In this case it was prudent to use a temperature above the melting point of tin (232 °C) for 10 minutes so as to minimise errors due to heating and cooling periods. A temperature of 240 °C was used for this series of heat-treatments.

It has been shown in this study, section 7.11, that the annealing of tinplate and subsequent production of intermetallics is time dependent and that after approximately 5 minutes at 240°C the majority of the diffusion of tin and iron has taken place, the formed  $\text{FeSn}_2$  acting as a barrier to the diffusion process. So the longer period of time of 10 minutes allows the samples to reach this state and hence reduce error.

Once the annealing process is complete then the excess tin that was not used to form intermetallics was removed using a solution of 50 g/l NaOH and 10 g/l  $\text{KIO}_3$  in the etching procedure set out in section 5.3.4. Once these procedures were finished then it was possible to analyse the samples using CEMS to obtain information about the quantity of intermetallics formed.

### 7.13.3 $^{57}\text{Fe}$ CEMS Analysis of Roughness Samples

CEMS analysis was then carried out on the prepared samples. Figures 7.129 to 7.134 show the Mössbauer spectra for the series of roughness samples that have been tin coated, heat-treated and etched. The fitted parameters for these spectra are shown in table 7.35. All six spectra show an intermetallic phase that most closely resembles  $\text{FeSn}_2$ .

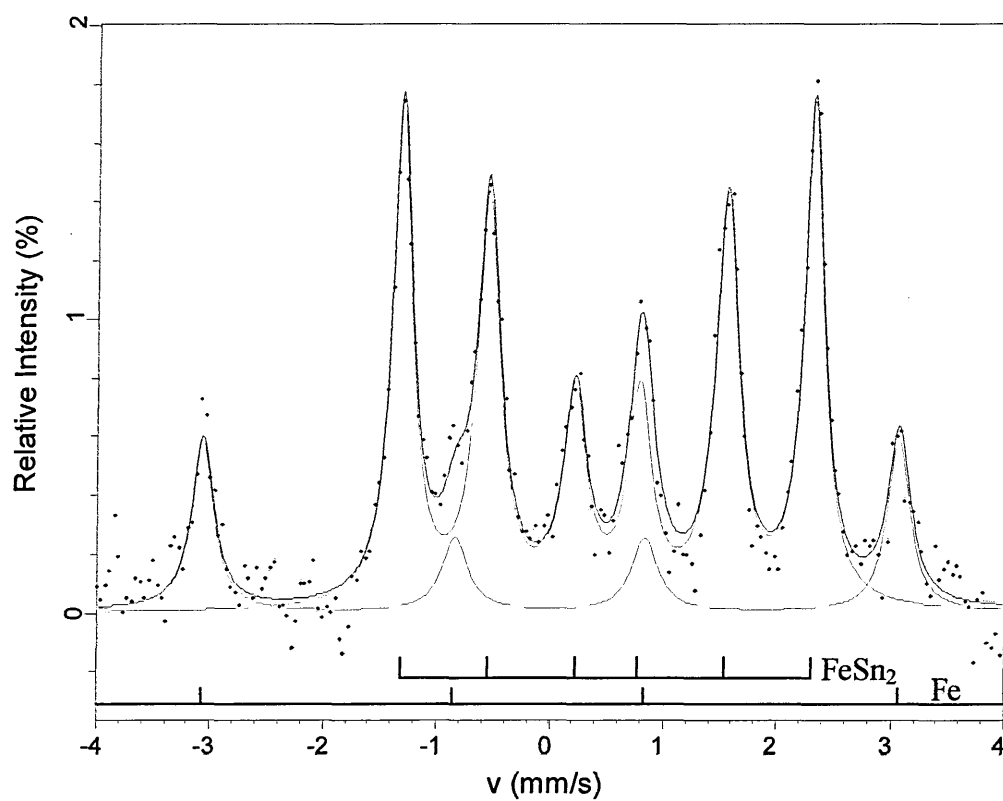


Figure 7.129. Mössbauer spectrum of the sample 1  $\mu\text{m}$ .

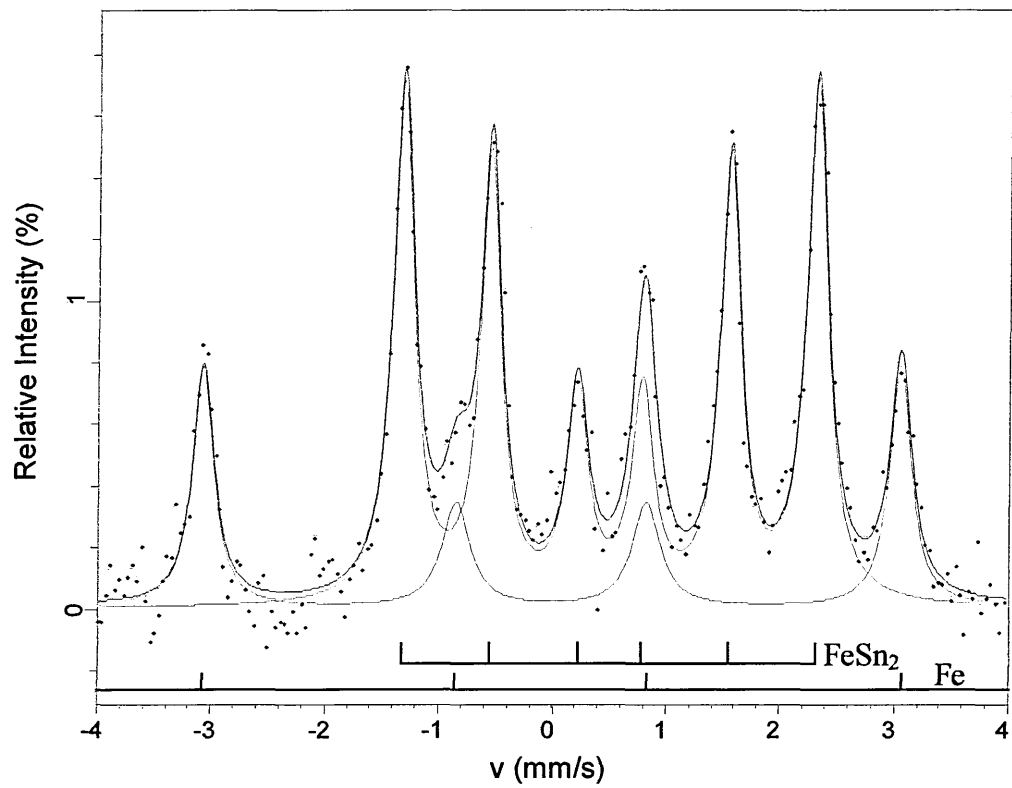


Figure 7.130. Mössbauer spectrum of the sample 6  $\mu\text{m}$ .

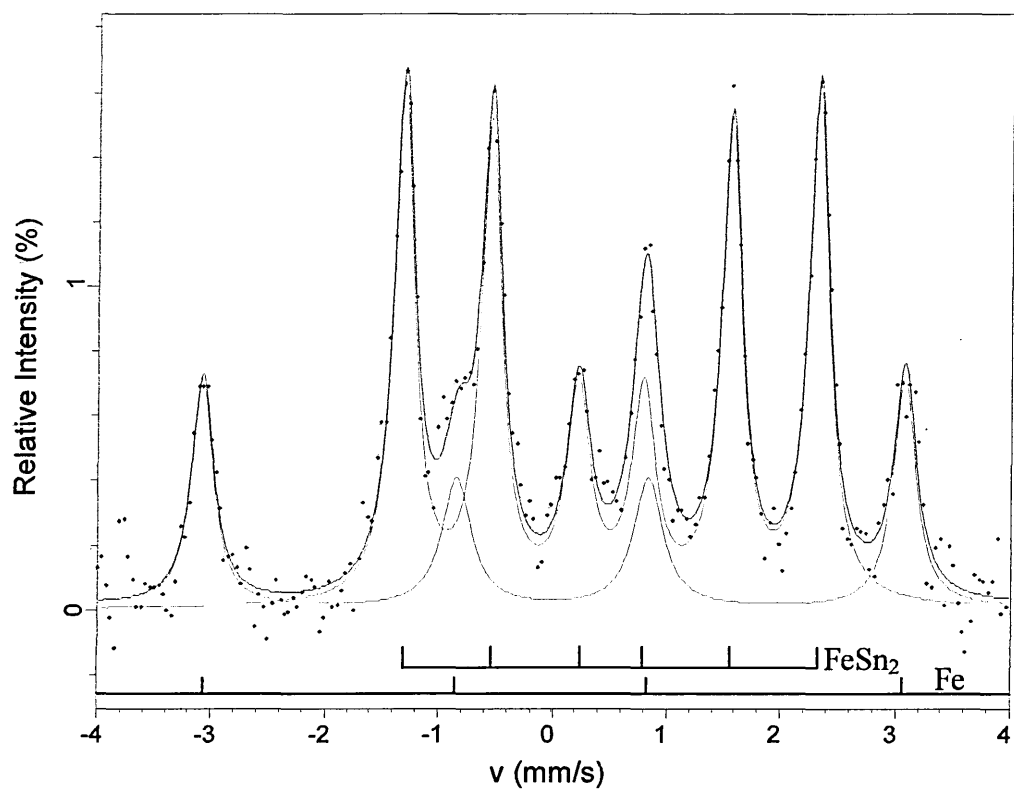


Figure 7.131. Mössbauer spectrum of the sample P1200.

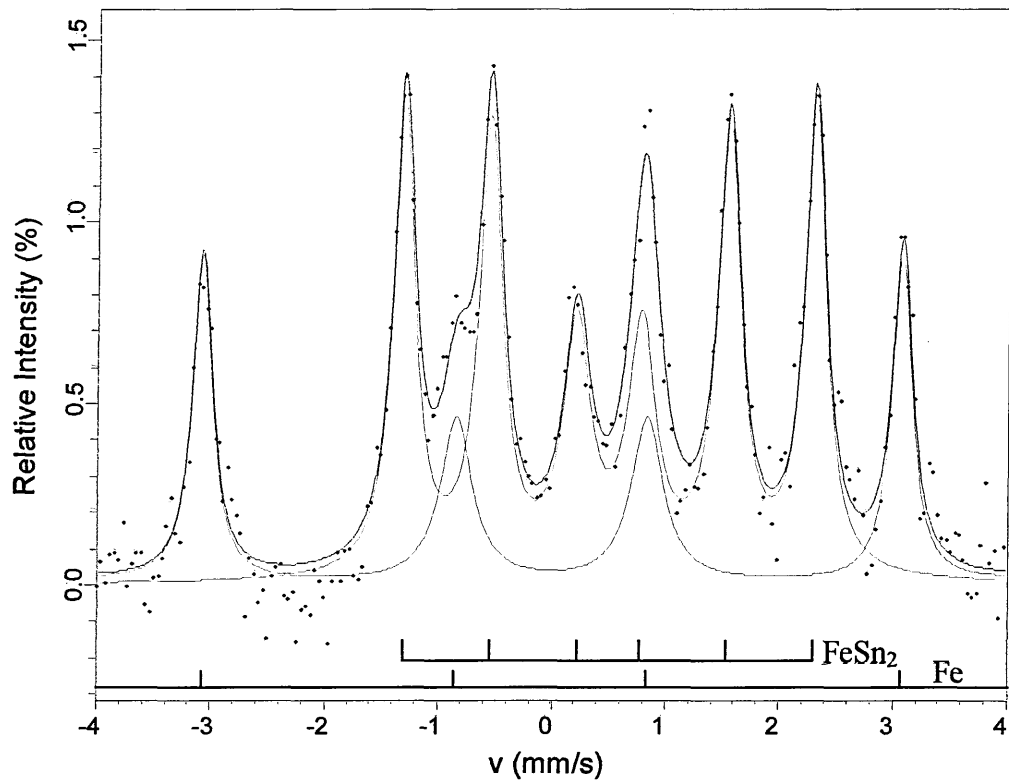


Figure 7.132. Mössbauer spectrum of the sample P600.

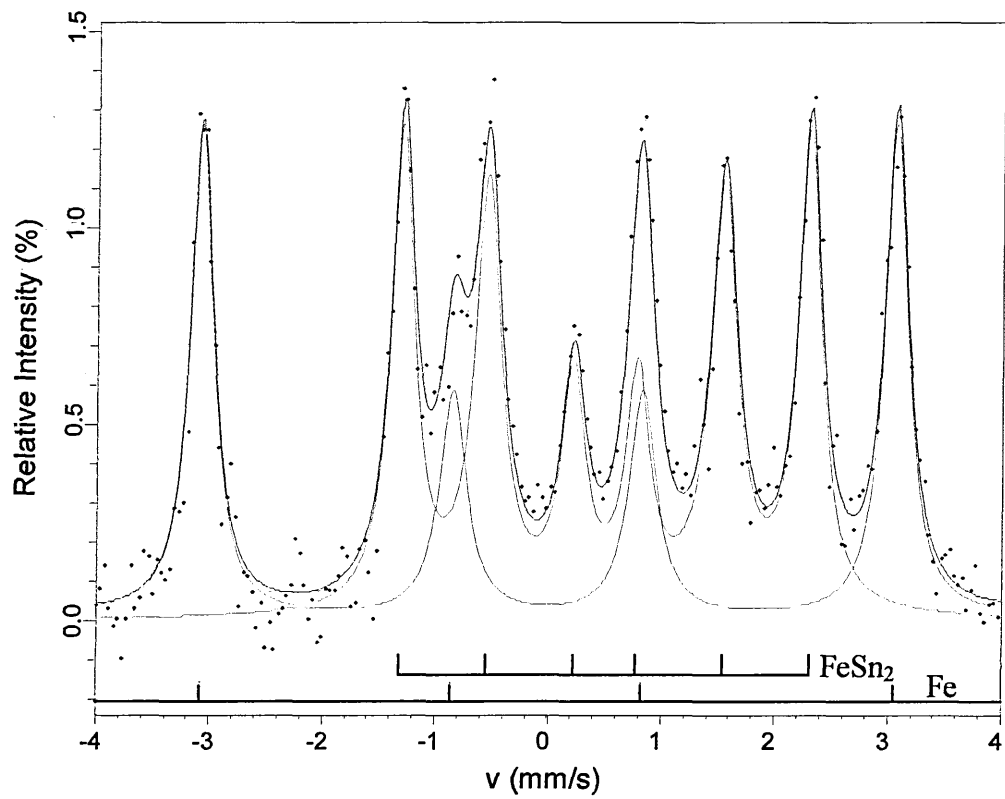


Figure 7.133. Mössbauer spectrum of the sample P240.

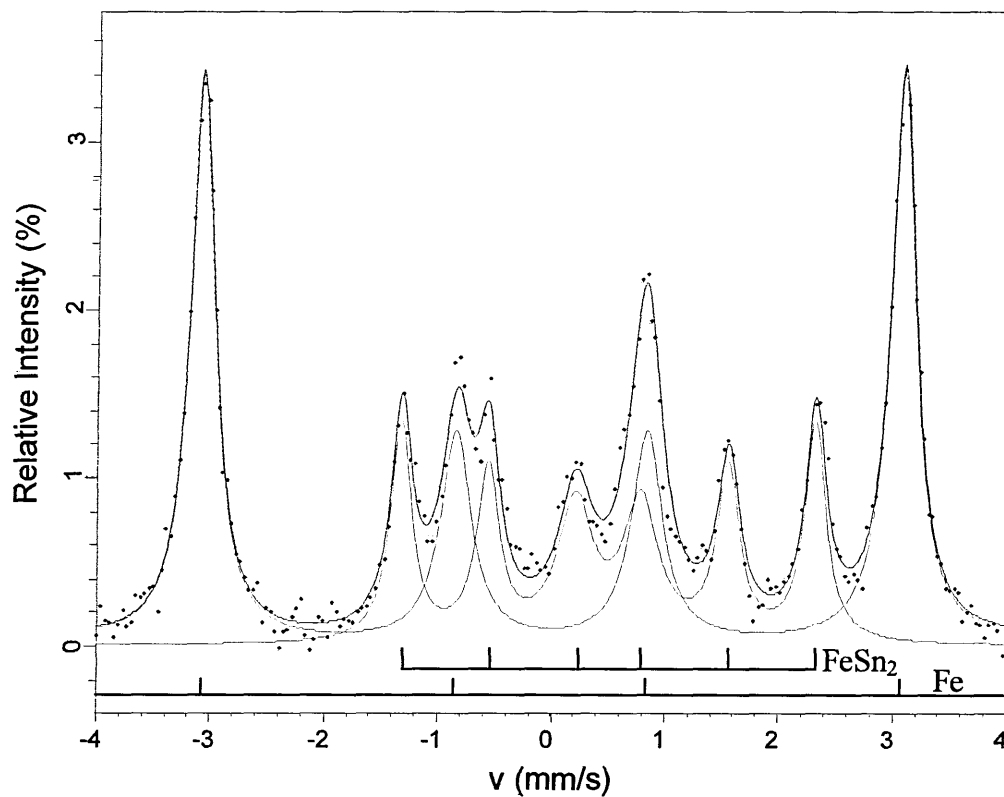


Figure 7.134. Mössbauer spectrum of the sample P120.

Sample Description	Average Roughness $\mu\text{m}$	Fig. No.	Mössbauer parameters, relative to $\alpha\text{-Fe}$ , at 295 K ( $\pm 0.02 \text{ mm s}^{-1}$ )			Magnetic Hyperfine Field ( $\pm 0.2 \text{ T}$ )	Phase Identified	Relative Phase Area %	$\chi^2$
			$\delta$	$\Delta$	$\Gamma/2$				
1 $\mu\text{m}$	0.008	7.129	0.00	0.00	0.131	32.87	$\alpha\text{-Fe}$	28.6	0.624
			0.50	0.00	0.117	11.26	$\text{FeSn}_2$	71.4	
6 $\mu\text{m}$	0.018	7.130	-0.01	0.00	0.134	32.82	$\alpha\text{-Fe}$	35.8	0.558
			0.50	0.00	0.112	11.29	$\text{FeSn}_2$	64.2	
P1200	0.060	7.131	0.00	0.00	0.139	32.98	$\alpha\text{-Fe}$	37.5	0.569
			0.51	0.00	0.114	11.28	$\text{FeSn}_2$	62.5	
P600	0.064	7.132	0.00	0.00	0.147	32.96	$\alpha\text{-Fe}$	42.2	0.630
			0.50	0.00	0.127	11.22	$\text{FeSn}_2$	57.8	
P240	0.219	7.133	0.00	0.00	0.136	32.90	$\alpha\text{-Fe}$	50.9	0.455
			0.50	0.00	0.130	11.16	$\text{FeSn}_2$	49.1	
P120	0.500	7.134	0.00	0.00	0.151	33.00	$\alpha\text{-Fe}$	72.0	0.668
			0.50	0.00	0.139	11.31	$\text{FeSn}_2$	28.0	

Table 7.35. Mössbauer parameters for roughness analysis.

The graph in figure 7.135 shows the phase area in counts plotted against the experimentally determined roughness values,  $R_a$ . The two lines represent the phase areas from the substrate (as  $\alpha$ -Fe) and  $\text{FeSn}_2$  layers.

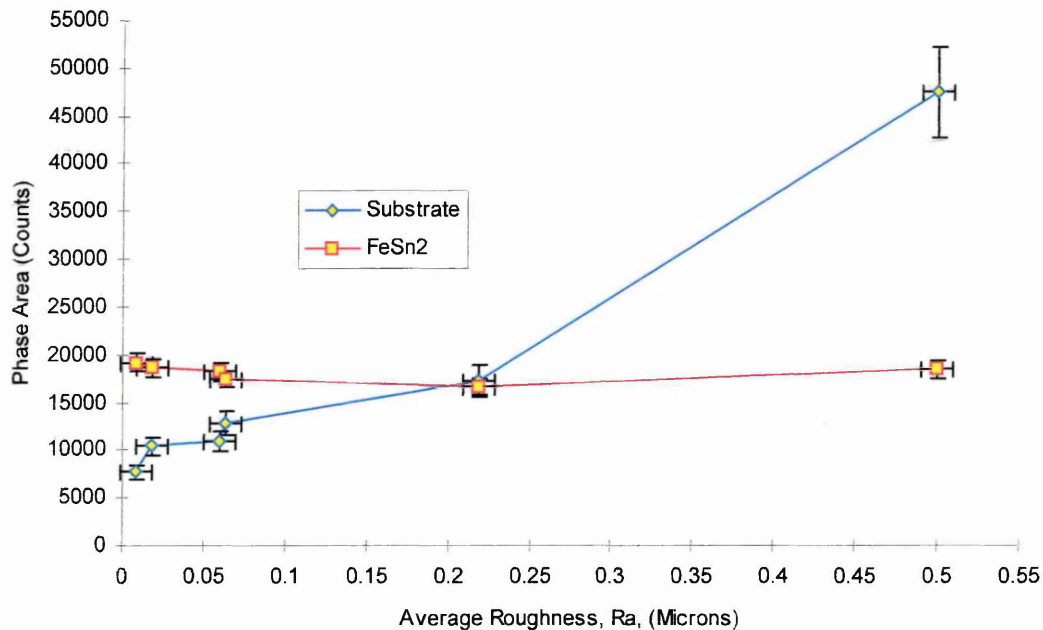


Figure 7.135. Graph of signal for phase area versus average roughness  $R_a$ .

From the graph and the corresponding CEMS spectra for these samples there is an observed increase in the steel substrate signal with increasing roughness but no corresponding signal increase arising from the detection of  $\text{FeSn}_2$ . The overall signal from the sample is increased as the sample roughness increases.

It was necessary to analyse samples of different roughness steel without the presence of intermetallics to see whether the increase observed with coated samples was simply due to increased effective substrate surface area or whether the intermetallics had a significant effect.

Figure 7.136 shows the Mössbauer spectrum for a sample of pre-can production steel polished with 1 $\mu$ m diamond paste and figure 7.137 shows the spectrum from a sample of steel ground with the roughest grit paper available, P120 graded paper. These two particular samples were chosen as they were expected to show the greatest difference in terms of signal. Both spectra were taken with the detector in the same position and the same experiment time. These conditions were also equivalent to those used in all of the roughness analysis. Parameters for the analysis of the different roughness steel substrates are shown in table 7.36. A comparison of the signal areas and peak intensities is shown in table 7.37.

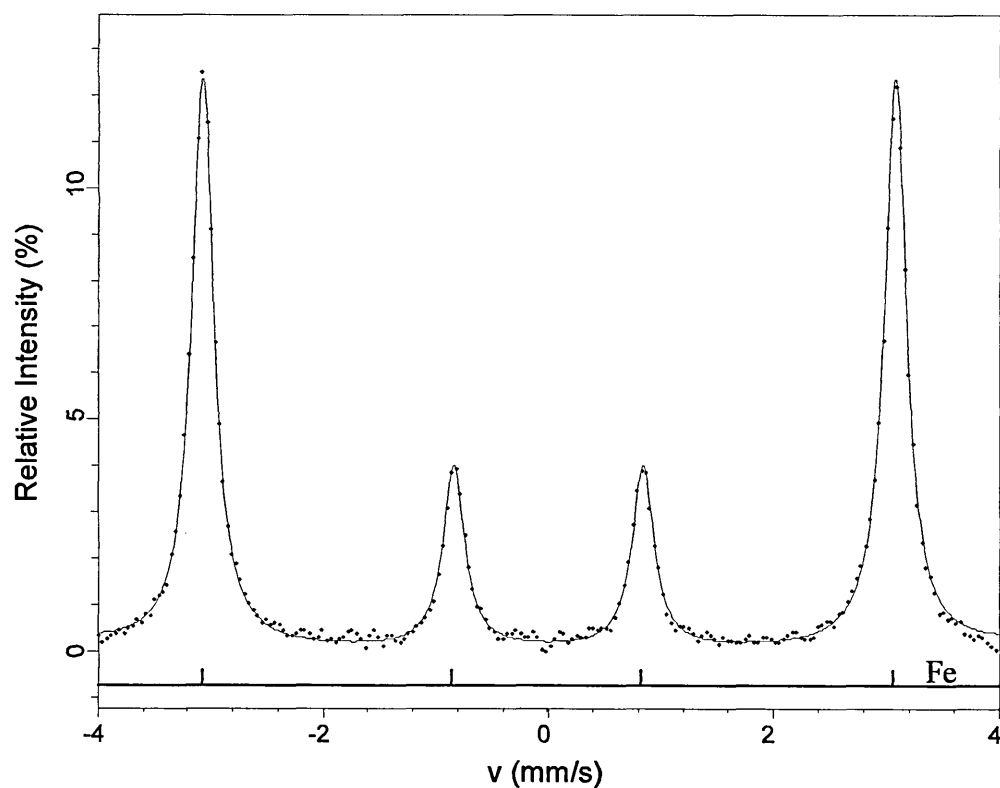


Figure 7.136. Mössbauer spectrum of the steel sample polished with 1 $\mu$ m diamond paste.

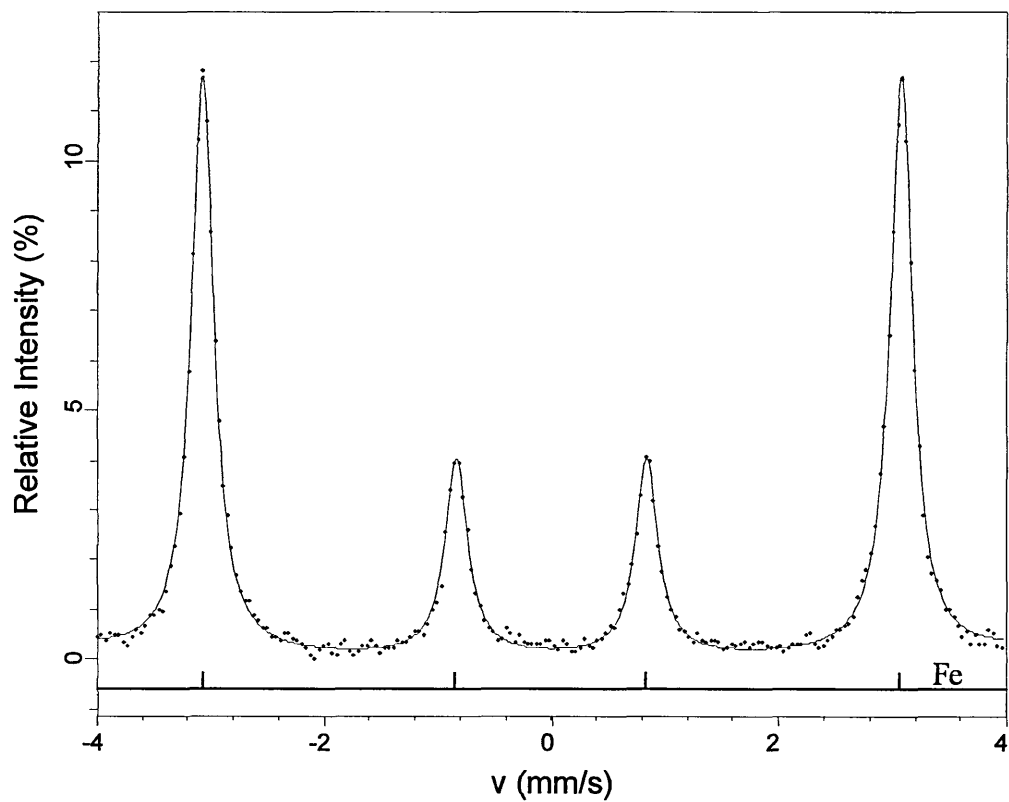


Figure 7.137. Mössbauer spectrum of the steel sample ground with P120 graded paper.

Sample Description	Figure No.	Mössbauer parameters, relative to $\alpha$ -Fe, at 295 K ( $\pm 0.02 \text{ mm s}^{-1}$ )			Magnetic Hyperfine Field ( $\pm 0.2 \text{ T}$ )	Phase Identified	Relative Phase Area %	$\chi^2$
		$\delta$	$\Delta$	$\Gamma/2$	H			
Polished steel sample ( $1\mu\text{m}$ )	7.136	0.00	0.00	0.12	33.0	$\alpha$ -Fe	100	0.843
Rough steel sample (P120)	7.137	0.00	0.00	0.12	33.0	$\alpha$ -Fe	100	0.814

Table 7.36. Parameters for roughness analysis of steel substrates.

	1 $\mu$ m Diamond Paste Polished Sample	P120 Paper Ground Sample
Peak counts (%) for peaks 2 and 5 of $\alpha$ -Fe	12.40	11.73
Peak counts (%) for peaks 3 and 4 of $\alpha$ -Fe	4.01	4.05
Background Counts	507551 $\pm$ 712	496218 $\pm$ 704
Sextet Area Counts	102654 $\pm$ 320	99197 $\pm$ 315

Table 7.37. Signal values from smoothest and roughest steel substrates.

It is clear from this analysis that the signals from the two samples do not differ in the same manner shown in the coated samples. The difference seen between the two samples indicates a slightly greater signal (approximately 3.5%) from the polished sample compared to the rough sample. Peaks 2 and 5 for the rougher sample are 95% that of the polished sample and less than 1% difference is observed for peaks 3 and 4 between the two samples, the rougher sample having the slightly greater peak intensity for the inner peaks.

Thus any greater surface area created by the roughness in the sample ground with P120 paper does not appear to lead to significantly greater observed signals. Previous studies using Monte Carlo simulations of varying roughness iron surfaces [22] showed that the degree of roughness is not too much of an issue in CEMS provided that the amplitude of undulation is less than one tenth of the wavelength of surface undulation with the amplitude being no greater than 100 nm. A smaller amplitude to wavelength ratio results in a slower oscillation of surface plane and a signal closer to that of the plane surface than that found with more rapidly oscillating surfaces, which have larger amplitude to wavelength ratios.

Although the talysurf traces are not as regularly undulating as the Monte Carlo modelled surfaces it is evident that there are between 50 to 100 significant peaks over the full range of 5.2 mm on the roughest sample analysed in this study. This gives a large wavelength of surface undulation, with an amplitude to wavelength ratio smaller than 1:100, however the amplitude of these peaks are generally somewhat larger than 100 nm. The smoother samples, polished with diamond paste have amplitudes much less than 100 nm and so the roughness of these samples is not expected to affect signal.

By extrapolating from the Monte Carlo simulation study of Liljequist and Ismail [22] it may be possible, even with the larger amplitudes over 100 nm observed through the talysurf measurements in this present study, that with the small amplitude to wavelength ratios found in this present study, the sample roughness may be deemed negligible.

Studies aimed at experimentally refining the Monte Carlo simulations whilst also considering surface roughness of 1  $\mu\text{m}$  to 1mm in size on iron coated stainless steel substrates found the low energy electrons to be most affected by roughness. Analytical calculations of the effects of roughness of this magnitude on electron scattering have met difficulties in these previous studies. However, experimentally, it was found that both the integral CEMS signal and that from the higher energy electrons (11.5 - 14.5 keV) were almost unaffected by the increase in roughness [23,24]. Thus the analysis of the rough and smooth steel samples in this present study agrees with these previous investigations.

So from the result of this analysis of these uncoated samples it can be concluded that the increase in substrate signal with increasing roughness in the series of roughness samples can be attributed in some way to the presence and distribution of the intermetallics.

In the series of intermetallic coated roughness samples, the rougher the sample surface the greater the signal from the substrate, see figure 7.135 (with the intermetallic signal varying between approximately 17000 counts and 19000 counts with a mean value of approximately 18000 counts). This effect is especially prevalent as the average roughness increases over 0.2  $\mu\text{m}$ . Unfortunately with the samples analysed it is difficult to say precisely at what roughness the substrate signal will increase most rapidly. However extrapolating from the results, this may be within the region of the escape depth of the K-conversion electrons in the CEMS spectrometer, which is in the order of 0.3 $\mu\text{m}$ .

The signals for the intermetallics obtained would suggest that with rougher samples we obtain a similar amount of intermetallics formed over the larger effective surface area to those formed on the smoother surfaces. Previous studies on rough samples [24] have discussed the effect of electrons emerging at small angles reentering into the sample surface. Thus it is possible that more intermetallic is formed in the valleys of the surface but some reentering of electrons from the intermetallic occurs reducing the effective signal detected.

However the substrate that forms the peaks of the rough surfaces protrudes above the intermetallic layer in these rougher samples whereas it is almost completely covered in the smoother samples giving rise to larger substrate signals from the rougher samples. Samples of intermediate roughness where the surface is covered by intermetallic may have areas coated in only a thin layer, which may give rise to some slight increase in substrate signal.

In all cases for these samples the intermetallic layer causes a reduction in the substrate signal. The marked increase in substrate signal with the greater roughness samples is likely to be due to the complete exposure of substrate allowing electrons to exit unhindered by any coating.

The tin deposited is approximately 2  $\mu\text{m}$ , which means in the rougher samples, upon reaching the tin melting point, tin is reflowed into the valleys leaving exposed steel substrate peaks. If more tin is deposited in the electrodeposition procedure then the significance of these peaks would become less as during the heat treatment procedure the melted tin would be more abundant and cover more of the peaks where intermetallics would be formed. The effect of different tin coatings is illustrated in figure 7.138. Wetting, by tin, of the substrate may mean some tin remains on the peaks even after heat-treatment, but the amount of tin on the peaks would be minimal compared to the situation arising when greater tin coatings are used.

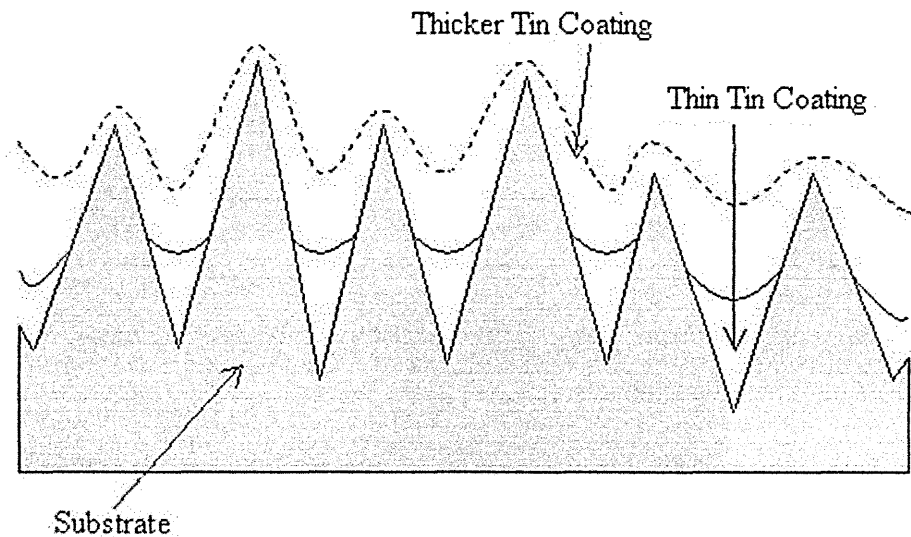


Figure 7.138. Effect of different tin coating weight on rough substrate.

In the case with greater tin coating, the situation where the effective area of the intermetallics increases with roughness giving a larger intermetallic signal may occur. Since the intermetallic layer would be more integral then the substrate signal would be effectively reduced. Such an effect may also be seen where the heat treatment temperature is less than the melting point of tin. In that case the tin would still diffuse as this study has shown but the tin would not be reflowed over the sample surface. However to form the same amount of intermetallic would require longer heat-treatment times.

The maximum peak to valley distances for the roughness samples are shown in table 7.33 and highlight the fact that the reflowed tin will leave greater protrusions of the substrate on the surfaces of the rougher samples.

#### 7.13.4 XRD Studies of Substrate Roughness

XRD was used to analyse the crystallographic structure of the heat-treated and etched tinplated steel of varying roughness. Bragg-Brentano geometry was used to analyse the samples and Glancing Angle X-Ray Diffraction (GA-XRD) was used to analyse the uppermost surface of the material. Bragg-Brentano XRD and GA-XRD with an incident angle  $\alpha = 1^\circ$  were carried out on three selected samples using a Philips PW3710 diffractometer.

As an indication of the effect of roughness on the samples it was prudent to first analyse various roughness steel substrates. The smoothest and roughest samples were chosen to illustrate any differences in iron signal between these roughness samples. By using the XRD in Bragg-Brentano configuration on both the smoothest sample, which was a polished mild steel substrate, polished with  $1\mu\text{m}$  diamond paste, and the roughest, ground with a P120 rotating grinding disc, clear iron signals were identified with the four peaks associated with the (110), (200), (211) and (220) planes identified at  $2\theta$  angles of  $44.671^\circ$ ,  $65.018^\circ$ ,  $82.329^\circ$  and  $98.940^\circ$  and relative intensities of 100, 20, 30 and 10 respectively in the JCPDS file for iron. The standard is of an exceptionally pure rolled sheet, in this experiment the sheet is rolled also but also surface ground to produce the various grades of roughness. It is of importance to note that the data acquired shows some of the peaks as two individually identified peaks where crystallographically there should only be one. This is a product of the software identification and is due to the asymmetry of some of the peaks.

Using the X-ray diffractometer with Bragg-Brentano geometry the diffraction trace in figure 7.139 was obtained for the smoothest steel sample. The peak fitting data are shown in tables 7.38 and 7.39.

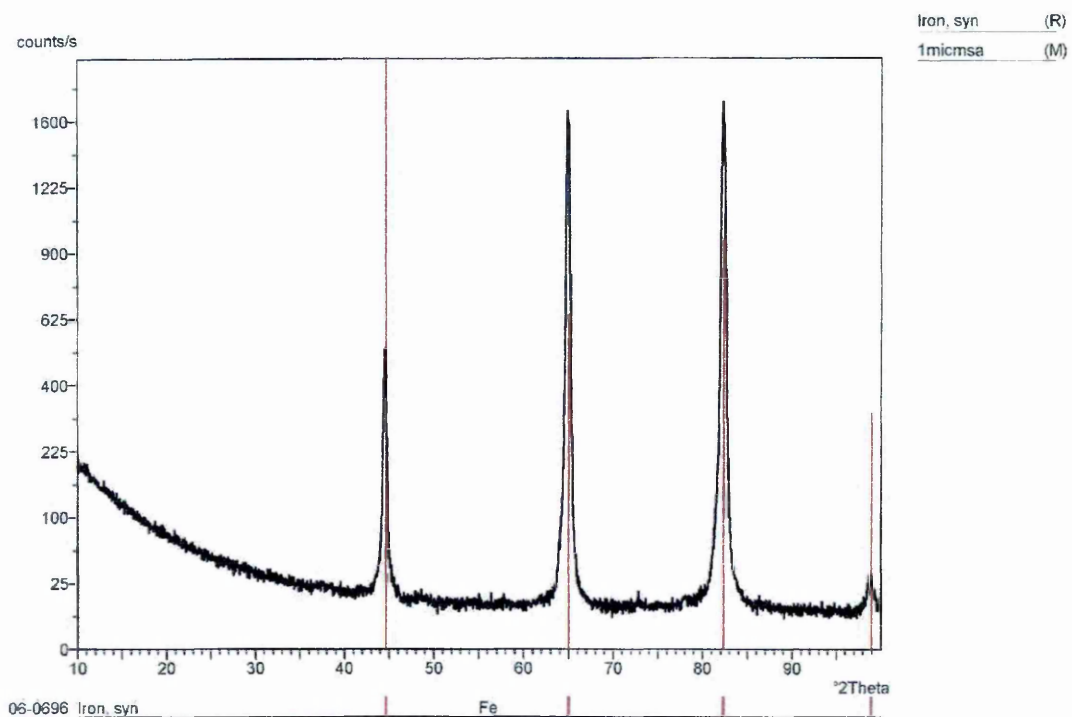


Figure 7.139. Diffraction trace of smoothest steel substrate obtained using Bragg-Brentano geometry.

Fe Standard				Sample			
d / Å	2θ / °	RI %	h k l	d / Å	2θ / °	RI %	d Diff. / Å
2.0268	44.6714	100	1 1 0	2.0330	44.5279	28.1	0.0062
1.4332	65.0182	20	2 0 0	1.4372	64.8151	97.6	0.0040
1.1702	82.3286	30	2 1 1	1.1724	82.1408	100.0	0.0022
1.0134	98.9399	10	2 2 0	1.0160	98.5975	1.0	0.0026

Table 7.38. Peak fitting data for Fe.

Sample Unidentified Peaks			
Peak no.	d / Å	2θ / °	RI %
1	1.8692	48.6705	0.1
2	1.1694	82.3972	67.8

Table 7.39. Sample unidentified peaks.

All four Fe peaks are identified in the X-ray diffraction trace. There are two unidentified peaks on this trace, however the first unidentified peak is fitted by the APD software incorrectly and has arisen because of noise. The second unidentified peak has arisen because of the APD software fitting two narrow peaks to the asymmetrical (211) Fe peak.

The relative intensities for the polished mild steel substrate are such that the (200) and (211) planes are 97.6% and 100% respectively, where as the (110) peak, the most intense in the standard, is only 28.1% in the sample. It is assumed that the lack of sample annealing and the introduction of surface grinding has caused such a difference between the sample and standard intensities.

Using the X-ray diffractometer with Bragg-Brentano geometry the diffraction trace in figure 7.140 was obtained for the roughest steel sample. The peak fitting data are shown in tables 7.40 and 7.41.

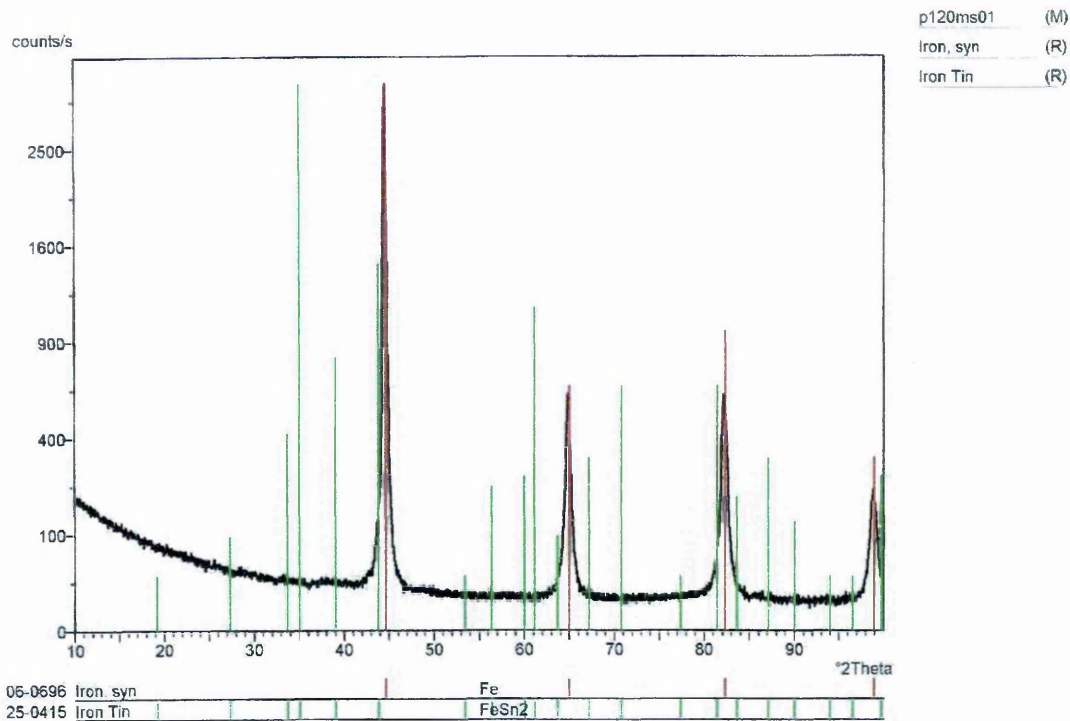


Figure 7.140. Diffraction trace of roughest steel substrate obtained using Bragg-Brentano geometry.

Fe Standard				Sample			
d / Å	2θ / °	RI %	h k l	d / Å	2θ / °	RI %	d Diff. / Å
2.0268	44.6714	100	1 1 0	2.0309	44.5764	100	0.0041
1.4332	65.0182	20	2 0 0	1.4377	64.7898	18.4	0.0045
1.1702	82.3286	30	2 1 1	1.1728	82.1067	18.3	0.0026
1.0134	98.9399	10	2 2 0	1.0143	98.8210	6.5	0.0009

Table 7.40. Peak fitting data for Fe.

Sample Unidentified Peaks			
Peak no.	d / Å	2θ / °	RI %
1	8.5814	10.2994	0.8
2	1.4334	65.0080	15.4

Table 7.41. Sample unidentified peaks.

The sample ground with P120 grinding paper shows the same peaks, identified as iron, however the intensities are very different to those found with the polished sample. The strongest peak on the standard is identified as the strongest peak on the ground sample. The (200) and (211) peaks have intensities around 18% as compared to 20% and 30% respectively in the standard. The (220) peak has a low intensity of approximately 6% as compared to 10% in the standard. There are also two unidentified peaks on this trace, as with the fitting of the data for the smoothest sample, figure 7.139, these have arisen because of incorrect identification in the software fitting routine.

Using the X-ray diffractometer with glancing angle geometry, with an angle of incidence of the X-ray beam,  $\alpha$ , set to  $1^\circ$ , the diffraction trace in figure 7.141 was obtained for the smoothest steel sample. The peak fitting data are shown in table 7.42.

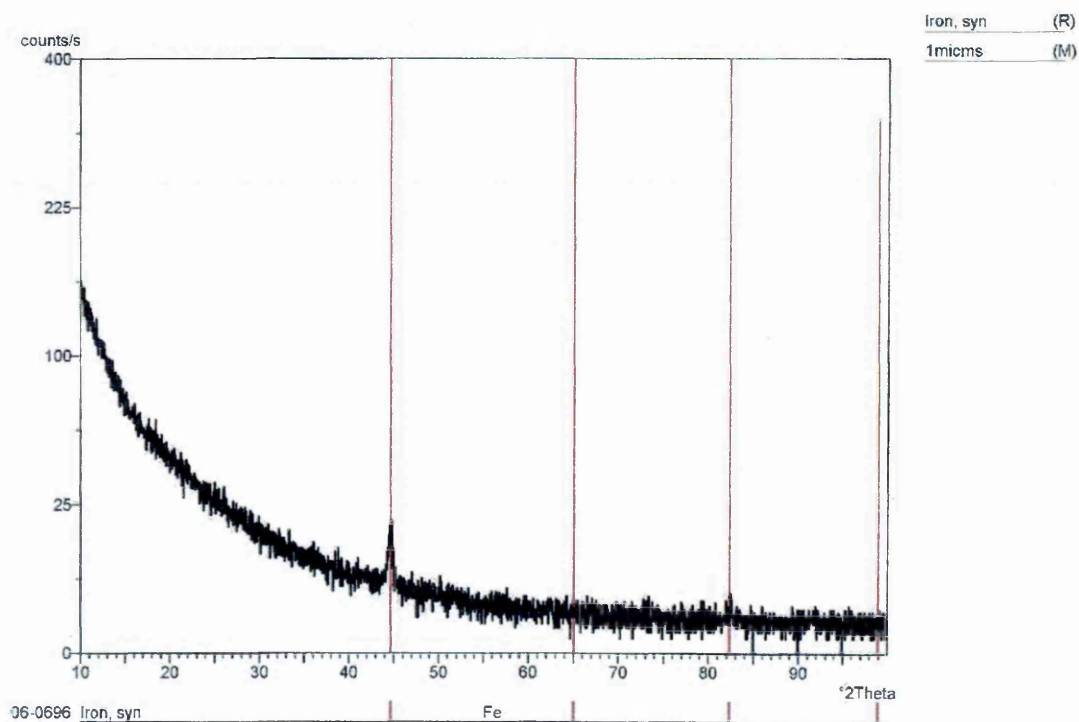


Figure 7.141. Diffraction trace of smoothest steel substrate obtained using glancing angle geometry.

Fe Standard				Sample			
d / Å	2θ / °	RI %	h k l	d / Å	2θ / °	RI %	d Diff. / Å
2.0268	44.6714	100	1 1 0	2.0285	44.6319	100	0.0017
1.4332	65.0182	20	2 0 0				
1.1702	82.3286	30	2 1 1				
1.0134	98.9399	10	2 2 0				

Table 7.42. Peak fitting data for Fe.

The results were not as expected as on the polished sample it was predicted that the signal would not significantly alter, however the resultant signal was considerably reduced compared to the signal obtained using Bragg-Brentano. In this case only two peaks were visible, the (110) and (211) peaks both of which were very weak reflections. The software has only identified the first of these peaks though the second is visible.

Using the X-ray diffractometer with glancing angle geometry, with an angle of incidence of the X-ray beam,  $\alpha$ , set to 1°, the diffraction trace in figure 7.142 was obtained for the roughest steel sample. The peak fitting data are shown in tables 7.43 and 7.44.

Fe Standard				Sample			
d / Å	2θ / °	RI %	h k l	d / Å	2θ / °	RI %	d Diff. / Å
2.0268	44.6714	100	1 1 0	2.0322	44.5463	100	0.0054
1.4332	65.0182	20	2 0 0	1.4365	64.8505	9.5	0.0033
1.1702	82.3286	30	2 1 1	1.1712	82.2431	21.4	0.001
1.0134	98.9399	10	2 2 0	1.0135	98.9267	11.1	0.0001

Table 7.43. Peak fitting data for Fe.

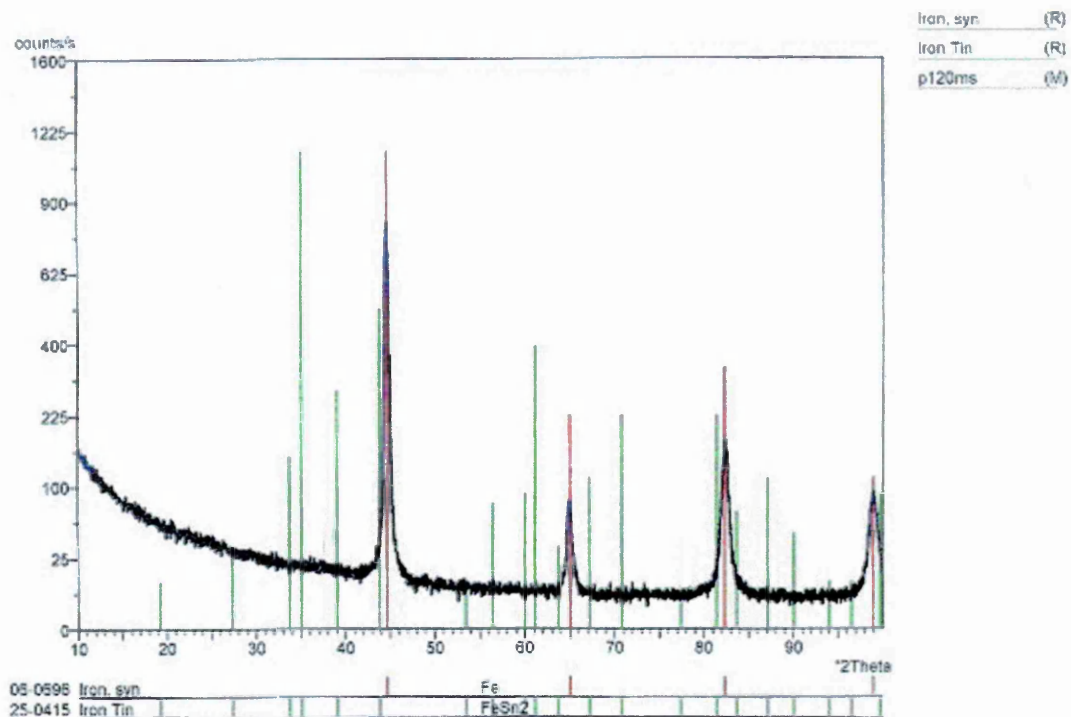


Figure 7.142. Diffraction trace of roughest steel substrate obtained using glancing angle geometry.

Sample Unidentified Peaks			
Peak no.	d / Å	2θ / °	RI %
1	1.1680	82.5175	16.9

Table 7.44. Sample unidentified peaks.

The glancing angle result for the ground sample was closer to that found with Bragg-Brentano. Again with the glancing angle configuration the overall signal was diminished from the Bragg-Brentano results, however all the first four iron peaks were identified this time with relative intensities of 100, 9.5, 21.4 and 11.1. Thus the relative intensity of the (211) and (220) peaks has increased and the intensity of the (200) peak is reduced. The unidentified peak has arisen because of the APD software fitting two peaks to the asymmetrical (211) Fe peak.

### 7.13.5 Introduction to XRD Analysis of Heat-Treated Tinplate Samples

One may expect the general results from section 7.13.4 for the substrate analysis to follow through to the etched tinplated roughness samples, however it does not. Instead the Fe and the FeSn<sub>2</sub> data for the three analysed tinplated samples follow more closely the peak intensities for the standard data.

The three etched tinplated samples analysed were a 1 µm polished sample, and two ground samples, one ground with medium grade P600 paper and one with rougher P120 paper. Within the range set for the 2θ angles in this analysis the first 21 peaks of FeSn<sub>2</sub> can be identified using the data though some of the reflections are very weak and are not identified. The data has been split into analysis compared to the two standards for Fe and FeSn<sub>2</sub>. For ease of comparing to the standard data, the relative intensities for the Fe, which are in all cases here less than the most intense peak for FeSn<sub>2</sub>, have been recalculated so that the strongest Fe peak is 100% and the other Fe peaks are relative to that peak. The original relative intensities are also shown in the tabulated data for comparison of intensities between Fe and FeSn<sub>2</sub> for each sample analysis. Any extra peaks have been tabulated and are discussed in terms of their relevance to the analysis.

### 7.13.6 XRD Results for Polished 1 µm Sample Using Bragg-Brentano Configuration

Using the X-ray diffractometer with Bragg-Brentano geometry the diffraction trace in figure 7.143 was obtained. The peak fitting data are shown in tables 7.45, 7.46 and 7.47.

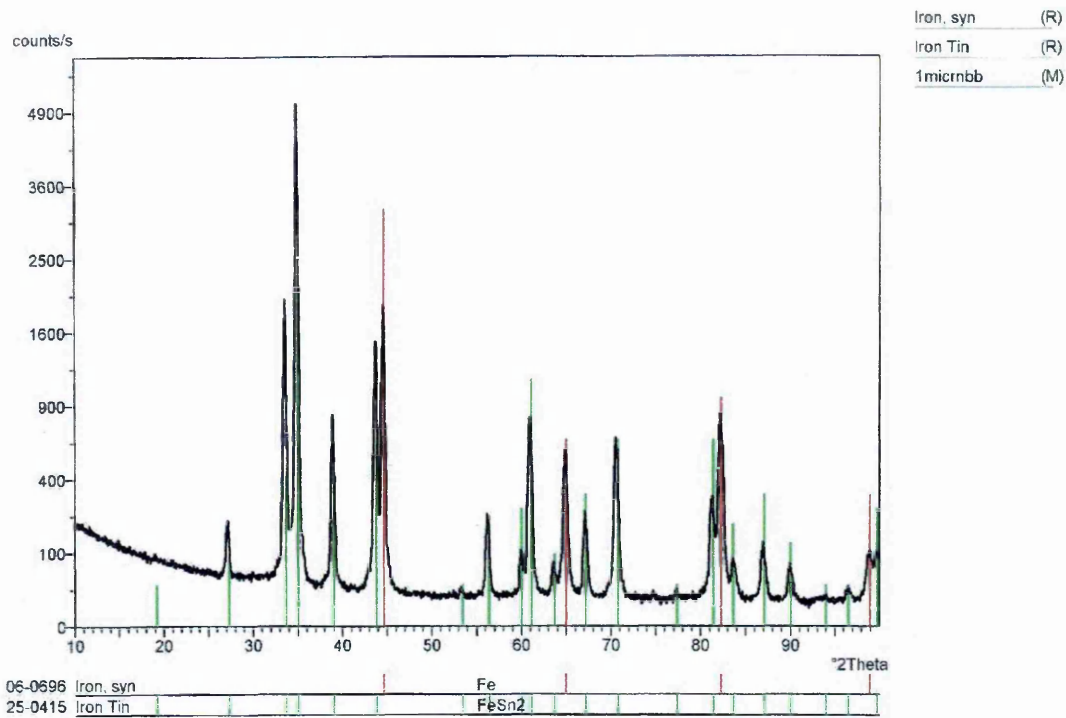


Figure 7.143. Diffraction trace of smoothest sample obtained using Bragg-Brentano geometry.

FeSn <sub>2</sub> Standard				Sample			
d / Å	2θ / °	RI %	h k l	d / Å	2θ / °	RI %	d Diff. / Å
4.610	19.2365	1	1 1 0				
3.260	27.3333	3	2 0 0	3.2794	27.1685	3.2	0.0194
2.656	33.7164	13	0 0 2	2.6682	33.5576	38.4	0.0122
2.556	35.0774	100	2 1 1	2.5691	34.8928	100.0	0.0131
2.304	39.0612	25	1 1 2	2.3119	38.9223	15.7	0.0079
2.063	43.8465	45	2 0 2	2.0695	43.7017	29.4	0.0065
1.713	53.4424	<1	3 2 1	1.7211	53.1711	0.1	0.0081
1.629	56.4371	7	3 1 2	1.6353	56.2003	3.9	0.0063
1.540	60.0215	8	3 3 0	1.5430	59.8928	1.6	0.003
1.515	61.1167	35	2 1 3	1.5190	60.9387	15.6	0.004
1.460	63.6826	3	4 2 0	1.4633	63.5222	1.2	0.0033
1.392	67.1930	10	4 0 2	1.3944	67.0620	4.6	0.0024
1.330	70.7795	20	0 0 4	1.3350	70.4749	12.4	0.005
1.232	77.3942	1	2 0 4	1.2344	77.2158	0.2	0.0024
1.181	81.4156	20	4 1 3	1.1831	81.2407	5.9	0.0021
1.155	83.6539	6	5 1 2	1.1564	83.5298	1.4	0.0014
1.118	87.0947	10	3 1 4	1.1196	86.9391	2.3	0.0016
1.089	90.0314	4	6 0 0	1.0899	89.9367	1.1	0.0009
1.053	94.0215	<1	4 3 3				
1.032	96.5532	1	4 0 4	1.0324	96.5034	0.3	0.0004
1.0073	99.7549	8	3 3 4	1.0089	99.5395	1.8	0.0016

Table 7.45. Peak fitting data for FeSn<sub>2</sub>.

There are only two of the FeSn<sub>2</sub> peaks missing from the sample data and both are listed as having relative intensities of 1 or less in the standard and so these can easily be lost in noise. Comparing to the standard data the relative intensities follow the general trend associated with FeSn<sub>2</sub> although the (002) peak is more intense than expected and the (211) peak is of greater intensity than expected as the majority of the other peaks are weaker than identified in the standard.

Fe Standard				Sample				
d / Å	2θ / °	RI %	h k l	d / Å	2θ / °	RI %	Adjusted RI %	d Diff. / Å
2.0268	44.6714	100	1 1 0	2.0322	44.5463	37.5	100	0.0054
1.4332	65.0182	20	2 0 0	1.4370	64.8252	10.9	29.1	0.0038
1.1702	82.3286	30	2 1 1	1.1721	82.1663	16.2	43.2	0.0019
1.0134	98.9399	10	2 2 0	1.0137	98.9002	1.7	4.5	0.0003

Table 7.46. Peak fitting data for Fe.

The Fe is identified fully in this sample with all four peaks quite intense in the trace. Comparing to the standard data the relative intensities follow the general trend associated with Fe.

Sample Unidentified Peaks			
Peak no.	d / Å	2θ / °	RI %
1	2.7388	32.6680	0.7
2	2.3240	38.7115	7.9
3	2.0407	44.3509	19.8
4	1.3977	66.8828	2.4
5	1.3381	70.2875	5.5
6	1.3316	70.6817	11.0
7	1.2931	73.1196	0.0
8	1.2706	74.6319	0.1
9	1.1690	82.4315	9.8
10	1.0161	98.5844	1.4

Table 7.47. Sample unidentified peaks.

There at first appear to be 10 unidentified peaks on this trace, but they are either noise or have arisen because of the APD software fitting a number of narrow peaks to what is in effect a single broad peak. The latter is due to the peaks being not entirely symmetrical and this is the case with peaks numbered 2, 4, 5 and 6, which are part of FeSn<sub>2</sub> peaks and peaks 3, 9 and 10 which are part of Fe peaks. Peaks 1, 7 and 8 are of low intensity and are considered to be noise. The relative intensities given for these unidentified peaks are relative to the strongest peak in the trace.

### 7.13.7 XRD Results for Polished 1 $\mu\text{m}$ Sample Using Glancing Angle Configuration

Using the X-ray diffractometer with glancing angle geometry, with an angle of incidence of the X-ray beam of 1°, the diffraction trace in figure 7.144 was obtained.

The peak fitting data are shown in table 7.48.

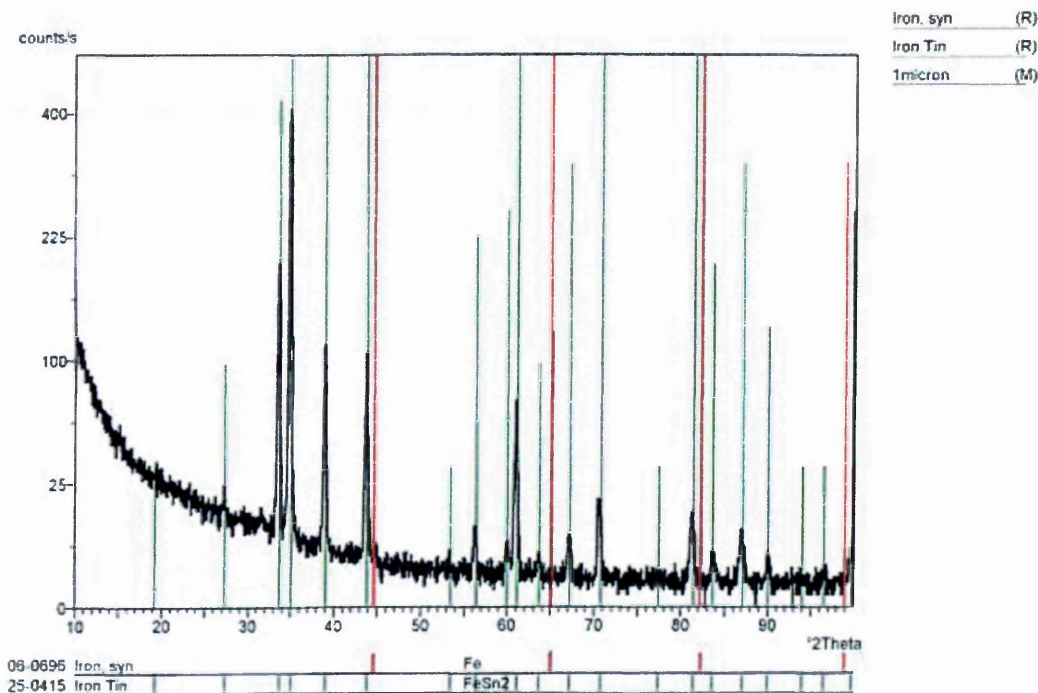


Figure 7.144. Diffraction trace of smoothest sample obtained using glancing angle geometry.

FeSn <sub>2</sub> Standard				Sample			
d / Å	2θ / °	RI %	h k l	d / Å	2θ / °	RI %	d Diff. / Å
4.610	19.2365	1	1 1 0				
3.260	27.3333	3	2 0 0	3.2665	27.2779	1.3	0.0065
2.656	33.7164	13	0 0 2	2.6682	33.5576	47.7	0.0122
2.556	35.0774	100	2 1 1	2.5702	34.8774	100.0	0.0142
2.304	39.0612	25	1 1 2	2.3119	38.9223	27.6	0.0079
2.063	43.8465	45	2 0 2	2.0697	43.6972	25.5	0.0067
1.713	53.4424	<1	3 2 1				
1.629	56.4371	7	3 1 2	1.6355	56.1929	1.9	0.0065
1.540	60.0215	8	3 3 0	1.5427	59.9057	1.1	0.0027
1.515	61.1167	35	2 1 3	1.5203	60.8810	17.1	0.0053
1.460	63.6826	3	4 2 0	1.4601	63.6778	0.7	0.0001
1.392	67.1930	10	4 0 2	1.3945	67.0566	1.7	0.0025
1.330	70.7795	20	0 0 4	1.3358	70.4264	4.7	0.0058
1.232	77.3942	1	2 0 4				
1.181	81.4156	20	4 1 3	1.1841	81.1577	3.5	0.0031
1.155	83.6539	6	5 1 2	1.1562	83.5475	0.9	0.0012
1.118	87.0947	10	3 1 4	1.12	86.9003	2.2	0.002
1.089	90.0314	4	6 0 0	1.0892	90.0103	0.6	0.0002
1.053	94.0215	<1	4 3 3				
1.032	96.5532	1	4 0 4	1.0318	96.5781	0.4	-0.0002
1.0073	99.7549	8	3 3 4				

Table 7.48. Peak fitting data for FeSn<sub>2</sub>.

There are five of the FeSn<sub>2</sub> peaks missing from the sample data the first four missing peaks are listed as having relative intensities of 1 or less in the standard and so these can easily be lost in noise. The fifth peak is close to the maximum 2θ value and can easily be unidentified by the fitting program in this case that appears to be the reason for its absence.

The relative intensities of the experimentally obtained data show similarities to the standard data for FeSn<sub>2</sub> however it appears that the (211) peak is of greater intensity than expected as the majority of the other peaks are weaker than identified in the standard. Exceptions to this observation are the (002) and (112) peaks which are more intense than identified in the standard.

There are no peaks on the trace that remain unidentified and there are no Fe peaks observed. The lack of any Fe peaks shows that with the glancing angle geometry the incident X-ray beam only impinges on the surface, which is, on the smooth polished sample, a uniform FeSn<sub>2</sub> layer.

### 7.13.8 XRD Results for Ground P600 Sample Using Bragg-Brentano Configuration

Using the X-ray diffractometer with Bragg-Brentano geometry the diffraction trace in figure 7.145 was obtained. The peak fitting data are shown in tables 7.49, 7.50 and 7.51.

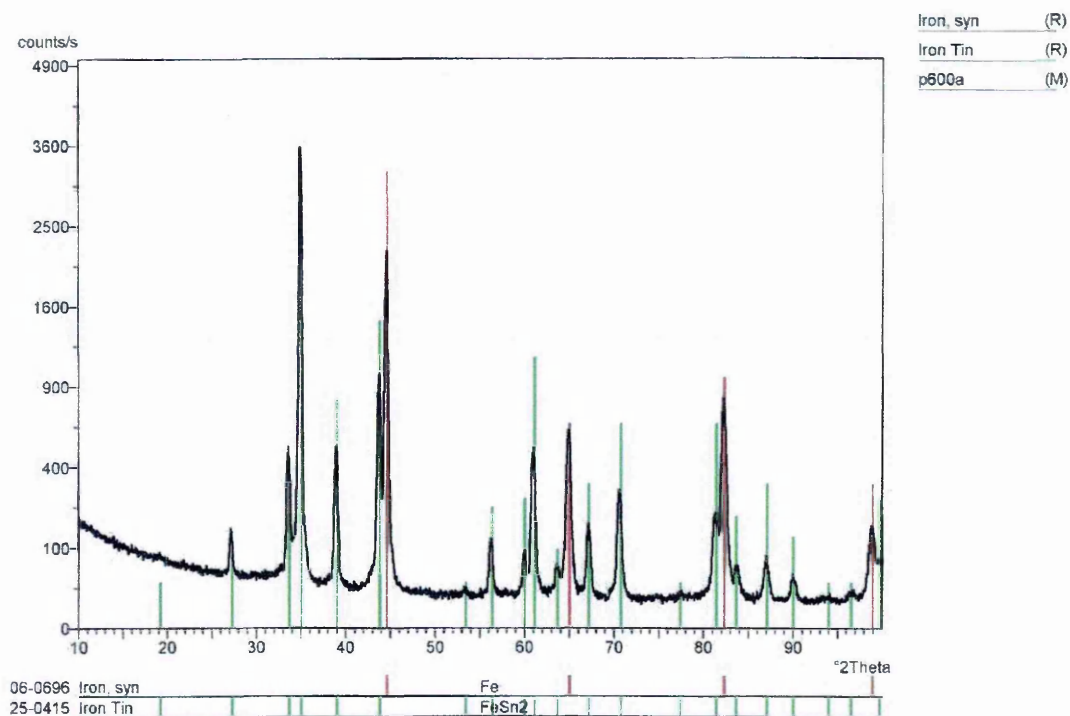


Figure 7.145. Diffraction trace of intermediate roughness sample obtained using Bragg-Brentano geometry.

FeSn <sub>2</sub> Standard				Sample			
d / Å	2θ / °	RI %	h k l	d / Å	2θ / °	RI %	d Diff. / Å
4.610	19.2365	1	1 1 0	4.6611	19.0236	0.1	0.0511
3.260	27.3333	3	2 0 0	3.2818	27.1483	3.1	0.0218
2.656	33.7164	13	0 0 2	2.6678	33.5628	13.3	0.0118
2.556	35.0774	100	2 1 1	2.5684	34.9026	100	0.0124
2.304	39.0612	25	1 1 2	2.3153	38.8628	13.2	0.0113
2.063	43.8465	45	2 0 2	2.0713	43.6617	25.7	0.0083
1.713	53.4424	<1	3 2 1	1.7206	53.1878	0.2	0.0076
1.629	56.4371	7	3 1 2	1.6338	56.2565	2.7	0.0048
1.540	60.0215	8	3 3 0	1.5436	59.8672	2.9	0.0036
1.515	61.1167	35	2 1 3	1.5222	60.7970	11.5	0.0072
1.460	63.6826	3	4 2 0	1.4638	63.4980	1.2	0.0038
1.392	67.1930	10	4 0 2	1.3934	67.1165	4.2	0.0014
1.330	70.7795	20	0 0 4	1.3347	70.4931	7.4	0.0047
1.232	77.3942	1	2 0 4				
1.181	81.4156	20	4 1 3	1.1837	81.1909	5.1	0.0027
1.155	83.6539	6	5 1 2	1.1562	83.5475	1.2	0.0012
1.118	87.0947	10	3 1 4	1.1197	86.9294	1.9	0.0017
1.089	90.0314	4	6 0 0	1.0906	89.8633	0.8	0.0016
1.053	94.0215	<1	4 3 3				
1.032	96.5532	1	4 0 4	1.0322	96.5283	0.1	0.0002
1.0073	99.7549	8	3 3 4				

Table 7.49. Peak fitting data for FeSn<sub>2</sub>.

There are three of the FeSn<sub>2</sub> peaks missing from the sample data. The first two missing peaks are listed as having relative intensities of 1 or less in the standard and so these can easily be lost in noise. The third peak is close to the maximum 2θ value and can easily be unidentified by the fitting program in this case that appears to be the reason for its absence. The relative intensity values follow the general trend of the standard with the (211) peak being the primary peak.

Fe Standard				Sample				
d / Å	2θ / °	RI %	h k l	d / Å	2θ / °	RI %	Adjusted RI %	d Diff. / Å
2.0268	44.6714	100	1 1 0	2.0322	44.5463	61.5	100	0.0054
1.4332	65.0182	20	2 0 0	1.4359	64.8810	16.1	26.2	0.0027
1.1702	82.3286	30	2 1 1	1.1727	82.1152	22.4	36.4	0.0025
1.0134	98.9399	10	2 2 0	1.0155	98.6631	3.5	5.7	0.0021

Table 7.50. Peak fitting data for Fe.

The Fe is identified fully in this sample with all four peaks visible in the diffractometer trace. Comparing to the standard data the relative intensities follow the correct general trend associated with Fe.

Sample Unidentified Peaks			
Peak no.	d / Å	2θ / °	RI %
1	1.3316	70.6817	6.5

Table 7.51. Sample unidentified peaks.

There at first appears to be an unidentified peak on the trace, however it has arisen because of the APD software fitting two narrow peaks to what is in effect a single broad peak. The unidentified peak is thus subsequently identified as FeSn<sub>2</sub>. The relative intensity given for this unidentified peak is relative to the strongest peak in the trace.

#### 7.13.9 XRD Results for Ground P600 Sample Using Glancing Angle Configuration

Using the X-ray diffractometer with glancing angle geometry, with an angle of incidence of the X-ray beam of 1°, the diffraction trace in figure 7.146 was obtained.

The peak fitting data are shown in tables 7.52, 7.53 and 7.54.

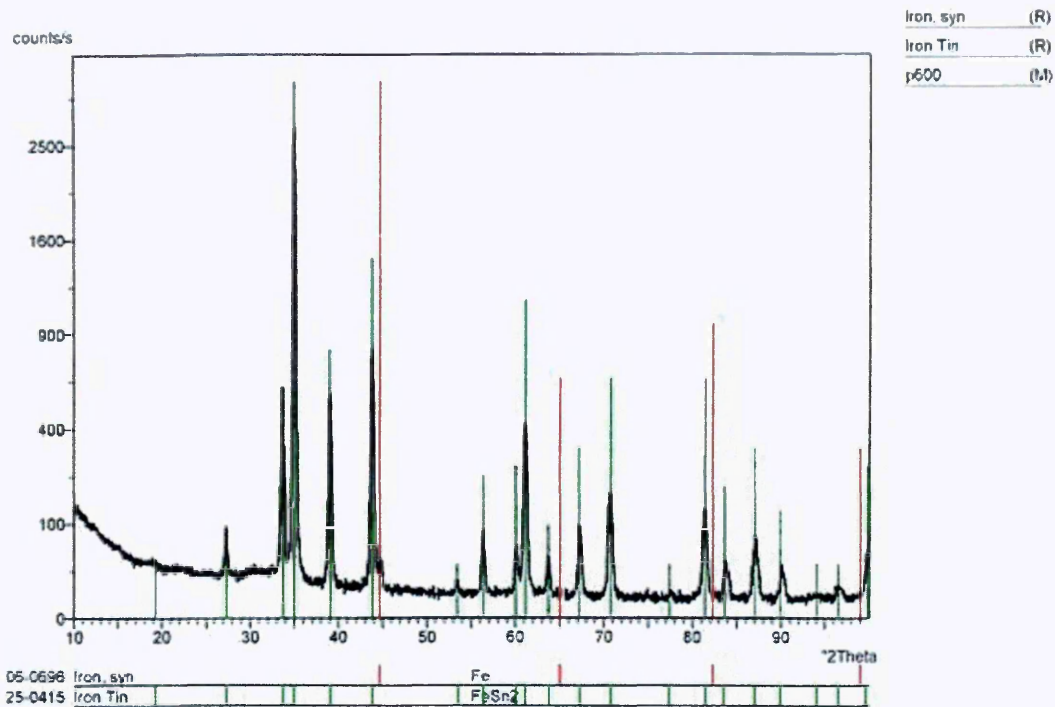


Figure 7.146. Diffraction trace of intermediate roughness sample obtained using glancing angle geometry.

FeSn <sub>2</sub> Standard				Sample			
d / Å	2θ / °	RI %	h k l	d / Å	2θ / °	RI %	d Diff. / Å
4.610	19.2365	1	1 1 0	4.6477	19.0790	0.1	0.0377
3.260	27.3333	3	2 0 0	3.2718	27.2329	2.1	0.0118
2.656	33.7164	13	0 0 2	2.6582	33.6876	21.9	0.0022
2.556	35.0774	100	2 1 1	2.5595	35.0279	100	0.0035
2.304	39.0612	25	1 1 2	2.3042	39.0576	20.4	0.0002
2.063	43.8465	45	2 0 2	2.0628	43.8509	29.7	-0.0002
1.713	53.4424	<1	3 2 1	1.7151	53.3718	0.2	0.0021
1.629	56.4371	7	3 1 2	1.6309	56.3655	2.9	0.0019
1.540	60.0215	8	3 3 0	1.542	59.9357	1.3	0.002
1.515	61.1167	35	2 1 3	1.5165	61.0498	15.5	0.0015
1.460	63.6826	3	4 2 0	1.4616	63.6047	1.3	0.0016
1.392	67.1930	10	4 0 2	1.3931	67.1329	3.1	0.0011
1.330	70.7795	20	0 0 4	1.3333	70.5781	6.1	0.0033
1.232	77.3942	1	2 0 4				
1.181	81.4156	20	4 1 3	1.1828	81.2656	4.8	0.0018
1.155	83.6539	6	5 1 2	1.155	83.6539	1	0
1.118	87.0947	10	3 1 4	1.1184	87.0557	2.5	0.0004
1.089	90.0314	4	6 0 0	1.09	89.9262	0.8	0.001
1.053	94.0215	<1	4 3 3				
1.032	96.5532	1	4 0 4	1.0321	96.5407	0.3	0.0001
1.0073	99.7549	8	3 3 4				

Table 7.52. Peak fitting data for FeSn<sub>2</sub>.

There are three of the FeSn<sub>2</sub> peaks missing from the sample data. The first two missing peaks are listed as having relative intensities of 1 or less in the standard and so these can easily be lost in noise. The third peak is close to the maximum 2θ value and can easily be unidentified by the fitting program in this case that appears to be the reason for its absence. The relative intensities of the experimentally obtained data follows the general trend of the standard data for FeSn<sub>2</sub> however it appears that the (211) peak is of greater intensity than expected as the majority of the other peaks are weaker than identified in the standard the exception to this observation being the (002) peak which is more intense than identified in the standard.

Fe Standard				Sample				
d / Å	2θ / °	RI %	h k l	d / Å	2θ / °	RI %	Adjusted RI %	d Diff. / Å
2.0268	44.6714	100	1 1 0	2.0236	44.7459	0.9	100	-0.0032
1.4332	65.0182	20	2 0 0					
1.1702	82.3286	30	2 1 1					
1.0134	98.9399	10	2 2 0					

Table 7.53. Peak fitting data for Fe.

The iron is only identified by a single peak, that being the (110) peak. It has a particularly low intensity in the trace but is visually identifiable, unlike the case with the polished sample analysed using glancing angle geometry. This observation coupled with the result from the polished sample would suggest that there is either exposed substrate or substrate that is close enough to the surface to be identified using the glancing angle geometry.

Sample Unidentified Peaks			
Peak no.	d / Å	2θ / °	RI %
1	5.9015	14.9990	0.2
2	2.7589	32.4234	0.3
3	1.3284	70.8776	3.9
4	1.2672	74.8664	0.1
5	1.2294	77.5884	0.1
6	1.1799	81.5075	3.6

Table 7.54. Sample unidentified peaks.

There are six peaks not clearly identified as FeSn<sub>2</sub> or Fe. Peaks 3 and 6 in table 7.54 are part of FeSn<sub>2</sub> peaks which the APD software has fitted with two peaks and the remaining peaks are noise, with relative intensities less than 0.3

#### 7.13.10 XRD Results for Ground P120 Sample Using Bragg-Brentano Configuration

Using the X-ray diffractometer with Bragg-Brentano geometry the diffraction trace in figure 7.147 was obtained. The peak fitting data are shown in tables 7.55, 7.56 and 7.57.

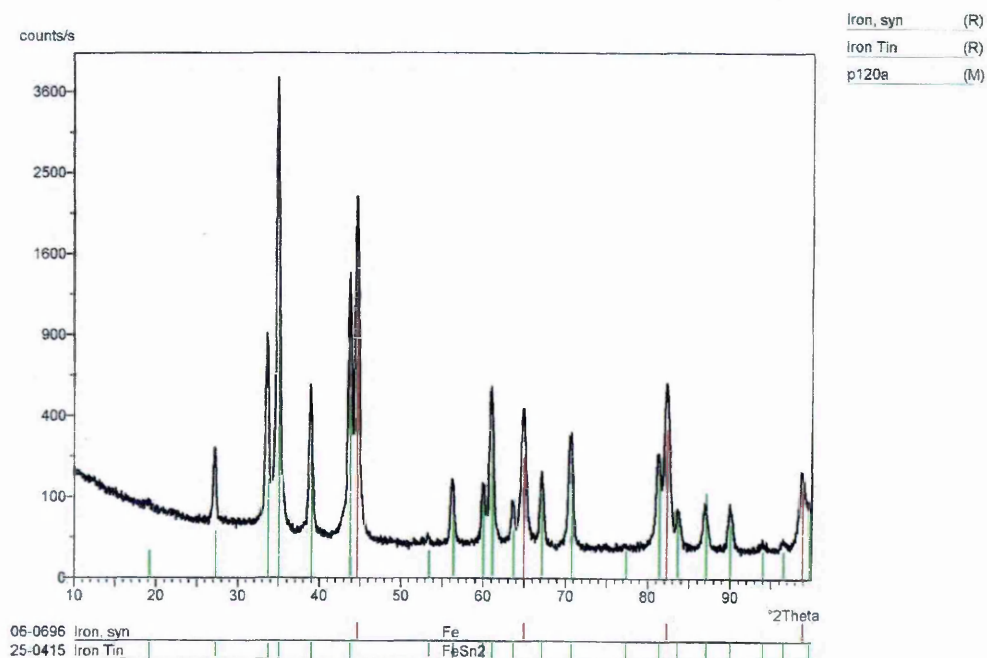


Figure 7.147. Diffraction trace of roughest sample obtained using Bragg-Brentano geometry.

FeSn <sub>2</sub> Standard				Sample			
d / Å	2θ / °	RI %	h k l	d / Å	2θ / °	RI %	d Diff. / Å
4.610	19.2365	1	1 1 0	4.6806	18.9436	0.2	0.0706
3.260	27.3333	3	2 0 0	3.2783	27.1778	5.5	0.0183
2.656	33.7164	13	0 0 2	2.667	33.5732	23.2	0.011
2.556	35.0774	100	2 1 1	2.5684	34.9026	100	0.0124
2.304	39.0612	25	1 1 2	2.313	38.9030	14.3	0.009
2.063	43.8465	45	2 0 2	2.0699	43.6928	36.9	0.0069
1.713	53.4424	<1	3 2 1	1.7175	53.2913	0.3	0.0045
1.629	56.4371	7	3 1 2	1.6358	56.1816	3.2	0.0068
1.540	60.0215	8	3 3 0	1.543	59.8928	3.2	0.003
1.515	61.1167	35	2 1 3	1.5184	60.9653	13.7	0.0034
1.460	63.6826	3	4 2 0	1.4639	63.4931	2	0.0039
1.392	67.1930	10	4 0 2	1.3945	67.0566	4.1	0.0025
1.330	70.7795	20	0 0 4	1.332	70.6573	8.2	0.002
1.232	77.3942	1	2 0 4				
1.181	81.4156	20	4 1 3	1.1848	81.0998	5.8	0.0038
1.155	83.6539	6	5 1 2	1.1567	83.5033	1.5	0.0017
1.118	87.0947	10	3 1 4	1.1197	86.9294	1.7	0.0017
1.089	90.0314	4	6 0 0	1.0904	89.8842	1.9	0.0014
1.053	94.0215	<1	4 3 3	1.0537	93.9398	0.1	0.0007
1.032	96.5532	1	4 0 4	1.0337	96.3420	0.2	0.0017
1.0073	99.7549	8	3 3 4				

Table 7.55. Peak fitting data for FeSn<sub>2</sub>.

There are only two of the FeSn<sub>2</sub> peaks missing from the sample data the first has a relative intensity of 1 in the standard and so is easily be lost in noise. The second peak is close to the maximum 2θ value and can easily be unidentified by the fitting program in this case that appears to be the reason for its absence.

The peaks with higher d spacings again appear to have relative intensities deviated from the standard data although the general trend associated with FeSn<sub>2</sub> is adhered to. The main exceptions are the (200) and (002) peaks which are more intense than expected and the (112) peak is of much less intensity than may be expected from the standard. The majority of the other peaks are weaker than identified in the standard and this could be partially due to greater intensity of the primary (211) peak.

Fe Standard				Sample				
d / Å	2θ / °	RI %	h k l	d / Å	2θ / °	RI %	Adjusted RI %	d Diff. / Å
2.0268	44.6714	100	1 1 0	2.0324	44.5417	58.4	100	0.0056
1.4332	65.0182	20	2 0 0	1.4363	64.8607	10.9	18.7	0.0031
1.1702	82.3286	30	2 1 1	1.1721	82.1663	14.9	25.5	0.0019
1.0134	98.9399	10	2 2 0	1.0154	98.6762	3.3	5.7	0.002

Table 7.56. Peak fitting data for Fe.

The Fe is identified fully in this sample with all four peaks visible in the diffractometer trace. Comparing to the standard data the relative intensities follow the general trend associated with Fe with the (110) peak appearing to be more intense than expected as the other three identified peaks are weaker.

Sample Unidentified Peaks			
Peak no.	d / Å	2θ / °	RI %
1	1.5386	60.0817	2.4
2	1.4600	63.6826	1.7
3	1.3350	70.4749	7.9

Table 7.57. Sample unidentified peaks

There are three peaks on this trace that are not identified after the FeSn<sub>2</sub> and Fe identification. All three peaks are very close to FeSn<sub>2</sub> peaks and are fitted by the APD software due to the asymmetry of the relevant FeSn<sub>2</sub> peaks, fitting two peaks where there should only be one. The relative intensities given for these unidentified peaks are relative to the strongest peak in the trace.

### 7.13.11 XRD Results for Ground P120 Sample Using Glancing Angle Configuration

Using the X-ray diffractometer with glancing angle geometry, with an angle of incidence of the X-ray beam of  $1^\circ$ , the diffraction trace in figure 7.148 was obtained.

The peak fitting data are shown in tables 7.58, 7.59 and 7.60.

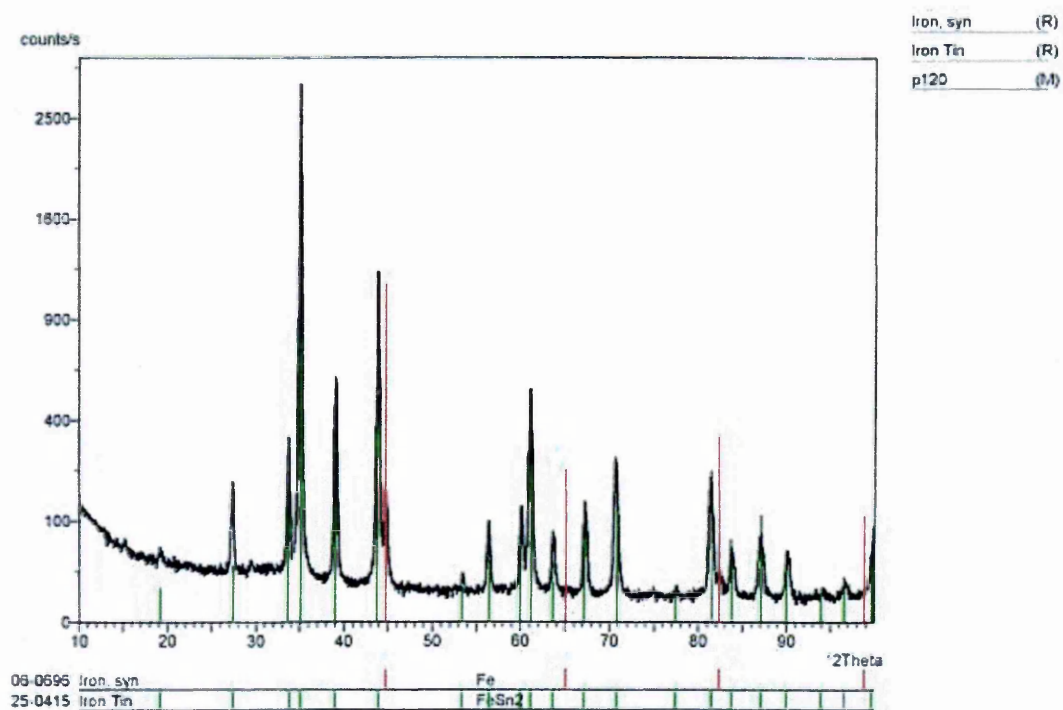


Figure 7.148. Diffraction trace of roughest sample obtained using glancing angle geometry.

FeSn <sub>2</sub> Standard				Sample			
d / Å	2θ / °	RI %	h k l	d / Å	2θ / °	RI %	d Diff. / Å
4.610	19.2365	1	1 1 0	4.6214	19.1886	0.5	0.0114
3.260	27.3333	3	2 0 0	3.2676	27.2685	5.6	0.0076
2.656	33.7164	13	0 0 2	2.659	33.6772	10.8	0.003
2.556	35.0774	100	2 1 1	2.5595	35.0279	100.0	0.0035
2.304	39.0612	25	1 1 2	2.3053	39.0382	20.5	0.0013
2.063	43.8465	45	2 0 2	2.0645	43.8130	42.3	0.0015
1.713	53.4424	<1	3 2 1	1.7151	53.3718	0.4	0.0021
1.629	56.4371	7	3 1 2	1.6319	56.3279	3.1	0.0029
1.540	60.0215	8	3 3 0	1.5394	60.0473	4.3	-0.0006
1.515	61.1167	35	2 1 3	1.517	61.0276	18.1	0.002
1.460	63.6826	3	4 2 0	1.4621	63.5804	2.2	0.0021
1.392	67.1930	10	4 0 2	1.3924	67.1711	4.5	0.0004
1.330	70.7795	20	0 0 4	1.3329	70.6025	9.0	0.0029
1.232	77.3942	1	2 0 4	1.2309	77.4762	0.1	-0.0011
1.181	81.4156	20	4 1 3	1.1831	81.2407	6.8	0.0021
1.155	83.6539	6	5 1 2	1.155	83.6539	1.5	0
1.118	87.0947	10	3 1 4	1.1181	87.0849	2.4	0.0001
1.089	90.0314	4	6 0 0	1.0894	89.9893	1.5	0.0004
1.053	94.0215	<1	4 3 3	1.0533	93.9865	0.1	0.0003
1.032	96.5532	1	4 0 4	1.0317	96.5905	0.4	-0.0003
1.0073	99.7549	8	3 3 4	1.0081	99.6471	1.8	0.0008

Table 7.58. Peak fitting data for FeSn<sub>2</sub>.

The full range of FeSn<sub>2</sub> peaks are identified. The relative intensities of the experimentally obtained data follows the general trend of the standard data for FeSn<sub>2</sub> however it appears that the (211) peak is of greater intensity than expected as the majority of the other peaks are weaker than identified in the standard the exception to this observation being the (200) peak which is more intense than identified in the standard.

Fe Standard				Sample				
d / Å	2θ / °	RI %	h k l	d / Å	2θ / °	RI %	Adjusted RI %	d Diff. / Å
2.0268	44.6714	100	1 1 0	2.0266	44.6760	5.7	100	-0.0002
1.4332	65.0182	20	2 0 0					
1.1702	82.3286	30	2 1 1	1.17	82.3458	0.6	10	-0.0002
1.0134	98.9399	10	2 2 0					

Table 7.59. Peak fitting data for Fe.

The iron is only identified by two peaks, the (110) and (211) peaks which are the most intense in the standard. They have low intensity in the trace but are visually identifiable, unlike the case with the polished sample analysed using glancing angle geometry where no peaks were identified and the intermediate roughness sample where only the first Fe peak was identified. This observation coupled with the result from the other two samples suggests that there is either exposed substrate or substrate that is close enough to the surface to be identified using the glancing angle geometry and this is more prevalent than in the intermediate roughness sample.

Sample Unidentified Peaks			
Peak no.	d / Å	2θ / °	RI %
1	5.8453	15.1441	0.4
2	3.0300	29.4533	0.3
3	1.2672	74.8664	0.1
4	1.0862	90.3273	1.2

Table 7.60. Sample unidentified peaks

There are four peaks not clearly identified as FeSn<sub>2</sub> or Fe. Peak 4 in table 7.60 is part of an FeSn<sub>2</sub> peak which the APD software has fitted with two peaks and the remaining peaks are noise, with relative intensities less than 0.4.

#### 7.13.12 Summary of Roughness Analysis Findings

The talysurf measurements of the prepared roughness samples shows a good spread of average roughness values that are suitable for the subsequent analysis. The electrodeposition procedure was shown to deposit approximately 2 μm of tin assuming a compact layer. Increasing roughness was shown to give rise to smaller crystalline

formations on the surface of the samples. The heat treatments subsequently applied to the range of samples formed a layer of FeSn<sub>2</sub>, which has been observed with both CEMS and XRD. Increased roughness leads to increased observed substrate signal using CEMS with the signal from the FeSn<sub>2</sub> remaining fairly constant throughout the range of samples. This effect was found to be due to the presence of intermetallics as rough substrates without intermetallic overlayers showed little difference when analysed using CEMS, much less than with the FeSn<sub>2</sub> layer.

In all the XRD traces as  $2\theta$  increases the relative intensities of the FeSn<sub>2</sub> diffraction are generally reduced compared to the relevant standard value. This is possibly due to differences in FeSn<sub>2</sub> thickness between the standard and those analysed here, with the samples analysed here being very thin and therefore angle of incidence being particularly important when considering the interaction volume and resultant intensity.

The GA-XRD results agree with those from CEMS where for the smoothest sample, GA-XRD figure 7.144, CEMS figure 7.129 only an FeSn<sub>2</sub> signal is obtained. For a sample of intermediate roughness, GA-XRD figure 7.146, CEMS figure 7.132, the ratio of the sum of the integrated intensity of peaks for FeSn<sub>2</sub> to Fe was 34 : 1 decreasing to 6 : 1 for the roughest sample, GA-XRD figure 7.148, CEMS figure 7.134.

## Results References

- [1] N. N. Greenwood, T. C. Gibb, "Mössbauer Spectroscopy", (Chapman and Hall, London, 1971).
- [2] G. Venturini, B. Malaman, G. Le Caër and D. Fruchart, Physical Review B, Vol. 35, No. 13 (1987), p. 7038.
- [3] G. Le Caër, B. Malaman, G. Venturini, D. Fruchart and B. Roques, J. Phys. F : Met. Phys. 15 (1985) pp. 1813 - 1827.
- [4] W. van Koesveld and J. S. van Westrum, From Blank to Can : Origin and Growth of the Morphology of the Wall of a DWI Can, Third International Tinplate Conference, ITRI, London (1985) pp. 310-318.
- [5] E. Morgan, Tinplate and Modern Canmaking Technology (Pergamon Press, Oxford, 1985) 166-175.
- [6] A. M. van der Kraan and K. H. J. Buschow, Physica B138 (1986) pp. 55-62.
- [7] Y. Ujihira, M. Fujinami, K. Yoshida and M. Terasaka, in "Applications of the Mössbauer Effect", Vol. 3, Y. M. Kagan and I. S. Lyubutin (Eds.) (1983) pp. 1213 – 1220.
- [8] V. I. Nikolaev, Yu. I. Shcherbina and S. S. Yakimov, Zh. Eksperim, i Teor. Fiz. 45, 1963, p. 1277. (J. Exptl. Theoret. Phys. (U.S.S.R.) 18, 1964, p. 878)
- [9] G. Fabri, E. Germagnoli, M. Musci and G. C. Locati, Il Nuovo Cimento, Vol. 40B, No. 1 (1965) p. 178.
- [10] S. J. Oh, D. C. Cook and H. E. Townsend, Hyperfine Interactions, 112 (1998), pp. 59-65.
- [11] D.L. Williamson et al. J. Appl. Phys. 60 (1986) 1493.
- [12] B. T. K. Barry and C. J. Thwaites, Transactions of the Institute of Metal Finishing, Vol 44 (1966) p. 143.
- [13] R. E. Smallman and R. J. Bishop, "Modern Physical Metallurgy and Materials Engineering", Sixth Edition, Butterworth Heinemann, 1999.
- [14] R. A. Higgins "Properties of Engineering Materials", Hodder and Stoughton, 1977, p. 163.
- [15] R. Pearce, "Sheet Metal Forming", Adam Hilger / IOP Publishing, 1991.

- [16] V. I. Nikolaev, Yu. I. Shcherbina and S. S. Yakimov, Zh. Eksperim, i Teor. Fiz. 45, 1963, p. 1277.(J. Exptl. Theoret. Phys. (U.S.S.R.) 18, 1964, p. 878).
- [17] J. L. Davidson, PhD Thesis: “<sup>57</sup>Fe Mössbauer Studies of Surface Interactions in a PVD Process”, Sheffield Hallam University, (1997).
- [18] T. S. V. Bonchev, A. Minkova, G. Kushev and M. Grozdanov, Nucl. Instr. Meth. 147 (1977) pp. 481-486.
- [19] M. J. Tricker, L. A. Ash and T. E. Cranshaw, Nucl. Instr. Meth. 143 (1977) p. 307.
- [20] R. A. Krakowski and R. B. Miller, Nucl. Instr. Meth. 100 (1972) p. 93.
- [21] J. R. Gancedo, J. Z. Dávalos, M. Gracia and J. F. Marco, Hyp. Interact. 110 (1997) pp. 41-50.
- [22] D. Liljequist and M. Ismail, Nucl. Instr. Meth. Phys. Res. A 239 (1985) pp. 273- 280.
- [23] A. P. Kuprin, A. A. Novakova, Yu. A. Durasova and S. I. Kharat’yan, Pribory i Technika Éksperimenta, No. 2, pp. 216-222, March-April 1992.
- [24] A. P. Kuprin and A. A. Novakova, Nucl. Instr. Meth. B62 (1992) pp. 493-504.

## **8. CONCLUSIONS AND FUTURE WORK**

In this study DWI tinplated steel cans have been analysed along with the material used to form such cans. This work is supplemented by more detailed analysis of the formation of Fe-Sn intermetallic layers on controlled laboratory produced samples and some attempts to improve intermetallic signal determination.

<sup>57</sup>Fe Conversion Electron Mössbauer Spectroscopy (CEMS) has been used to try to identify intermetallic products in commercially and laboratory produced tinplated steels. Scanning Electron Microscopy (SEM), X-Ray Diffraction (XRD), <sup>119</sup>Sn transmission geometry Mössbauer analysis, Inductively Coupled Plasma Mass Spectrometry (ICP-MS) and Glow Discharge Optical Emission Spectrometry (GDOES) have been used to complement the CEMS work within this study.

It was prudent to analyse the sheet materials before can processing to determine whether any subsequent observations of the DWI cans could be attributed to DWI processing or were observable prior to such processing. Analysis of the sheet steel using SEM showed a highly grooved surface resulting from the rolling of the sheet material to the desired thickness. Subsequent electrodeposition of tin onto the steel sheet would therefore give rise to a non-uniform sheet material with varying tin thickness. Indeed the final form of the DWI cans was that of a grooved steel substrate with grooves occupied by the tin, outside of which little tin was seen and the substrate was prevalent, indicating that the initial sheet steel topography affects the final can structure and topography.

The sheet material commercially electrodeposited with tin showed no sign of intermetallics on either side of the sheets, even after etching, indicating that the electrodeposition procedure used was not conducive to such intermetallic formation. The etched sheets when analysed using CEMS showed only an  $\alpha$ -Fe signal that was observed to be equal on both sides as would be expected when no intermetallics are present. In an unetched state the CEMS signal from the two sides of the sheets differed. This is in contrast to what was expected as the can material is expected to have coating weight  $2.8 \text{ g cm}^{-2}$  and to be even on both sides. Thus the coating weights on the two sides of the sheet tinplate could be an area of future study. Given that there are no identified intermetallics on the tinplate it is clear that the subsequent identification of intermetallics on the can walls are a product of the DWI manufacturing process.

Analysed by using  $^{57}\text{Fe}$  CEMS, the as-produced DWI cans show no evidence of intermetallic formation. Analysis using the SEM shows an uneven tin layer, which is due to the deformation of the tinplate material during the various stages of can processing. The SEM analysis of the processed cans shows areas of tin occupying vertical valleys in the steel substrate. Such valleys arise from the drawing of the uneven sheet tinplate material. All the valleys appear vertically on the can walls but the can bases, formed using compressive forces with a domed punch, show much less material deformation and none of the valleys that are observed on the can walls. Other markings on the can walls are shown to be generally perpendicular to the valleys and are formed after the wall ironing stage of production. They are postulated to be due to

the contact of the cans with barriers on the conveyors of the production line since the markings are across both tin and steel areas.

From the CEMS analysis the tin appears to be more prevalent on the inside of the can wall and is more concentrated at the top of the wall. From the SEM analysis the variation is more clearly defined on the outer can wall with the inner can wall having more uniform tin distribution. However the difference observed using the SEM is small and thus this analysis proves relatively inconclusive in this respect. Such differences in tin concentration could be due to the frictional forces acting on the inner and outer can wall being different or, as identified in the analysis of the matte tinplate, different coating weights on the two sides of the tinplate material. More in depth analysis of the process, perhaps using more precise coating weights, could be an area for future study. The can bases are observed to have a more uniform tin coating which is much thicker than that found on the can walls, which is expected as the can base does not have such an overall reduction in thickness nor is it subject to the same frictional forces.

EDX analysis indicates a low concentration of carbon on the sample surfaces and  $^{119}\text{Sn}$  Mössbauer analysis shows some  $\text{SnO}_2$ , which has formed on the exposed tin surface. The carbon does not seem to be in the form of cementite to any detectable concentration when using  $^{57}\text{Fe}$  CEMS. GDOES analysis shows a gradual falloff of tin signal with increasing depth into the surface. This falloff rather than a specific cut off level was attributed to be unevenness of the sample surface with the tin occupying the

unknown depth valleys in the steel substrate. The tin signal in the GDOES analysis is relatively insignificant below a depth of 500 nm.

Observations of washed and lacquered cans indicate that these processing steps lead to reduced CEMS signals and difficulties in making observations using other surface sensitive techniques. The lacquering process introduces an inert layer by its very definition. However the wash process appears to also introduce an inert layer, reducing the signal in CEMS. Further work analysing the wash process could reveal the reasons for such a decrease in signal. For these studies unwashed cans were analysed before any lacquering process was applied to the cans.

A method of helping to distinguish intermetallics at the interface of the steel and tin on the cans was required in order to determine categorically whether or not intermetallics existed. By removing the tin overlayer, found on the DWI cans, by etching using a potassium iodate and sodium hydroxide solution, any intermetallics from the uppermost surface layer of the samples can be more readily identified by CEMS as the tin is removed whilst leaving any intermetallics intact.

Commercially produced DWI tinplate etched and subsequently analysed using CEMS shows some signs of intermetallics on the ironed walls, where temperatures reach 200 °C during processing, but no intermetallics are observed on the can bases where mainly compressive forces have been used to compact the tinplate to a required thickness.

In all of the  $^{57}\text{Fe}$  CEMS analysis within this study the intermetallics identified were of the form of  $\text{FeSn}_2$ . This is due to a combination of factors. Firstly the maximum temperature of any material analysed here is only slightly higher than the tin melting point. Indeed the maximum temperature of the DWI is less than the melting point. Secondly the time of heat treatment of any samples is low, very low for the can processing being seconds as opposed to minutes for some of the heat treatments in the laboratory. Finally the weight percentage of tin at the interface is said to be initially 100% a concentration at which  $\text{FeSn}_2$  formation is prevalent. The parameters of the intermetallics identified were  $H = 11.2 \pm 0.2 \text{ T}$  and  $\delta = 0.52 \pm 0.02 \text{ mm s}^{-1}$  with no quadrupole interaction, comparable to bulk  $\text{FeSn}_2$  analysis by other researchers.

Unfortunately the analysis of the etched material using  $^{119}\text{Sn}$  Transmission Mössbauer spectroscopy produced a signal comprising only of a low level of  $\text{SnO}_2$  because of an inadequate etch. An area of future work would certainly be to analyse further the DWI cans using  $^{119}\text{Sn}$  Mössbauer spectroscopy, using longer etch times. The benefit of such analysis is that only the intermetallics would be identified as the metallic element under examination would be removed. SEM analysis of the etched cans revealed in further detail the topography of the steel can with vertical valleys formed from the high friction drawing and ironing procedure of the already uneven base material.

What may be drawn from this study is that even with fast can formation times on the production line, the ironing process, which is previously found to introduce temperatures in the material up to  $200 \text{ }^\circ\text{C}$ , is likely to produce very low levels of  $\text{FeSn}_2$  at the iron-steel interface. The effect of such an amount of intermetallic product

is undetermined and should be considered for future study by the use of corrosion tests and other material properties tests.

The flowbrightened tinplate analysed during this study clearly exhibited evidence of intermetallics on both sides of the sheets of tinplate. The parameters for the intermetallic sextets are close to those of FeSn<sub>2</sub> and this is therefore the likely phase present. When etched the spectra for both sides of the sheets are very similar with 17.2% of the overall signal area for the upper side being due to the FeSn<sub>2</sub> component and 19.2% FeSn<sub>2</sub> for the reverse side. The difference in FeSn<sub>2</sub> concentration is postulated to be due to either slightly uneven heating or quenching after heating.

Compared to the matte tinplate, which is used to form the DWI cans, the flowbrightened tinplate exhibits a reduced  $\alpha$ -Fe signal as the intermetallic layer forms the uppermost layer of the sample. The high surface sensitivity of the CEMS technique means that a thin intermetallic layer will be identified whilst the substrate signal is significantly reduced.

On the marked matte tinplate it is difficult to identify the material that forms the dark markings. CEMS analysis revealed a slightly greater signal for iron in the marked areas prior to etching and again after etching where the non-marked area exhibited a greater FeSn<sub>2</sub> signal. The SEM analysis showed two very different surfaces with the unmarked area being composed of a tin coated surface with exposed iron islands and the marked area composed of more globular formation of tin on the steel substrate. Thus it appears likely that the dark markings are contamination on the steel substrate

prior to plating that prevents tin forming a homogenous layer. However the contaminant was not identified and further work could be carried out in this area in order to help reduce this defect.

From the analysis of the as-produced cans it is clear that the intermetallics are difficult to detect without further sample treatment. Etching of the sample gives a greater signal from the steel substrate and any Fe-Sn intermetallics present. Heat treatment fundamentally alters the sample structure, in particular the composition of the interface between the steel substrate and tin coating, however in order to further investigate the production of intermetallics a series of heat treatments were carried out. Heat treatment of both the commercially produced DWI material and the laboratory produced electrodeposited sheet steel gave rise to an FeSn<sub>2</sub> layer formed at the tin-steel interface.

By heat treating the laboratory produced samples created under controlled conditions, intermetallics have been formed and identified as FeSn<sub>2</sub> using CEMS. The complementary XRD also showed clear evidence of FeSn<sub>2</sub> and no other intermetallic product. The glancing angle XRD analysis was better at identifying the surface dwelling FeSn<sub>2</sub> as the intermetallics occupy a thin surface layer. The formation of these intermetallics at different temperature and time heat treatment has been investigated.

The heat treatments of the tin electroplated steel substrates have shown that the formation of FeSn<sub>2</sub> occurs down to 190 °C, where the signal in the spectrum from <sup>57</sup>Fe

CEMS analysis is only just observable above the background. This minimum temperature is below the temperature observed in DWI processing but is applied for a longer length of time than in such processing.

This analysis of the heat treatment parameters has shown that temperatures observed in the can processing are certainly high enough to form intermetallics. A small amount of intermetallics will be formed even with short heating times, which will then subsequently affect the mechanical and chemical properties of the cans. GDOES showed the depth range of any tin in the samples to be 10 nm, this would be in the form of  $\text{FeSn}_2$ .

The applicability of a method for helping to distinguish substrate and surface layer signals is also shown and discussed in the results included herein. The carbon coating was shown to have much less photoelectron production and emission than surface sensitivity analysis experiments with other coatings. Therefore carbon was used to coat a sample of steel with surface dwelling intermetallics. A 20 nm thickness of carbon was deposited on the sample surface. This thickness was chosen as being suitable from the earlier experiments into photoemission from the carbon layer, as the overall signal was decreased compared to the uncoated substrate. Thus by applying the carbon layer to such samples it was hoped that some preferential reduction of substrate signal would be observed.

The carbon coat was found to preferentially reduce the  $\alpha$ -Fe signal from the substrate compared to the signal from the intermetallic surface layer. In terms of peak counts,

peaks 2 and 5 were reduced to 53% of the value prior to coating, whereas the signal from the FeSn<sub>2</sub> intermetallics was not significantly reduced being 98% of the value prior to coating. The relative area of the  $\alpha$ -Fe is reduced when carbon coated from 88.3% to 79.8% and the relative area of the FeSn<sub>2</sub> is increased from 11.7% to 20.2%. Thus the application of the carbon coating allows the differentiation between substrate and surface signals, and can in some cases thus allow for easier identification of low levels of surface dwelling compounds. However it should be noted that the surface layer signal is also slightly reduced and thus with very low levels of identifiable surface compound the technique could prove to be detrimental in its use.

In the case analysed here this technique proves to be a simple and non-destructive way of making the CEMS technique, using a gas-flow proportional counter, more surface sensitive without any equipment alteration.

The effect of steel surface roughness on the electrodeposition and subsequent identification of the intermetallics formed has also been investigated and increased roughness was found to effectively increase the substrate signal. The talysurf was used to accurately analyse the substrates before electrodeposition. The electrodeposition procedure was shown to deposit approximately 2  $\mu\text{m}$  of tin assuming a compact layer. However the layer is formed of crystallites or globular formations, which are not ideally compact.

Smaller crystalline formations were observed from the electrodeposition onto rougher surfaces compared to the smoother surfaces. The heat treatments subsequently applied

to the range of samples formed a layer of FeSn<sub>2</sub>, which has been observed with both CEMS and XRD. The analysis using CEMS then shows increased substrate signals for increasingly rough samples with the signal from the FeSn<sub>2</sub> remaining fairly constant throughout the range of samples. This effect was found to be due to the presence of intermetallics, since rough substrates without intermetallic overlayers showed little difference when analysed using CEMS, much less than with the FeSn<sub>2</sub> layer.

The results from the glancing angle XRD analysis follow the trend of the CEMS analysis where for the smoothest sample only an FeSn<sub>2</sub> signal is obtained in the GA-XRD trace when there is the greatest FeSn<sub>2</sub> signal in the corresponding CEMS spectrum. However there is still some  $\alpha$ -Fe signal in the CEMS spectrum indicating that a greater depth is analysed using CEMS than GA-XRD. For a sample of intermediate roughness the ratio of the sum of the integrated intensity of GA-XRD peaks for FeSn<sub>2</sub> to Fe was 34 : 1 decreasing to 6 : 1 for the roughest sample.

Thus it has been observed that, prior to processing, the tinplate used to form DWI cans does not contain intermetallics at the iron-tin interface. The observation of intermetallics in the can walls after the drawing and wall ironing procedures indicates that during processing conditions arise that are favourable for intermetallic growth. The intermetallic formed is of the FeSn<sub>2</sub> type and subsequent analysis of intermetallic growth simulating different heating conditions of tinplate also gives rise to FeSn<sub>2</sub> formation. No other intermetallics are identified. Surface roughness is shown to have an effect on the deposition and analysis of tinplate samples using CEMS, rougher samples leading to more exposed substrate, but similar amounts of identified

intermetallics after identical sample heat treatments. Carbon coating of the sample surfaces is identified as being a suitable method to help distinguish substrate and near surface signals giving rise to reduced substrate signals compared to the near surface layer. In previous studies using heavier element materials such signal differentiation reduced near surface signals more than the substrate signal. Further research should be carried out to investigate the effect of the intermetallics on the corrosion resistance of the cans as well as their effect on other properties such as lacquer adhesion, can strength and deformation resistance. This will help to determine whether the intermetallics formed are detrimental to the properties of DWI tinplated steel cans.

**APPENDIX 1 : Carbon Evaporation Calculations**

## Carbon Rod Evaporation Calculations

The carbon is sputtered from the carbon source, which consists of a pointed carbon rod forced against a second rod with a 45° angle surface, figure A1.1.

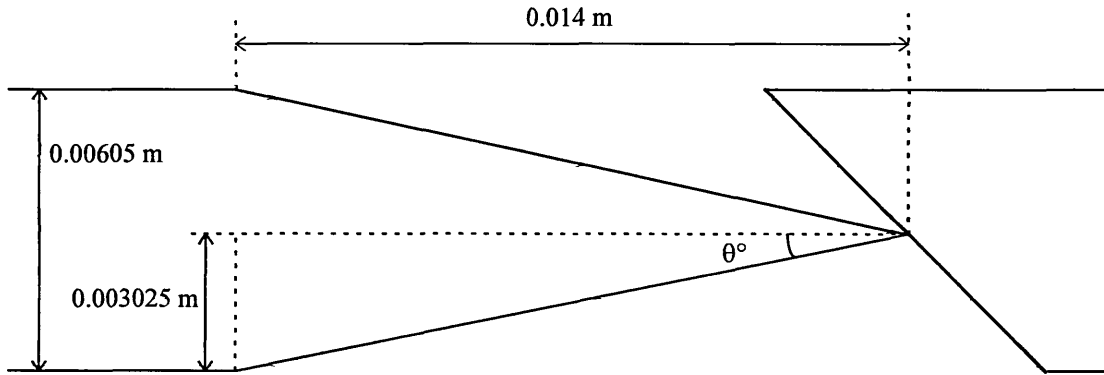


Figure A1.1. Carbon rod arrangement.

Angle  $\theta$  is calculated as follows,

$$\tan \theta = \frac{0.003025\text{m}}{0.014\text{m}}$$

$$\theta = \tan^{-1}\left(\frac{0.003025\text{m}}{0.014\text{m}}\right)$$

$$\theta = 12.2^\circ$$

A diagram of the cross section of carbon sputtered from the rod is shown in figure A1.2 where  $t$  is the distance of carbon rod travel. In this case  $t$  is set to 3mm. All relevant angles have been included.

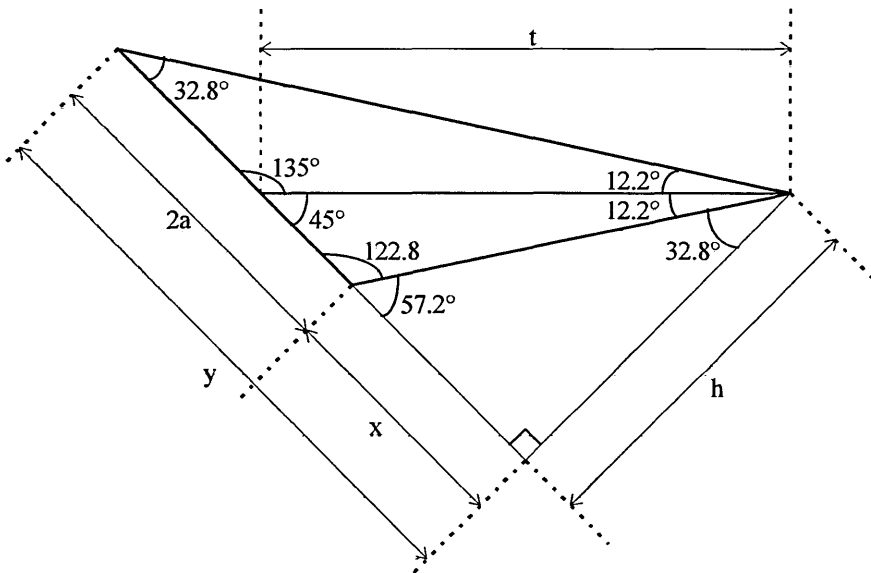


Figure A1.2. Sputtered carbon rod cross section.

Since the cone is oblique height  $h$  is required in order to calculate the volume. The base area is elliptical and therefore the distance  $2a$  is required. The base area will be the area of the ellipse defined by the length of the major axis,  $2a$ , and the length of the minor axis,  $2b$ .

To calculate  $h$ , the height of the oblique cone we can use simple geometry as shown in figure A1.3.

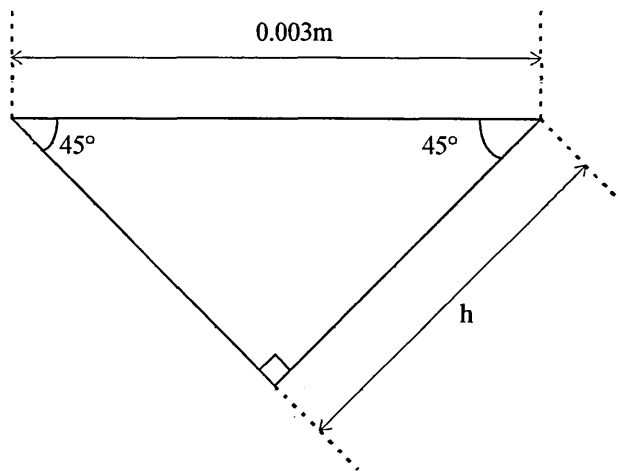


Figure A1.3. Diagram for calculation of oblique cone height.

$$\cos 45^\circ = \frac{h}{0.003\text{m}}$$

$$h = 0.003\text{m} \times \cos 45^\circ$$

$$h = 2.12 \times 10^{-3}\text{m}$$

For the calculation of the major axis diameter,  $2a$ , values for  $x$  and  $y$  need to be calculated. The diagram for calculation of  $x$  is shown in figure A1.4. The diagram for calculation of  $y$  is shown in figure A1.5.

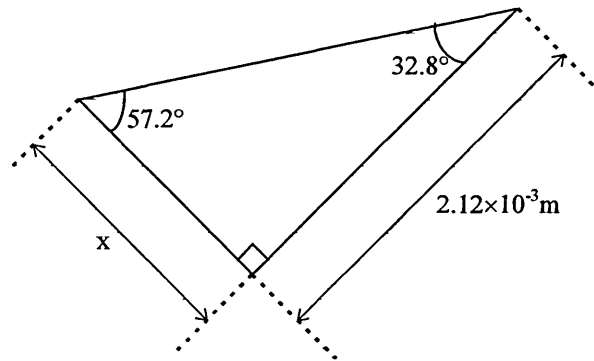


Figure A1.4. Diagram for calculation of distance  $x$ .

$$\tan 32.8^\circ = \frac{x}{2.12 \times 10^{-3}\text{m}}$$

$$x = 2.12 \times 10^{-3}\text{m} \times \tan 32.8^\circ$$

$$x = 1.37 \times 10^{-3}\text{m}$$

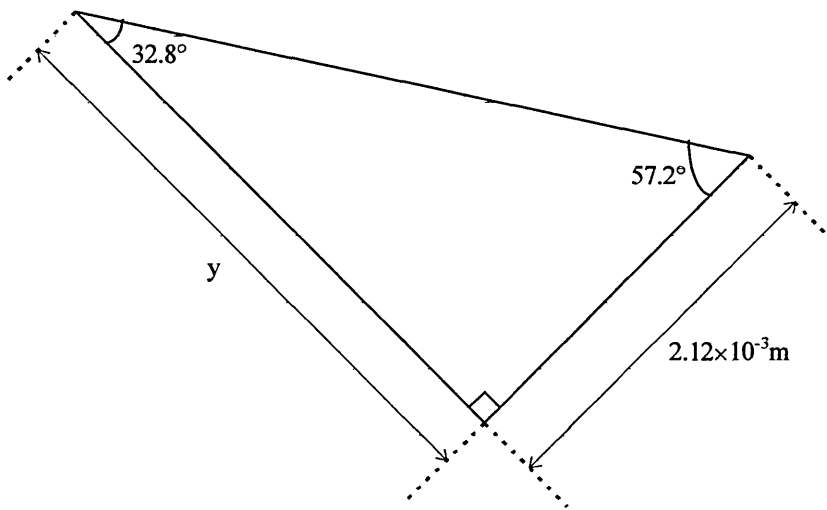


Figure A1.5. Diagram for calculation of distance  $y$ .

$$\tan 57.2^\circ = \frac{y}{2.12 \times 10^{-3} \text{ m}}$$

$$y = 2.12 \times 10^{-3} \text{ m} \times \tan 57.2^\circ$$

$$y = 3.29 \times 10^{-3} \text{ m}$$

Therefore, with the values of  $x$  and  $y$ ,  $2a$  can be calculated as follows,

$$2a = y - x$$

$$2a = 3.29 \times 10^{-3} \text{ m} - 1.37 \times 10^{-3} \text{ m}$$

$$2a = 1.92 \times 10^{-3} \text{ m}$$

The minor axis diameter,  $2b$ , is simply found by calculating the diameter of a normal right cone. In this case the carbon rod travel is 3 mm and the diameter of a 3 mm right cone base is shown in figure A1.6.

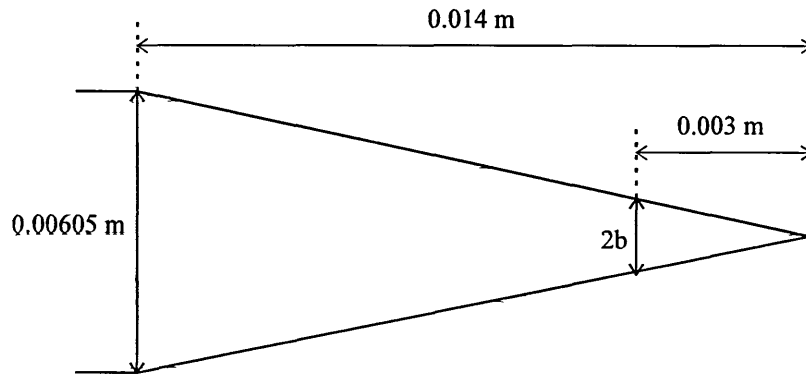


Figure A1.6. Diagram for calculation of 3mm high right cone diameter.

$$\frac{2b}{0.003\text{m}} = \frac{0.00605\text{m}}{0.014\text{m}}$$

$$2b = 0.003\text{m} \times \frac{0.00605\text{m}}{0.014\text{m}}$$

$$2b = 1.30 \times 10^{-3} \text{ m}$$

The major and minor axes of the ellipse, calculated previously, define the following ellipse, shown in figure A1.7.

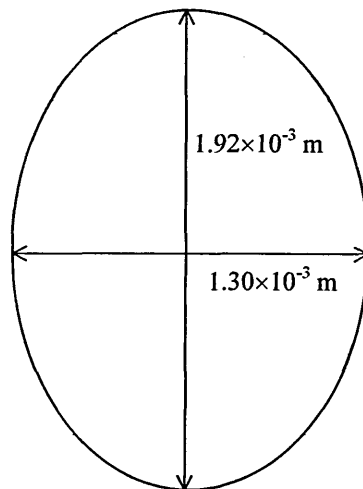


Figure A1.7. Elliptical base of sputtered carbon cone.

The area of this ellipse is defined as  $B = \pi ab$  where the major axis has diameter  $2a$  and the minor axis has a diameter  $2b$ . Thus,

$$a = 0.96 \times 10^{-3} \text{ m}$$

$$b = 0.65 \times 10^{-3} \text{ m}$$

$$B = \pi \times 0.96 \times 10^{-3} \text{ m} \times 0.65 \times 10^{-3} \text{ m}$$

$$B = 1.96 \times 10^{-6} \text{ m}^2$$

The volume of the cone,  $V$ , is given by,

$$V = \frac{1}{3} \pi B h$$

And so the volume is,

$$V = \frac{1}{3} \pi \times (1.96 \times 10^{-6} \text{ m}^2) \times (2.12 \times 10^{-3} \text{ m})$$

$$V = 4.35 \times 10^{-9} \text{ m}^3$$

If it is assumed that the carbon is evaporated from the point of contact for the two carbon rods, evenly over the chamber base, and we assume a cone of coverage partially limited by the angle produced by the contact of the two carbon rods we can calculate an area of carbon coverage and hence a thickness of carbon coating. The area covered below the source is inevitably complex due to the complexity in geometry of the source, however using the simplified case of a cone of evaporated carbon from the source will lead to an approximation of carbon thickness. A number of other assumptions must also be made. Of all the carbon sputtered from the carbon source some will travel upwards leaving less to coat the samples however there is a small

amount of carbon sputtered from the rod angled at 45°, which will increase carbon coat thickness. It is also likely that there may be more carbon deposited directly below the carbon source, but this difference remains unquantified. By assuming all of these other effects to be negligible and that there is an even cone of carbon evaporated then an area of coverage can be calculated using figure A1.8.

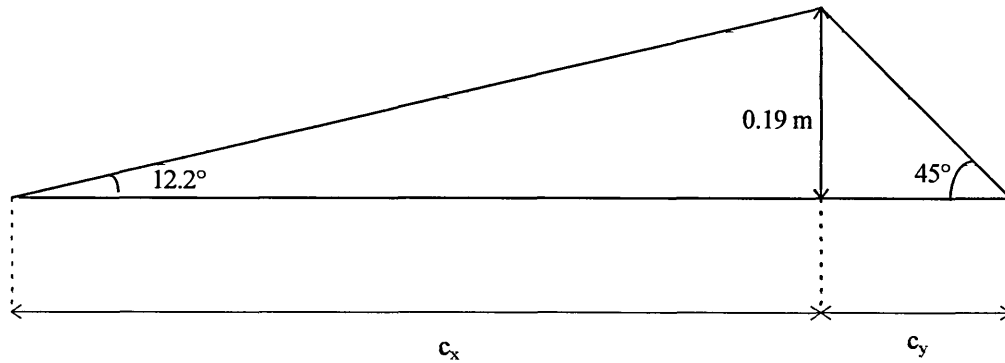


Figure A1.8. Cross section of cone of coverage.

The source of carbon is 0.19 m above the sample stage and with the angles defined by the minimum angle between the two carbon rods shown in figure A1.8. The diameter of the base of the cone of carbon can be calculated as the distance  $c_x + c_y$ , where the following show the calculated  $c_x$  and  $c_y$  values.

$$\tan 12.2^\circ = \frac{0.19\text{m}}{c_x}$$

$$c_x = 0.879\text{m}$$

$$\tan 45^\circ = \frac{0.19\text{m}}{c_y}$$

$$c_y = 0.190\text{m}$$

Therefore,

$$c_x + c_y = 1.069\text{m}$$

And so the area covered by the carbon at the level of the sample stage,  $A_c$ , is,

$$A_c = \pi r^2 = \pi \left( \frac{1.069\text{m}}{2} \right)^2 = 0.898\text{m}^2$$

And thus the thickness of carbon on the samples,  $c$ , is given simply by,

$$c = \frac{4.35 \times 10^{-9} \text{m}^3}{0.898\text{m}^2} = 4.85 \times 10^{-9} \text{m}$$

The same calculations can be made for 4mm, 5mm and 6mm carbon rod travel when  $t = 0.004\text{m}$ ,  $0.005\text{m}$  and  $0.006\text{m}$  respectively. The diagram of the cross section of carbon sputtered from these rods is the same as that shown in figure A1.2.

Following the same calculations for these carbon rod travel distances we obtain the following carbon thickness values.

$$\text{When } t = 0.004\text{m } c = 11.65 \times 10^{-9} \text{m}$$

$$\text{When } t = 0.005\text{m } c = 22.53 \times 10^{-9} \text{m}$$

$$\text{When } t = 0.006\text{m } c = 38.96 \times 10^{-9} \text{m}$$

**APPENDIX 2 : Courses and Events Attended**

## **Courses Attended**

Research Methods (15 M credits) – Including taught units on electron microscopy and crystallography and X-ray techniques.

Research Studies (15 M credits) – Including units on project planning and management, literature analysis and oral and written communication.

## **Events Attended**

Postgraduate induction day, Sheffield Hallam University, Tuesday 20<sup>th</sup> October 1998.

MRI day, Materials Research Institute, Sheffield Hallam University, 25<sup>th</sup> May 1999.

Mössbauer Conference, Greenwich, England, 2000.

ICAME 2001 Mössbauer Conference, Oxford, England, 2<sup>nd</sup> September – 8<sup>th</sup> September 2001.

### **APPENDIX 3: Publications**

# $^{57}\text{Fe}$ Conversion Electron Mössbauer Spectroscopy of Factors Influencing Fe–Sn Intermetallic Phase Formation in Tinpated Steel

R. A. ELLIS<sup>1</sup>, S. D. FORDER<sup>1</sup>, T. H. ENGLISH<sup>2</sup> and C. BREEN<sup>1</sup>

<sup>1</sup>*Materials Research Institute, Sheffield Hallam University, Sheffield S1 1WB, UK*

<sup>2</sup>*Corus plc, Swinden Technology Centre, Rotherham, UK*

**Abstract.** The formation of intermetallic phases influences the properties of commercial alloys. CEMS can be used to reveal the presence of Fe–Sn intermetallics at the interface on tinplated steels. The work presented investigates the sensitivity of CEMS to detect intermetallics. Varying amounts of Fe–Sn intermetallics have been identified by CEMS having been produced by heat treating samples of tinplated steel at selected temperatures and times. The effect of surface roughness of the substrate on the Mössbauer signal has also been investigated. The intermetallic formation was found to reach a limiting value with increased heat treatment. Using CEMS, intermetallic formation was observed at temperatures as low as 190°C. Sample roughness was found to affect intermetallic formation and their observation using CEMS and GA-XRD.

## 1. Introduction

Fe–Sn intermetallics have been previously investigated using Mössbauer Spectroscopy [1]. The effect of sample surface roughness in Integral Conversion Electron Mössbauer Spectroscopy (ICEMS) and Depth Selective CEMS has been investigated in a number of studies [2–4]. The aim of this study was to observe the formation of  $\text{FeSn}_2$  intermetallics on samples of heat treated tinplate and the effect of substrate roughness on the electrodeposition of tin onto steel substrates and subsequent heat treatment of those samples.

## 2. Experimental

The samples analysed in this study are polished mild steel substrates onto which tin was subsequently electrodeposited. The samples were heat treated in a tube furnace for the required time under a flow of nitrogen in order to prevent oxidation. CEM spectra were obtained in a gas flow proportional counter using 95% He and 5%  $\text{CH}_4$ . A mylar window, fixed between the collimator and the main body of the detector absorbs the Fe K X-rays without significant absorption of the 14.4 keV  $\gamma$ -rays thus reducing the creation of non-resonantly produced electrons. The sample constitutes the cathode and the application of a positive 1.2 kV to a 25  $\mu\text{m}$

diameter stainless steel anode enables the detection of the 7.3 keV conversion and 5.6 keV Auger electrons. Spectra were fitted using a Lorentzian site analysis software package [5] and calibration is relative to  $\alpha$ -Fe.

A set of samples was heat treated at 240°C for 1, 2, 5 and 10 minutes to investigate the intermetallic formation with time. A second set of samples was heat treated for 2 minutes at temperatures between 190°C and 240°C to investigate the amount of intermetallics formed and detected by CEMS. This would help in the identification of the lower detection limit of CEMS. Inductively Coupled Plasma Mass Spectrometry (ICP-MS) has been used to find the concentration of tin in these samples.

A third area of work examined the roughness of sample surfaces and the effect on the formation and detection by CEMS of intermetallics on these sample surfaces. CEMS experiments were carried out on equal sample areas for the same experiment time. Mild steel substrates were ground to selected roughness levels and the roughness determined using a Taylor Hobson 120L laser form talysurf. These samples were electroplated with a 2  $\mu\text{m}$  coating of tin and then heat treated in the tube furnace under nitrogen for 10 minutes at 240°C. Glancing Angle X-Ray Diffraction (GA-XRD), incident angle  $\alpha = 1^\circ$ , was carried out on these samples using a Philips PW3710 diffractometer. For all three series of experiments the excess tin was removed after heat treatment by etching with a solution of 50 g/l NaOH and 10 g/l  $\text{KIO}_3$ .

### 3. Results and discussion

All CEM spectra, e.g., Figure 1, show sextets for (a)  $\text{FeSn}_2$ ,  $CS = 0.52 \pm 0.02 \text{ mm s}^{-1}$ ,  $H = 11.2 \pm 1.0 \text{ T}$  and (b) mild steel,  $CS = 0.00 \pm 0.02 \text{ mm s}^{-1}$ ,  $H =$

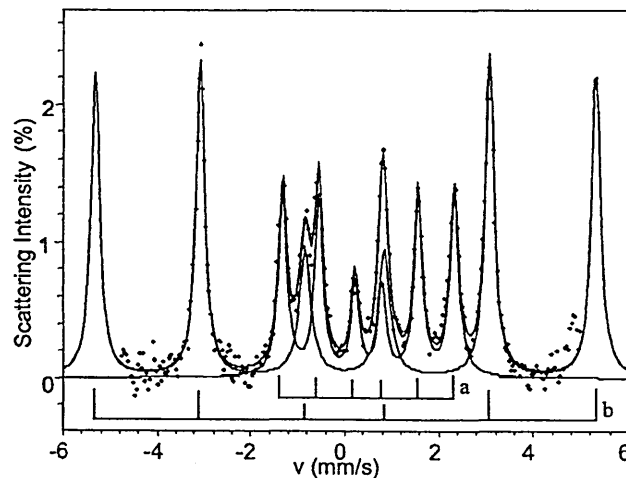


Figure 1. Typical CEM Spectrum showing Fe and  $\text{FeSn}_2$  sextets.

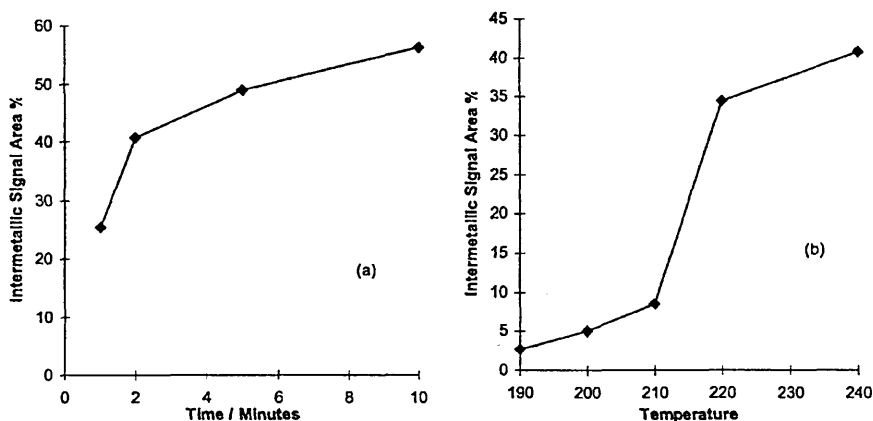


Figure 2. Results for (a) varying heating time at 240°C and (b) varying heating temperature, for 2 minutes.

$33.0 \pm 1.0$  T, with no observed FeSn phase, and this work uses the % area of the sextets to follow the formation of the intermetallics. The levelling off of the amount of FeSn<sub>2</sub> formed at longer heating times shows the transport of the tin into the steel substrate reaches a limiting value, Figure 2(a). The FeSn<sub>2</sub> layer forms a barrier to further diffusion and further intermetallic production. Figure 2(b) shows that the diffusion of tin and steel substrate occurs down to temperatures as low as 190°C where the percentage of the FeSn<sub>2</sub> sextet is only 2.7% and only just distinguishable from the background. Much more intermetallic formation occurs at temperatures near the melting point of tin, and it decreases significantly below 220°C. A comparison of the ppm concentrations for Sn and Fe in acid digested solution from Inductively Coupled Plasma Mass Spectrometry (ICP-MS) analysis confirms the decrease in the amount of Sn, in the form of FeSn<sub>2</sub>, from 2.92% at 240°C to 2.39% at 190°C.

The effect of surface roughness on the CEMS signal is shown in Figure 3, with the roughness values shown in Table I. To determine whether the increase in substrate signal was due to increased effective surface area or the presence of FeSn<sub>2</sub>, CEM spectra were obtained from two samples of mild steel, one polished with 1 μm diamond paste and the second ground with P120 grit paper.

The signals from the two samples agree within experimental limits, indicating that the increase in substrate signal with increasing roughness, Figure 3, can be attributed to the presence and distribution of the FeSn<sub>2</sub>. No FeSn<sub>2</sub> signal increase is seen. This effect is especially prevalent when the average roughness increases above 0.2 μm towards the value of the escape depth of the K-conversion electrons, ~ 0.3 μm.

The FeSn<sub>2</sub> signal suggests that with rougher samples a similar amount of FeSn<sub>2</sub> is formed over the larger effective surface area, while peaks of substrate protrude above the FeSn<sub>2</sub> layer in the rougher samples. In smoother samples the FeSn<sub>2</sub>

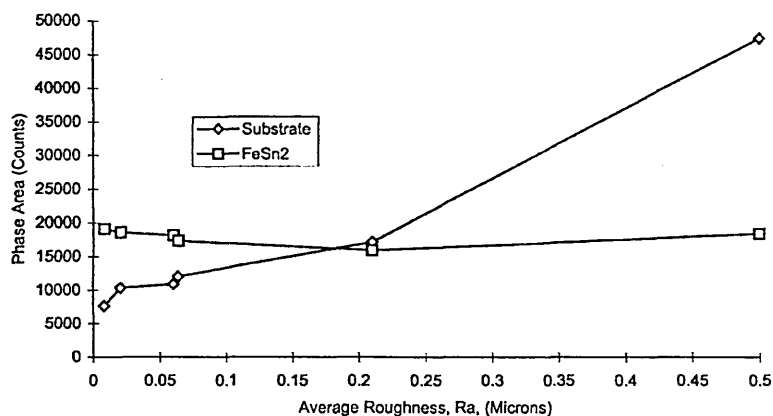


Figure 3. Graph of signal for phase area versus average roughness  $R_a$ .

Table I. Talysurf measurements of sample roughness

Sample identification	Average roughness ( $R_a$ ) [ $\mu\text{m}$ ]	Error (average deviation from mean of results) [ $\mu\text{m}$ ]	Max. peak to valley distance ( $R_t$ ) [ $\mu\text{m}$ ]
1mic	0.008	0.002	0.066
6mic	0.021	0.004	0.313
p1200	0.060	0.013	0.693
p600	0.064	0.008	0.764
p240	0.210	0.012	2.965
p120	0.500	0.045	7.574

suppresses the substrate signal. These results agree with those from GA-XRD where for the smoothest sample only an FeSn<sub>2</sub> signal was obtained. For a sample of intermediate roughness the ratio of the sum of the integrated intensity of peaks for FeSn<sub>2</sub> to Fe was 34 : 1 decreasing to 6 : 1 for the roughest sample.

The electrodeposited tin was less than 2  $\mu\text{m}$  thick so that for the two roughest samples, upon reaching the tin melting point, tin reflowed into the valleys exposing substrate peaks. The two largest peak to valley distances, Table I, highlight that the reflowed tin will leave greater protrusions of the substrate on the rougher samples.

#### 4. Conclusions

CEMS has been able to detect different amounts of FeSn<sub>2</sub> formed under different heat treatment conditions. The limit of detection for this system was identified as 2.39% Sn, in the form of FeSn<sub>2</sub>, using ICP-MS for the sample heat treated at 190°C for 2 minutes.

The CEMS and GA-XRD study of samples of selected roughness suggests that the intermetallics do not form a homogeneous layer in that the substrate signal increases with increasing roughness.

### Acknowledgements

The author acknowledges the assistance of Mr. M. Jackson during the talysurf work, Mr. P. Burbidge during the roughness analysis, Dr. P. Gardiner during the ICP-MS work, Dr. B. Lewis during the XRD work and the financial support of Corus plc and the MRI.

### References

1. Van Der Kraan, A. M. and Buschow, K. H. J., *Physica* **138B** (1986), 55.
2. Liljequist, D. and Ismail, M., *Nucl. Instr. Meth. Phys. Res. A* **239** (1985), 273.
3. Kuprin, A. P., Novakova, A. A., Durasova, Yu. A. and Kharat'yan, S. I., *Pribory i Tekhnika Éksperimenta* **2** (1992), 216.
4. Kuprin, A. P. and Novakova, A. A., *Nucl. Instr. Meth. Phys. Res. B* **62** (1992), 493.
5. Lagrec, K. and Rancourt, D. G., Recoil: Mössbauer spectral analysis software for windows (1998), <http://www.physics.uottawa.ca/~recoil/>.